Imperial College London

Department of Materials

Bioactive glass scaffolds for wound healing

Elizabeth Norris

February 2019

Submitted for the degree of Doctor of Philosophy (PhD)

ABSTRACT

Bioactive glasses are an exciting group of materials used in regenerative medicine. They are designed to degrade in the body, releasing therapeutic ions which have been shown to provide a beneficial response *in vivo*. Traditionally used in bone regeneration, they are now being investigated for use in wound healing applications. A major challenge is to produce a material for wound healing that promotes cellular activity, e.g. angiogenesis, and that has a structure which is easy for clinicians to insert into wounds. Bioactive glasses are very flexible compositionally, allowing metal oxides to be incorporated into the bioactive glass structure, providing a range of potentially valuable therapeutic properties for wound healing.

When wounds fail to heal following the usual pathways, they are at risk of becoming chronic and can place a significant burden on the patient and on the healthcare system. Chronic wounds are caused by a number of different routes, however foot ulcers in diabetic patients are some of the most common. Improving angiogenesis and the supply of nutrients to the wound bed should improve healing. Copper is known to stimulate vascular endothelial growth factor (VEGF) expression in several cell types (such as in endothelial cells and in human bone marrow stromal cells) and promote angiogenesis. In this thesis, copper ions were incorporated into a sol-gel derived bioactive glass structure and were investigated for their ability to stimulate VEGF production by human dermal fibroblasts.

The bioactive glass compositions were fabricated by electrospinning which produced unique, copper containing, 3D cotton-wool-like structures. This 3D fibrous scaffold mimics the appearance of the extracellular matrix (ECM) and is ideal for packing into large defects such as wounds. The 3D scaffold structure was obtained through the control over relevant electrospinning and material properties which were identified through experimentation outlined in this thesis.

DECLARATIONS

Declaration of originality

I hereby certify that the work presented in this thesis is the result of my own research and investigations that was carried out at Imperial College London during the period of November 2014 to February 2019. Except where otherwise stated. Other contributors have been truly and properly acknowledged.

Copyright declaration

The copyright if this thesis rests with the author and is made available under a Creative Commons Attribution Non-Commercial No Derivatives licence. Researchers are free to copy, distribute or transmit the thesis on the condition that they attribute it, that they do not use it for commercial purposes and they do not alter, transform or build upon it. For any reuse or redistribution, researchers must make clear to others the licence terms of this work.

ACKNOWLEDGEMENTS

I would like to acknowledge and thank the Engineering and Physical Science Research Council for funding this project via Centre of Doctoral Training in Advanced Characterisation of Materials (CDT-ACM). The work outlined here would not have been possible without the support of my supervisors, the CDT directors, my colleagues and family.

I would like to thank Prof. Julian Jones for welcoming me into his research group and guiding me through this project. I am incredibly grateful for the help he has given me throughout, and for the wonderful opportunity to spend three months working with a research group in Japan at the Nagoya Institute of Technology (NITech). I owe him a great debt of gratitude for supporting me in developing my research and laboratory skills, helping me to gain confidence in my own academic abilities and through personal developments over the course of the PhD.

From UCL, I would like to thank Dr. Gavin Jell for making me feel part of his group at the Royal Free Medical School. His support in helping me undertake my cell work has been invaluable and I would have not achieved the results presented here without his help and the help of his group. I would particularly like to thank Carolina Ramos-Rivera for all her patience in guiding me through experiments and becoming such an important friend throughout the PhD.

My PhD would not have been possible without the CDT-ACM. I would like to thank Prof. Stephen Skinner and Dr. Neil Curson for supporting me throughout, and to Hafiza Bibi and Claire Smithson for all they do to make the CDT such a joy to be part of. I would like to extend my thanks to my cohort; Sofia, Tim, Nadir, Shiny, Jon, Martin, Mak and Josh who have helped me at every stage of the PhD and made it enjoyable throughout.

I would also like to extend my thanks to Prof. Toshihiro Kasuga and Prof. Akiko Obata from NITech who supported me through my first months of the PhD and have enabled me to be part of an amazing collaboration. I am particularly grateful to Prof. Akiko Obata and Qun Ju for teaching me the electrospinning and sol-gel process and for helping me design the initial stages of my project. I would also like to thank the group at the Department of Physics, University of Warwick for collecting NMR data for

my project, thank you to Dr. John Hanna, Dr. Joshua Clark and to Ms. Nicole Kelly for providing and helping me to interpret the results.

To Richard Sweeney and Victoria Bemmer, thank you for the help with XRD and for always being friendly and happy to help me. Also to Dr. David Payne who has consistently encouraged me in my research and provided training and guidance in XPS analysis. To Mahmoud Ardakani, Ecaterina Ware and Ben Chan, thanks for all the help with SEM, ICP and FTIR.

To my lab mates in my group at Imperial; you have made the last few years an absolute pleasure. I am very grateful to Dr Gowsihan Poologasundarampillai (Gowsh) for introducing me to my project and guiding me through the initial stages, to Dr Francesca Tallia (Fra) for all time she devotes to supporting and managing the group, and to Dr Silvia Rodrigues Mendes Ferreira for helping me to interpret my cell studies results. I would like to thank Dr Alessandra Pinna (Ale) for her help with the BET, Dr Parichart Naruphontjirakul for teaching me all I know about ICP-analysis and to Dr Breno Rocha Barioni for inviting me to collaborate with him on some exciting XPS studies. To everyone else in the group, you have made every day enjoyable and I couldn't have completed the PhD without you: Gloria, Zhen, Ali, Stella, Tian, Maria, Amy, Louise, Sarah, Anna, Anu and Hung-Kai.

Thanks you to my friends who have provided support over the past few years and to my family; my aunts and uncles, cousins, grandparents and to Will's family who have all played such a pivotal role in encouraging me.

Finally to my mum, Bea and Will. Thank you so much for all you have done for me over the years, I really could not have done this without your guidance and patience.

INTRODUCTION

The rise of chronic wounds

In recent years there has been an increasing need to produce treatments to heal chronic wounds. A worldwide surge in diabetes [1] and ageing population [2] has created an increased demand for treatments that can speed up healing and protection against infection. Chronic wounds are wounds that fail to heal in a timely manner or following the ordinary stages of healing that most wound healing progresses through [3]. Patients with wounds that fail to heal often have to spend significant time in recovery, either in hospital or at home. Chronic wounds on the leg or feet are particularly difficult as it may mean the patient has to be off their feet for long periods of time. In many cases wounds that fail to heal can become infected or continue to re-open. In few cases, wounds that fail to heal can result in amputations.

There are a large selection of products currently available to aid in the healing of wounds. Many of these include the use of skin substitutes and growth factors. These have both been shown to reduce healing times of chronic wounds, but also provide limitations in terms of their cost. Skin substitutes are vastly expensive and are usually only used when other options have been exhausted whereas the use of growth factors has to manage systematically for a sustained period of time.

The need for new materials

In recent years, the use of bioactive glasses have emerged as a promising solution to the problems of healing wounds. In tissue engineering strategies, scaffolds are used along with cells and ions to aid in the regeneration of tissue. The scaffolds can be placed in the body without rejection and provide a surface for which cells can proliferate on producing the desired tissue.

Research into the use of bioactive glasses have predominantly focused on its use for bone healing. Professor Larry Hench developed the first reported bioactive glass, Bioglass® in 1969, he found that Bioglass uniquely and successfully bonded with bone [4] . The original Bioglass 45S5 is comprised of 46.1 mol. % SiO_2, 24.4 mol. % Na_2O, 26.9 mol. % CaO and 2.6 mol. % P_2O_5 and has been used commercially as synthetic bone grafts as NovaBone® and Perioglas® (NovaBone Products LLC, Jacksonville FL), and additionally as an ingredient in toothpaste for hypersensitivity (GlaxoSmithKline, UK). Many other bioactive glass compositions have now been developed. One major advantage of using bioactive glasses is that they are very flexible compositionally. Produced either through a melt-derived or sol-gel derived route, different

metal oxides can be added which offer different valuable properties for wound healing amongst other things.

Many patients suffering from chronic wounds have complicated underlying conditions, such as diabetes, and have a weakened response to hypoxia. The role of hypoxia is to activate the Hypoxia Inducible Factor (HIF) which helps to stimulate proteins and the cellular response to the wound [5]. It has been shown that ions such as copper and cobalt can activate HIF improving the healing of chronic wounds. Copper bioactive glasses have shown promise in providing antibacterial properties and in promoting the process of angiogenesis in wound healing applications [6].

Outline of the thesis

In 2013, Poologasundarampillai *et al.* published a paper reporting the first successful electrospinning of a 3D fibrous bioactive glass scaffold with a structure similar in appearance and texture to cotton wool or cotton candy [7]. This 3D structure, which mimics the extracellular matrix (ECM) is ideal for packing into complex defects and is extremely novel. Typically, a 2D fibremat structure is produced when electrospinning bioactive glasses, so this structure is very different architecturally.

The general aim of this thesis is to produce a 3D electrospun bioactive glass which can provide controlled release of copper ions and be easily be packed into a wound environment and stimulate wound healing as it biodegrades.

The literature review presents an overview of chronic wounds and a summary of the current practices used to heal wounds. It highlights the development of bioactive glasses, their applications in wound healing and the impact of the incorporation of different ions on their structure, their ability to degrade and consequently, their impact in *in vitro* and *in vivo* studies. It investigates the use of electrospinning as a technique to produce sol-gel derived bioactive glass fibres and the factors that can affect the formation of desirable fibres. The experimental work is outlined in Chapters 4 – 7, and the final conclusions and further work are presented in Chapter 8.

In Chapters 4 and 5, bioactive glass compositions were electrospun in the silica-calcium system to produce 3D cotton-wool-like structures. The main focus was to identify and understand the mechanisms behind the creation of the 3D fibrous structure, to characterise them and to compare the compositions for their suitability in wound healing applications. The material and physical parameters for electrospinning were

investigated to optimise the production of uniform, regular and reproducible fibres. Dissolution and cellular studies were carried out on the dissolution product to determine the impact of the bioactive glass fibre compositions on the metabolic activity and the proliferation of cells. The impact of the compositions on the production of VEGF by human dermal fibroblasts (HDFs) was also investigated.

The second part of this thesis (Chapters 6 and 7) explores the use of copper in promoting angiogenesis. A single composition was selected from the results outlined in Chapter 4 and was doped with different quantities of copper producing copper-containing bioactive glass compositions. Several copper compositions were investigated in their potential to stimulate VEGF production by HDFs. Their degradation was studied, and cellular studies were carried out on the dissolution media to analyse the influence of copper on metabolic activity and cell proliferation. Materials characterisation techniques were employed in Chapter 6 to gain further insight into how the incorporation of copper effects the chemistry of the bioactive glass.

TABLE OF CONTENTS

ABSTRACT 1

DECLARATIONS 2

ACKNOWLEDGEMENTS 3

INTRODUCTION 5

TABLE OF CONTENTS 8

LIST OF FIGURES 12

LIST OF TABLES 17

LIST OF ABBREVIATIONS 19

CHAPTER TWO - LITERATURE REVIEW 20

2.1 The problem with healing wounds 21

2.1.1. Stages of wound healing 21

2.1.2. Chronic wound healing 23

2.1.3. Factors affecting wound healing 23

2.1.4. Role of hypoxia in wound healing 24

2.1.5. Current wound healing products and strategies 25

2.1.6. Role of VEGF in wound healing 26

2.1.7. The role of copper in VEGF and angiogenesis 27

2.1.8 Wound healing summary 28

2.2 Bioactive glasses 29

2.2.1. The structure of glasses 31

2.2.2. The mechanism of bioactivity 32

2.2.3. Making bioactive glasses 35

2.2.4. The sol-gel process 35

2.2.5. Variables affecting the sol-gel process 36

2.2.6. The glass making process 37

2.2.7. Bioactive glasses in wound healing 39

2.2.8. Different Cations 40
2.2.9. Borate glasses 43
2.2.10. Wound healing, bioactive glasses and HCA formation 45
2.2.11. Bioactive glasses summary 45
2.3. Electrospinning 46
2.3.1. Variables affecting electrospinning 48
2.3.2. Electrospinning bioactive glass scaffolds 50
2.3.3. 3D cotton-wool-like electrospun fibres 50
2.3.4. Electrospinning summary 52
2.4. Thesis objectives 53
CHAPTER THREE 54
3.1. Physical analysis 55
3.1.1. Scanning electron microscopy (SEM) 55
3.2. Chemical analysis 56
3.2.1. Fourier transform infrared spectroscopy (FTIR) 56
3.2.2. Solid-state ^{29}Si magic angle spinning-nuclear magnetic resonance (^{29}Si MAS-NMR) 56
3.2.3. X-ray diffraction (XRD) 57
3.2.4. Inductively coupled plasma atomic emission spectroscopy (ICP-AES) 58
3.2.5. X-ray photoelectron spectroscopy (XPS) 58
3.2.6. Energy Dispersive X-Ray Spectrometer (EDX) 59
3.3. Biological analysis 59
3.3.1. AlamarBlue® cell viability 59
3.3.2. Total DNA 60
3.3.3. Vascular endothelial growth factor (VEGF) ELISA 60
CHAPTER FOUR 61
4. 1. Introduction 62
4.1.2. Material parameters 63
4.1.3. Electrospinning parameters 64

4.2. Methods and materials 65
4.2.1. Preliminary sol-gel method 65
4.2.2. Preliminary electropsinning of samples 66
4.2.3. 70S30C sol-gel study 67
4.2.4. 70S30C electrospinning study 71
4.2.5. Dissolution study 75
4.3. Results and discussion 76
4.3.1. Preliminary sol-gel method 76
4.3.2. 70S30C Electrospinning study 85
4.2.5. Dissolution study 98
4.4. Concluding remarks 103
CHAPTER FIVE 106
5.1 Introduction 107
5.2.1. Electrospinning and characterisation of fibres 108
5.2.2. Dissolution in DMEM 111
5.2.3. Cell Studies 113
5.3. Results and discussion 116
5.3.1. Characterisation of fibres 116
5.3.2. Degradation in DMEM 123
5.3.3. Cell study with HDFs 128
5.4. Concluding remarks 134
CHAPTER SIX 136
6. 1. Introduction 137
6. 2. Methods and materials 138
6.2.1. Preliminary Study of copper containing glass fibres 139
6.2.2. Cellular response to copper control solutions 142
6.2.3. Assessing the therapeutic effect of copper containing bioactive glasses 144
6. 3. Results and discussion 147

6.3.1. Preliminary study of copper containing fibres 147
6.3.2. Cellular response to copper control solutions 161
6.3.3. Assessing the therapeutic effect of copper containing bioactive glasses 166
5.4. Concluding remarks 173
CHAPTER SEVEN 176
7.1. Introduction 177
7.2. Methods and materials 178
7.2.1. Fourier-transform infrared spectroscopy (FTIR) 179
7.2.2. X-ray photoelectron spectroscopy (XPS) 179
7.2.3. Solid-state ^{29}Si magic angle spinning-nuclear magnetic resonance (29Si MAS-NMR) 180
7.3. Results and discussion 181
7.3.1. Fourier-transform infrared spectroscopy (FTIR) 181
7.3.2. X-Ray photoelectron spectroscopy (XPS) 182
7.3.3. Solid-state ^{29}Si magic angle spinning-nuclear magnetic resonance (29Si MAS-NMR) 186
CHAPTER EIGHT 189
8.1. Review of objectives 190
8.1.1. The factors determining the formation of a 3D electrospun scaffold 191
8.1.2. 3D bioactive glass scaffold development and its effect on HDFs 191
8.1.3. Incorporation of Copper ions, stimulation of VEGF in HDFs and characterisation 192
8.2. Further Work 193
8.2.1. Cell attachment studies 193
8.2.2. Optimising copper concentration 193
8.2.3. Optimising the electrospinning process 193
9.0 REFERENCES 194

LIST OF FIGURES

Figure 1. Schematic composition map showing the degree of bioactivity in of different glass compositions. Adapted from Hench et al., [4] 29

Figure 2. Schematic representation of the structure of glass adapted from 'Coleman and Nicholson (2006)' [72]. 31

Figure 3. Showing the multiple stages of bioactivity [77] [66] 34

Figure 4 Schematic of the Electrospinning set up and the components required. 47

Figure 5. Schematic of the formation of a Taylor cone and production of electrospun fibres A. depicts the end of a spinneret where no voltage is applied, the liquid moves through the spinneret. B. A voltage is applied which causes the end of the spinneret to be charged and the liquid elongates producing a Taylor Cone. C. When the electric field reaches a certain value, the repulsive forces overcome that of the surface tension on the liquid and a charge jet emerges from the cone tip. D. Bending instability of the Jet can cause the formation of several branches. 48

Figure 6. The electrospinning apparatus set up at Imperial College. 72

Figure 7. Graphical representation of the viscosities obtained at each R ratio. This representation highlights the number of repeats at each R ratio (data points) and indicates the median and average values for viscosity. Significance was measured using a Brown-Forsythe and Welch ANOVA test followed by an Dunnett's T3 multiple comparisons tests where each of the results was compared with the result for R ratio =12. (* $P < 0.05$, *** $P < 0.001$). 78

Figure 8. SEM images of electrospun bioactive glass fibres produced from sol-gels with an H_2O/TEOS R ratio of (A) 12, (B) 9.5, (C) 7.8, (D) 6.1 and (E) 4.3. The images show the production of long, uniform fibres where R ratios of 6.1 and 4.3 and an increase in beads as the R ratio increases. 79

Figure 9. The change in viscosity of the sol as the quantity of polyvinyl butyral is increased. The ratio of the polyvinyl butyral to ethanol is increased and this increase shows an increase in the viscosity of the sol. This representation highlights all the data points in addition to the average viscosity value at each polyvinyl butyral quantity. 80

Figure 10. FTIR spectra from electrospun 70S30C sol-gel as a function of sintering temperature. The FTIR spectra show that the 600°C – 700°C range is appropriate as it removed all the unwanted nitrates. 83

Figure 11. XRD patterns of electrospun 70S30C sol-gel as a function of sintering temperature. The XRD shows a smooth, amorphous halo on in the 550°C, 600°C and 700°C sintering temperatures. 84

Figure 12. (A-D) Photographs showing the structure of 70S30C sol electrospun at different relative humidity values (A) 27%, (B) 35%, (C) 55% and (D) 65%. (E-H) SEM-SE images of the morphology of 70S30C electrospun samples. The relative humidity in each of the samples (E), (F), (G) and (H) was found to be (E) 27%, (F) 35%, (G) 55% and (H) 65%. 86

Figure 13. (A-D) SEM-SE images showing the individual fibres of the 70S30C electrospun samples. The relative humidity in each of the samples (A) 27%, (B) 35%, (C) 55% and (D) 65%. 87

Figure 14. SEM-SE image showing a bead in the 70S30C sample electrospun at a relative humidity of 65%. 88

Figure 15. SE SEM image showing the Atomic % of Si and Ca at points along A) a straight section of 70S30C fibre and B) along a bent section of 70S30C fibre. 90

Figure 16. (A-C) Photographs showing the structure of 100S electrospun cotton wool at relative humidity values of (A) 36%, (B) 66% and (C) 80%. (D-F) SEM images show the fibre morphology at relative humidity values of (D) 36% (E) 66% and (F) 80%. 91

Figure 17. (A) Photographs showing the morphology of bioactive glass fibres: 100S, 90S10C, 80S20C, 70S30C and 60S40C electrospun at a relative humidity of 37%. (B) The graph shows the range of samples electrospun at different relative humidity values, the key in key indicates the relative humidity region for each composition whereby 3D cotton-wool-like structures were produced with few beads and fibres which were long and uniform. 94

Figure 18. FTIR spectra of electrospun 60S40C, 70S30C, 80S20C, 90S10C and 100S sol-gel compositions. 96

Figure 19. XRD of electrospun 60S40C, 70S30C, 80S20C, 90S10C and 100S sol-gel compositions. The XRD shows a smooth, amorphous halo in the 100S, 90S10C, 80S20C and 70S30C samples. The 60S40C displays peaks which could be attributed to calcium silicates of either Anorthic (00-014-0693) or Orthorhombic (00-024-0234) crystal systems. 97

Figure 20. Dissolution profiles from ICP-AES of electrospun sol-gel glass samples as a function of time in TRIS, (A) Si and (B) Ca of the TRIS during glass dissolution. 100

Figure 21. pH profile of the TRIS during glass dissolution of the samples over the 7 day study. 101

Figure 22. SE-SEM images of the 70S30C and 80S20C fibres 116

Figure 23. Solid-state 29Si MAS-NMR data of electrospun sol-gel glass 70S30C and 80S20C samples. 119

Figure 24. XPS Survey spectra of the bioactive glass compositions: (A) 70S30C and (B) 80S20C. 120

Figure 25. High-resolution XPS spectra of Si 2p for the bioactive glass compositions (A) 70S30C and (B) 80S20C. 121

Figure 26. High-resolution XPS spectra of Ca 2p for the bioactive glass compositions (A) 70S30C and (B) 80S20C. 121

Figure 27. High-resolution XPS spectra of O 1s for the 70S30C and 80S20C bioactive glass compositions (A) 70S30C and (B) 80S20C. 122

Figure 28. (A) Dissolution profiles from ICP of electrospun sol-gel glasses in DMEM at time points of 4 h, 1 day, 3 day and 7 day, (B) pH profile of DMEM during glass dissolution. 123

Figure 29. FTIR spectra electrospun sol-gel glasses before and after being soaked in DMEM for 7 days: (A) 70S30C and (B) 80S20C. 125

Figure 30. XRD patterns of electrospun sol-gel glasses before and after being immersed in DMEM for 7 days (a) 70S30C and (b) 80S20C. Peaks associated with calcite are also included. Calcium carbonate oxide peak reference file number 00-005-0586. (*) inducates the presence of peaks not identified as Calcium Carbonate. ICDD identified this to be Halite with a reference of 00-001-0994. Samples were scanned at room temperature. 126

Figure 31. SEM image of 70S30C and 80S20C electrospun sol-gel glasses after being immersed in DMEM at 4 h, 1 day, 3 days and 7 days. 127

Figure 32. The metabolic activity of the HDFs after immersion in the dissolution product of the 70S30C and 80S20C samples, the Si control and the DMEM control at day 1, day 3 and day 7. The metabolic activity is displayed as a percentage of the DMEM control. None of the samples cause a significant change in metabolic activity of the HDFs. A Krustal-Wallis test followed by Dunn's Multiple Comparison were used to determine statistical significance in the metabolic activity relative to the DMEM result of samples at each time point. (n=6, * $P < 0.05$, ** $P < 0.01$, *** $P < 0.001$, **** $P < 0.0001$). 129

Figure 33. The proliferation [µg/mL] of HDF cultures exposed to DMEM containing the dissolution products of the 70S30C and 80S20C samples, the Si control and DMEM after 1 day, 3 day and 7 day. HDFs exposed to the 80S20C sample expressed a significant increase in proliferation at day 3 and day 7. Kruskal-Wallis test followed by Dunn's Multiple Comparison to detect significant changes in the proliferation of each composition with respect to the cell proliferation of HDFs at day 0, pre-exposure of HDFs to the different conditions. (n=6, * $P < 0.05$, ** $P < 0.01$, *** $P < 0.001$, **** $P < 0.0001$). 131

Figure 34. The metabolic activity of the HDFs normalised to cell number (calculated as percentages with respect to DMEM). The normalised metabolic activity per cell of HDFs immersed in the 70S30C bioactive glass was significantly increased at day 7. A Krustal- Wallis test followed by Dunn's Multiple Comparison were used to detect any statistical significance between each control and the DMEM at each time point. (n=6, * P < 0.05, ** P < 0.01, *** P < 0.001, **** P < 0.0001)..... 132

Figure 35. Normalised VEGF production of HDF cultures exposed to DMEM containing the dissolution products of bioactive glasses 70S30C and 80S20C, the Si control samples and DMEM after 1 day, 3 day and 7 day normalised to tDNA. A Kruskal-Wallis test followed by Dunn's Multiple Comparison was used to detect statistical significance of each composition with respect to DMEM at each time point (n=3, * P < 0.05, ** P < 0.01, *** P < 0.001, **** P < 0.0001). 133

Figure 36. XRD patterns of 5% CuBG, 1% CuBG and 0% CuBG electrospun bioactive glass samples. (*) indicates possible peaks of copper nitrate but analysis carried out using PANalytical X'Pert HighScore plus software did not concretely provide any matches. 147

Figure 37. FTIR spectra of electrospun 5% CuBG, 1% CuBG and 0% CuBG bioactive glass compositions..... 148

Figure 38. SEM images of electrospun bioactive glass fibres: (A) 5% CuBG, (B) 1% CuBG, (C) 0% CuBG; and (D) photographic images of the 5% CuBG and 1% CuBG 3D bioactive glass samples. 149

Figure 39. Dissolution profiles from ICP of electrospun sol-gel glasses in TRIS at time points of 1 h, 2h, 3h, 4h, 8h, 1 day, 2 days, 3 days, 4 days and 7 days of (a) Si [mg L^{-1}], (b) Ca [mg L^{-1}] and (c) Cu [mg L^{-1}]. TRIS was omitted as it was found to be at zero in each graph. 152

Figure 40. pH profiles of TRIS during the bioactive glass dissolution of the 0% CuBG, 1% CuBG and 5% CuBG samples. 153

Figure 41. Dissolution profiles from ICP of electrospun sol-gel glasses in DMEM at time points of 1 h, 2 h, 3 h, 4 h, 8 h, 1 day, 2 days, 3 days, 4 days and 7 days of (A) Si [mg L^{-1}], (B) Ca [mg L^{-1}], (C) Cu [mg L^{-1}] and (D) P [mg L^{-1}]..... 155

Figure 42. pH profile of DMEM during the bioactive glass dissolution of the 0% CuBG, 1% CuBG and 5% CuBG samples. ... 156

Figure 43. The metabolic activity of the HDFs after immersion in the dissolution product of the 5% CuBG, 1% CuBG and 0% CuBG samples and Si, Cu amnd DMEM controls at day 1, day 3 and day 7. The metabolic activity is displayed as a percentage of the DMEM control. The 5% CuBG fibre composition inhibited the metabolic activity of HDF at day 1 and 7. A Krustal-Wallis test followed by Dunn's Multiple Comparison were used to determine statistical significance in the metabolic activity relative to the DMEM result of samples at each time point. (n=6, * P < 0.05, ** P < 0.01, *** P < 0.001, **** P < 0.0001). 157

Figure 44. The proliferation [µg/mL] of HDF cultures exposed to DMEM containing the dissolution products of the 5% CuBG, 1% CuBG and 0% CuBG samples, the Si and Cu controls and DMEM after 1 day, 3 day and 7 day. The 5% CuBG composition significantly inhibited the the proliferation of HDFs at day 1 and 3 indicating its cytotoxicity to HDFs. Statistical analysis was carried out via a Kruskal-Wallis test followed by Dunn's Multiple Comparison to detect significant changes in the proliferation of each composition with respect to the cell proliferation of HDFs at day 0, pre-exposed to the different conditions. (n=6, * P < 0.05, ** P < 0.01, *** P < 0.001, **** P < 0.0001). 158

Figure 45. Diagram showing the difference in the dissolution setup between (A) the dissolution studies conducted over 7 days with samples taken over multiple time points (including at 4 h). The cellulose membrane is used to prevent accidental removal of fibres which have become loose (but have not fully dissolved) into the media. The cellulose membrane should allow full movement of ions into the dissolution product, and (B) the dissolution of fibres for cell studies. The fibres are removed after 4 h and the dissolution product is used directly onto the HDF cell lines. As only one time point is required, and the fibres are removed fully through filtering, no cellulose membrane is required. 160

Figure 46. The metabolic activity of the HDFs after exposure to copper concentrations for 1, 3 and 7 days. The metabolic activity is displayed as a percentage of the DMEM control. A Krustal-Wallis test followed by Dunn's Multiple Comparison were used to determine determine statistical significance in the metabolic activity relative to the DMEM result of samples at each time point. (n=6, * P < 0.05, ** P < 0.01, *** P < 0.001, **** P < 0.0001). 163

Figure 47. The proliferation [µg/mL] of HDF cultures exposed to DMEM containing the copper controls and DMEM after 1 day, 3 day and 7 day. None of the copper inhibit the proliferation of HDFs at day 1, 3 or 7. Statistical analysis was carried out via a Kruskal-Wallis test followed by Dunn's Multiple Comparison to detect significant changes in the proliferation of each composition with respect to the cell proliferation of HDFs at day 0, pre-exposed to the different conditions. (n=6, * P < 0.05, ** P < 0.01, *** P < 0.001, **** P < 0.0001). 164

Figure 48. Metabolic activity of the HDFs normalised to cell number (tDNA). The metabolic activity as a percentage of DMEM was normalised to the tDNA as a percentage of DMEM at each time point. There is a significant reduction in the metabolic activity of the HDFs per cell at day 7 when exposed to copper controls containing 6 mg L^{-1} at day 3 and 3 mg L^{-1} and 2 mg L^{-1}. A Krustal-Wallis test followed by Dunn's Multiple Comparison were used to firstly detect any statistical significance between each control and the DMEM at each time point. 165

Figure 49. The metabolic activity of the HDFs after immersion in the dissolution product of the 1% CuBG, 0.5% CuBG, 0.1% CuBG and 0% CuBG samples,Cu and DMEM controls at day 1, day 3 and day 7. The metabolic activity is displayed as a percentage of the DMEM control. The 1% CuBG and 0.5% CuBG fibre compositions inhibited the metabolic activity of HDF at day 1 and 7. A Krustal-Wallis test followed by Dunn's Multiple Comparison were used to determine statistical significance in the metabolic activity relative to the DMEM result of samples at each time point. (n=6, * P < 0.05, ** P < 0.01, *** P < 0.001, **** P < 0.0001). 168

Figure 50. The proliferation [µg/mL] of HDF cultures exposed to DMEM containing the dissolution products of the 1% CuBG, 0.5% CuBG, 0.1% CuBG and 0% CuBG samples, the 1.2 mg L^{-1} and 4 mg L^{-1} Cu controls and DMEM after 1 day, 3 day and 7 day. The 1% CuBG sample was the only sample not to exhibit a significant increase in proliferation of the HDFs at day 7. Statistical analysis was carried out via a Kruskal-Wallis test followed by Dunn's Multiple Comparison to detect significant changes in the proliferation of each composition with respect to the cell proliferation of HDFs at day 0, pre-exposed to the different conditions. (n=6, * P < 0.05, ** P < 0.01, *** P < 0.001, **** P < 0.0001). 169

Figure 51. Metabolic activity of the HDFs normalised to cell number (calculated as percentages with respect to DMEM). The normalised metabolic activity of HDFs immersed in the 0.5% CuBG bioactive glass dissolution product was considered to be significantly reduced compared to DMEM at day 7. A Krustal-Wallis test followed by Dunn's Multiple Comparison were used to detect any statistical significance between each control and the DMEM at each time point. (n=6, * P < 0.05, ** P < 0.01, *** P < 0.001, **** P < 0.0001). 170

Figure 52. LIVE/DEAD™ assay showing the presence of Live (green) and dead (red) cells for each bioactive glass composition at each time point. An increase in quantity of cells can be seen at each time point for each composition. 171

Figure 53. Normalised VEGF production [pg/µL] of HDF cultures exposed to DMEM containing the dissolution products of bioactive glass glasses 1% CuBG, 0.5% CuBG, 0.1% CuBG and 0% CuBG and controls in DMEM, 1.2 mg L^{-1} and 4 mg L^{-1} Cu at 1 day, 3 day and 7 day normalised to tDNA [µg/mL]. A Kruskal-Wallis test followed by Dunn's Multiple Comparison was used to detect statistical significance of each composition with respect to DMEM at each time point (+n=3, * p < 0.05, ** p < 0.01, *** p < 0.001, **** p < 0.0001). 172

Figure 54. FTIR absorbance spectra of the copper containing bioactive glasses. 181

Figure 55. (A) The Si2p, (B) O1s and (C) Ca2p photoelectron spectra for the four copper containing bioactive glass compositions and 70S30C glass fibres. All spectra show a shift in binding energy with the incorporation of copper into the bioactive glass compositions. 182

Figure 56. The Cu 2p photoelectron spectra for the four copper containing bioactive glass compositions and 70S30C glass fibres. 183

Figure 57. The Cu 2p high resolution XPS spectra for the 5% CuBG composition. Peaks at 933.2 eV and 953.1 eV alongside the characteristic satellites indicate the presence of CuO. The secondary shoulders at 935.7 eV and 955.7 eV can be attributed to long exposure 184

Figure 58. The N 1s high resolution XPS spectra for the 5% CuBG, 1% CuBG and original 70S30C (0% CuBG) post heat treatment and the 70S30C (0% CuBG) compositions post heat treatment. 185

Figure 59. Solid-state 29Si MAS-NMR data of electrospun sol-gel glass 5% Cu, 0.1% Cu and 0.5% Cu samples. PPM can be equated to mg L^{-1} 186

LIST OF TABLES

Table 1. Showing the quantities of reagents used in the initial protocol developed by collaborators Dr. Akiko Obata and Dr. Gowsihan Poologasundarampillai [165] [7]. 65

Table 2. The electrospinning parameters used by Poologasundarampillai et al., [7] and used as a starting point for the present study. 73

Table 3. The different sol gel compositions synthesised with differing R ratios and the corresponding viscosities when combined with the polyvinyl butyral binder in a ratio of 1:1. The R ratio takes into account the water in the entire system (including the water in the HNO_3 and the calcium nitrate in addition to the added water). 77

Table 4. Showing the surface tension of 70S30C compositions with differing R ratios and comparing those with literature results from Poologasundarampillai et al. [7]. The R ratio appears to affect the surface tension of the sol. 82

Table 5. The composition of the 70S30C calculated through a Lithium Metaborate analysis 89

Table 6. The composition of the 70S30C fibres as calculated through EDX analysis 89

Table 7. Summary of the electrospinning solution properties and conditions used for each sol nominal composition (100-X SiO2,XCaO). All samples had the same voltage, flow rate, distance between the collector plate and viscosity. These were set up to be 10.0 kV, 0.4 mL/h, 100-120 mm and 0.12-0.20 Pa.s respectively..... 93

Table 8. The actual compositions produced in mol.% for the 100S, 90S10C, 80S20C, 70S230C and 60S40C compositions as determined by lithium metaborate analysis. 93

Table 9. Summary of sol-gel and electrospinning parameters selected..... 105

Table 10. The nominal sol-gel compositions and electrospinning parameters used. Prior to electrospinning a Polyvinyl butyral binder was combined with the sol gel. This was comprised of 1 g of Polyvinyl butyral was combined with 11.4 mL of ethanol and was mixed in a ratio of 1:1 with the sol-gel. 108

Table 11. The parameters used for the high resolution XPS scans. 111

Table 12. Electrospun sol-gel bioactive glass fibre diameter and specific surface area determined by N2 sorption..... 116

Table 13. Relative Qn unit distribution in the glass structure (from solid-state 29Si MAS-NMR) and degree of condensation of the 70S30C and 80S20C bioactive glass samples. Dc is defined as the degree of condensation 118

Table 14. Measured silica and calcium concentration (ICP) after 4 h immersion in DMEM after filtering..... 128

Table 15. Nominal sol-gel compositions and the quantities of TEOS, nitric acid, ethanol, calcium nitrate and copper nitrate used. The samples were named 0% CuBG (70S30C), 1% CuBG (70S29C1Cu) and 5% CuBG (70S25C5Cu). 139

Table 16. The electrospinning parameters used to produce copper containing bioactive glass fibres. 139

Table 17. Electrospun sol-gel bioactive glass fibre diameter of 0% CuBG, 1% CuBG and 5% CuBG compositions 150

Table 18. The actual compositions produced in molecular weight for the 0% CuBG, 1% CuBG and 5% CuBG compositions as determined by lithium metaborate analysis. 150

Table 19. The ion release rate in mM at the 4 h time point from the dissolution study in DMEM. 155

Table 20. Comparison of the copper ion concentrations at 4 h of the dissolution study value using a cellulose membrane with that of the actual copper concentrations in the dissolution product used for HDF cell studies. 161

Table 21. The compositions investigated and the actual copper compositions. 162

Table 22. The bioactive glass compositions made via the sol-gel route..... 166

Table 23. The actual CuBG compositions as determined by lithium metaborate analysis. 167

Table 24. Shows the release rate at 4 h of the bioactive glass compositions in mg L^{-1} and mM. 167

Table 25. The sol-gel compositions and the quantities of TEOS, nitric acid, ethanol, calcium nitrate and copper nitrate used. .. 178

Table 26. The parameters use for the high resolution XPS scans. 180

Table 27. Percentage of Qn Si species determined from the 29Si MAS NMR (vr = 5 kHz) data for 5% Cu, 0.1% Cu and 0.5% Cu 187

LIST OF ABBREVIATIONS

BET	Brunauer, Emmett and Teller
BO	Bridging oxygen
DMEM	Dulbecco's Modified Eagle Medium
ELISA	Enzyme-Linked Immunosorbent Assay
FBS	Foetal Bovine Serum
FTIR	Fourier Transform Infrared Spectroscopy
HCA	Hydroxycarbonate Apatite
HDF	Human Dermal Fibroblasts
HIF	Hypoxia Inducible Factor
HUVECs	Human Umbilical Vein Endothelial Cells
mol.%	Mole Percent
NBO	Non Bridging Oxygen
PPM	Parts per million
ROS	Reactive Oxygen Species
SBF	Simulated Body Fluid
SD	Standard Deviation
SEM	Scanning Electron Microscopy
Si NMR	Silicon Nuclear Magnetic Resonance
tDNA	Total DNA
TEOS	Tetraethyl Orthosilicate
TRIS	Tris(hydroxymethyl)aminomethane
VEGF	Vascular Endothelial Growth Factor
wt. %	Weight Percent
XRD	X-ray Diffraction
XPS	X-ray Photoelectron Spectroscopy

CHAPTER TWO - LITERATURE REVIEW

Soft tissue regeneration, bioactive glasses and electrospinning

2.1 The problem with healing wounds

The primary role of skin is to protect the body from external physical, chemical and microbial damage [8]. As the largest organ in the body [9] its structure is complex consisting of the epidermis, dermis and hypodermis in addition to containing nerves, hair follicles and an extensive vascular network [10]. In addition to providing a barrier against infection, the skin holds a vital role in protecting the homeostasis of the body [11] such as through regulating water from the internal environment [8]. When the skin becomes damaged, the body is exposed to potential external damage and so successful and timely wound healing is of importance.

In recent years, the successful treatment of wounds has becoming a growing challenge for healthcare systems worldwide. In the UK alone, the National Health Service (NHS) treated an estimated 2.2 million wounds in 2012/2013 costing a total of £5.3 billion for the management and associated comorbidities of the wounds [12]. These figures are set to increase due to a rise in an ageing population [2], one of the main demographics who risk suffering from wounds that fail to heal, an increasing prevalence of diseases such as diabetes which can cause delay to wound healing and an increase in antibiotic resistance [1].

Wound healing is comprised of four stages: hemostatis, inflammation, proliferation, and remodelling. Successful wound healing requires these stages to act in sequence within a correct time frame and at the right intensity [2]. Many factors can interfere with this process causing wounds to heal incorrectly or not completely; this can be serious as delayed or failed wound healing can lead to infection and further damage to the body [13] [2].

2.1.1. Stages of wound healing

Wound healing is categorised into four stages. Homeostasis, the first stage of wound healing, also known as the acute stage, begins immediately with the constriction of blood capillaries and clot formation to prevent further blood loss and create a barrier to the outside. Clot formation takes place when platelets change shape and release chemical signals activating the fibrin which behaves like a mesh, binding the platelets together and sealing the wound [3].

The second stage is known as the inflammatory stage. The purpose of this stage is to remove unwanted debris and prevent infection in the wound. In the early inflammatory stage, which occurs 24-48 hours after injury [13], neutrophil granulocytes (polymorphonuclear leukocytes) travel to the wound site and adhere to cells in nearby blood vessels. The polymorphonuclear leukocytes move though the walls of the blood

vessels to infiltrate the wound. By releasing degrading enzymes and free radicals derived from oxygen molecules, they destroy bacteria and other foreign particles left in the wound after injury [3].

In the later stages of inflammation, monocytes arrive at the wound and undergo a change to become tissue macrophages. Macrophages are the most important cells in the later stages as they are the key regulatory cells providing repair [3]. Macrophages are responsible for producing a spectrum of growth factors such as TGF-β and EGF, these regulate the inflammatory response in addition to stimulating angiogenesis (the development of new blood vessels) and providing tissue formation [13]. This stage of wound healing will continue for as long as necessary to ensure all debris is removed where possible. Inadequate healing at the stage can lead to significant problems in the third and fourth stages of healing where tissue can be damaged, delays to proliferation resulting in the possibility of chronic wounds [13].

The proliferation phase focuses on the new tissue formation. It overlaps with the inflammatory phase and is comprised of many events such as the re-eithelialization, angiogenesis, collagen synthesis and the formation of the extracellular matrix [3].

Fibroblasts typically enter the wound several days after injury. They multiply and produce key matrix proteins such as collagen [3]. Their role is to help the construction of the new extracellular matrix. By producing a substrate for cell adhesion, the extracellular matrix supports the movement, growth and differentiation of cells.

The formation of granulation tissue is another indicator of the proliferation phase. It is characterised by the formation of new blood vessels and enables re-epithelialization to take place. Epithelium is the thin tissue which forms the outer surface layer of the body. In the final stages of wound healing epithelial cells travel from the edges of the wound to the surface of the wound, covering it with a thin layer [14]. For successful epithelialization to take place, a moist, bacteria-controlled environment is required [3]. This stage may extend to weeks, months or years after injury. It is very dependent on the size and the severity of the wound [14].

Remodelling focuses on the continual synthesis and breakdown of collagen as the extracellular matrix. Over this period, the tensile strength of the wound increases eventually becoming 80% as strong as normal tissue. As activity at wound site reduces, any scarring loses its red appearance [15].

2.1.2. Chronic wound healing

Wounds can typically be classified into two different groups: acute and chronic. Wounds considered to be 'acute' are typically those involving the epidermis and superficial dermis, and are typically caused by things like surgical incisions, heat or abrasions. The most serious complications resulting from acute wounds is normally infection [1].

Wounds that fail to heal in a timely manner or those that demonstrate delayed healing 12 weeks after injury [13], frequently re-occur or fail to progress through the normal stages of healing are known as chronic wounds [3]. Chronic wounds usually occur as complications from underlying health conditions and other diseases, which compromise biochemical signalling, deposition of the extracellular matrix and the migration of cells [1]. Other external factors such as age, lifestyle and medication can also increase their likelihood of occurrence [13] [2]. Venous, arterial and diabetic foot ulcers are some of the most common types of chronic wounds [16], and patients typically experience prolonged and excessive inflammation and are at persistent risk of infection due to the wound's inability to heal [17].

Chronic wounds can severely impede the quality of life for patients. They are painful, can impair mobility and require long periods of hospitalisation, preventing patients from their normal routines and require frequent dressing changes [18]. Conditions such as diabetic neuropathy can contribute to the formation of ulcers or deformities which can increase the risk of lower-extremity amputations in extreme cases [19]. The persistence of chronic wounds and the resulting life-changing treatments can additionally cause patients psychological symptoms [20].

2.1.3. Factors affecting wound healing

The healing of wounds is complex, with the interwoven movements and interactions of many different cell types and growth factors, it is easy to appreciate that effective wound healing can be impaired by a number of different factors. These factors are normally separated into two categories: local factors and systematic factors.

Systematic factors that affect wound healing include the age of the patient, stress levels, diabetes, other medication the patient maybe taking, in addition to general lifestyle factors such as obesity, nutrition, alcohol consumption and smoking.

A significant systematic factor is diabetes. Diabetes is a condition which affects in excess of 170 million people worldwide [21]. Diabetic foot ulcers are said to effect 15% of those with diabetes [22]. Elevated

blood sugar causes stiffening of the arteries narrowing blood vessels leading to decreased blood and oxygen flow vital for wound healing. Wound healing may also be impaired by diabetic neuropathy where loss of sensation may mean that the patient is unable to feel changes in the wound in addition to the effects of a lower immune system leading to infection [23].

When patients suffer from foot injury, the body maybe unable to provide the inflammatory response adequate to heal the wound and prevent infection. In many cases this can lead to sepsis and eventually amputation [24]. Local factors are defined as those which directly influence the wound itself [2]. These could include factors such as infection, lack of oxygenation or the presence of a foreign bodies in the wound.

2.1.4. Role of hypoxia in wound healing

The oxygenation of wounds is important in every stage of wound healing, from preventing infection to inducing angiogenesis and stimulating growth factors at the wound site [25]. In cells, oxygenation promotes the differentiation, migration and the re-epithelialization of keratinocyte cells and enhances the proliferation of fibroblasts [2]. However, acute injury to the skin can cause the affected microenvironment to be devoid of oxygen. This is partly due to disruption resulting from the injury itself but also an increase in oxygen consumption resulting from the granular tissue which seeks to remove unwanted foreign particles [26]. This oxygen deprivation is known as Hypoxia and it can affect the body generally or locally where an area of tissue has an inadequate supply of oxygen.

Despite the need of oxygen to heal wounds, it is this hypoxia which stimulates the repair of tissues. Hypoxia is thought to create an oxygen gradient which enables diffusion of oxygen into the wound area which induces the production of growth factors stimulating the healing of the wound [5]. Prolonged hypoxia in the wound area is problematic however, as oxygen is necessary for healing throughout the rest of the process [25], therefore the appropriate oxygen levels are critical for healing wounds. The main pathway whereby the cells respond to hypoxia is known as the Hypoxia Inducible Factor (HIF) pathway. It enables the cells to respond to hypoxia through the blockage of the hydroxylation of one of the two sub-units of HIF (HIF-1α). The HIF-1α then accumulates in the cells forcing it to bind with the second sub-unit HIF-1β, which forms HIF-1 that then activates the response of genes such as VEGF required to start their process of responding to hypoxia [27].

2.1.5. Current wound healing products and strategies

There are many wound healing products and therapies that are widely available commercially. Clinical procedures for healing chronic wounds tend to be categorised into one of four different treatment types: skin substitutes, negative pressure wound therapies, growth factors and hypobaric oxygen therapies.

One of the main treatment processes used in wound healing is that of debridement. It refers to the removal of dead or damaged tissue and its presence in wounds impedes healing. When this unwanted tissue is removed, the clean tissue beneath is exposed and epithelial cell migration is free to take place to proliferate and fill the wound [28]. Debridement is typically carried out surgically however Mulder *et al.,* [29], have developed wound dressings using the process of Autolytic debridement, which create a moist environment with a hydrocolloid dressing that activates endogenous enzymes capable of lysing fibrin on the wound surface. Prete *et al.,* [30] combined the two types of debridement by applying maggots/larvae to wounds which was found to stimulate fibroblast proliferation.

Skin substitutes are a rapidly expanding area of development for wound healing applications. Designed to replace (either partially or totally) the skin [31], many of these tissue-engineered products have been advanced in recent years. The skin substitutes typically consist of a mesh (or scaffold) with a biologically active substance which are placed onto the wound area [28]. Dermagraft® has developed a promising product which uses a temporary polyglactin mesh which degrades over time and an extracellular matrix combined with fibroblasts derived from newborn foreskin tissue. Studies conducted by Marston *et al.,* [32] highlighted its success at improving wound closure by 12 weeks compared to a control group and suggest that the combination of HDFs and ECM facilitate angiogenesis [33] and aids the closing of the wound through the proliferation and movement of epithelial cells from the patient [34]. This has been developed further with allograft-based bilayered cultured skin equivalents, products such as Apligraf® (Organogenesis), which are comprised of fibroblasts and bovine type I collagen in a dermal layer combined with a epidermal layer comprised of cultured keratinocytes [8-9] producing an environment similar to that of a normal healing wound [28]. While tissue-engineered skin is a promising solution, producing skin with a well-defined epidermis and dermis, it lacks components found in normal, healthy skin such as pigments, hair follicles, sweat glands and immune cells [36]. Another consideration is the expense of skin substitutes as they can be substantially more expensive and should be reserved for treatments in wounds which have failed to respond to current standard care methods [37]. Langer *et al.,* [38] however, calculated that the reduction in wound healing time and complications resulting from use of skin substitutes actually may offset the initial high costs of the products reducing the total care cost of the patient.

Negative pressure wound therapy (NPT) uses a foam dressing and an evacuation tube which creates a suction force enabling the drainage of wounds. The therapy is able to alleviate some of the factors which prevent chronic wounds from healing as the therapy keeps blood flow to the wound high, removes unwanted liquids and applies pressure which stimulates the closure of wounds [28]. NPT is beneficial in surgical wounds, where excess fluid may deter wound healing [39] and interestingly can be used to aid the closing of the wound through reducing volume and simplifying the surgical repair [40] [28].Growth factors and cytokines are essential for successful wound healing and tissue regeneration. The direct application of growth factors onto the wound bed is also used as an approach to wound healing. Greenhalgh *et al.,* [41] applied between 1- 10 µg of FGF and PDGF growth factors to full thickness skin wounds applied to mice and found that the wounds treated with growth factors had significantly greater closure after 21 days. VEGF [42]. Galiano *et al.*, [42] applied 20 µg of VEGF every second day providing a total of 5 doses to diabetic mice. The growth factor was applied to one wound whereas phosphate-buffered saline was applied to the other. It was observed that the VEGF-treatment accelerated repair with an average resurfacing time of 12 days compared with 25 days in the untreated wound. Many studies using growth factors show promising results, however, as described by Han *et al.*, [28] the implementation of a single growth factor to a difficult wound, which is chronic typically due to deficiencies in a number of growth factors, is unlikely to be sufficient to rescue the chronic wound. Carriers must be able to deliver growth factors in a sustained manner for extended periods. There are still many concerns surrounding the duration, efficiency and control of their release rate to surrounding tissues when they are implanted [43][44]. The sensitivity of control required to deliver the correct growth factors and signalling molecules makes stimulating angiogenesis in this way complicated. The development of inorganic materials which are able to provide their own mechanism to promote angiogenesis is increasingly attractive [45].

There is a huge body of research focused on dressings to reduce wound healing times and prevent infection. However, due to the complicated nature of the wound healing process, there are no dressings which offer a universal solution to all wound types and stages of the wound healing process. Additionally, current dressings are not always successful in healing diabetic foot ulcers or large wounds.

2.1.6. Role of VEGF in wound healing

Vascular endothelial growth factor (VEGF) stimulates angiogenesis, the growth of blood vessels in the body, and plays a critical role in the wound healing process [46]. It is believed to be one of the more

prominent proangiogenic influencers in wound healing and has several roles in wound healing [47]. VEGF is produced through numerous cell types and when injury strikes, many cells respond by increasing their production of VEGF. Fibroblasts [48], macrophages and keratinocytes [49] all actively produce VEGF in injured skin. VEGF production is critical in the acute and proliferative phases of wound healing. In the acute phase, VEGF plays a role in regulating inflammation. Detmar *et al.,* [50] have shown that VEGF aids interactions between the endothelial and circulating inflammatory cells through its ability to affect the expression of selectins and intercellular adhesion molecules on endothelial cells which is important in ensuring the movement of circulating inflammatory cells to the wound area [46]. VEGF has an extensive role in the proliferative phase, it is produced by many cell types and contributes to the repair of the dermis and the epidermal barrier [46]. Studies by Vranckx *et al.,* [51] and Corral *et al.,* [52] highlight that enhancing VEGF in healthy animals at the proliferation stage of wound healing does not result in improved wound closure and at high levels can impair it [52]. Conversely, when VEGF is reduced in healthy animals, studies show that wound healing is delayed [47] [53]. This suggests that the VEGF levels need only to be sufficient for effective wound healing to take place, and that enhancing them does not necessarily correspond to improvements in wound closure. There is evidence that VEGF contributes to scar tissue formation. Wilgus *et al.,* [54] have shown a reduction in scar size in mice models when neutralising VEGF antibodies are applied. Conversely, additions of VEGF resulted in the formation of scars in embryonic foetal wounds.

2.1.7. The role of copper in VEGF and angiogenesis

The direct role of copper in facilitating angiogenesis has been understood for several decades. In an early study, Raju *et al.,* [55] bound copper to ceruloplasmin molecules and observed that the molecules, only when bound to the copper, could induce the formation of capillaries in the corneas of rabbits. Copper has angiogenic properties in vivo and studies have shown that these properties can be used to accelerate the healing of dermal wounds. Sen *et al.,* [56] showed that a 25 μm layer topical treatment of copper ions (copper sulphate) significantly increased VEGF expression and accelerated wound healing when applied for five days and improved the quality of the tissue regenerated.

Hu *et al.,* [57] showed that copper II ions from $CuSO_4$ stimulate the proliferation of endothelial cells in vitro, demonstrating that, Cu (II) ions improved the proliferation of Human umbilical vein endothelial cells (HUVEC) to a similar extent as bFGF, an endothelial growth factors. They also showed that the presence of copper does not appear to induce any morphological or metabolic changes to cells cultured within the

tested concentrations. However, this copper induced proliferation extended only to endothelial cells and did not appear to have any effect on human fibroblasts or smooth muscle cells [57].

Studies from Feng *et al.,* [6] and Xie *et al.,* [58] show that angiogenic properties of copper are partly due to its ability to mimic the effects of hypoxia through activation of the hypoxia-inducible factor-1 (HIF-1α). Feng *et al.,* [6] describes the mechanism for the ability of copper to activate HIF-1. It is believed that copper binds to the subunit α of the HIF factor, this may prevent the activity of the FIH-1 (factor inhibiting HIF-1) ensuring that HIF-1α is free to bind to other cofactors. It is this combination with the cofactors that enables stabilisation of HIF-1 which in turn triggers processes such as VEGF production. It is also important to note however, that the production of proteins such as VEGF, which are regulated by the HIF pathway can be increased with the use of several transition metals such as copper, cobalt and manganese [59] [60].

2.1.8 Wound healing summary

In summary, the healing of chronic wounds is not new problem and multiple treatments and dressings have been developed with the aim of improving healing times and reducing occurrences of other complications such as infection. Many promising solutions are very expensive and are often unjustifiable for patients due to their cost. It seems the development of a low cost solution which can be freely used alongside other treatments and dressings is desirable.

A wealth of research describes the importance of angiogenesis in wound healing, and the stimulation of VEGF production is critical to that. While the direct application of specific growth factors to the wound area has been shown to promote wound healing, there are questions surrounding the consistency and control of their application. It seems unlikely that the application of a single factor is sufficient enough to ignite the healing process in a wound which has likely become chronic due to many issues in the wound healing response.

A better solution is perhaps one that using materials to stimulate the body's natural wound healing mechanisms. The use of copper ions to mimic the effects of hypoxia through the activation of HIF-1α is a promising. It enables a cascade of events such as the production of VEGF and other growth factors by cells to aid the natural wound healing mechanisms of the body.

2.2 Bioactive glasses

Bioactive glasses are a fascinating group of materials that exhibit a particular range of properties that enable them to induce a beneficial biological response in the body [61]. They are also frequently defined as having an ability to form a hydroxycarbonate apatite (HCA) layer following stages of surface reactions [62] [63], enabling a bond with bone *in vivo*. Bioactive glasses can be designed to contain elements which are all completely compatible with the body, making them a particularly interesting choice in the field of tissue engineering.

Their ability to degrade, releasing ions *in vivo* means that they have the ability to locally deliver ions that have a therapeutic affect to targeted areas of the body, or to behave as a vessel carrying and delivering drugs to specific locations in the body. Traditionally, bioactive glasses have been used in bone repair. However, more recently, research has shown that they can be utilised successfully in the regeneration of soft tissues and in wound healing. Research shows that bioactive glasses may have advantages over traditional healing methods in these areas [64].

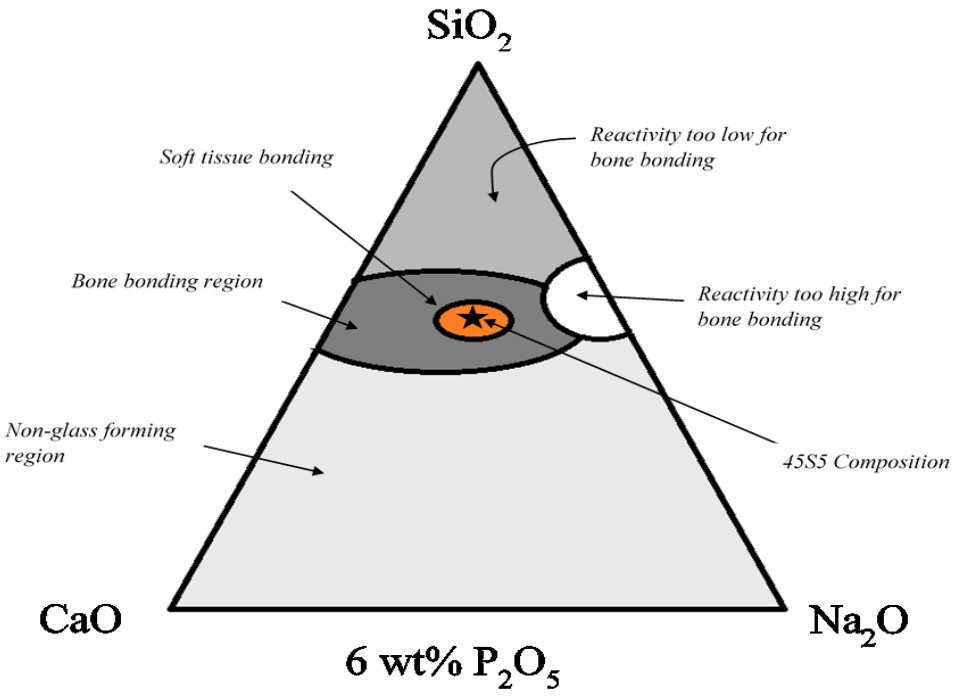


Figure 1. Schematic composition map showing the degree of bioactivity in of different glass compositions. Adapted from Hench et al., [4]

Bioactive glasses were first developed in 1969 by Professor Larry Hench who sought to provide a solution to the problem of rejection from artificial implants in the body [4]. He developed a melt-derived bioactive glass, called Bioglass, which was comprised of silica, sodium, calcium and phosphorous oxides in a composition of 46.1 mol% SiO_2, 24.4 mol% Na_2O, 26.9 mol% CaO and 2.6 mol% P_2O_5 (45S5) [65]. Through a series of dissolution and precipitation steps, he found that the glass composition produced an HCA layer on the surface of the material, which lead to the formation of a bond with bone in a rat femur model [65]. This crystalline apatite layer is critical in forming a bond with bone and causes complete integration of the Bioglass and the bone without the formation of fibrous tissues [66].

The Bioglass composition has unique properties which make it suitable for use in biological applications. The degree in which a glass is bioactive is dependent on its chemical composition. Bioglass falls perfectly within this range where bone bonding is possible due to the ratio of oxides contained in the composition. *Figure 1* shows an estimate of the range of compositions which display bioactive properties, which are dependent on the dissolution rate of the glass [67][68][69].

Since Bioglass, several other glasses have been developed which also fit within this range of properties defined in *Figure 1*. Their properties differ slightly, from their different degradation properties to their ability to form scaffolds with a higher porosity and that offer different properties mechanically [70].

2.2.1. The structure of glasses

A glass is an amorphous material. Structurally, it lacks atomic order in the long range and displays a glass transition temperature [71]. The structure of glass is made up atoms which can be defined by the role they play in the structure, these are typically defined as network formers and network modifiers.

Network formers are the oxides which make up the glass network. For glass to be produced they must be present, and they can form glass without any additional components. Examples of these include silica, borate and phosphate.

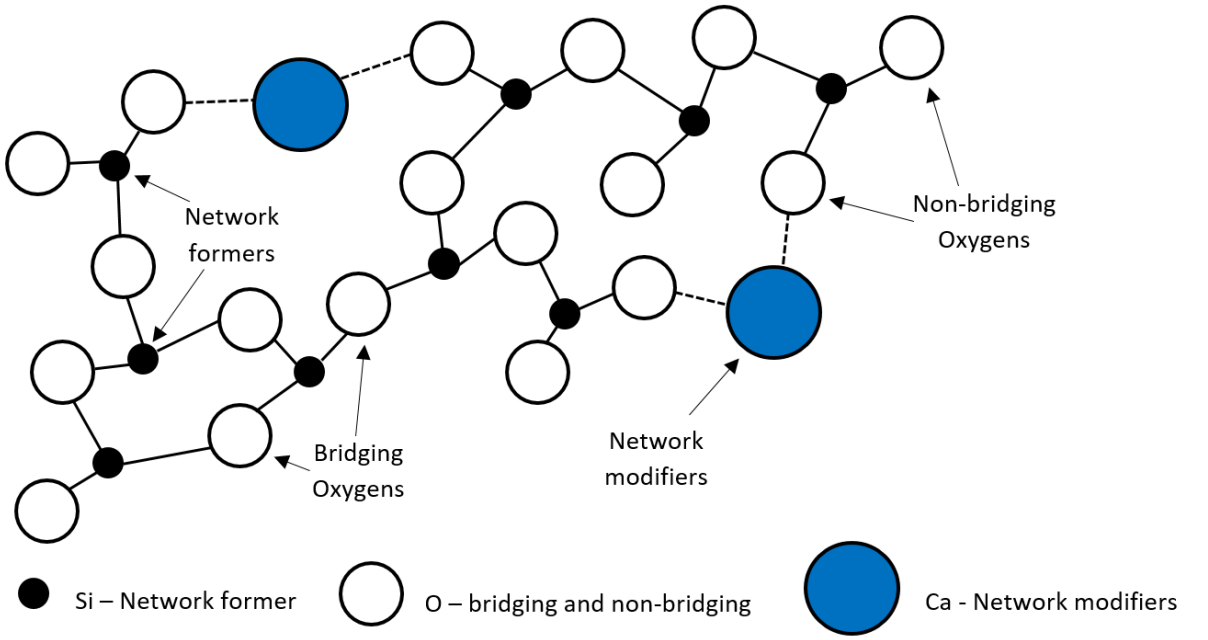


Figure 2. Schematic representation of the structure of glass adapted from 'Coleman and Nicholson (2006)' [72].

Network modifiers change the network through the insertion of additional oxides, these are typically the oxides of calcium, sodium and strontium. They insert themselves into the network through breaking an oxygen bond with a cation [71].

When network modifiers are added to network formers, the modifier breaks bridging oxygens and creates two non-bridging oxygen atoms. The oxide cation is normally randomly located and balances the negative charge on the non-bridging oxygen atom [73]. This process can be seen in *Figure 2.*

A number of oxides behave as intermediates, which means that they can behave either as a network former or modifier depending on their concentration or presence of other oxides present in the glass structure. Typically examples of these are cobalt oxide and magnesium oxide [74] [73].

The Q^n structure of a glass describes the number of bridging oxygens there are around each network forming cation. For example, a Q^n structure of Q^3 means that there is 1 non-bridging oxygen around the network forming cation and 3 bridging oxygens. The network connectivity (NC) can be used to define glasses and predict the likely Q^n structure of the glass [75]. This information can be used calculate the expected properties of the glass such as the surface reactivity, solubility and glass transition temperature.

2.2.2. The mechanism of bioactivity

Research [76] describes the mechanism of bonding of bioactive glasses to bone as an multi stage process summarised by ion transfers, dissolution and finally the biological response of bone. This can be seen in Figure 3.

Much less focus has been given to role bioactive glasses may play on soft tissue. Of the multiple stages of bioactivity, stages one to five focus on the chemical ion exchange and the dissolution of the glass which can be applied to soft tissues. Stages six and onwards focus more on the biological response of the bone, although these are not proven [77] [66]. The ion exchanges described in the first five stages are typically characterised by the ability of the glass to form HCA on the surface. The presence of HCA can be determined through FTIR, XRD and through imaging using SEM. To enable the formation of HCA *in vitro*, bioactive glass samples are normally immersed in Simulated Body Fluid (SBF) and maintained in a temperature of 37.5°C to mimic physiological conditions [78]. This buffer is used because it provides a similar environment to blood plasma and therefore an effective model to observe the exchange of ions and formation of HCA.

A second process used to measure the degradation of bioactive glasses is through using TRIS buffer. As with SBF, samples are immersed and incubated in TRIS buffer and changes in the pH are measured which provide indication as to the ability of the glass to produce HCA.

Cell culture media is also becoming more widely used to investigate the degradation of bioactive glasses. This is useful particularly in soft tissue applications where degradation of the bioactive glasses are welcomed as, when released, they provide a therapeutic effect to the targeted tissue, but the formation of

HCA may not necessarily be desired. The use of cell culture media enables direct comparison to the behaviour in in vitro cell studies [79] [80].

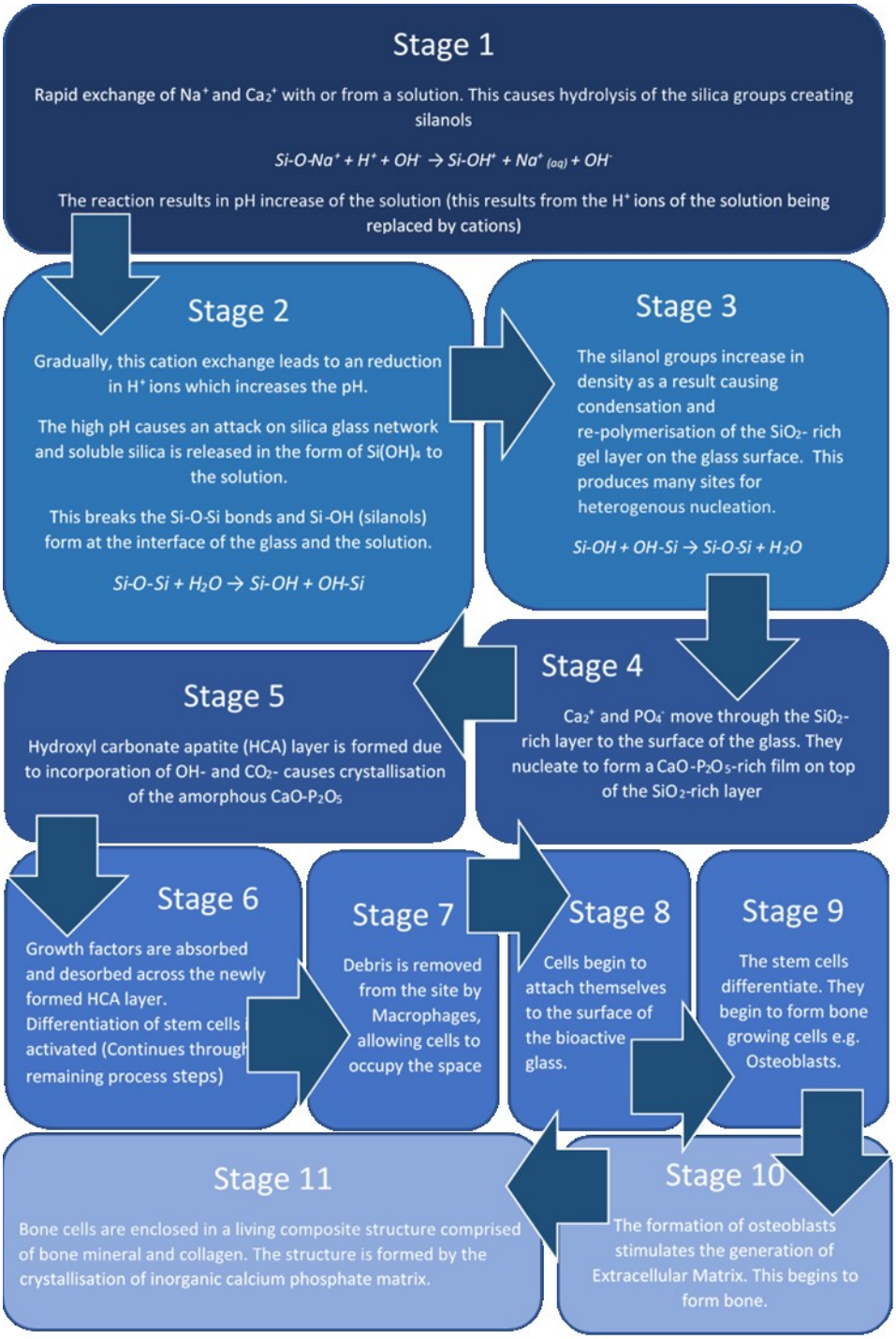


Figure 3. Showing the multiple stages of bioactivity. [77] [66]

2.2.3. Making bioactive glasses

There are two main methods used for producing bioactive glasses: the melt derived and the sol-gel process. The initial bioactive glass composition Bioglass (45S5) was made via the melt-derived process. This traditional glass making process takes place at high temperatures (exceeding 1300°C), where oxides are melted together in a platinum crucible and then are quenched in a graphite mould or in water depending on the desired form (monoliths or rods for example) [61].

The sol-gel process is a versatile, chemistry-based method. Synthesis using this method takes place when a solution containing oxide precursors undergo hydrolysis and condensation reactions to form an inorganic network of covalently bonded silica called a gel [81]. This gel can then be dried and heated to become a glass.

Melt-derived and sol-gel derived glasses have many physical differences making them suitable for different applications. Sol-gels typically have increased control of the cellular response as their surface chemistry is easily controlled and can be tailored more flexibility to the needs of the glass [82]. Sol-gels have a higher nanoporosity compared with their melt-derived counterparts, which is advantageous when it comes to be bioactive applications where a high surface area is important in increasing dissolution and improving cellular response [83].

Compositionally, melt-derived glasses are more complex. Many contain oxides such as Na_2O to aid the materials processing such as decreasing the melting point of the glass [61]. The sol-gel compositions can focus much purely on the bioactive response, making them very adaptable and tailorable depending on the application for the glass. Sol-gels can also be produced as powders, foams, 3D printed and electrospun.

2.2.4. The sol-gel process

In the sol-gel process, a colloidal liquid "sol" transforms into a "gel" by the gelation of precursors. The silica network is formed through hydrolysis (*Equation 1*) and condensation reactions (*Equations 2 and 3*) and can be catalysed in acid or base reactions.

An alkyl silicate precursor such as tetraethyl orthosilicate (TEOS) is used to produce silica nanoparticles when H_2O is added under catalysis in acidic conditions. As hydrolysis and condensation reactions occur, hydrolysis replaces the alkoxide groups with hydroxyl groups.

Hydrolysis

$Si(OC_2H_5)_4 + 4\,H_2O \rightarrow Si(OH)_4 + 4\,C_2H_5OH$ Equation 1

Condensation

$Si(OH)_4 + Si(OH)_4 \rightarrow (HO)_3\,Si\text{-}O\text{-}Si(OH)_3 + H_2O$ Equation 2

$Si(OH)_4 + Si(OC_2H_5)_4 \rightarrow (HO)_3\,Si\text{-}O\text{-}Si(OC_2H_5)_3 + H_2O$ Equation 3

The silica network starts forming via the condensation reaction, where the silanol groups produce siloxane bonds (Si-O-Si). The condensation reactions commence as the hydrolysis reactions start, they both happen simultaneously. As a 3D SiO_2 network of Si-O-Si links form throughout the solvent medium, a silica network is formed. This network is formed by condensation reactions and the sol becomes a gel when it becomes rigid, it is characterised by increase in elastic and viscous moduli [81][84]

2.2.5. Variables affecting the sol-gel process

Effect of pH

The pH of the sol is important as it determines not only the rate of, but also the mechanism of hydroloysis and condensation reactions. Acid catalysts such as HNO_3 and HCl are used to reduce the pH of the sol below isoelectric point of silicic acid in water (pH 2.2). Below this point, the transition state is positively charged, protons form protonated silanol species from the silanol groups, making silicon more electrophilic (more attracted to electrons) and therefore more susceptible to a Sn_2^- type nucleophilic attack (a nucleophilic substitution is where electron nucleophile selectively bonds or attacks positive charges or atoms or groups of atoms) [85]. As the pH increases above the isoelectric point, a base catalyst is used, the concentration of SiO^- increases and hydrolysis becomes the determining step. Gelling times decrease and more linear chains are produced as a result [85]. Sols that are very weakly acid have large numbers of deprotonated silanol (SiO^-) which exhibit high nucleophility which affects increases the speed of condensation. Hydrolysis then determines the rate of reaction. Weakly acidic sols lead to high branched silica species and gelation of these leads to the formation of mesopores (pores between 2 and 50 nm) once they are dried [84].

The catalysts used for hydrolysis reactions also catalyse the condensation reactions [81]. It is well known that acid catalysts, i.e. when the pH is lower than the isoelastic point and H_3O^+ ions are present in the solution, the rate of hydrolysis reaction increases. Whereas basic conditions, when the pH is larger than the isoelectric point, when OH^- ions are in the solution, the condensation reaction increases [82].

Effect of Water

The ratio of water and TEOS (known as the R-ratio) also affects the rate of hydrolysis and condensation. Sacks *et al.,* [86] and Sakka *et al.,* [87] quote that an R ratio of 2 is required to ensure the complete hydrolysis of TEOS for drawing silicate fibres. If the R ratio is increased, the rate of hydrolysis is increased, however if it is increased to an R ratio = 10 or higher, it reduces the concentrations of particles in the sol and slows down the rate of condensation, increasing the gelling time [88]. Therefore, H_2O acts a solvent in addition to a reagent.

Water content is also known to affect textural properties [89]. Under acid conditions, the surface area and porosity increased with an increase in R ratio [90]. This is because complete hydrolysis eliminates the alkoxy groups which when stabilised give rise to larger pores.

2.2.6. The glass making process

Composition

Increasing or decreasing the quantity of silica in the glass can also affect the rates of hydrolysis and condensation and the structural properties. Balas *et al.,* [91] found that as silica content increased, pore volume and diameter decreased, whereas surface area increased. Arcos *et al.,* [92] found that gel-derived glasses with 68 wt% silica exhibited higher levels of mesoporosity and therefore higher specific surface area than glasses containing 58 wt% silica.

Salinas *et al.* [93] found that as phosphate content increased, from 0 to 5 mol%, pore volume and pore diameter decreased for ternary gel-derived $CaO\text{-}P_2O_5\text{-}SiO_2$. Variations were thought to be due to the reduction in calcium in the glass silica network as phosphate content increased, due to calcium-phosphorous bonding.

Casting

In conventional sol-gel, while the sol is in its low viscosity form, it can be cast into a mould for gelling and ageing. It is important that casting be controlled to prevent precipitation occurring and to avoid the formation of bubbles in the gel during casting as they will remain as defects in the gel.

Ageing

Ageing consists of four stages: polycondensation, syneresis, phase transformation and coarsening. Ageing must be carefully controlled as the strength of the gel increases rapidly with ageing putting it at risk from cracking during drying. Polycondensation continues into ageing as cross linking and network formation continues and strengthens the gel [84] [82].

Syneresis is defined as the spontaneous shrinkage and densification of the gel, which leads to expulsion of pore liquid. The time taken for this process to take place is dependent on the density of the gel and the concentration of the reactive groups. The temperature at which gelling takes place also contributes to the rate of syneresis as does the shape and dimension of the gel [84]. Coarsening is defined as the irreversible decrease in pore surface area. This results from the phenomenon ostwald ripening where large pores grow at the expense of small ones [84]. Ostwald ripening describes the phenomenon of the dissolving of small particles in a liquid while the large particles increase in size. The process is due to the fact that smaller particles are less energetically favourable than larger ones. They detach and diffuse into the solution increasing the amount of free molecules in a solution, which, when saturated, condense of the surface of larger particles, resulting in an increase in size of the larger particles.

Drying

In this phase, liquid is removed from the interconnected pore network by evaporation of solvents at temperature. The gel network shrinks and experiences weight loss during drying and the process must be carefully controlled as large capillary stresses can develop during drying where pores are small leading to cracking [94]. The process can be controlled in many ways such as setting the optimal thermal drying conditions and increasing the ageing time as it prevents the bioactive glass from cracking [85]. The process can also be controlled by decreasing the surface energy of the liquid by using the precursor to control the rates of hydrolysis and condensation reactions [90].

Stabilisation

After drying, the material surface still contains chemically active surface groups, this concentration of silanols at the pore surface makes them unstable at room temperature. The active chemical groups can be removed from the pore network when heated to in excess of 500°C. This will eliminate the isolated silanol groups resulting from irreversible dehydration and will lead to structural relaxation [95].

This stabilisation process is also useful in decomposing and removing other substances in the gel such as the nitrates or the ceramics. Network modifiers such as Ca in the form of $Ca(NO_3)_2$ is used widely in bioactive glasses. This decomposes at 561°C and so thermal stabilisation must be carried out above this temperature [96]. Stabilization should be undertaken with caution as different thermal treatments at higher temperatures (500-800°C region) can lead to changes in the textural properties of the glass [92]. For example, Arcos investigated the bioactive glass 58S (60 mol% SiO_2, 36 mol% CaO, 4 mol% P_2O_5) and found that the pore volume and specific surface area decreased when a sintering temperature of 800°C was reached. This needs to be taken into consideration when choosing stabilization temperatures as it can affect many other material properties.

With regard to Ca incorporation, increases of stabilization up to approximately 700°C enables the release of activation energy for calcium release, this implies that calcium is incorporated into the network (above 450°C). This increase in temperature also increased the skeletal density as a result of changes in the silica network driven by continued polycondensation and reduction interfacial energy of the mesopores. While heating the glass up to these temperatures is beneficial in removing any unwanted materials and necessary for making dehydration irreversible, it is important not to heat the glass in excess of the glass crystallisation temperature as it can eliminate all nanopores [97].

2.2.7. Bioactive glasses in wound healing

Bioactive glasses are biodegradable devices which have traditionally been used in bone regeneration [11-12]. However, more recently, research has shown that they can be utilised successfully in the regeneration of soft tissues and may have advantages over traditional healing methods such as grafting [64]. They have also been shown to form adhesion to soft tissues [99].

Recently, the original bioactive glass composition, Bioglass® [65] , has been investigated for soft tissue applications, such as its ability to stimulate angiogenesis [63] [64]. Day *et al.,* [100] demonstrated potential angiogenic properties of 45S5 through the ability to stimulate the expression and release of VEGF and bFGF by CCD18Co human fibroblasts. This suggests that Bioglass has the potential to stimulate

neovascularisation through its ability to stimulate VEGF expression. Boccaccini *et al.,* [101] found that silicate- and zinc-based glasses were capable of controlling the secretion of cytokines from activated human macrophages and monocytes in response to inflammatory stimuli.

Studies have focused both on the contact of bioactive glasses with soft tissue and the impact of the conditioned media from the bioactive glasses. While a study by Wilson *et al.,* [102] showed that solid Bioglass implants did not have a cytotoxic affect when inserted into the soft tissues of rabbits and rats, many studies focus on the impact of the conditioned media on cells *in vitro* and not the direct application of bioactive glasses. The conditioned media alone does offer therapeutic benefit. The increase in pH alone associated with the dissolution of the silicate-based glass (e.g. S53P4) is reported to have an antibacterial effect on Staphylococcus aureus bacteria [103]. This is particularly useful in chronic wound applications where the risk of infection is high.

2.2.8. Different Cations

Compositionally, bioactive glasses are very flexible. It is very easy to add different metal oxides offering different valuable properties which may provide useful in wound healing. Studies include the addition of gallium, silver and copper which all offer useful potential properties [45]. Caution must be taken when adding in different cations as modification of bioactive glass network can affect glass transition and crystallisation temperatures so factors such as sintering temperatures may need to be readdressed.

Silicon

Silicon ions are the major component released from silicate-based bioactive glasses. Si^{4+} has been shown to have a significant role in the stimulation of collagen production [104] which is critical in bone regeneration, however it has also been found to be important in skin repair as modulating collagen production may prevent the formation of scar tissue [105]. Transforming growth factor-beta (TGF-b) is a growth factor which can increase the production of collagen, it also has other roles in supporting wound healing in the inflammation, proliferation and tissue remodelling stages [105] [106] .

A study from Xie *et al,* [107] highlighted the response of fibroblasts to a sol-gel derived silicate bioactive glasses with a composition of 90Si-6Ca-4P_2O_5 which suggested that the Si heavy bioactive glasses may play a role in the modulating the TGF-b pathway [107]. The study compared bioactive glass compositions with differing amounts of Si (90S, 80S, 70S and 60S) and found that the 90S sample increased the proliferation of human foreskin fibroblasts by the biggest margin. The study also went on to demonstrate that the 90S composition supported the migration and proliferation of fibroblasts in addition to regulating

the expression of collagen types I and III. In another study conducted by Yu *et al.,* [108] the ionic dissolution products from a silicate-based bioactive skin graft was shown to stimulate fibroblasts to secrete some of the essential growth factors required for vascularization and for the healing process. It also demonstrated a significant wound closure and formation of new blood cells in vivo.

Calcium

The second major component typically found in bioactive glass compositions is that of calcium. Studies have shown that the presence of Ca^{2+} in wound healing applications can promote the formation of blood clots in addition to aid the migration of epidermal cells [108] [109]. Calcium particles have also been shown to enhance the wound closure. Kawai *et al.,* [110] produced calcium-based nanoparticles which were applied topically and intravenously to bilateral dorsal cutaneous wounds on female mice. The Ca^{2+} was found to increase fibroblast production, accelerate blood coagulation and enhancing collagen lattice contraction.

Silver

Antibiotic resistance is becoming a big problem in patients and so the use of silver ions in bioactive glasses has become increasingly investigated [111] [112]. Silver exhibits toxic properties to wide range of organisms [112]. The bactericidal mechanism of silver is not very well understood. Research suggests that ionic silver inactivates the thiol groups of enzymes [113] and other experimental evidence suggests that DNA loses its ability to replicate once bacteria has been treated with silver ions [114].

Bellatone *et al*., [115] compared the effect of incorporating 3 wt% of Ag_2O into a sol-gel bioactive glass resulting in the system SiO_2-CaO-P_2O_5-Ag_2O. This was then compared with SiO_2-CaO-P_2O_5 which while displays excellent bioactivity had no reported antibacterial properties. The addition of Ag_2O confirmed antibacterial properties and did not compromise any bioactivity, in terms of HCA formation *in vitro* [115]. One disadvantage of using silver is the need to synthesise with the sol-gel in the dark or under infrared light. It must be stored in the dark afterwards to prevent the silver nitrate and Ag_2O in the glass returning to silver metal [61]. Studies have also looked at the incorporation of silver nano particles into melt-derived glasses, these resulted in improved bactericidal properties compared to the equivalent, silver-free glasses [116].

Cobalt

Sol-gel derived bioactive glasses doped with Co ions have shown an increase in VEGF production in human bone marrow stromal cells (BMSCs). Glasses were produced with a composition of 80 mol.% SiO_2, 5 mo.% P_2O_5, 15 mol.% CaO and were compared with glasses formed with 2 and 5 mol.% CoO added in exchange

for the CaO. Maximum Co release (~20 mg/L at 7 day immersion) occurred from the sample with the higher (5 mol.%) quantity of cobalt. When human bone marrow cells were cultured onto the samples, proliferation was similar for the 0 and 2% samples but decreased for the 5% sample. VEGF secretion at day seven was increased with 2% Co and HIF-1α was enhanced with increasing Co concentration [117].

Azevedo *et al.,* [118], substituted melt-derived SiO_2-P_2O_5-CaO-Na_2O glass with up to 4 mol.% cobalt ions (again for Ca). Two glass compositions were formed: one where the cobalt ion was assumed to enter the glass network and the second, where cobalt was used as a network modifier. Due to Cobalt's charge to size ratio, it is able to enter the silicate network, but also act as a network former and replace bridging oxygen for non-bridging oxygens. The role Cobalt takes within the glass determines the bioactive glass properties. In this reported study, cobalt oxide was added to the composition in different concentrations, the presence of cobalt as a modifier in the network was found to change the T_g of the bioactive glass. The small amount of cobalt which entered the bioactive glass network caused the replacement of Si-O-Si bonds with weaker Si-O-Co bonds resulting in a reduction in Tg.

More recently Barrioni *et al.,* [119] highlighted the importance of precursor selection when incorporating cobalt into a sol-gel network as XPS identified different cobalt precursor solutions altered the cobalt species formed. Where copper chloride was used, XRD and XPS identified crystalline cobalt (II, III) oxide (Co_3O_4) phase formation and the presence of Co^{3+} species. However, the use of cobalt nitrate as a precursor however produced amorphous glasses containing mainly Co^{2+}. This presence of the crystalline phases caused by the use of copper chloride reduced the Co release rate during dissolution.

Copper

A review paper from Naseri *et al.* [106] highlights some of the common ions incorporated into bioactive glasses used for wound healing applications. Copper is one of several ions which have been investigated for wound healing, and while copper was included in the Naseri *et al.,* review article, the majority of studies investigated its antimicrobial properties [120][121], with far fewer discussing the angiogenic properties of copper [122]. Studies have shown however that copper ions can significantly increase the VEGF production in primary and transformed human keratinocytes [56], human umbilical vein endothelial cells (HUVECs) [123] and human bone marrow stromal cells (hBMSCs) [124].

Bejarano *et al.* [125] incorporated 1, 5 and 10 mol% CuO into 58S bioactive glass and $60SiO_2$–$25CaO$–$11Na_2O$–$4P_2O_5$ (NaBG) bioactive glass compositions replacing the CaO. The cytotoxicity of both bioactive glass compositions was found to be related to the concentrations of Cu-ions in the media. An MTT assay osteoblast-like cells (SaOS-2) at 24 h showed a cell viability of just ~10% in the 1Cu, 5Cu and 10Cu

concentrations in 58S and < 20% in the 5Cu and 10Cu concentrations in NaBG. Dissolution studies in DMEM/F2 show a Cu-ion concentration at 24 h of ~12 mg L^{-1} (0.19 mM) for 1Cu, ~70 mg L^{-1} (1.10 mM) for 5Cu and ~75 mg L^{-1} (1.18 mM) for 10 Cu in 58S and ~5 mg L^{-1} (0.08 mM) for 1Cu and ~10 mg L^{-1} (0.16 mM) for both the 5Cu and 10Cu compositions in NaBG.

Copper ions have also been incorporated into porous mesoporous bioactive glass sponges [126] where sol-gel derived copper containing bioactive glass compositions containing 1, 2, and 5 mol.% copper were found to stimulate HIF-1α and VEGF expression in hBMSCs. Ion extracts and the Cu-scaffold were both shown to promote osteogenic differentiation. Over a 7-day exposure, proliferation of hBMSCs was reduced in the 5 mol% Cu sample however this did not appear to affect the VEGF expression despite a high copper ion concentration at 7 days of 152.7 mg L^{-1} (2.40 mM). This indicates that different cell types may respond very differently to differing copper ion concentrations.

In a recent study, Zhao *et al.,* [123] incorporated copper into 13-93B3 melt-derived borate glass microfibres. A full thickness skin wound model was used in Sprague-Dawley rats and all four samples tested (0 wt.% CuBG, 0.5 wt.% CuBG, 1 wt.% CuBG and 3 wt.% CuBG) were found to enhance VEGF, BFGF and PDGF in primary dermal fibroblasts and HUVECs. The 3 wt.% CuBG composition caused the highest relative expression of all three growth factors in fibroblasts. None of the samples caused cytotoxic affects despite dissolution studies showing an ion concentration of 180 mg L^{-1} (2.83 mM) at 7 day immersion for the 3Cu BG sample. This is an interesting result, as previous studies have reported that copper does not appear to have an effect on fibroblasts [57].

2.2.9. Borate glasses

A large amount of research has been carried out on bioactive glasses which are borate based [63]. Borate glasses support cell proliferation of bone marrow stromal cells and the proliferation and differentiation of murine MLO-A5 cells (an osteogenic cell line) in *in vitro* experimentation [127]. Borate glasses have also been successfully used commercially in the animal market, manufacturers such as Rediheal® (Mo-Sci, Missouri, USA) use borate-based glasses for wound healing and dental applications.

The interest of borate glasses over silicate based bioactive glasses is due to their faster reaction time with the body to form HCA and their ability to convert at a more controllable rate [128][129][130]. They have also shown promise in wound healing applications more recently [106]. The success of borate glasses over silicate based borate glasses is due to their greater increase in local pH, their high degradation rate [129] and the ability of boron to stimulate angiogenesis [131]

Silicate based glasses are also reported to convert incompletely to HCA compared with borate glasses in some cases, this results in unconverted silicate glass remaining in the body for extended periods [128] [129]. The mechanism of conversion for borate glasses to HCA in phosphate solution is thought to be similar to that of silicate bioactive glasses through a dissolution-precipitation mechanism [130].

The main reservations for using borate based bioactive glasses is their toxicity. As it degrades, boron is released into the solution in the form of borate ions. When toxicity levels were tested in standard static *in vitro* culture conditions, the levels of boron released were deemed to be toxic to cells. However, in dynamic testing, this toxicity was greatly reduced, this is however also the case in silica based glasses such as 45S5 at certain concentrations [81].

This toxicity difference was demonstrated in studies by Fu *et al*, [130] where borate bioactive scaffold composition was obtained by substituting SiO_2 with B_2O_3 in a 13-93 glass. Three scaffolds were developed: one of silicate (13-93) and one borosilicate composition (13-93B1). In the third composition, one-third of the SiO_2 content was replaced by B_2O_3 producing 13-93B3. The scaffolds showed no toxicity to cells *in vivo* and supported new tissue infiltration when implanted into subcutaneous pockets in the dorsum of rats. It was found that the slower degradation rate of the silicate 13-93 and the borosilicate 13-93B1 scaffolds supported cell proliferation and function much better than the rapidly dissolving 13-93B3 composition [132].

Previous work has shown the ability to control the degradation rate of borate glasses closely by changing the composition [129]. In melt derived glasses, by partially replacing SiO_2 in silicate 45S5 glass with B_2O_3 (producing borosilicate bioactive glasses), or fully replacing the SiO_2 with B_2O_3 the degradation rate has been varied considerably. The four different glass compositions were 0B (45S5); 3B (same composition as 45S5 but with all the SiO_2 replaced with B_2O_3);1B and 2B with intermediate borosilicate compositions with 1/3 and 2/3 of the SiO_2 concentrations [128]. All samples were placed in 0.2 M K_2HPO_4 and their weight loss and change in pH measured. The reaction rates varied enormously with the change in weight reaching its limiting value at under 60 hours for 3B and in over 600 hours for 0B. This also corresponded to pH values, where the value changed most rapidly for the 3B sample [128]. Careful control over the composition like this, means that it possible to closely match the degradation rate of borate glasses with the regeneration rate of tissue [63].

2.2.10. Wound healing, bioactive glasses and HCA formation

Naseri *et al.,* [106] summarised several studies looking at the impact of HCA formation on wound healing. The impact of HCA on wound healing is not well understood and studies show conflicting results. Lin *et al,* [133] and Hongfei *et al,* [108] investigated the impact of bioactive glass particles inserted into Vaseline, including the HCA forming 45S5, and showed an ability to accelerate wound healing compared to plain Vaseline in studies conducted on rats [133] and mice [108]. Naseri *et al,* [106] highlighted a relationship between the ratio of silica and calcium in bioactive glasses, and their impact on the clotting activity in wound healing. Clotting rates were reduced in bioactive glass compositions such as 58S with a lower ratio of silica and calcium (typically associated with higher HCA deposition rates) compared to compositions such as 80 mol% SiO_2, 16 mol% Ca, 4 mol % P_2O_5 with a higher ratio of silica to calcium and associated with lower HCA deposition rates [134] [135].

However, in many studies, calcium deposits have been shown to impede the healing of diabetic ulcers [136][137]. HCA formation can be reduced by producing a glass which is more resistant to degradation, however for wound healing to be optimised, it would be key to have a higher release rate of ions to induce a stronger biological response. For wound healing application therefore, it may be required to have new glass compositions which do not precipitate HCA but are still able to degrade and release therapeutic ions in a timely manner.

2.2.11. Bioactive glasses summary

Literature suggests that the sol-gel route preferable for achieving better bioactivity over more traditional, melt-forming techniques. The flexibility of sol-gel glasses compositions is additionally attractive as it has been shown that copper can easily be incorporated into sol-gel glasses and that it provides a beneficial response in stimulating the production of VEGF. The concentration of copper incorporated will however have to be determined as literature shows that different some cell types are affected by concentration more than others.

The bioactive glass scaffold must be designed in such a way to enable the synthesis of new tissue, but also must eventually degrade leaving the new organ or tissue behind in its place. The precise design of the scaffold is vital in ensuring the optimum microenvironment for tissue generation and to enable flow of nutrients between the cells and the surrounding environment [138].

2.3. Electrospinning

Electrospinning is becoming an increasingly investigated technique in biomedical research. The ability to spin fibres on the nano- and micro scale has proved to be useful for many applications in tissue engineering. The electrospinning of bioactive glasses for wound healing is particularly interesting as the large surface area obtained in electrospun materials makes it a useful technique for producing scaffolds for tissue engineering. These are able to mimic some of the key structural features of the ECM structure [139] [24] with the potential to provide a familiar scaffold for cells to attach and adhere to. The simplicity and versatility of the technique makes it a very attractive fibre fabrication method.

Literature shows successful electrospinning of many synthetic and natural polymers [138]. The versatility of electrospinning has also enabled modifications to be made easily such as where electrospinning slow, dual syringes have been used to increase yield and to enable crosslinking of different nanofibres by reactive methods [141].

As with 3D printing, the orientation of electrospun fibres can influence cell proliferation, orientation and eventual tissue growth. Musculoskeletal tissues exhibit anisotropic mechanical properties [142] . Recent literature shows that it is possible to generate nanofibre based scaffolds with controlled fibre orientations [143]. Investigations by Murugan *et al.,* [144], and Ayres *et al.,* [145] show that small changes in fibre alignment can control the material properties of scaffolds.

Electrospinning is a fabrication method which is used to produce continuous, fine fibres from a solution. The fabrication technique uses an electric field to induce an electric charge on a solution emerging from a needle, which, when sufficiently high to overcome surface tension, ejects a charged jet of the solution in the form of a long, thin solid fibre. This technique has become of interest in tissue engineering applications as the electrospun fibres are typically very fine (2 nm to micrometer range [146]) have a high surface area and are flexible compositionally, meaning that a wide range of materials can be formed as fibres via electrospinning processes [147] [148].

The electrospinning machine is typically comprised of just four components: a high voltage power supply, a spinneret, a grounded collecting plate and a syringe pump [149] and can be seen in *Figure 4*. The syringe pump is filled with a solution, typically a polymer, or a sol-gel which normally combined with a solvent, which is forced through a metallic needle at a controlled rate. The process of the formation of the Taylor cone and an electrospun fibre is described in *Figure 5*. As the liquid moves through the needle, drops of the liquid appear at the tip. A high voltage is placed across the solution creating an electric field which imparts a charge on to the solution, as the intensity of this electric field increases, the surface of the liquid at the tip

becomes distorted and elongated leading to the formation of a Taylor cone [150]. When the electric field reaches a certain value, the repulsive forces overcome that of the surface tension forces and a charged jet emerges from the tip of the cone. This charged jet accelerates towards the collector and an unstable rapid whipping of the jet occurs in the process. As the jet reaches the collector the solvent is evaporated, leaving behind a solid fibre [150] [151]. The bending instability caused by the electric field [152] causes a reduction in the fibre diameter and the evaporation of the solvent. The bending instability can cause several different variations in the types of fibres that are produced. The formation of several branches from a single jet is common or beads (lumps of solid solution) on the fibres if the charge is too low [152].

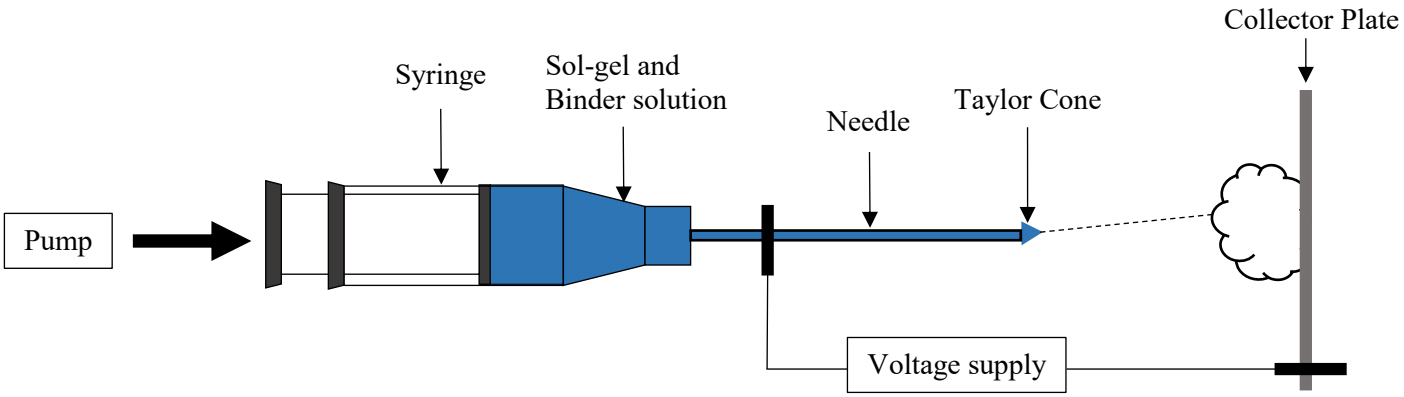


Figure 4. Schematic of the Electrospinning set up and the components required.

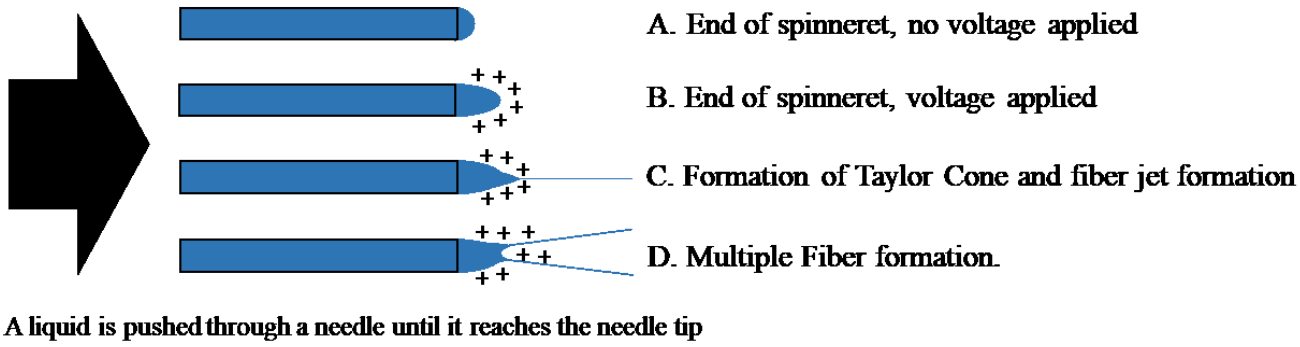


Figure 5. Schematic of the formation of a Taylor cone and production of electrospun fibres A. depicts the end of a spinneret where no voltage is applied, the liquid moves through the spinneret. B. A voltage is applied which causes the end of the spinneret to be charged and the liquid elongates producing a Taylor Cone. C. When the electric field reaches a certain value, the repulsive forces overcome that of the surface tension on the liquid and a charge jet emerges from the cone tip. D. Bending instability of the Jet can cause the formation of several branches.

2.3.1. Variables affecting electrospinning

While the electrospinning set up itself is simple, the morphology of the fibres depends on a range of factors such as solution properties, processing conditions and ambient conditions such as temperature, humidity and atmospheric pressure. Factors affecting electrospinning can be split into two categories: those affecting the properties of the solution and those affected by the properties of the electrospinning set up.

Material parameters

Viscosity has a significant impact on the spinnability of the sol. At low viscosity there is no continuous fibre formation, however as the viscosity increases it becomes difficult for fibres to eject from the solution when the electric field is applied [153]. At the right viscosity for the sol, long fibres are produced with a more uniform diameter [146].

Two significant factors that can affect the viscosity of the solution include the concentration and the molecular weight of the solution. In polymers, a minimum solution concentration is required for the formation of fibres [154]. At concentrations that are too low, a mixture of beads and fibres are formed. With an increase in concentration, the fibres become more spindle like before eventually forming uniform fibres once an adequate concentration is reached [154].

Polymer molecular weight can affect rheology and the electrical properties of the sol. A high molecular weight sol is generally more viscous and so sols with lower molecular weights tend to form beads and fibres produced are not uniform and long [154].

Surface tension is also believed to contribute to the spinnability of the sol. Generally, a solution with a high surface tension prevents the formation of fibres inhibiting electrospinning. This is due to the instability of the jets and the generation of sprayed droplets [155]. Despite this, it does not necessarily follow that a lower surface tension will always be more suitable for electrospinning, it is more that an understanding of the surface tension provides an idea of the upper and lower boundaries of the electrospinning window when all other variables are held constant [156] [157].

Processing parameters

This spinning distance is defined as the distance between the syringe tip and the collector plate. Varying this distance has a less significant effect on fibre formation compared with other parameters. Zhang *et al.,* [157] reported no significant effect on fibre morphology when electrospinning PVA. The same observations have also been made in gelatin [158] and in chitosan [159]. An important aspect to note is that a minimum spinning distance is needed to enable the fibres to dry before they reach the collector plate. Lee *et al.,* [160] observed, when electrospinning PVA, that distances which are too short have resulted in the formation of non-uniform fibres and the presence of beads.

The applied voltage to the solution in electrospinning is one of the most critical factors that determine the impact of the fibres produced. A minimum voltage is required in the first instance to induce the formation of the Taylor cone leading to the ejection and formation of fibres.

There are numerous studies which have attempted to define the impact of applied voltage on the diameter of the fibres produced. It has been shown, that when electrospinning polyethylene, that changes in the electric field, supplied by the voltage, has little effect on the diameter of fibres [161]. However, the application of higher voltages, more polymer is ejected from the tip of needle resulting in the formation of thicker fibres [157] [162]. Conversely Larrondo *et al.,* [163] [164] [165] have found that doubling the applied voltage, decreased fibre diameters by a half. Katti *et al.,* [166] electrospun poly(lactide-co-glycolide) (PLGA) for wound healing applications and found that increasing voltage, did result in a decrease in the average fibre diameter. The study investigated several factors such as the needle gauge and the concentration of the polymer. It found that any changes in fibre diameter due to voltage were less marked than changes in the fibre diameter resulting from changes in the polymer concentration.

The flow rate controls the speed and the rate of transfer of material from needle tip to collection plate at any one time. A minimum flow rate, sufficient for electrospinning, is required for fibre formation. A flow rates too low, insufficient material is fed through the needle eye and therefore the rate of electrospinning is not constant and uniform fibres can fail to form [154]. At flow rates too high however, the formation of beads is more likely as the fibres are not given sufficient time to dry before collecting on the collector plate [167] [168]. The morphology of fibres can be impacted by the flow rate. Megelski *et al.,* [169] found that the pore diameter and fibre diameter of electrospun polystyrene (PS) fibres can be increased by increasing the flow rate of the solution.

2.3.2. Electrospinning bioactive glass scaffolds

Kim *et al.,* [170] reported the first electrospun nanoscale, one-dimensional sol-gel derived bioactive glass fibre. The 70 wt% SiO_2, 25 wt% CaO, 5 wt% P_2O_5 composition electrospun and tested for its osteogenic potential with BMSCs. Fibres as small as 84 nm were achieved and a polymer binder (polyvinylbutyral) was added to the sol prior to electrospinning to achieve suitable sol-gel parameters in terms of viscosity and surface tension for electrospinning. The increased surface area created by the fibres resulted in a faster dissolution compared with the equivalent composition in disc form. Kim *et al.,* [170] also showed *in vitro* attachment and the differentiation of BMSCs placed on the nanofibres and compared it with glass films of the same composition. The fibres and films both yielded similar results, however the nanofibres displayed enhanced expression of alkaline photophatase (ALP) which is an important marker indicating osteogenic potential and bone forming ability.

The spinning of bioactive glass fibres extends beyond the sol-gel route, with melt-derived fibres formed by laser spinning [171] and the successful spinning of borate glass fibres through a melt blowing route to form fibres which reported good clinical results when used for healing diabetic foot ulcers [172].

2.3.3. 3D cotton-wool-like electrospun fibres

Electrospinning typically produces a 2D fibremat structure which provide a scaffold for shallow wounds or burns [138]. Where wounds are deep, a 3D structure which fills the wound, mimicking the ECM and encouraging cell migration and proliferation would be of benefit. Coined as ‘cotton-wool-like’ structures, several groups have developed 3D structures through electrospinning or similar techniques.

Poologasundarampillia *et al.,* [7] produced 3D electrospun bioactive glass fibres with a composition of 70 mol% SiO_2 and 30 mol% CaO (70S30C) for bone applications. This composition was electrospun directly

from the sol, uniquely without the need for a polymer binder, and had an appearance similar to cotton wool or cotton candy with the ability to be packed into bone or wound defect. This '3D' structure is different from some literature definitions which define '3D' as 2D fibremats which are thicker (~0.5–2 mm) than conventional fibremats (<0.5 mm) [30-31].

Obata *et al.,* [175] and Kasuga *et al.,* [176] also produced the characteristic 'cotton wool' structure for poly(lactic acid) and siloxane-doped vaterite (SiV) composites using chloroform as the solvent. This was produced using an ethanol stirring method [176] and a fan method [175] to produce 3D structure. The fan method prevented fibres from sticking to one another by blowing air against the fibres enabling the immediate evaporation of solvent. In the ethanol stirring method, fibres were electrospun into an ethanol bath which neutralised the charge and dissolved the solvent.

The method used by Poologasundarampillai *et al,* [7] to produce the 3D structure without the use of a binder, required careful control of ethanol evaporation to ensure accurate control of the viscosity. Poologasundarampillai *et al*, compared the structure formed when electrospinning 100S and 70S30C compositions. It was found that a very narrow evaporation window of 40–43 wt.% solvent was required to successfully electrospin the 70S30C structure while a higher wt% of approximately 63 wt% was required for the 100S. Long, uniform fibres were produced in both cases. The expected fibremat was produced when electrospinning the 100S composition. However, with the 70S30C structure, the Taylor cone formed, followed by a jet which subsequently split up into several different strands before it unstable bending, leading to the production of the 3D structure [7]. This unstable bending, known as splaying, has been reported in a number of papers [177] [178]. Reneker *et al,* found that in some cases during electrospinning, the electrified fluid jet undergoes an electrically driven bending instability and for some materials such as polymer solutions, can cause secondary branches, which changes the structure of the fibremat produced [178]. Zong *et al.,* showed how fibre morphology can be changed by the addition of salts to PDLLA. It was found that the addition of salts creates a higher charge density on the liquid surface during spinning. Higher elongation forces are imposed as the charge on the jet increases, the morphology is altered by changing the diameter of the fibres and reducing bead formation [177]. Reneker *et al.,* and Srinivasan *et al.,* have commented [152] [179] on the electrospinning of the conductive polymer polyaniline, which experiences fibre entanglement and reorientation during spinning. Here the typical 2D fibremat was not formed, instead, the charged fibres became entangled during electrospinning and formed a network in the direction of the electric field. It is believed that the conductivity within the solution, lead to the re-distribution of charges at certain ends or sections of the fibres, which stretched the fibres in the direction of the applied field, forming a structure unlike the 2D fibremat typically seen in electrospinning.

Poologasundarampillai *et al.,* [7] attributed the formation of the 3D structure to two factors: i) the rheological properties and surface tension of the sol; ii) the distribution of conductive ionic species. It was suggested that during the application of an electric field, the silica and calcium species in the homogenous sol began so separate, resulting in a heterogeneous distribution of Ca^{2+} and SiO_4^{4-} at the Taylor cone. This separation of charges caused a difference in force on the fibres as they travelled towards the collector plate. Depending on the charge distribution within the fibre, sections of the fibres were whipped and bent in different directions causing the formation of interwoven, or cotton-wool-like fibres to form. Similar affects have been documented in polymers [32-33], an example includes polyaniline, where charge carriers are concentrated at various points within the fibres due the presence of an electric field through a conductive medium.

2.3.4. Electrospinning summary

Production of 3D scaffolds has exciting commercial applications as it is able to be packed into defects which may make it easier for clinicians to use in wound healing applications compared with other, currently available, treatments. A disadvantage with the production of the 70S30C 3D fibres is the complexity of the sol preparation. Ethanol evaporation has to be carefully controlled as there is a narrow window where the fibres can be electrospun. A revised protocol needs to be developed that will produce long, uniform fibres more reliably.

Many factors such as viscosity and humidity may affect the ability of the sol to electrospin and voltage and distance can be used to control the diameter of the fibres produced. These factors and their impact on the fibres produced will need to be investigated to provide a full understanding so that they can be used to control the morphology and the structure of the fibres produced.

2.4. Thesis objectives

The literature review has highlighted the need for a new, affordable and effective wound healing product that can be effectively used alongside other treatment methods.

The use of bioactive glasses in soft tissue applications, and more recently for wound healing, is starting to gain traction. Although the mechanism is still unknown, there is a wealth of evidence to suggest that bioactive glasses do have a positive therapeutic effect in wound healing applications. The flexibility of the sol-gel derived glasses are also attractive as it enables the easy incorporation of metal oxides such as copper which have been shown to promote VEGF production and therefore angiogenesis in wounds which is vital for successful healing.

The use of techniques such as electrospinning which produce scaffolds with high surface areas should enable concentrations of therapeutic ions to reach wounds quickly. 3D electrospun structures are interesting as they are able to mimic the structure of the ECM and can potentially be inserted deep into wound beds without the need for removal as the scaffold should fully degrade.

The main aim of the studies presented here are to investigate the use of Bioactive Glasses for wound healing applications. The 3D structure of the electrospun bioactive glasses scaffolds have a potentially useful architecture which can be placed into deep wounds enabling the release of ions deep into the wound and additionally providing a structure for cell proliferation. The overriding objective is to design a bioactive glass for wound healing applications which has a chemical structure that can stimulate the production of VEGF for angiogenesis and enable the proliferation of HDFs.

The objectives of this thesis are to:

- Understand the factors that determine the formation of a 3D electrospun scaffold and develop a protocol to reliably and repeatedly produce a 3D structure with long and uniform fibres
- Design a 3D bioactive glass scaffold produced via the electrospinning technique which degrades producing ion concentrations which do not cause cytotoxicity issues to HDFs
- Successfully incorporate copper ions into the bioactive glass structure which release at a controllable rate and stimulate VEGF production in HDFs
- Use characterisation techniques to investigate the chemical, bonding and physical properties of 3D copper containing bioactive glasses.

CHAPTER THREE

CHARACTERISATION TECHNIQUES

A mixture of physical and chemical techniques were used to characterise the bioactive glasses produced. These were used to understand the physical parameters of the bioactive glasses produced, such as the size and topography of the fibres but also to analyse the chemical composition of the materials and their response to changes in their chemistry or their presence of physiological fluids and cells on the materials. This chapter provides a brief oversight into the characterisation techniques and how they work. More information on the specific set up and parameters used to analyse the materials is outlined and discussed in the results chapters.

3.1. Physical analysis

3.1.1. Scanning electron microscopy (SEM)

SEM is used to view the morphology and the topography of a specimen surface. For SEM, samples must be conductive or be coated in a conductive layer. The glass samples investigated here were coated with chromium. Electrons are accelerated to and interact with the conductive surface of the material. The interaction produces signals which include: X-rays, secondary electrons, backscattered electrons and Auger electrons. Secondary electrons are used to produce images of the sample surface whereas the others are useful in obtaining an understanding of the composition of the material.

The secondary electrons are produced as a result of excitation from the primary electron beam. They are low energy and occur from just under the sample surface. They undergo elastic and inelastic collisions as the move to the surface of the sample, where they can be detected. They can provide details of the topography of the sample. Topographical information about the sample surface was very important in this thesis. SEM was used to make measurements of features such as fibre diameters and the presence of pores on the sample surface.

A consideration that has to be made when using SEM is the preparation of the sample surface. For good images to be obtained, a flat surface is surface is important. This could provide a challenge if looking a 3D fibrous surface as images should be flat so as to provide a good surface to obtain high magnification images in focus. As the bioactive glass fibres are not conductive, they will have to be coated in chromium, finding the correct coating of chromium can be an iterative process as the charging of samples which can cause images to be blurry. Sample charging is the result of a lack of conducting path for the electrons from the surface of the sample to flow to ground, it is a problem because the electrons that remain on the sample are repelled by other electrons. The magnification can be used to determine if a sample is charging (by the presence of a dark or bright square on the sample surface after viewing the sample at a high magnification

followed by a low magnification). Some experimentation will need to be conducted to ensure samples have the correct coating and that a sufficient conducting path is produced in order to obtain high quality images.

3.2. Chemical analysis

3.2.1. Fourier transform infrared spectroscopy (FTIR)

FTIR is a spectroscopy technique which is used for the identification of different materials. When a beam of infrared light is directed at a material, the energy of the beam amplifies the vibrational excitation of atoms within the molecules present in the material. The infrared beam is comprised of many frequencies, and atoms respond to different frequencies by either absorbing or reflecting the beam. The absorbance is measured at different frequencies by comparing changes in intensity of the beam before and after it travels through the material. Fourier-transform is used to obtain a characteristic 'fingerprint' spectrum of the material by converting the absorbance measurements to the amount of energy absorbed by the material at each wavelength. The majority of these bending and stretching vibrations occur within the 600 cm^{-1} to 1400 cm^{-1} range, although for the bioactive glasses being investigated in this thesis, the area of interest predominately lies in the 600 cm^{-1} to 2000 cm^{-1} region. FTIR will be one of the primary characterisation techniques used for chemical analysis.

3.2.2. Solid-state ^{29}Si magic angle spinning-nuclear magnetic resonance (^{29}Si MAS-NMR)

^{29}Si MAS-NMR is used to provide information regarding the bonding and chemical state of molecules within a material. The technique applies a magnetic force to a material which causes a spin of atoms with the material. Each atom has a characteristic spin, but this spin is heavily dependent on the other electrons in the bonds which surround the nucleus. This is useful in gaining information about the state of the atoms present in a material.

Si atoms are of particular interest as this work focuses on a silica glass structures. NMR can be used to determine the connectivity of the silica networks which can be used to determine how different processes affect it. Si atoms bonded to four oxygen atoms are defined as the Q species, and Si atoms which are bonded to four bridging oxygens will have a different chemical shift to those bonded to three bridging oxygens and non-bridging oxygens (Si-OH). Q^1 refers to one bridging and three non-bridging oxygens, Q^2 refers to two bridging and two non-bridging oxygens and so on.

Knowledge of the Q species can calculate the degree of condensation (Dc) (Equation 4) and can be used to compare the network connectivity of the silica network of different samples.

$$D_c = \frac{Q^1\% + 2Q^2\% + 3Q^3\% + 4Q^4\%}{4}$$ Equation 4.

3.2.3. X-ray diffraction (XRD)

XRD is a well-known technique used to analyse crystallinity in a material. The technique works by heating a filament to produce electrons which are accelerated towards a material. The bombardment of electrons on the material, which is typically copper, dislodges electrons from the inner shells of the material, releasing characteristic x-rays which are filtered to produce a monochromatic X-ray source.

When the incident X-rays reach the sample, they are diffracted by the atomic plans within the crystalline structure of the material, they can constructively or destructively interact producing a diffraction pattern which is characteristic of different materials.

The specific arrangement of atoms in the sample can be calculated using Bragg's Law. This can be used to identify different crystalline structures in materials with the same chemical composition.

$$n\lambda = 2dsin\theta$$ Equation 5

Where *n* is an integer, λ refers to the wavelength, 2θ is the range of angles and d refers to the spacing of the crystalline structure. The obtained d spacing values are then compared with standard reference patterns.

The glasses investigated in this thesis are designed to be amorphous materials, these have a wide distribution of atomic spacing meaning that characteristic d spacing values will not be obtained. Amorphous materials will instead produce a spectrum known as an amorphous halo. This technique will be useful in identifying any unwanted crystalline phases in the material resulting from fabrication techniques or heat treatments and to monitor the response of materials to cell media.

For the crystallinity of samples to be accurately assessed and any peaks identified, sample noise needs to be reduced. Sample interference can be common in samples like the bioactive glasses which should produce amorphous halos when analysed. To understand this for the bioactive glasses presented here, the scanning

time may have to be increased to allow more time per step to reduce sample interference. As with the SEM, it is advantageous for samples to be powdered and be completely flat in the sample holder, therefore some planning in sample preparation may be required to ensure enough sample is available to powder and fill the sample container and to produce a flat surface for XRD analysis.

3.2.4. Inductively coupled plasma atomic emission spectroscopy (ICP-AES)

ICP-AES is an analytical technique is used to determine the ion concentration of elements within a particular solution. It works by producing plasma through the ionisation of argon gas. When the samples come in contact with the plasma, they collide with the charged particles and electrons present in the plasma which break them down into atoms and repetitively excite them to higher energy states. When they return to lower energy states, they emit a characteristic wavelength specific to the element which is detected by an optical emission spectrometer.

The concentration of ions within a sample are determined by the intensity value of wavelength, the intensity is compared to previous measured standards of elements of interest (typically between 1 mg L^{-1} and 40 mg L^{-1} in required for glasses).

This technique is particularly useful in the dissolution of glass samples in media or buffer solutions, ICP will help to determine the degradation of the sample and provide an indication of potential cytotoxicity issues if high concentrations of ions are obtained.

3.2.5. X-ray photoelectron spectroscopy (XPS)

X-ray photoelectron spectroscopy (XPS) is used to investigate the surface chemistry of a material. The technique uses X-rays to irradiate the surface of a material while analysing the electrons and kinetic energy which is emitted from the top 1 – 10 nm of the surface of the material. The ejected electrons are counted over a range of kinetic energies producing a photoelectron spectrum. The spectra can be used to determine the elemental composition, empirical formulas and the chemical states of a material.

Before XPS was carried out, the selected samples were dried at 120 °C for 24 h before being mounted onto black carbon tape. The carbon tape was mounted onto a base plate before being placed into the sample holder. In situations where there was a delay between preparing the sample and loading it into the XPS analysis chamber, samples were stored mounted onto their base plates in a desiccator. The role of drying at

and 120 °C and then storing in a desiccator prior to inserting into the XPS analysis chamber was to reduce as much moisture on the sample as possible as it can impact the ability of the chamber to obtain the desired pressure.

3.2.6. Energy Dispersive X-Ray Spectrometer (EDX)

SEM-EDX analysis was additionally used as a technique to determine the chemical composition of samples. EDX analysis is often coupled with SEM analysis, which is described in Section 3.1.1. EDX focuses on the role of X-rays which are emitted as a result of the acceleration of electrons which interact with the conductive surface of the material.

While with SEM, it is the secondary electrons which are used to produce an image of the sample surface, with EDX, it is the emission of X-rays which is required. The X-rays emitted are derived from the excitation and movement of electrons between different energy levels within the sample. The radiation produced is therefore characteristic of the material it has come from. Therefore, it can be used to detect the chemical composition and relative amounts present within the material. As with SEM analysis the substrate surface has to be conductive for any signal to be detected.

3.3. Biological analysis

3.3.1. AlamarBlue® cell viability

AlamarBlue reagent is a solution which provides information regarding the viability or cytotoxicity of the cells. It is a common indicator of the metabolic activity of the cells. The indigo-coloured detects metabolically active cells present within a cell well, when viable cells are present, their reducing environment results in a colour change of the reagent which becomes red and highly fluorescent. This colour change and fluorescence can be detected using a plate reader which ca be used to correspond to the viability of the cells.

The AlamaBlue reagent is comprised chemically of resazurin which is reduced to resorurfin in the presence of viable cells resulting in a distinct colour change. The sample is incubated in the dark for between 1-4 h (4 h in the studies within this thesis) before using a fluorescence-based plate reader to determine changes in the viability. The colour change can be detected using absorbance at 570 mm and 600 mm.

For this research, the use of the AlamarBlue reagent is advantageous over more commonly used viability assays such as the MTT because cells are kept intact to enable further analysis. This meant that total DNA analysis could be carried out on the same cells.

3.3.2. Total DNA

The AlamaBlue study is conducted to provide an indication of the metabolic activity of the cells, it does not provide an idea of the total DNA concentration of the cells present. While the metabolic activity of the cells is an important indicator of cell health, it does not provide all the information fully required to determine the response of the cells to a change in environment, such as the additional presence of a new bioactive glass. Hoechst dye is a commonly used reagent to determine the viability of cells through measuring the Total DNA concentration in cells present. The dye penetrates the membrane of the cells and binds to regions of DNA in live cells. Quantification is determined through enhanced fluorescence as the DNA stain becomes excited by ultraviolet light. This is detected by a fluorescence-based plate reader.

3.3.3. Vascular endothelial growth factor (VEGF) ELISA

The VEGF ELISA is used to measure the levels of VEGF in supernatants from cell cultures. The kit (R&D systems) is comprised of a monoclonal antibody which is pre-coated onto the base of each well of a microplate. When the samples, standards and controls are pipetted into each cell well, the antibody binds the VEGF present in the added supernatants. The rest of the supernatant is removed, leaving the bound VEGF in the cell well, an enzyme-linked polyclonal antibody for human VEGF is then added and removed followed by a substrate solution. Supplied colour reagents are added and the intensity of the colour is measured, using a plate-reader, which is proportional to the amount of VEGF bound to the monoclonal antibody.

CHAPTER FOUR

PRODUCING ELECTROSPUN BIOACTIVE GLASSES

4. 1. Introduction

The use of electrospun bioactive glasses for soft tissue regeneration is a relatively new application. With the majority of literature focusing on electrospinning bioactive glasses for bone regeneration, there is a gap in knowledge of how bioactive glasses in the silica-calcium system can impact the healing and regeneration of soft tissues. The use of electrospinning has many potential benefits in soft tissue applications, particularly of those in wound healing as electrospinning can be used to produce fibrous structures at a scale which can mimic key structural features of the extracellular matrix (ECM) of the skin [7], [140], [146], [180]. Here, the overall aim was to identify and produce an electrospun bioactive glass composition for wound healing applications, produced via a sol-gel route, which can release Si and Ca ions into the wound bed, producing a concentration which has physiological benefits for wound healing. The morphology and form of the scaffold should be easy to insert into the wound bed by clinicians and should be able to dissolve into the wound bed.

This Chapter focuses on investigating how silica-calcium bioactive glass compositions and electrospinning variables affect the morphology of the glass. In this Chapter, the aim is to develop a new and easily reproducible sol-gel protocol which can be successfully electrospun to produce a three-dimensional (3D) cotton-wool-like structure. The attraction of the use of a 3D fibrous "cotton-wool" structure stems from the work of Poologasundarampillai *et al.,* [7] and Obata *et al.,* [175] where the produced 3D structure could be inserted into a deep wound bed. The cotton-wool like structure is hypothesized to be advantageous as it provides a similar structure to the ECM by the composition of fibres allowing cells to infiltrate and proliferate through the structure, which is often not the case in 2D fibres.

Three-dimensional (3D) cotton-wool-like fibres were first produced by Poologasundarampillai *et al.,* [7] at Nagoya Institute of Technology (NITech), Japan. Their 70S30C sol gel composition was electrospun without the use of a polymer binding agent. They found that by evaporating between 40 wt.% and 43 wt.% of the solvent, the remaining sol had an optimum viscosity to produce the desired stable, long and continuous fibres when electrospun. The electropun 70S30C sol is comprised of 70 mol.% SiO_2 and 30 mol.% CaO and the research hypothesised that the formation of the 3D structure was due to the presence and movement of calcium ions in the sol as a result of the applied electric field when electrospun. It was supposed that at the point of electrospinning, the Ca^{2+} and SiO_4^{4-} charges in the 70S30C sol would separate, leading to regions along the length of the fibres having higher or lower concentrations of calcium ions. As a result, different regions within the fibres where subject to different charges and so responded by stretching and bending at different rates as the electric field was applied during electrospinning. This caused a 3D

structure to be produced at the collector plate. Since this, other methods for producing three-dimensional fibres have been developed [175], [181].

The literature review (Chapter 2.3) identifies that both material and electrospsinning parameters have a significant impact on determining the ability of a solution to electrospin. Research demonstrates that different electrospinning and material parameters are utilised by groups when producing fibrous samples.

The objectives were to: obtain an understanding of the sol-gel process in terms of its suitability for electrospinning; produce a suitable electrospinning and heat treatment protocol; to investigate how the variables affect the dissolution rate of the fibres and to investigate the potential for the spun material for soft tissue applications such as in wound healing through analysing the dissolution of the fibres.

4.1.2. Material parameters

The viscosity and surface tension of the sol are considered to be significant parameters when preparing a solution for electrospinning [152]. To obtain a desirable viscosity, many groups [170] [182] have reported the use of a polymer binder when electrospinning as this can be tailored easily to provide the correct viscosity parameters for electrospinning. The use of a polymer binder however means that electrospun fibres need to be heat treated to remove traces of binder after electrospinning. The ability to control the viscosity easily makes the reliability and repeatability of electrospinning the sol much easier.

The initial approach was to determine the viscosity range of the sol-gel so that continuous, long and uniform fibres could be produced consistently. The viscosity of the sol was investigated through changing the use of the polymer binder and through altering the R ratio of the sol. The R ratio refers to the ratio of water to TEOS (the silica source) in the sol.

$$R = [H_2O]/[Si(OR)_4] \qquad \text{Equation 6.}$$

Literature shows that an R ratio of 2 or more is needed for the hydrolysis and condensation reactions to take place to produce fibres [86][87]. However an increase in the amount of water in the sol affects both the surface tension and the viscosity of the sol, which can affect electrospinning. By analysing these parameters, it was hoped that a favourable viscosity would be identified that would electrospin to produce long and uniform fibres.

The surface tension of the sol becomes important at the formation of the Taylor cone. The charged solution needs to overcome the surface tension of the solution in order for a jet of solid sol-gel to be released and

the electrospinning process to be initiated. Solvents such as ethanol have a low surface tension and adding them to the sol produces fibres which are smoother [183].

4.1.3. Electrospinning parameters

The literature review (Chapter 2.3) identified a number of variables which can affect the ability of a solution to electrospin or the quality of the fibres produced. The applied voltage, separation between needle and collector place, flow rate, needle size and relative humidity of the surroundings were all considered to be important factors in producing electrospun fibres [146].

The flow rate and needle diameter were kept uniform throughout all investigations. A flow rate of 0.4 mL h^{-1} µL s^{-1} consistent within the range determined by Poologasundarampillai *et al.,* [7] was used consistently throughout experiments as a number of review articles have highlighted the impact flow rate can have on the morphology of electrospun fibres [184]. Zhang *et al.,* [157] showed that when electrosinning poly(vinyl alcohol) (PVA) fibremats, a flow rate of 0.3 mL h^{-1} changed the morphology by causing beads to form on the fibres. The relative humidity of the surroundings at the point of electrospinning was investigated as a number of review articles have also highlighted that the humidity of the surroundings can affect the morphology of fibres [146] [151].

Megelski *et al.,* [169] and Casper *et al.,* [185] have observed that the atmospheric humidity and the solvent vapour pressure strongly affected the formation of pores in the electrospinning of PC, Poly(methyl methacrylate) (PMMA) and Polystyrene (PS). Megelski *et al.,* found that increasing the relative humidity of electrospun polymer/solvent solutions (PC, Poly(methyl methacrylate) and Polystyrene) increased the pore formation on fibres electrospun at a range of between 20% and 50% relative humidity values (50%, 30% and 20% were tested [169]. In the research carried out by Capser *et al.,* [185] it was observerd that the presence of pores in PS fibres became evident at relative humidity values of 30% or more. Increasing the relative humidity correlated with an increase in the quantity, diameter, shape and distribution of the pores within the fibre.

4.2. Methods and materials

To electrospin the bioactive glasses, suitable bioactive glass compositions and electrospinning parameters had to be identified. Unless stated, all chemicals were purchased from Sigma-Aldrich, UK and used as received.

4.2.1. Preliminary sol-gel method

Table 1. Showing the quantities of reagents used in the initial protocol developed by collaborators Dr. Akiko Obata and Dr. Gowsihan Poologasundarampillai [170] [7].

TEOS [mL]	H_2O [mL]	1 M HNO_3 [mL]	Ethanol [mL]	Calcium nitrate [g]
7.2	4.5	1.7	3.7	3.2

An initial sol-gel composition was prepared according to the protocol supplied by collaborators Dr. Akiko Obata [175] and Dr. Gowsihan Poologasundarampillai [7], based on the SiO_2-CaO system. This initial 70 mol.% SiO_2 and 30 mol.% CaO (70S30C) composition was produced with a final ratio of TEOS:water:HNO_3:ethanol:$Ca(NO_3)_2$*$4H_2O$ of 1:12.02:0.07:1.95:0.29. A polyvinyl butyral binder was developed according to Kim *et al.,* [170] before being combined with the sol to produce a sol-gel suitable for electrospinning. To electrospin successfully, the method required some adaptation as Sacks *et al.,* [86] and Sakka *et al.,* [87] reported the need for a lower ratio of water to TEOS (R ratio) for electrospinning to take place.

The electrospun sol-gel protocol was developed to obtain the appropriate levels of viscosity and surface tension to ensure that long and uniform fibres were electrospun. The revised sol-gel protocols were based on the work of Kim *et al.,* [170] and Poologasundarampillai *et al.,* [7]. The specific quantities for the initial composition are summarised in *Table 1*. Other than changes to the water content and ratios of silica and calcium in the sol-gel compositions, all other reaction stages remained the same. Room temperature was set to be 22°C for ageing and electrospinning. At this stage, the electrospinning, heat treatment and rheology parameters of the sol-gels were not yet determined.

Synthesis of sol-gel samples

For all of the sol-gels produced, the first step was the hydrolysis and condensation of TEOS (ACS ≥99.0%) with deionised water. This was done under an acid catalyst of nitric acid (HNO_3) (68% (CAS 7697-37-2) Analysis grade) made up to 1 M nitric acid and used to promote condensation and hydrolysis reactions in the formation of the sol-gel. Ethanol (≥99.0% CAS 64-17-5) was used for diluting the alkoxide [87]. The sol was prepared by adding the components in the following order: 1 M HNO_3, ethanol, deionised water (where required), and TEOS. The R ratio was 12 and the volume ratio of water/HNO_3 was 2.64. The solution was stirred for approximately 1 h before calcium nitrate tetrahydrate (ACS grade 99.997% CAS 35054-52-5) was introduced as the calcium source to the solution. Once added, this was left to stir at room temperature for 24 h at 400 rpm. After 24 h, the solution was removed from the stirrer and aged further at room temperature for 24 h.

The binder was produced by adding polyvinyl butyral (CAS 63148-65-2**)** to ethanol gradually while it stirred on a magnetic plate stirrer at 400 rpm. The binder was not mixed with the sol-gel until all the visible lumps of polyvinyl butyral have been combined into the ethanol. 2 mL of the sol-gel solution was then combined with 2 mL of the polyvinyl butyral binder. The combination was then placed into a 10 mL syringe and kept at room temperature for electrospinning. The sol gel and binder combination was always used on the same day as it was combined into the syringe.

The aim here was to determine the most compatible sol-gel composition for electrospinning in addition to finding the most suitable parameters for electrospinning. As the sol-gel was aged, the polyvinyl butyral binder added and the composition itself was altered, all these affects had a substantial change on the suitability of the solution for electrospinning. The variables of viscosity, surface tension and relative humidity were all investigated.

4.2.2. Preliminary electropsinning of samples

Once the ‘electrospinning range’ was determined, the range at which electrospinning produced long, uniform fibres without beads was reached, five different compositions were electrospun and compared. To develop an effective process for electrospinning, the electrospinning parameters and sol-gel methods were closely tied and interdependent on each other.

Electrospinning of sol-gel samples

The solution comprised of sol and binder was loaded into an Omnifix 17A09CB Luer lock plastic 10 mL syringe and a gauge 22 Nordson 0.016x 0.5 7018272 needle was attached. The syringe and needle were placed onto a Harvard Apparatus PHD Ultra syringe pump which was set to a feed rate of 0.4 mL h^{-1}. Crocodile clips were used to connect the needle to a Genvolt high voltage power supply which was set to 10 kV. The power supply was connected to the collector plate using an additional crocodile clip which was set in front of a sheet of aluminium foil. Before the syringe was loaded into the syringe pump, all bubbles would be removed from the syringe and through the needle. The syringe was then inserted and the pump switched on so that sol moved through the syringe and out through the needle. The voltage source was turned on when these droplets were visible creating a visible Taylor cone at end of the needle.

The dry electrospun fibres were collected onto a grounded aluminium foil sheet, which was set at a distance of 100-120 mm from the end of the needle. To prevent excessive build-up of fibres, fibres were frequently removed from the aluminium foil. The frequency of need to do this depended heavily on factors such as the composition and the set up. Every time this was done, the voltage source was turned off prior to removing the fibres.

After electrospinning, the fibres were sealed in a polypropylene pot until they were placed in a Carbolite Gero furnace, where they were sintered for 3 h before cooling to room temperature naturally. Electrospinning took place in a CleanAir ltd. fume hood and the relative humidity inside the fume hood was taken each time a sample was electrospun. A collection of samples were weighed before and after heat treatment to ascertain the weight reduction due to the desired removal of the binder during heat treatment.

4.2.3. 70S30C sol-gel study

The initial 70 mol. % SiO_2 and 30 mol. % CaO (70S30C) composition was a good starting point for defining the sol-gel properties and determining its effectiveness for electrospinning. To obtain an electrospinning range for the composition, the viscosity and surface tension of the sol were investigated. For electrospinning 3D 70S30C cotton-wool like bioactive glass, Poologasundarampillai *et al.,* [7] suggested a viscosity within the range of 0.56–0.95 Pa.s.

Sol-gels prepared for electrospinning are different compared with those produced as monoliths. Factors such as the R ratio are reduced in compositions for electrospinning which may suggest that the water content of the sol has an impact on the ability for it to electrospin through altering properties such as the viscosity

or the surface tension of the sol. Viscosity has been previously controlled by ethanol evaporation during the ageing process. Poologasundarampillai *et al*., [7] demonstrated this to be the case when he developed an electrospinnable 70S30C composition without the need for a binder. To monitor the effects of viscosity and surface tension on the rheology of the sol and its ability to electrospin the study aimed to determine the following:

1. How the R ratio affects the viscosity and surface tension of the sol-gel on the 70S30C compositions;
2. The impact of the binder on the sol-gel viscosity and the surface tension determining the upper limit of the 'viscosity range' for electrospinning of 70S30C;
3. How heat treatment of electrospun samples affected the morphology of the scaffolds.

Viscosity and surface tension measurements were made at different polyvinyl butyral binder concentrations and at different R ratios. FTIR, XRD and SEM provided information regarding the structure of the fibres and of the chemistry.

Viscosity

Viscosity measurements were taken as the sol-gels were prepared with different R ratios and polyvinyl butyral binder quantities to determine the lower and upper limits of the viscosity range for electrospinning. The R ratio of the composition was altered by reducing the water content from the initial composition. The water content of the initial composition was 4.5 mL, this was reduced to 3.0 mL, 2.0 mL, 1.0 mL and 0.0 mL and the corresponding viscosities were compared. The quantity of polyvinyl butyral in the binder was also compared, with 1 g of polyvinyl butyral in the initial composition, this was compared with 1.25 g, 1.50g, 1.75 g, 2 g, 2.25 g and 2.5 g. The effect of changing the polyvinyl butyral quantity on the sol viscosity was also compared.

The viscosity of the sol-gels investigated was measured at Nagoya Institute of Technology (NiTech), using an AntoPar Modular Compact Rheometer MCR. The viscosity of the sol-gel compositions was measured after the compositions had been aged stirring for 24 h and then rested for 24 h at room temperature. 1 mL of the sol-gel was combined with the polyvinyl butyral binder in a ratio of 1:1. The sol and binder combination were placed on the centre of the rheometer dish before a flat-headed probe was automatically lowered onto the sample. The probe and sample were encased to prevent the effects of ethanol evaporation from the sample while readings take place. Twelve readings for viscosity were taken over a time frame of 120 s, each 10 s apart. The results were averaged and a minimum of three repeats were made per sample.

Scanning electron microscopy (SEM)

The structure of the fibres was imaged using SEM at the different R ratios. This lead to the identification of a viscosity range producing the desired fibre structure SEM images were obtained using the JEOL-6V and LEO-1525 (Imperial College London). The samples were observed under a 5 kV accelerating voltage and at a working distance of 8 mm. A 5 kV accelerating voltage was selected as this enabled best observation of the sample topography, it was selected and used throughout all SEM experiments focused on SEM imaging. The working distance of 8 mm was selected and maintained throughout all experiments. This was important as the 3D nature of some of the samples meant that often there were different clusters of fibres in one image and that focusing was difficult, the consistent working distance was useful in aiding with this.

Samples in the form of fibres were mounted on black conductive carbon tape and placed on aluminium stubs. The non-conductive samples were sputter coated with chromium (Q150T S sputter coater, Quorum Technologies, UK*)* to a maximum coating of 20 nm to enable imaging and avoid charging in the sample.

Surface Tension

The effect of surface tension on the electrospinnability of a sol-gel has received much less documentation than studies which have investigated viscosity. Surface tension measurements were taken of at different R ratios, with water contents of 4.5 mL and 0.0 mL in the 70S30C sol-gel combined with 1 g polyvinyl butyral binder. This was compared with the binder free 70S30C composition produced by Poologasundarampillai *et al.,* [7] which was replicated in the laboratory at Imperial College.

Surface tension of the sols was measured using capillary action. Capillary tubes were purchased from Hirschman, UK. Surface tension measurements were taken by placing a capillary tube on the surface of the sol. The height of the sol rose a noted distance (d) in the capillary tube, this was repeated three times and the density of the sol was calculated using the following Equation 7:

$$s = \frac{\rho hga}{2} \qquad \text{Equation 7.}$$

Where s = surface tension, ρ = density, h = height, g = acceleration due to gravity and a = radius. The density of the sol was calculated by weighing a set volume of each of the sols and then calculating through the known mass and volume.

X-Ray diffraction (XRD)

XRD was used to analyse the amorphous structure of the bioactive glass fibres produced, to identify any areas of crystallinity and to assess the effect of heat treatments on the glass compositions. In the studies presented here, measurements were carried out on a Bruker D2 PHASER desktop X-ray diffractometer. XRD uses step scanning with a Cu anode with Kα radiation (λ = 1.54184 Å) at 30 kV and 10 mA, with 0.035° 2θ step size and a count rate of 12 second per step, from 6° to 70° 2θ.

The collected data was analysed with PANalytical X'Pert HighScore software plus. The measurements were performed by adopting the Bragg-Brentano camera geometry. The raw XRD spectra was loaded onto the software, a background was identified and adjusted for significance before the peak search and match function was executed. The software enabled the identification of multiple phases compared with a database of reference patterns from the International Centre for Diffraction Data (ICDD).

The samples were analysed in their powder form where possible. The fibres were ground manually using a pestle and mortar. Where a powdered form was not possible, the fibres were packed together levelled in the sample holder to provide a flat surface for the XRD measurement. Samples were mounted on a substrate made from an off-axis cut, silicon single crystal. The zerobackground signal produced no diffraction signal due to its diffracted peak laying above 2θ = 120° which is higher than the range investigated in these studies.

Fourier transform infrared spectroscopy

Attenuated total reflectance-Fourier transform infrared spectroscopy (ATR-FTIR) was used to understand the bonding within the fibres and to see how heat treatment and compositional changes effected it, using an ATR-FTIR Nicolet iS10. Spectra were collected in absorbance mode using a diamond ATR accessory in the range of 500-4000 cm^{-1} with a resolution of 4 cm^{-1}. Once background analysis was complete, the sample was placed across the beam and secured. After analysis, the surface was cleaned with ethanol. Post processing of data included the normalisation of data to the Si-O-Si band situated at a wavelength of approximately 1050 cm^{-1}.

4.2.4. 70S30C electrospinning study

The objective of the sol-gel study was to investigate and determine the properties affecting the viscosity and surface tension of the sol-gel and how they impacted the reliability of electrospinning long and uniform fibres. Once a reliable protocol for producing the sol-gel had been produced, factors introduced by electrospinning were investigated.

Electrospinning is a technique which produces fibrous structures which can mimic some of the key structural features of the extracellular matrix (ECM) [180]. The technique is versatile and typically produces a 2-dimensional (2D) fibremat structure. Research from Poologasundarampillai *et al.,* [7] showed the ability to produce a 3D structure with the 70S30C composition. Poologasundarampillai *et al*., [7] attributed the presence of the 3D structure to the movement of Ca^{2+} ions in the composition. It is suggested that during the application of an electric field to the 70S30C sol, the calcium ions and silicate species start to separate and move apart in solution. This result in the heterogeneous distribution of Ca^{2+} and SiO_4^{4-} at the Taylor cone. He concluded that the position and quantity of these separated charges at the cone determined the forces on the fibres as they spin and consequentially affects how the fibres are whipped as they move towards the collector plate.

Literature [146] shows that there are many physical factors which affect the ability for a solution to electrospin. While the main body of research shows that voltage, current, distance and the flow rate of the sol can all affect the ability of a sol to electrospin and the quality of the fibres produced, the research does not indicate that any of these factors impacts the ability to electrospun different structures (such as a 3D or 2D structure). Research from Casper *et al.,* [185] indicates that electrospinning may additionally be susceptible to climatic changes such as temperature and humidity.

To verify this, and obtain a clearer understanding of physical factors that may affect the ability of the sol to electrospun, and the formation of a 3D structure, the study aimed to investigate the following:

1. Physical electrospinning factors;
2. Electrospinning the 70S30C structure at a range of different relative humidity values and measure any impact on the structure produced;
3. The impact of different quantities of calcium in the SiO_2-CaO system, and see if the presence of Ca^{2+} does impact the structure produced when electrospun.

Electrospinning set up

The electrospinning equipment was set up (*Figure 6*) using the voltage, current and needle to collector distance as described by Poologasundarampillai *et al.,* [7]. These parameters (*Table 2*) were each manually adjusted until long and uniform fibres were produced. Although these individual parameters can have a significant impact on the quality of the fibres produced dependent on their final application, at this stage, the focus was to assess the formation of the 3D structure. The physical parameters were adjusted and once chosen, were keep consistent throughout the experiments.

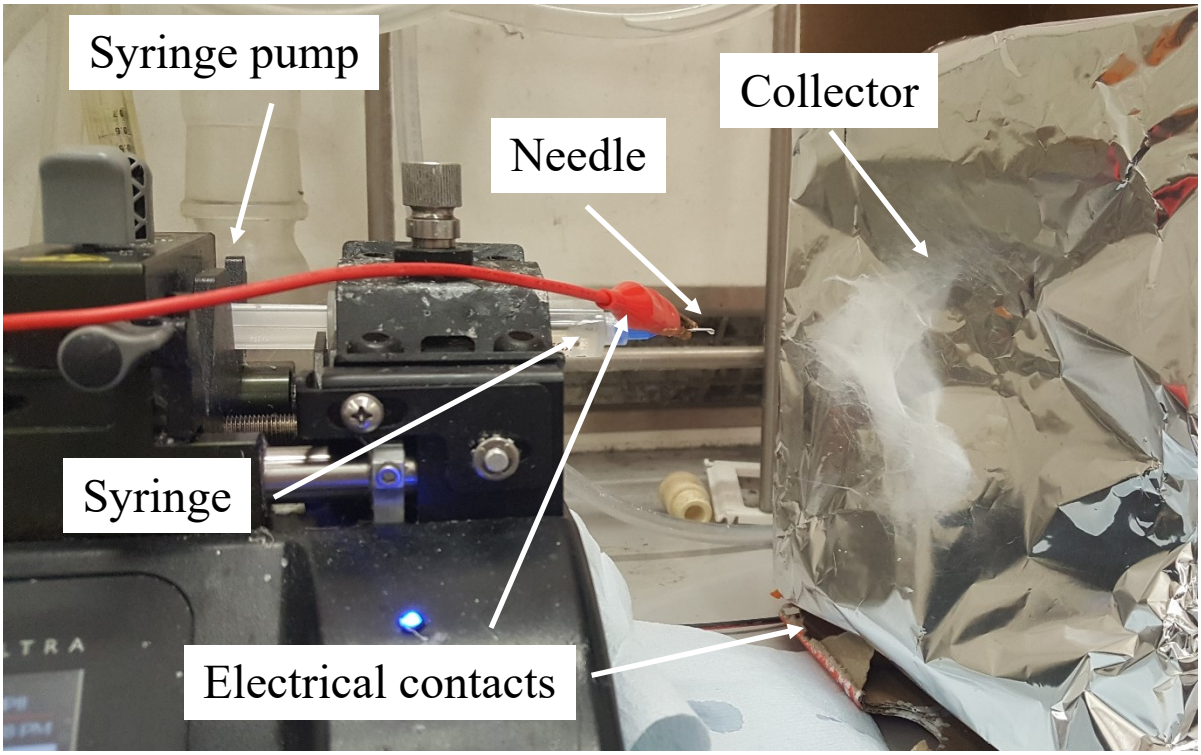


Figure 6. The electrospinning apparatus set up at Imperial College.

Table 2. The electrospinning parameters used by Poologasundarampillai et al., [7] and used as a starting point for the present study.

Voltage (kV)	Distance (mm)	Flow rate (μL s^{-1})
15.00	10.00	0.68

Humidity

Measurements for relative humidity and room temperature were taken as the 70S30C sol-gel composition was electrospun. Readings were taken prior and after to electrospinning and typically remained consistent throughout the electrospinning process. Relative humidity was measured using a humidity monitor, and was taken with each sample at the start and end of every electrospinning session. If electrospinning took place over a number of hours, and the relative humidity had changed, an average of several results was taken. The relative humidity values were checked alongside a second relative humidity monitor on occasion. Temperature was taken using the same device and at the same times and consistency as the relative humidity. Relative humidity was measured at values from 25% up to 80% relative humidity. The structure of the electrospun fibres was assessed through photographically and through SEM imaging to see if differences could be seen at the microscopic level.

The laboratory environment made it very difficult to control the relative humidity of the surroundings. However, the relative humidity could be reduced by approximately 5-10% relative humidity with the use of a dehumidifier, the humidity could not however be safely increased.

Impact of Ca^{2+} on the structure

To measure the significance of Ca^{2+} on the structure of the electrospun fibres, different nominal sol-gel compositions were used. The 70S30C structure was compared to 100S, 90S10C, 80S20C and 60S40C and all were electrospun under the same parameters and at the same relative humidity values.

The structure of the samples were analysed photographically and by using SEM. XRD and FTIR were also used to analyse the chemical structure and identify any changes due to the different quantities of Ca^{2+} in the sol-gel solution. The conditions for SEM, XRD and FTIR were the same as those outlined in section 4.2.3.

Scanning electron microscopy (SEM)

SEM was also used here to image the structure of the fibres electrospun at different relative humidity values and at with different compositions, looking specifically at the impact of different quantities of Ca^{2+} added to the SiO_2-CaO bioactive glass structure. SEM images here were obtained using the LEO-1525 (Imperial College London) SEM. As described above, the samples were observed under a 5 kV accelerating voltage, at a working distance of 8 mm and with an aperture at 30 μm. The 5 kV accelerating voltage was selected as this enabled best observation of the sample topography due to charging issues across some fibre areas of the samples therefore a low accelerating voltage of 5 kV was selected and used throughout experiments. The working distance of 8 mm was selected and maintained throughout all experiments. This was important as the 3D nature of some of the samples meant that often there were different clusters of fibres in one image and that focusing was difficult, the consistent working distance was useful in aiding with this.

Samples in the form of fibres were mounted on black conductive carbon tape and placed on aluminium stubs. The non-conductive samples were sputter coated with chromium (Q150T S sputter coater, Quorum Technologies, UK*)* to a maximum coating of 20 nm to enable imaging and avoid charging in the sample.

Energy Dispersive X-Ray Spectrometer (EDX)

EDX was used to determine the chemical composition of the fibres viewed using the SEM (LEO-1525). The SEM was set up and sample preparation was carried out as described in the SEM section above. To carry out EDX analysis, several changes were made to the setup of the SEM. The accelerating voltage of the SEM was increased to 20 kV and the aperture size increased to 60 μm,.The LEO SEM was fitted with INCA EDX (Oxford Instruments) for the compositional analysis. The SEM was operated as before, and an area of interest was found and selected. The INCA software was used to capture the area of interest and a scan of this area was 'acquired' and made visible on the INCA software. Points on individual fibres were selected on the INCA software which were analysed to obtain the elemental composition of the spot selected as an atomic percentage (atomic %).

Lithium metaborate study

The nominal compositions of the different samples was assessed through a lithium metaborate study. This study was used to compare the nominal compositions with the actual. To determine the composition, 50 mg of each glass fibre composition was combined with 150 mg of the lithium metaborate flux in a platinum crucible and heated in to 1050°C. When cooled, the combination of flux and sample was dissolved in 2 mol. nitric acid. The dissolved sample was then placed directly into an inductively coupled plasma-atomic emission spectrometer (ICP-AES). Standard solutions were produced diluted in 2 mol. nitric acid as the

samples. A standard curve was produced at wavelengths of 317.9 nm (Ca) and 251.6 nm (Si) for 1 mg L^{-1}, 2 mg L^{-1}, 5 mg L^{-1}, 10 mg L^{-1}, 20 mg L^{-1} and 40 mg L^{-1}.

4.2.5. Dissolution study

A dissolution study was used to ascertain the release of silica and calcium ions from the bioactive glass fibres over time. This was done to provide an insight into the speed and quantity of the release of ions under conditions mimicking that of the body. The release of ions in the 70S30C sample was compared to that in the 100S sample, the 60S40C, 80S20C and the 90S10C compositions.

The dissolution study was conducted in 5 mM tris(hydroxymethyl)aminomethane, (TRIS) ($(CH_2OH)_3CNH_2$) buffer solution, with 37.5 mg of each of the bioactive glass fibrous sample immersed in 25 mL of TRIS buffer (n=3). These quantities are based on the recommendations of Maçon *et al.* [186]. The TRIS buffer solution was produced by adding 6.118 g of tris(hydroxymethyl)aminomethane to 800 mL of deionized water at 37.5 °C stirring at a rate of 400 rpm. 1 mol. solution of HCl was added until the pH of the buffer solution was reduced to 7.4, the TRIS buffer was then stored in an incubator shaker at 37.5 °C 120 rpm [186] until required. When required, pH of the TRIS buffer solution was checked and adjusted using 1 mol. HCl and deionised water was added to make up the buffer to 1000 mL [186].

Prior to immersion in TRIS buffer, each 37.5 mg fibrous sample of each composition were placed in an individual cellulose Snakeskin® Dialysis tubing which was firmly tied at one end. 2 mL of TRIS was then placed into the tube with the fibres and the Snakeskin® Dialysis tubing was firmly tied at the other end. The samples were then immersed in the remaining 23 mL of TRIS buffer solution, and stored in an incubator shaker at 37 °C and 120 rpm [186]. At each time point (1, 2, 4, 8, 24, 48, 96, and 168 h), 0.5 mL of the TRIS supernatant was removed from each sample and placed in a 15 mL falcon tube. 0.5 mL of fresh TRIS was then placed back into the sample pot. This was done so that the overall quantity of TRIS remained the same throughout the experiment. Snakeskin® Dialysis tubing was used to contain the fibres but also allow the movement of ions through the tubing and into the media. This was used to ensure that no fibres were accidently removed from the study at each time point when TRIS was removed.

Prior to ICP analysis, the 0.5 mL of sample removed was filtered with a 0.2 µm surfactant-free cellulose acetate filter (Corning, USA) and diluted with 4.5 mL of 2 M nitric acid. Samples were analysed using ICP-AES analysis at wavelengths of 317.9 nm (Ca), 251.6 nm (Si). The pH of each sample was measured at each time point by a pH meter with a thermal probe (Oakton pH 11 meter with Oakton general purpose glass pH probe, Ag/AgCl electrode, and Oakton ATC probe) attached to it.

4.3. Results and discussion

A sol-gel was produced using an initial protocol which was assessed through characterisation of the viscosity, the surface tension and its ability to be electrospun. The correct sintering treatment was established once the initial sol-gel protocol had been developed to successfully and reliably produce 3D bioactive glass fibres. The mechanism for the 3D cotton wool formation was discussed and different Ca^{2+} containing compositions were developed. The dissolution of the samples was then carried out and the suitability of each of the compositions was discussed.

4.3.1. Preliminary sol-gel method

In this study, the initial sol-gel composition outlined by collaborators Dr. Akiko Obata and Dr. Gowsihan Poologasundarampillai was prepared as described in *Section 4.2.1*. The exact quantities of each of the reagents can be seen in *Table 1*.

Viscosity

The initial composition outlined in *Table 1* was successfully electrospun under parameters described in *Table 2*. The voltage was initially set to 15 kV and the distance between the collector place and the needle was set to 10 mm to remain aligned to those described by Poologasundarampillai *et al.,* [7]. This distance was found to be too close to the collector plate as the electrospinning fibres bridged the gap between the collector plate and the end of the needle, blocking the formation of further fibres. The fibres formed at this distance of 10 mm were visibly broken and clumped together. This distance was additionally not sufficient to enable the evaporation of solvent as the fibres moved across the needle to collector plate gap. As a result, the needle to collector plate gap was increased to 50 mm and then to 100 cm. At a distance of 100 mm, the fibres broke away from the needle and formed in a cotton-wool-like structure on the collector plate. The distance was therefore set to between 100-120 mm. The flow rate was initially set to 0.68 μl s^{-1} as described by Poologasundarampillai *et al.,* [7]. This flow rate was found to be too fast, as the formation of fibres was followed by the sputtering and dripping of sol as the sol protruded too quickly through the needle for charge to build up and the Taylor cone to form. The flow rate was reduced 0.1 μl s^{-1} so that a continuous Taylor cone could be viewed while the electrospinning took place. The voltage was also reduced to 10kV which aided the production of long and continuous fibres.

Table 3. The different sol gel compositions synthesised with differing R ratios and the corresponding viscosities when combined with the polyvinyl butyral binder in a ratio of 1:1. The R ratio takes into account the water in the entire system (including the water in the HNO_3 and the calcium nitrate in addition to the added water).

Sample No.	H_2O [mL]	1 M HNO_3 [mL]	TEOS [mL]	R ratio [H_2O/TEOS]	Viscosity [Pa.s]
A	4.5	1.7	7.2	12.0	0.035 ± 0.006
B	3	1.7	7.2	9.5	0.044 ± 0.003
C	2	1.7	7.2	7.8	0.047 ± 0.001
D	1	1.7	7.2	6.1	0.068 ± 0.045
E	0	1.7	7.2	4.3	0.069 ± 0.025

Table 3 shows an increase in viscosity as the water content in the sol-gel reduced, indicating the impact of changing the R ratio on the viscosity of the sol. The water in the sol represented in the R ratio comprised all the water in the entire system, this includes the distilled water added to the sol-gel and water introduced into the system from the addition of the HNO_3 catalyst and the calcium nitrate. The R ratio has to take into account the total water in the system and not just the added DI water. Even when 0 mL of distilled water is added to the system, hydrolysis and condensation reactions take place and a sol is produced. The R ratio in the initial protocol was 12. Several groups have reported that an R ratio (H2O:TEOS) of 2 is required for the hydrolysis and condensation of TEOS to Si-O-Si under acidic catalysis for drawing silicate fibres [86][87].

Graphical representation of the viscosities obtained at each R ratio shows (*Figure 7*) shows the mean and median values for the solution viscosity at each R ratio. The individual data points are also shown (*Figure 7*) and indicate a large deviation in viscosity for each of the R ratios. This deviations suggests that the R ratios cannot be used as a factor in reliably determining a target viscosity for the sol. Average and median viscosity values have been taken for the population of data points at each R ratio, which are summarised in *Table 3.1*. The significance of each of results was compared with that of the R ratio = 12 sample (Sample A in *Table 3*). The viscosity values of Sample E in *Table 3* (R ratio = 4.3) were considered to be significantly higher ($P < 0.001$) compared with the viscosity values of Sample A. The viscosity measurements for Sample

C (R ratio = 7.8) were also found to be significantly higher ($P < 0.05$). There was so significant difference compared with the other samples.

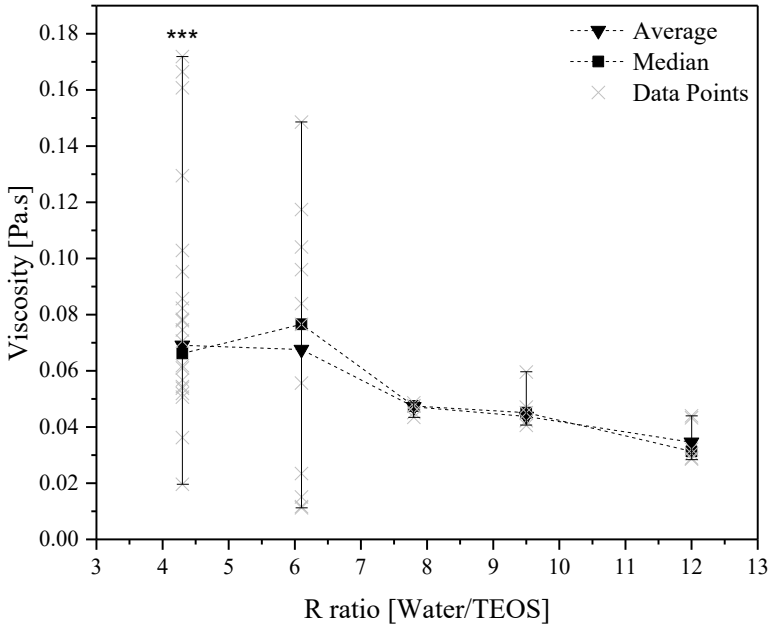


Figure 7. Graphical representation of the viscosities obtained at each R ratio. This representation highlights the number of repeats at each R ratio (data points) and indicates the median and average values for viscosity. Significance was measured using a Brown- Forsythe and Welch ANOVA test followed by an Dunnett's T3 multiple comparisons tests where each of the results was compared with the result for R ratio =12. ($P < 0.05$, *** $P < 0.001$).*

The sols were electrospun according to the setup described in *Section 4.3.1*. The diameter of the needle (gauge 22), the voltage and the distance between the needle point and the collector plate were kept uniform throughout. The electrospun fibres were heat treated to a temperature of 600°C and the morphology of the fibres were analysed using scanning electron microscopy.

The SEM images of the fibres show a strong correlation between an increase in R ratio and the presence of beads. *Figure 8E* with an R ratio of 4.3 (where no additional water has been added into the sol) shows long, uniform fibres with the presence of few beads. As the R ratio increased, the morphology of the fibres became less consistent, and the presence of shorter, broken fibres was more prominent in *Figure 8A* where

the R ratio was 12. The sample in *Figure 8A* did not electrospin, producing visible fibres as was done with the other compositions analysed, but produced pellet-like pieces of sol which dried on the collector plate.

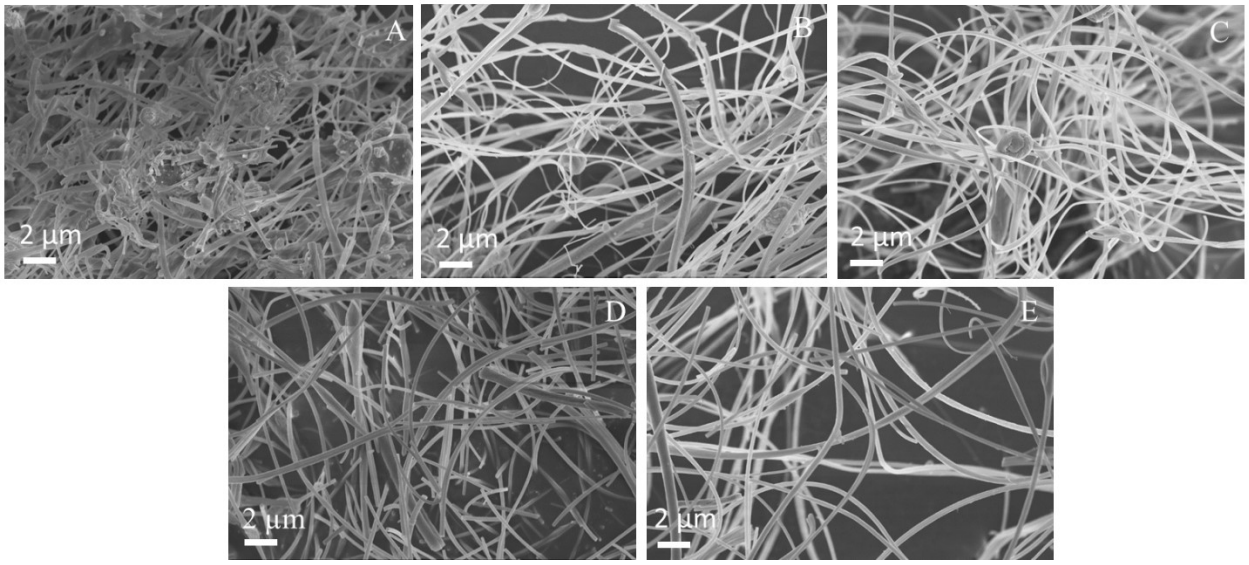


Figure 8. SEM images of electrospun bioactive glass fibres produced from sol-gels with an H_2O/TEOS R ratio of (A) 12, (B) 9.5, (C) 7.8, (D) 6.1 and (E) 4.3. The images show the production of long, uniform fibres where R ratios of 6.1 and 4.3 and an increase in beads as the R ratio increases.

While there was a difference in the viscosity of the sols produced with differing R ratios, this difference is not considered to be statistically significant as the difference in viscosities of the sols had a low standard deviation. The SEM images however suggested that the difference in the morphology of fibres produced was much more marked. The SEM images show a considerable difference in the formation of the fibres between the five different R ratios investigated, indicating that the water content of the sol has a major effect on the fibre morphology.

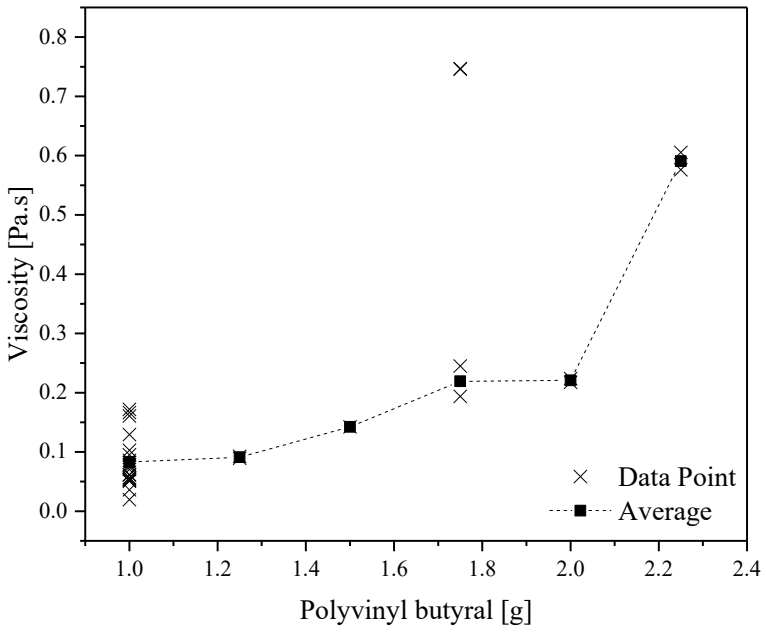


Figure 9. The change in viscosity of the sol as the quantity of polyvinyl butyral is increased. The ratio of the polyvinyl butyral to ethanol is increased and this increase shows an increase in the viscosity of the sol. This representation highlights all the data points in addition to the average viscosity value at each polyvinyl butyral quantity.

The upper limits of the viscosity for suitable electrospinning were investigated by increasing the amount of polyvinyl butyral added to ethanol to produce the binder. Increasing the quantity of polyvinyl butyral in the binder changed the viscosity of the sol-binder combination. The sol and binder were mixed in a ratio of 1:1 in each case. The viscosity of the binder was measured after combining 1 g, 1.25g, 1.5 g. 1.75g 2g and 2.15 g of polyvinyl butyral with 11.4 mL of ethanol. An increase in viscosity (*Figure 9*) corresponded to an increase in the amount of polyvinyl butyral added to ethanol. The standard deviation of the repeats was low compared to that observed when changing the water content in *Figure 7*, with the exception of the result at 1.75 g of polyvinyl butyral where a very high viscosity was measured. Repeated viscosity measurements with 1.75 g of polyvinyl butyral did not confirm this result, and further sols with the addition of higher quantities of polyvinyl butyral also did not result in viscosity measurements this high. This result was therefore considered to be an outlier.

The statistical difference in viscosity of the 1.25g, 1.5 g. 1.75g 2g and 2.15 g compositions shown in *Figure 9* compared with the first result at 1.0 g of polyvinyl butyral were considered to be insignificant between the data points. The composition containing 2.25 g of polyvinyl butyral was produced however failed to electrospin indicating that the maximum viscosity for electrospinning below 0.6 Pa.s.

Poologasundarampillai *et al*. [7] found the viscosity range for successful electrospinning of his 3D electrospun 70S30C bioactive glasses to be between 0.6 Pa.s to 0.95 Pa.s which is higher than that found to be possible using the sol-gel protocol used above. Therefore, it is of interest to consider other factors such as the surface tension which may affect the sol contributing to the successful electrospinning of a solution.

Surface tension

The surface tension of the 70S30C samples with R ratios of 4.3 and 12 were compared though the capillary rise method. *Table 4* presents this information and that of the 70S30C sol-gel produced using the protocol used by Poologasundarampillai *et al*., [7] wherein sol-gel 'C' with an R ratio of 2.23 with a corresponding surface tension of 0.023 ± 0.001 J m^{-2}, this is similar to the 70S30C composition with an R ratio of 4.3 'B' with a surface tension of 0.026 ± 0.002. R ratio compositions 'B' and 'C' produced long and uniform fibres. The 'A' composition with an R ratio of 12 produced fibres which were short, non-uniform and with the presence of whiskers. The result suggests that the R ratio does have an effect on the surface tension of the sol, and subsequently on the ability to electrospin long and uniform fibres.

Table 4. Showing the surface tension of 70S30C compositions with differing R ratios and comparing those with literature results from Poologasundarampillai et al. [7]. The R ratio appears to affect the surface tension of the sol.

No.	Sample	R ratio	Binder	Height of liquid [mm]	Surface tension [J/m^2]
A	70S30C	4.30	Yes	20.6 ± 1.5	0.026 ± 0.002
B	70S30C	12.00	Yes	25.7 ± 1.2	0.032 ± 0.002
C	70S30C [7]	2.23	No	18.0 ± 1.4	0.023 ± 0.001

Heat Treatments

With the optimum R ratio and binder protocol identified, the final electrospun composition was dried and heat treated. Bioactive glass sol-gel monoliths are typically sintered through the full sol-gel heat treatment (dried at 60−130 °C and stabilized at 700 °C with some sintered at 800 °C after stabilization) [81]. Lu *et al*., [182] show an incremental increase up to 600°C followed by annealing at 600°C for 5 h in air. Martinez *et al.,* [187] who produced thin disks of 70S30C, among other glasses in the SiO_2-CaO, system showed successfully sintered glass by heating them to 700°C for three hours following the use of thermogravimetric and differential thermal analysis (TG/DTA) to determine sintering temperature. Zhong *et al.,* [188] sintered sol-gel derived powders of ternary 58S and 77S compositions to 700°C but observed the formation of peaks around 600 cm^{-1} indicating that powders are more crystalline than the monolithic samples. This is perhaps due to the fine nature of powders, and by extension the fibres, compared with monoliths. The fibres were heat treated to different sintering temperatures of 950°C, 700°C, 600°C, 550°C and room temperature (labelled as the pre heat treatment sample) to determine an appropriate protocol for the electrospun fibres.

The characterisation technique FTIR was used to analyse the covalent bonding present in the fibres after electrospinning and again after heat treatments at different sintering temperatures. *Figure 10* presents the FTIR spectra of the 70S30C bioactive glass fibres heat treated to different sintering temperatures. All samples show bands at approximately 1040 cm^{-1} and 790 cm^{-1} which were attributed to Si-O-Si. The bands present in the pre-heat treatment sample at 1410 cm^{-1} and 1340 cm^{-1} are attributed to calcium nitrate within the dried fibres before the calcium has entered the glass network and the nitrates have been removed. These bands were not present in any of the samples post sintering. The sample sintered to 950°C shows a collection of peaks between 900 cm^{-1} and 1200 cm^{-1} which could be attributed to Si-OCa and suggest the formation of calcium silicate. Similar bands have been observed by Meiszerics *et al.*, [189] in the sol-gel formation

of calcium silicate systems. However none of the bands present in any of the samples match with this band exactly, therefore the presence of calcium silicate is not certain.

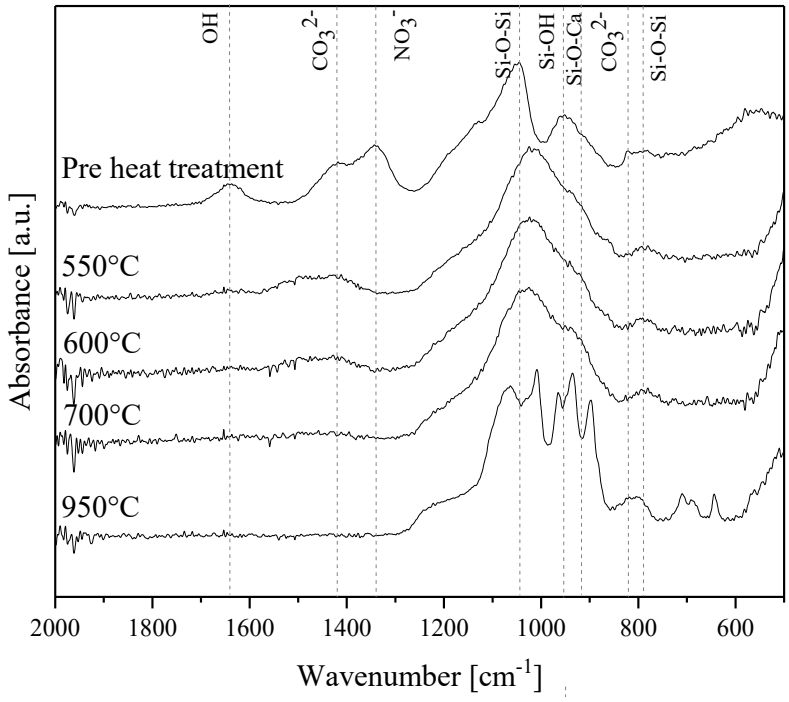


Figure 10. FTIR spectra from electrospun 70S30C sol-gel as a function of sintering temperature. The FTIR spectra show that the 600°C – 700°C range is appropriate as it removed all the unwanted nitrates.

XRD was used to analyse the crystallinity of the 70S30C samples sintered at different temperatures (*Figure 11*). In the samples heated to 550°C, 600°C and 700°C, amorphous halos were observed indicating an amorphous structure in the bioactive glass when sintered to these temperatures. Peaks were observed in the pre heat treatment sample and in the sample heated to 950°C. The XRD spectra of the pre heat treatment sample displays two phases, an amorphous phase similar to that observed in the samples heat treated to 550°C, 600°C and 700°C but also a second, where multiple peaks can be observed. Peak fitting software (PANalytical X'Pert HighScore Plus) was used on the pre heat treatment sample and identified Calcium Nitrate Hydrate as a likely candidate, with the ICDD reference of 01-070-0394 in a monoclinic crystal system. This provides evidence that he heat treatment process impacts the incorporation of the Calcium into the bioactive glass network. The hydrolysis and condensation reactions, followed by the drying process of the electrospinning are enough to produce an amorphous Si-O-Si network, but heating to temperatures in the range of 550-700 °C are required for calcium incorporation. The 70S30C glass heat treated to 950 °C

also shows evidence of the presence of multiple phases. Peak fitting software was also used to identify possible candidates for this spectra but no strong conclusions could be drawn. Orthorhombic calcium silicates (00-023-1043) were identified in repeats taken but no overall phase could be identified. It is likely that the spectra contains overlapping phases of calcium silicates. As a result of this investigation into the heat treatments and their impact on the chemistry of the glass structure, heat treatments between the temperatures of 550°C and 700°C were found to be appropriate for the sintering of bioactive glass fibres. The temperature of 600°C was selected as the protocol temperature for sintering to be used in future studies as it is a midpoint between the three temperature points investigated which produced amorphous halos without the presence of peaks. 550°C was considered a bit too low as there is potential for the addition of additional ions into the glass network in future studies which may result in the need for a higher sinterisation temperature. The 700°C temperature point is often used for sintering 70S30C monolith structures which are much more densely packed, and therefore the 600°C sintering temperature was seen to be sufficient when working with fine fibres with a large surface area.

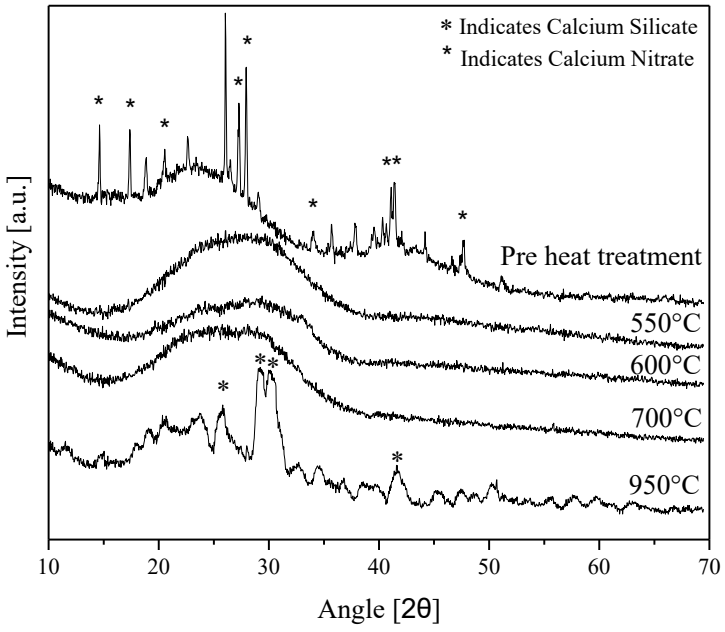


Figure 11. XRD patterns of electrospun 70S30C sol-gel as a function of sintering temperature. The XRD shows a smooth, amorphous halo on in the 550°C, 600°C and 700°C sintering temperatures.

4.3.2. 70S30C Electrospinning study

The electrospinning parameters were setup as described in section 4.2.2. These were used for the following experiments for the investigation of the electrospinning variables.

The Humidity

The 70S30C composition was mixed with the 1 g polyvinyl butyral and 11.4 mL binder combination and was electrospun at relative humidity values from 25% to 80% and observations were made about the structure of the fibres electrospun. Changes in the relative humidity varied between 27% and 65% which corresponded to significant changes in the macrostructure of the cotton wool produced. At 27% relative humidity, a 2D fibremat structure was produced (*Figure 12A*). *Figure 12A* shows a flat, tissue-paper-like structure, with the corresponding SEM image (*Figure 12E*) showing long, uniform fibres which are tightly interwoven. Increasing the relative humidity to 35% and 55% (*Figure 12B* and *Figure 12C*) produced a structure with a 3D cotton-wool-like appearance, similar to that attained by Poologasundarampillai *et al.* [7]. The corresponding SEM images show morphologies (*Figure 12F* and *Figure 12G*) where the fibres were long and uniform in diameter without the appearance of beads similar to that of the 2D structure found in *Figure 12E*. However the SEM images of sols electrospun at relative humidities of 35% and 55% show a structure which is much more undulating than that of the 2D structure electrospun at 27% relative humidity, creating the appearance of a 3D structure. At a relative humidity of 65% (*Figure 12D*), the appearance of the bioactive glass structure was cotton-wool-like, however SEM images of the fibre (*Figure 12H*) morphology showed fibres which are non-uniform in length and diameter and the presence of beads in the fibres.

The results depicted in *Figure 12* show clearly the change in structure of the fibres which arise as the relative humidity of the surroundings increases. Multiple studies have indicated that the relative humidity can affect the morphology of electrospun fibres, but many of these have focused on relative humidity affecting the formation of pores in the electrospinning of polymers such as PC, Poly(methyl methacrylate) (PMMA) and Polystyrene (PS) [169] [185]. Poologasundarampillai *et al.,* [7] reported that the formation of a 3D 'cotton-wool' like structure was a response to the presence of Ca within the bioactive glasses. The result presented in Figure 12 show that this may not be the case as at a relative humidity of 27%, the 70S30C bioactive glass composition produces a 2D structure much like the one obtained by Poologasundarampillai *et al.,* [7] for the 100S bioactive glass sample with no Calcium content.

To investigate the presence of pores within the fibres and to determine whether changes in relative humidity affects pore formation, further SEM images were taken at higher magnification.

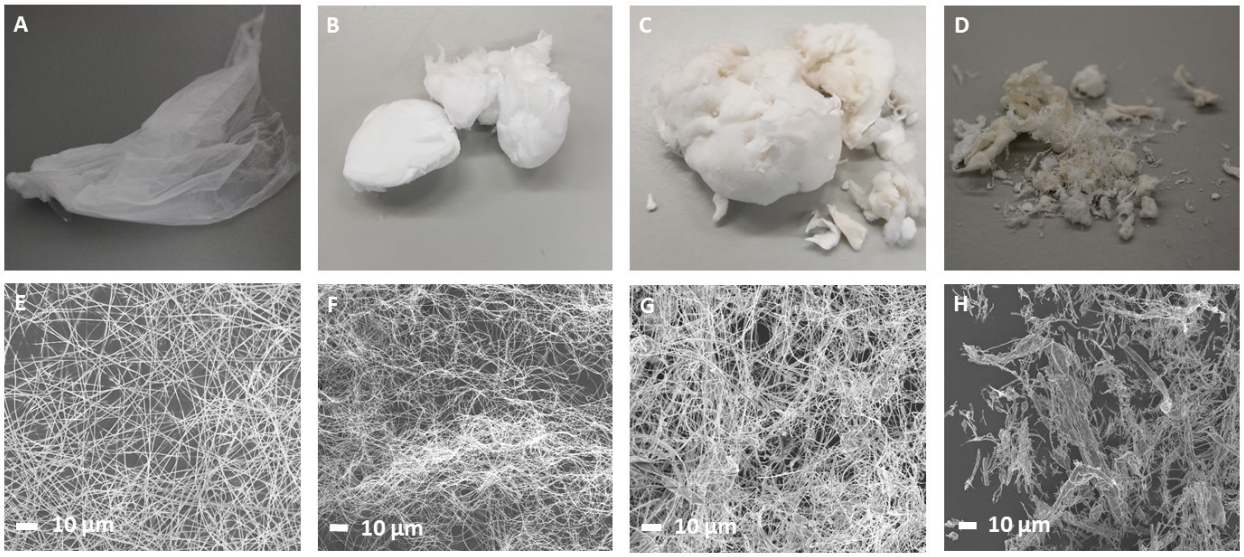


Figure 12. (A-D) Photographs showing the structure of 70S30C sol electrospun at different relative humidity values (A) 27%, (B) 35%, (C) 55% and (D) 65%. (E-H) SEM-SE images of the morphology of 70S30C electrospun samples. The relative humidity in each of the samples (E), (F), (G) and (H) was found to be (E) 27%, (F) 35%, (G) 55% and (H) 65%.

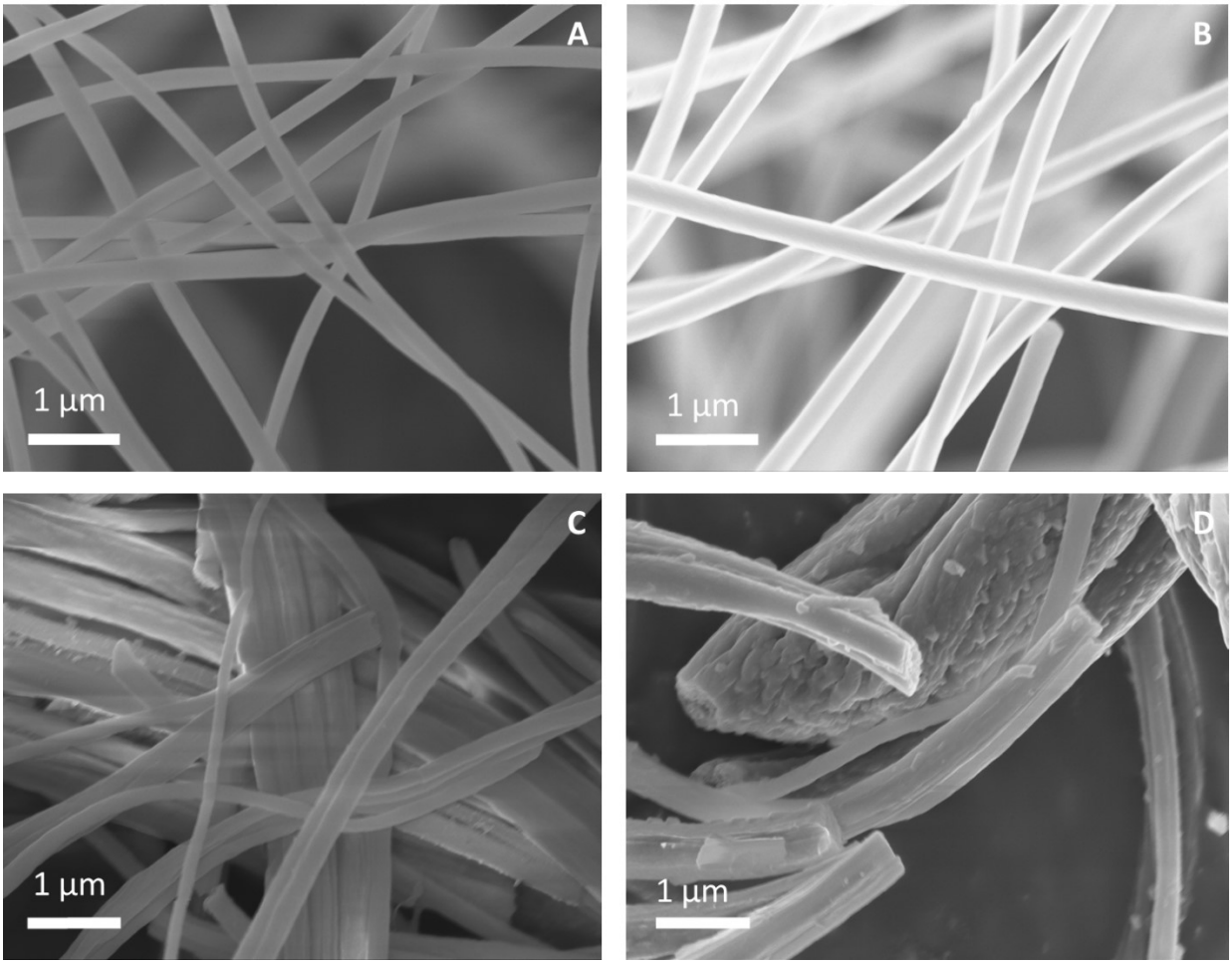


Figure 13. (A-D) SEM-SE images showing the individual fibres of the 70S30C electrospun samples. The relative humidity in each of the samples (A) 27%, (B) 35%, (C) 55% and (D) 65%.

The highly magnified SEM images shown in *Figure 1*3 clearly shows the morphology of the individual fibres and the effect of different relative humidity levels on them. The fibres electrospun at 27% and 35% relative humidity are visibly uniform in diameter and are distinctly separate fibres which do not appear to clump together. Neither beads nor pores are present in the fibres electrospun at 27% and 35% which depict long fibres with a smooth and uniform surface. The fibres electrospun at 55% relative humidity show long fibres grouped together in pairs or more with easily identifiable variances in diameter. The topography of these fibres show marks or lines along the fibres indicating a fibre surface which is less smooth in comparison to those electrospun at 27% and 35%. Tiny fragments of solid gel can also be seen attached to some of the fibres in *Figure 13C*. Fragments of dried gel and small fibres are much more prevalent in *Figure 13D* which shows multiple fibre lengths, diameters and the presence of beads. *Figure 14* shows the bead

in more detail. The topography of the bead appears to be rough compared with that of the smooth fibres shown in *Figure 13* electrospun at relative humidities 27% and 35%. The bead additionally appears to be comprised of and interwoven with smaller, finer fibres which contribute to the formation of a rough surface on the bead.

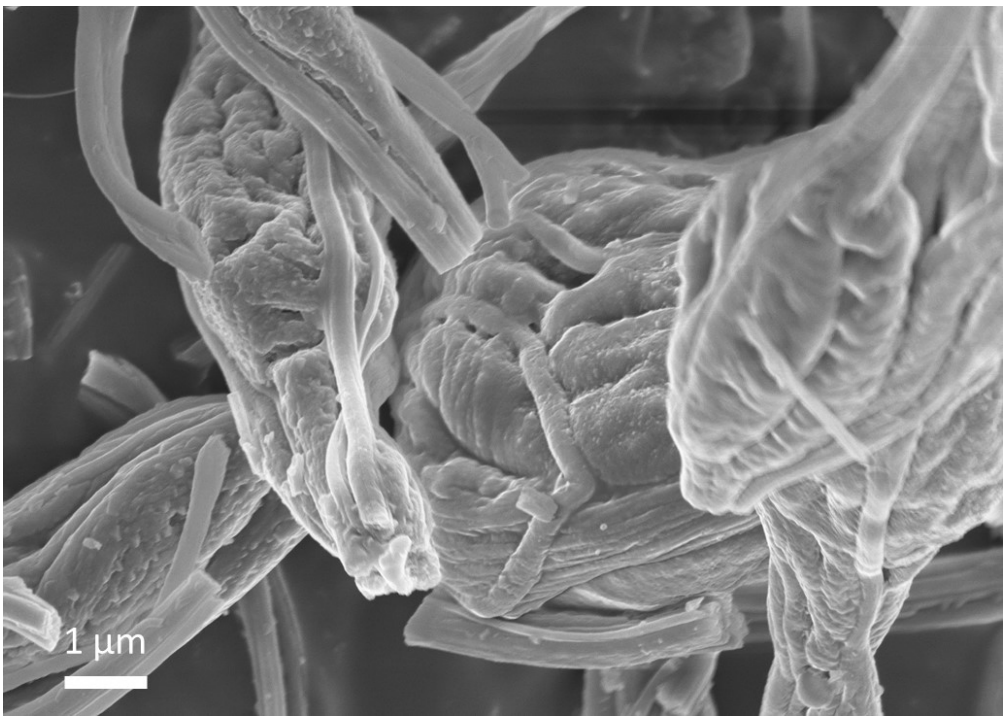


Figure 14. SEM-SE image showing a bead in the 70S30C sample electrospun at a relative humidity of 65%.

Composition analysis was undertaken on the 70S30C electrospun fibres to determine the ratios of Si and Ca obtained as a result of the sol-gel processing and electrospinning process. Lithium metaborate was used to determine the actual composition of the 70S30C fibres. This can be seen in *Table 5* and shows a molecular weight percentage of 68.1 mol. % Si and 31.9 Ca mol. %. SEM EDX was additionally used to determine the ratio of Si and Ca within the 70S30C fibres. The atomic percentages were determined by using the point analysis function. On each fibre analysed, three point measurements were taken along the length of the fibre and were averaged to provide further evidence of the ratio of Si and Ca in the fibres (n=3). The composition analysis using EDX is shown in *Table 6*. The EDX data shows an atomic percentage of 72.6 atom% Si and 27.6 atom% Ca. The standard deviation in results is higher for the EDX values compared to those analysed through the lithium metaborate process. The increased standard deviation in the results obtained through EDX analysis could be a result of measurements taken at different points along the fibre length.

Table 5. The composition of the 70S30C calculated through a Lithium Metaborate analysis.

Sample	Composition [mol.%]	
	SiO	CaO
70S30C	68.1 ± 0.2	31.9 ± 0.2

Table 6. The composition of the 70S30C fibres as calculated through EDX analysis.

Sample	Composition [atomic %]	
	SiO	CaO
70S30C	72.6 ± 4.8	27.6 ± 4.8

Observations made by Poologasundarampillai *et al.,* [7] indicated that the quantity of Si and Ca may vary throughout the length of the electrospun fibres due to the force from the electric field at the point of electrospinning causing the Ca^{2+} and Si^{4-} to separate. It was suggested that it is this presence of Ca^{2+} within the fibre that is responsible for the production of the 3D structure. In the research outlined by Poologasundarampillai *et al,* [7] TOF SIMS was used to assess the distribution of Si and Ca through a single fibre embedded in an epoxy matrix. The scanned fibre produced secondary ion maps showing areas which were rich in Si and depleted in Ca and other areas rich in Ca but depleted in Si. TEM energy dispersive X-ray (EDX) analysis was also conducted on the straight and bent sections of fibres which showed that in sections of the fibres, the quantity of Ca was higher in the bent section of the fibre compared with the straight section [7].

In the study presented here, EDX point analysis was carried out on selected points along the length of the fibres to determine the ratio Ca and Si atomic percentage present in the selected point of the fibre. *Figure 15* shows SEM images of a straight fibre and a bent fibre and the atomic percentages of Si and Ca found at each of the three points. The point analysis undertaken on the straight fibre shown in *Figure 15A* shows a standard deviation of 3.77 atomic % whereas the bent fibre in *Figure 15B* has a standard deviation of 6.44 atomic %, indicating that there is more variation in the Si to Ca ratio in the bent fibre in *Figure 15B*. The higher standard deviation in *Figure 15B* suggests that the bending of fibres may be the result of composition

changes throughout the length of the fibre, leading fibre sections to be enriched or depleted of Si or Ca. This, as described in observations by Poologasundarampillai *et al.,* [7] may provide causation of the bending of fibres during the electrospinning process.

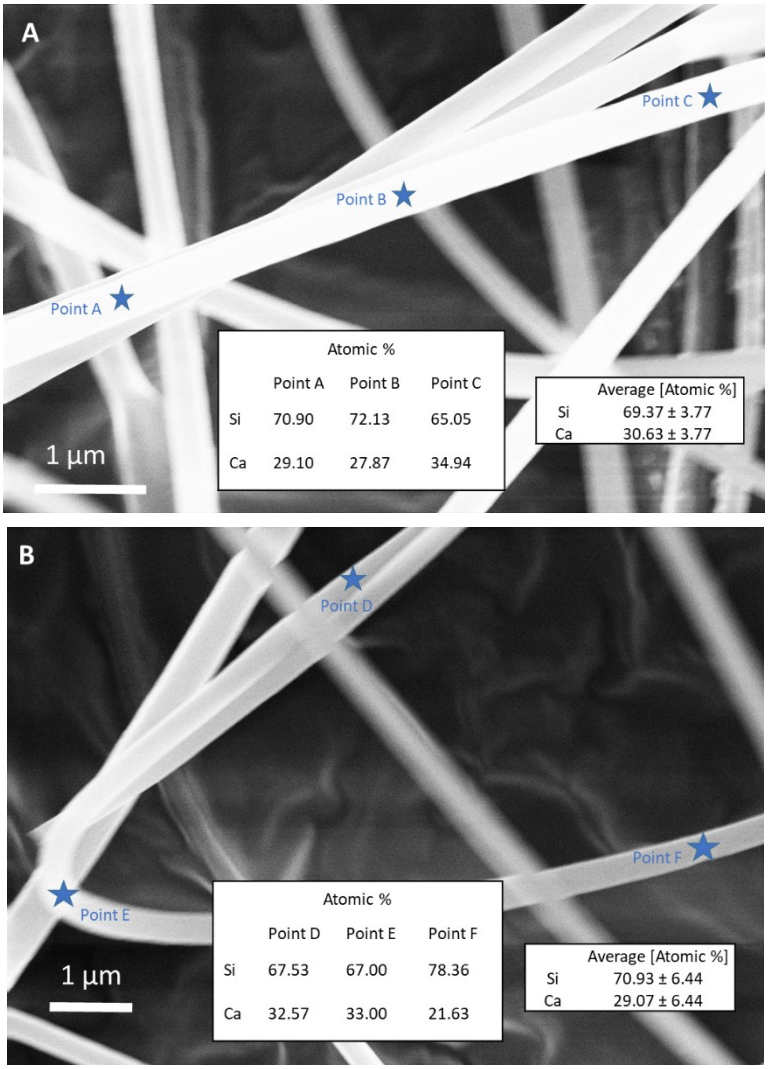


Figure 15. SEM-SE image showing the Atomic % of Si and Ca at points along A) a straight section of 70S30C fibre and B) along a bent section of 70S30C fibre.

However, results in *Figure 12* indicate that relative humidity has a role to play in the formation of a 3D structure. To test this further, a 100S bioactive glass composition was produced and electrospun at relative humidity values of 36%, 66% and 80% relative humidity (*Figure 16*), to investigate the role of calcium in morphology evolution. The samples electrospun at 66% and 80% relative humidity had the appearance of

a 3D cotton-wool-like structure, despite no presence of Ca^{2+} in the sol. The sample electrospun at 36% relative humidity had a 2D structure (*Figure 16A*) with long, uniform, undulating fibres with the presence of some beads (*Figure 16D*). A relative humidity of 66% produced 100S fibres with a 3D structure (*Figure 16B*) which were long, heterogeneous and contained some beading (*Figure 16E*), the sample electrospun at 80% also a produced a 3D structure (*Figure 16C*) but produced fibres which were short, with some whiskers and a larger quantity of beads (*Figure 16F*).

Observations made by Poologasundarampillai *et al.,* [7] indicated that the presence of Ca^{2+} was responsible for the 3D structure. However, results in *Figure 16* show that relative humidity additionally has a role to play in the formation of a 3D structure. This is especially prominent in the 100S sample where no calcium is present and a 3D structure is produced at relative humidity values of 66% and 80%.

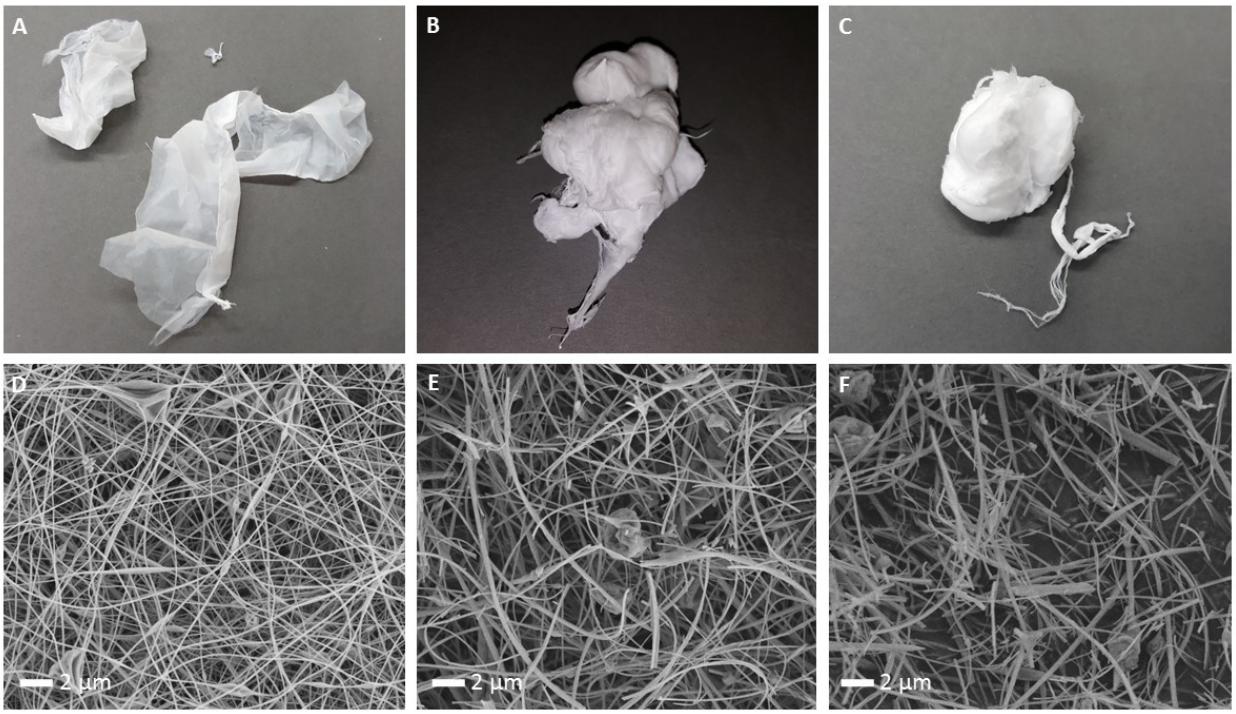


Figure 16. (A-C) Photographs showing the structure of 100S electrospun cotton wool at relative humidity values of (A) 36%, (B) 66% and (C) 80%. (D-F) SEM-SE images show the fibre morphology at relative humidity values of (D) 36% (E) 66% and (F) 80%.

The formation of beads in electrospun fibres are typically created as a result of capillary instability, this causes the conversion of a cylindrical jet into droplets of sol, which then solidify forming beads when they

reach the collector [152]. In polymers, a beads-on-a-string structure has been reported by groups [190] as a result of capillary instability where beads were spaced at similar, repeating distances and patterns along the length of the fibres. The bead formation observed on the 70S30C and 100S sol-gel solutions above relative humidity values of 55% did not have this appearance. While some beads were formed along the length of fibres, the beads were not consistent nor evenly spaced along fibres. It was observed that a higher relative humidity values (e.g. 80% for 100S in *Figure 16C*) that the sol sputtered while electrospinning, causing the sol to 'spit' beads of dried sol on to the collector place. This additionally caused the formation of beads alongside the fibres and would explain the inconsistent size and shape of the beads.

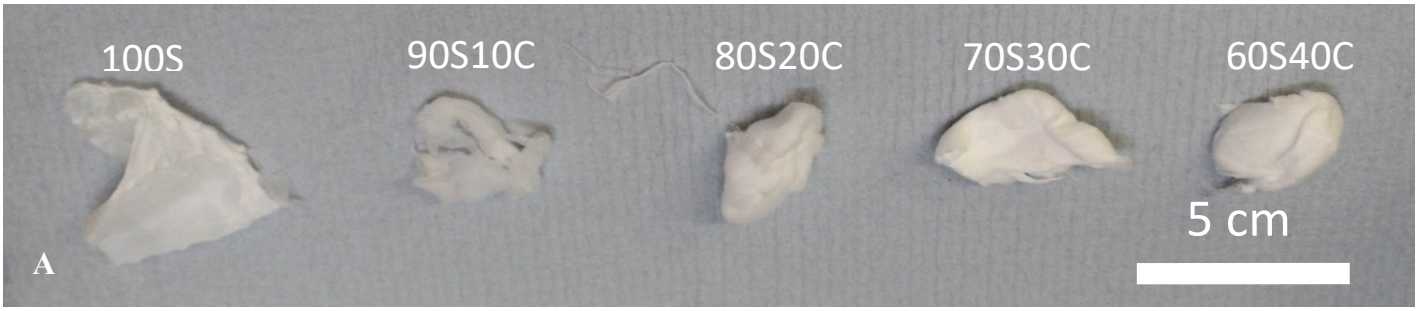
The nature of the structure produced is also reliant on the calcium content of the sol-gels (*Figure 12*). This is demonstrated by the 70S30C sample electrospun at a relative humidity of 35% (*Figure 12B*) and the 100S sample electrospun at a relative humidity of 36% (*Figure 16A*). The relative humidity are similar, but the electrospinning results in stark differences in the macrostructure produced over the two compositions, suggesting that the composition also had an impact. To investigate this further, five nominal sol-gel derived bioactive glass compositions (60S40C, 70S30C 80S20C, 90S10C and 100S) were produced with differing amounts of calcium present in the structure. *Table 7* outlines the quantities of each of the different reagents used to produce these samples. Lithium metaborate was used to determine the actual compositions made, these can be seen in *Table 8*. All the examples produced the expected composition, with the exception of the 90S10C composition which contained approximately 8% more silica ions than expected.

Table 7. Summary of the electrospinning solution properties and conditions used for each sol nominal composition (100-X SiO2,XCaO). All samples had the same voltage, flow rate, distance between the collector plate and viscosity. These were set up to be 10.0 kV, 0.4 mL/h, 100-120 mm and 0.12-0.20 Pa.s respectively.

Compositions	TEOS [mL]	Nitric Acid [mL]	Ethanol [mL]	$Ca(NO_3)_2 \bullet 4H_2O$ [g]	Water [mL]
60S40C	6.2	1.5	3.1	4.3	0.0
70S30C	7.2	1.7	3.7	3.2	0.0
80S20C	8.2	1.9	4.2	2.1	0.3
90S10C	9.3	2.2	4.8	1.1	0.7
100S	7.2	1.7	3.7	-	-

Table 8. The actual compositions produced in mol.% for the 100S, 90S10C, 80S20C, 70S230C and 60S40C compositions as determined by lithium metaborate analysis.

Sample	Composition [mol.%]	
	SiO	CaO
60S40C	62.4 ± 0.5	37.6 ± 0.5
70S30C	68.1 ± 0.2	31.9 ± 0.2
80S20C	77.4 ± 0.2	22.6 ± 0.2
90S10C	97.8 ± 0.2	2.1 ± 0.2
100S	100.0	0.0



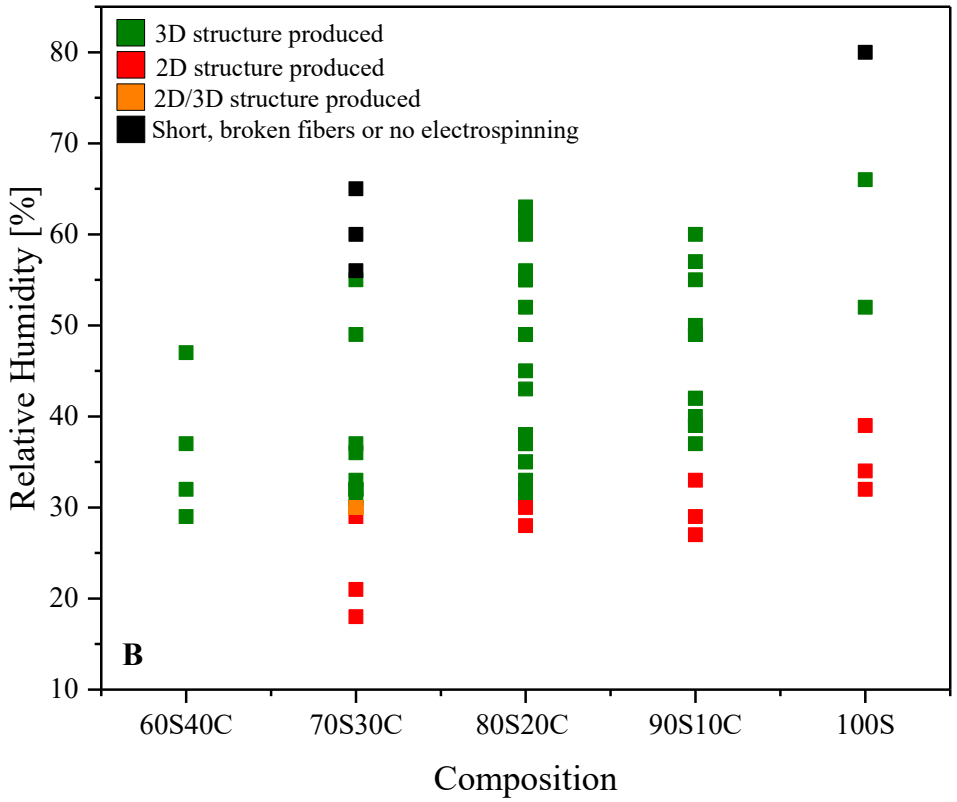


Figure 17. (A) Photographs showing the morphology of bioactive glass fibres: 100S, 90S10C, 80S20C, 70S30C and 60S40C electrospun at a relative humidity of 37%. (B) The graph shows the range of samples electrospun at different relative humidity values, the key in key indicates the relative humidity region for each composition whereby 3D cotton-wool-like structures were produced with few beads and fibres which were long and uniform.

Figure 17 shows each of the compositions electrospun at a range of relative humidity values between 25% and 80%. The 60S40C composition shows that 3D fibres were produced within the humidity range of 29% and 47%, however electrospinning outside this range was not attempted. The 70S30C and 80S20C compositions were electrospun over a wider range of relative humidity values. 3D structures were formed for both compositions within the range of ~30%, below this relative humidity value, 2D structures were formed. Above 55% relative humidity, 70S30C produced fibres as seen in *Figure 12C*, which were shorter and less uniform. The 80S20C composition produced long and uniform fibres at 64% relative humidity but compositions were not electrospun at higher relative humidity values so the point at which fibres become non-uniform and shorter are unknown for this composition. The 90S10C composition produced long and uniform 3D fibres between 35% and 60% relative humidity. Higher humidity was not investigated because this experiment was reliant on the natural relative humidity of the laboratory and this was not artificially changed, therefore experiments were subject to these constraints. The 100S structure produced 3D structures at a relative humidity of approximately 50%, and long and uniform fibres were produced 66%, whereas at 80% the produced fibres were non-uniform and much shorter in length with the presence of whiskers. These can be seen in *Figure 16F*.

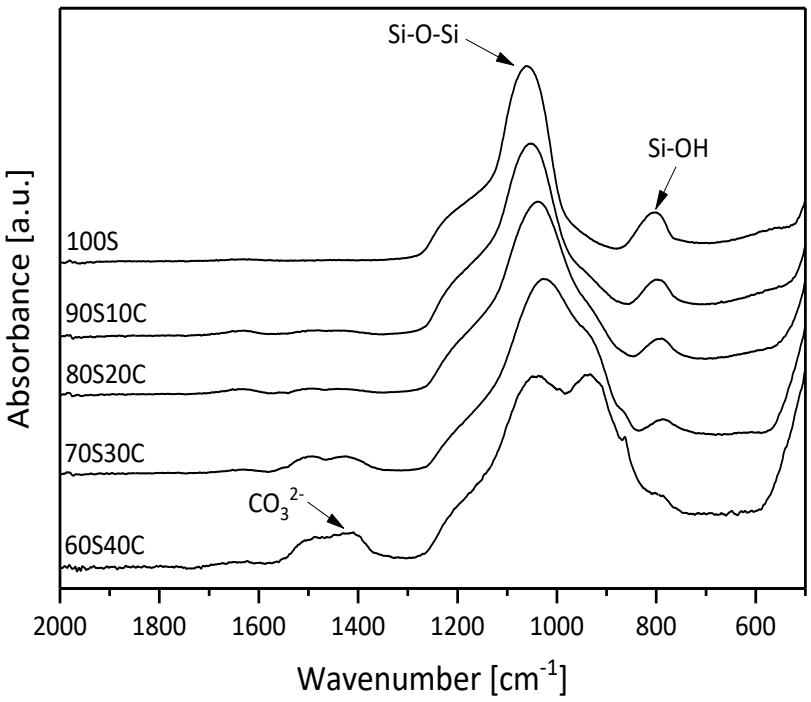


Figure 18. FTIR spectra of electrospun 60S40C, 70S30C, 80S20C, 90S10C and 100S sol-gel compositions.

FTIR was used to analyse the bonding in the different electrospun compositions. *Figure 18* presents the FTIR spectra of the 100S, 90S10C, 80S20C, 70S30C, and 60S40C fibres electrospun after heat treatment to 600°C. Bands attributed to the Si-O are found at 1058.73, 1053.91, 1038.48, 1027.39 and 1037.03 cm^{-1} respectively, and for Si-OH at 801.67, 801.28, 796.56, 787.78 and 942.54 cm^{-1}. The 60S40C sample shows a prominent band at ~910 cm^{-1} which can be assigned to the $Si\text{-}O_{NBO}$ [191] which decreases in relative intensity as the calcium content is decreased. An increase in the calcium content of bioactive glasses additionally corresponds to a shift in wavenumber of the bands attributed to Si-O stretching [192]. Bands (1500 and 1410 cm^{-1}) in the 60S40C composition can be attributed to CO_3^{2-} groups [187]. This band is more intense in samples with higher calcium content, where the increased calcium content is responsible for the presence of carbonate, attributed to a carbonation process of the material due to the atmospheric CO_2 and moisture present [193].

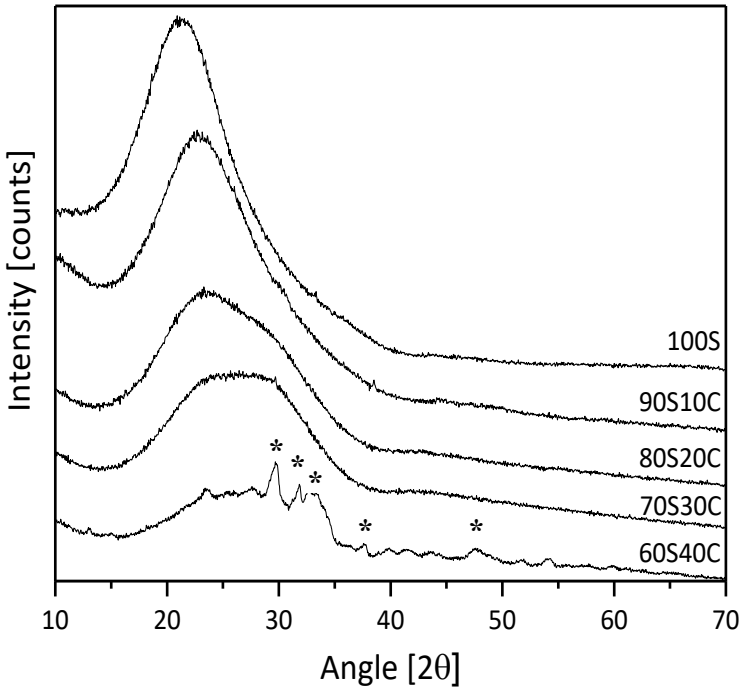


Figure 19. XRD of electrospun 60S40C, 70S30C, 80S20C, 90S10C and 100S sol-gel compositions. The XRD shows a smooth, amorphous halo in the 100S, 90S10C, 80S20C and 70S30C samples. The 60S40C displays peaks which could be attributed to calcium silicates of either Anorthic (00-014-0693) or Orthorhombic (00-024-0234) crystal systems. (*) indicates the presence of which can be attributed to either Anorthic (00-014-0693) or Orthorhombic (00-024-0234) crystal systems.

XRD patterns (*Figure 19*) of the 60S40C, 70S30C, 80S20C, 90S10C and 100S sol-gel compositions all show amorphous silica halos. The 60S40C composition shows multiple peaks at 29°, 32°, 34°, 37° and 48° 2θ, which can be attributed to crystalline phases of calcium silicates, such as wollastonite. PANalytical X'Pert HighScore peak fitting software identified that these peaks could be either Anorthic (00-014-0693) or Orthorhombic (00-024-0234) calcium silicates however no overall conclusions could be drawn. These peaks were not found in compositions with lower calcium contents and these presence of peaks suggests that the 60S40C composition is inhomogeneous. The presence of peaks could also be attributed to the electrospinning process, particularly, as outlined by Poologasundarampillai *et al.,*[7], if the 3D structure is dependent on the movement of Ca^{2+} and the electric field provokes a heterogeneous distribution of Ca^{2+} in the silicate. Martinez *et al.* [187] showed sol-gel derived 60S40C 13 mm diameter discs gave XRD diffraction patterns with amorphous halos without peaks.

4.2.5. Dissolution study

A high proportion of calcium and silicon content were released to the surrounding solution within 50 h of soaking in TRIS (*Figure 20*). All compositions released a similar quantity of silicate species, with 60S40C releasing the most silica over the 7 day period.

The calcium ion concertation profile showed a more marked difference between the compositions. The calcium ion concentration of 60S40C was the highest with 323.6 mg/L at the 7 day time period; 70S30C had an ion concentration of 251.7 mg/L and 80S20C of 193.0 mg/L at the same time point. The 90S10C composition had an ion concentration of 71.3 mg/L and the 100S of 0 mg/L. The lithium metaborate analysis of the 90S10C sample showed the ratio of silicon to calcium of 0.98:0.02 instead of the expected 0.9:0.1 which may explain the reduced ion concentration of calcium compared with the concentration trend of the 60S40C, 70S30C and 80S20C samples.

Figure 20 shows that increasing the calcium content of the bioactive glass fibres increased the dissolution of both silica and calcium species into the TRIS. This is further shown in *Figure 21* wherein the pH of the 60S40C sample shows the biggest increase throughout the 7 day study. In the 60S40C sample, the pH value peaks at 8 h immersion in TRIS producing a pH of 7.85, were higher than the 70S30C at ~7.7 and 80S20C at 7.6. The pH of the 90S10C and 100S samples was lower at ~7.35 and ~7.25 respectively. The effects of pH on the wound healing process are discussed by Percival *et al.,* in their review paper [194] highlights studies carried out by Hoffman *et al.,* [195] which report that within alkaline pH conditions, the progression of wound healing decreased. Gethin *et al.,* [196] reported that wound healing of chronic wounds occurs more readily in an acidic environment. Chronic wounds have an elevated alkaline environment but healing should ensure that the wound progresses from this alkaline, to neutral and finally, acidic state during healing, therefore, it has been suggested that pH could be used as a diagnostic tool, providing an indicator of how well a wound is healing [197]. It is important to note the influence the release of ions from the degrading cotton-wool bioactive glass fibres will have on the pH of the wound bed. The increase in calcium in the bioactive glass composition does create an increase in pH over the 7 day study. The increase of pH [97] [198] during bioactive glass degradation is a result of the exchange between modifier cations, such as Ca^{2+}, from the glass and protons from the dissolution media [199]. During dissolution studies, changes in the pH providing an indication of the amount of ion exchange occurring [200] in the solution.

The 70S10C and 100S samples investigated by Poologasundarampillai *et al.,*[7] show an ion concentration of approximately 100 mg L^{-1} for silica for both samples and a concentration of approximately 120 mg L^{-1} calcium for 70S30C and 145 mg L^{-1} for the 100S sample. While these results can provide a guide to the

dissolution of the materials they cannot provide a complete comparison to the study conducted by Poologasundarampillai *et al.,*[7] as this study was carried out in SBF and the one presented here was carried out in TRIS.

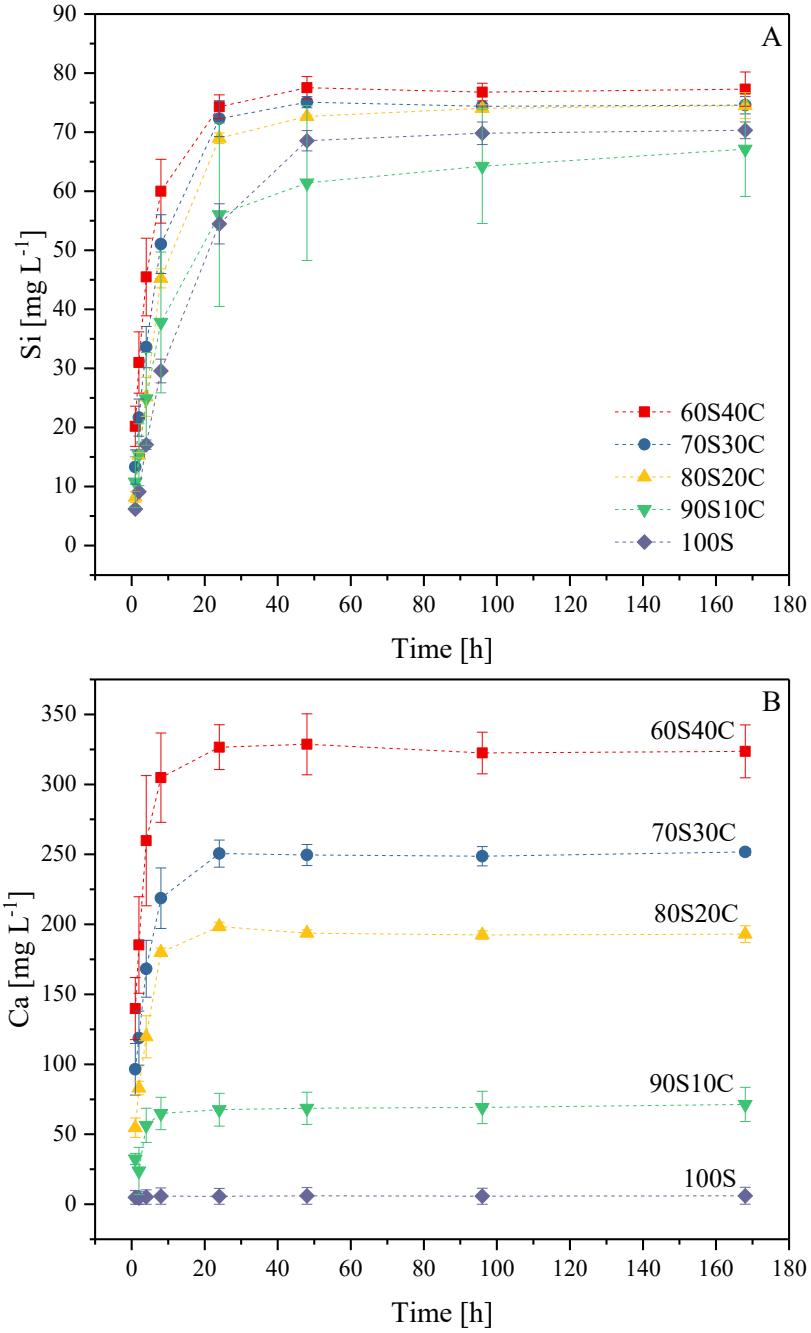


Figure 20. Dissolution profiles from ICP-AES of electrospun sol-gel glass samples as a function of time in TRIS, (A) Si and (B) Ca of the TRIS during glass dissolution.

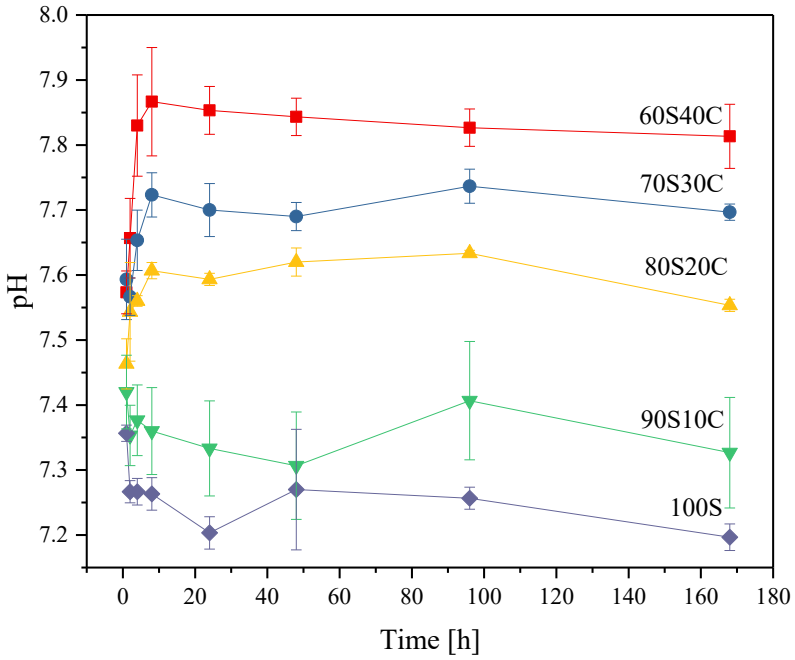


Figure 21. pH profile of the TRIS during glass dissolution of the 100S, 90S10C, 80S20C, 70S30C and 60S40C electrospun bioactive glass samples over the 7 day study.

Studies which focus on the cytotoxicity of silica nanoparticles with HDFs have largely focused on the effect of the size of the nanoparticle on the cell viability and less on the concentration. Vicente *et al.,* [201] found that silica nanoparticles of 20 nm reduced cell viability of HDFs concentrations of 100 mg/L and higher. Silica nanoparticles of 500 nm were however found not to decrease cell viability in concentrations of 200 mg L^{-1}. Similar results were also identified by Zhang *et al.,* [202] who compared 80 nm and 500 nm SiO_2 particles and found a significant reduced cell viability in HDFs for the 80 nm particles at concentrations of 25 mg $L^{-1}$and higher, the 500 nm particles however showed no reduction in cell viability or cell proliferation at concentrations of 200 mg L^{-1}. It is clear from this that the fibre diameter may exhibit an impact on the cytotoxic effect of silica on HDFs, particularly if the diameter is found to be small compared to other reported electrospun bioactive glass fibres such as those described by Obata *et al.*.[175]. The 60S40C fibres where found to have a calcium ion concentration at 7 days of 77.3 mg L^{-1}, higher than the concentrations found to be cytotoxic in the Zhang *et al.,* [202] study which suggests that determining the diameter of the fibres may be key in determining the cytotoxicity to HDFs and compositions with reduced silica concentrations may be more suitable for use in this investigation. The other compositions produced a

similar silica concentration with 70S30C at 74.6 mg L^{-1}, 80S20C at 74.8 mg L^{-1}, 90S10C at 67.1 mg $L^{-1}$and 100S at 70.3 mg L^{-1}.

A review article [109] highlights that for HDFs, a minimum calcium concentration of 1.4 mM (56.1 mg L^{-1}) is beneficial for the growth of fibroblasts. A study from McNeil *et al.,* [203] shows that concentrations of between 2-4 mM (40.1 – 80.2 mg L^{-1}) Ca^{2+} Rat-1 fibroblasts expressed signalling pathways which are associated with cell proliferation in rats. Neither of the studies outlined an upper limit for Ca^{2+} ion concentrations in fibroblasts. All of the calcium containing compositions shown in *Figure 20B* released calcium ions in excess of 56.1 mg L^{-1}over the seven day study. The 60S40C had the highest concentration at 7 days of 323.6 mg L^{-1}, 70S30C 251.7 mg $L^{-1}$and 80S20C produced a Ca concentration of 193.0 mg L^{-1}. The 90S10C composition produced a concentration of 71.3 mg L^{-1}.

4.4. Concluding remarks

SiO_2-CaO sol-gels were developed and electrospun in order to create a composition suitable for wound healing applications. The primary objective was to identify a protocol which produced electrospun bioactive glass fibres with a structure suitable for use in wound healing applications. It was also of key importance to understand the factors, in terms of the sol-gel composition and electrospinning variables, affected the production and morphology of fibres.

For the sol-gel solution, factors such as viscosity, surface tension and heat treatment were investigated. The conditions selected for electrospinning were to reduce the Water:Teos (R ratio) of the sol which lead to a slight increase in the viscosity ad reduction of the surface tension of the sol .While the impact on the viscosity and the surface tension were relatively small, the visual impact of reducing the water content of the sol (through changing the R ratio) on the appearance of the fibres was significant. SEM images showed that the morphology of the fibres with a higher water content were shorter and less uniform than those electrospun with lower quantities of water within the sol. The sols with the highest water content failed to electrospin at all and the application of an electric field only produced pellet-like pieces of dry sol. An R ratio of 4.3 was chosen as this produced long and uniform fibres and negated the need for additions of DI water when producing the sol.

The binder composition of 1 g of polyvinyl butyral combined with 11.4 mL of ethanol was selected to keep the sol within the electospinnable range. The heat treatment selected for the electrospun fibres was to heat to 600°C at a rate of 1° per minute followed by annealing at 600°C for 3 h and cooling down naturally to room temperature. While literature shows that viscosity is a key factor in the ability for a sol-gel in the SiO_2-CaO to electrospin, these results show that the 'viscosity window' to electrospin can be very broad and very specific to each sample. Poologasundarampillai *et al.* [7] identified a narrow viscosity window of 0.56–0.95 Pa.S for electrospining to be successful. They showed that the viscosity range could be reached through a 40-43 wt% ethanol evaporation 70°C, and when electrospun, produced long and uniform fibres. The ethanol evaporation negated the need for a binder prior to electrospinning. Allo *et al.* [204] obtained a favourable viscosity of 25–35 mPa when electrospinning ε-polycaprolactone bioactive glass hybrids. The work here shows successful electrospinning with a binder at a viscosity range determined by the R ratio and that of the binder (the polyvinyl butyral to ethanol ratio). Samples will be electrospun if they have a viscosity range of 0.047 Pa.s to 0.067 Pa.s. Investigations into surface tension compared an R ratio of 12

with that of 4.3 (each combined with the binder) and found the surface tension associated with the 4.3 R ratio was similar with that of the Poologasundarampillai *et al.* [7] binder-free composition.

The impact of relative humidity on electrospinning was found to be significant. 100S and 70S30C sol-gel samples were electrospun at a range of different relative humidity values and were found to both form 2D and 3D structures, despite previous research indicating that is the presence of Ca^{2+} which cause electrospinning to produce 3D structures. The 100S sample was found to produce a 2D structure at a relative humidity of 33% but produced a 3D structure at relative humidity value of 66% and 80%. The 70S30C structure produced a 2D structure at samples up to 28-30% relative humidity and produced a 3D structure at relative humidity values above this. This is a significant factor to consider when designing a sol and determining a desirable structure for electrospinning. To investigate the claims associated with the presence of Ca^{2+}, compositions with varying quantities of Ca^{2+} were produced. 60S40C, 80S20C, 90S10C and 100S compositions were electrospun and were found to produce 2D or 3D structures at different relative humidity values indicating that as the quantity of Ca^{2+} in the sol was reduced, a higher relative humidity was required to produce the 3D structure, this suggests something about an overall charge required to produce 3D structure, either from the charged Ca^{2+} itself or from the moisture in the surroundings.

Dissolution studies were carried out in TRIS in all electrospun compositions and showed that the 60S40C sample had the highest release rate of Si and Ca of all the samples, and that the 90S10C had the lowest release of Si and Ca. The 100S had no release of Ca.

The purpose of this chapter was to determine the electrospinning range for samples to produce long and uniform structures, to understand the causation for the formation of a 3D structure and how to control its formation and to determine a range of samples to take forward for further analysis and testing to be used as a potential base composition for wound healing. Five compositions were produced and electrospun, dissolution studies were carried out in TRIS for a period of 7 days to determine the ion release of samples.

The 60S40C was one of the most promising samples in terms of a obtaining a high ion concentration of silica and calcium ions during dissolution however studies by Vicente *et al.,* [201] and Zhang *et al.,* [202] showed that the ion concentration of the 60S40C could be cytotoxic to HDFs but is dependent on the fibre diameter. Therefore it is important that the diameter of the electrospun fibres are investigated to further understand the cytotoxic effect silica may present in future cell studies.

Analysis by XRD showed evidence of some crystallisation in the 60S40C sample, with the peaks indicating calcium silicate formation. The FTIR result showed an unusual formation of Si-O-Si band structure

compared with the other compositions and bands attributed to CO_3^{2-} groups. This suggests that the 60S40C sample is inhomogeneous in its structure.

Further studies were therefore carried out on the 70S30C sample and on the 80S20C sample as these both produced a 3D structure reliably when electrospun. Both samples had a very similar ion concentration of silica at Day 7 with the 70S30C sample having a higher calcium ion concentration compared with for the 80S20C. Future cell work will be interesting in determining if and how the quantity of calcium and silica affect the proliferation and metabolic activity of HDFs. *Table 9* shows the electrospinning parameters chosen going forwards.

Table 9. Summary of sol-gel and electrospinning parameters selected

Voltage [kV]	Distance [mm]	Flow rate [$\mu L\ s^{-1}$]	Viscosity [Pa.s]	Relative humidity [%]	Heat treatment
10.0	10 – 12	0.12	0.047 – 0.067	30 – 45%	600 °C at 1° C / min for 3 h

CHAPTER FIVE

DEVELOPING BIOACTIVE GLASSES FOR WOUND HEALING

5.1 Introduction

The results from Chapter 4 show that 3D bioactive glass fibres in the SiO_2-CaO system can be electrospun in a controllable and repeatable way. Changes in the relative humidity and the quantity of Ca^{2+} in the sol-gel composition, a 2D or 3D structure can be obtained as desired. Investigation of the sol-gel parameters identified a viscosity window for successful electrospinning and an understanding of the surface tension of the material was obtained.

The 70S30C and 80S20C compositions produced promising results in terms of ability and ease to electrospin the compositions into a 3D structure. XRD and FTIR showed the formation of amorphous structures after sintering at 600°C. Analysis using FTIR found that unwanted components of precursors such as nitrates from the calcium nitrate and the binder used to adjust the viscosity for electrospinning were removed after sintering, producing a glass structure. When dissolution studies were carried out, both samples released Ca^{2+} and silicate ions.

In this chapter, the 70S30C and 80S20C compositions were taken forward for further characterisation to assess their suitability for use as an aid in wound healing applications. The aims were to carry out a dissolution study in Dulbecco's Modified Eagles Medium (DMEM) and to investigate the response of human dermal fibroblasts (HDFs) to the dissolution products. Previous dissolution studies for 70S30C electrospun fibres have been carried out in SBF [7], and for 70S30C sol-gel derived foam scaffolds in minimum essential medium (α-MEM) [205] and DMEM [206]. In this chapter, cell studies will be conducted on the dissolution products of the 70S30C and 80S20C compositions on HDFs in DMEM. The dissolution products will contain ions released from the two 3D bioactive glass fibrous compositions and will provide an indication into how the samples affect the metabolic activity, the proliferation of the cells and their ability to produce VEGF to gauge their suitability in wound healing applications.

The literature review (Chapter 2.1) outlined the complex nature of wound healing and some of the many cell types that are involved in the process. Here, the role of HDFs in wound healing are investigated. Fibroblasts are a key cell type in wound healing, they multiply and produce key matrix proteins such as collagen [3] and help the construction of the new extracellular matrix.

5.2. Methods and materials

The 3D electrospun compositions required some more in depth characterisation to further assess their suitability for wound healing applications. Firstly, SEM was used to ascertain the fibre diameter of the compositions and their suitability for contact with HDFs. The surface area of the compositions were assessed using Brunauer–Emmett–Teller (BET) theory. Solid state ^{29}NMR-MAS was used to determine the atomic structure of the bioactive glasses. XPS, a surface analysis technique, was additionally used to determine the elemental composition. A dissolution study was carried out in DMEM on the two compositions to determine the time points at which the quantity of ions released into the dissolution product would have a therapeutic effect on human dermal fibroblasts. The samples were labelled depending on their content of silica and calcium. Unless stated, all chemicals were purchased from Sigma-Aldrich, UK and used as received.

5.2.1. Electrospinning and characterisation of fibres

The 3D fibrous 70S30C and 80S20C scaffolds were generated using the sol-gel method and electrospinning parameters as described in Chapter 4 and *Table 10* below. SEM and dissolution studies in Chapter 4 showed that the structure of the fibres produced within the relative humidity range of 30% - 55% produced the desired 3D structures, and released silica and calcium ions in TRIS buffer, therefore the same conditions were used here.

Table 10. The nominal sol-gel compositions and electrospinning parameters used. Prior to electrospinning a Polyvinyl butyral binder was combined with the sol gel. This was comprised of 1 g of Polyvinyl butyral was combined with 11.4 mL of ethanol and was mixed in a ratio of 1:1 with the sol-gel.

Compositions	TEOS [mL]	Nitric Acid [mL]	Ethanol [mL]	$Ca(NO_3)_2 \cdot 4H_2O$ [g]	Voltage [kV]	Distance [mm]	Flow rate [µL s^{-1}]
70S30C	7.2	1.7	3.7	3.2	10.0	10 – 12	0.12
80S20C	8.2	1.9	4.2	2.1	10.0	10 – 12	0.12

To further ascertain the characteristics of the compositions produced and their suitability for use in wound healing applications, the following aspects were investigated:

1. SEM used to determine fibre diameter to understand how HDFs interact with the fibres;
2. The overall surface area of the bioactive glass fibre samples to develop an understanding of the potential surface area in contact with a wound bed ;
3. To further quantify the compositions investigated and to understand chemical structure and state of each of the elements present in the bioactive glass structure.

Fibre morphology and surface area

The electrospun fibres were further investigated to ascertain their surface area and fibre diameter so that possible potential interaction between the fibres and fibroblasts could be understood. Analysis of the 70S30C and 80S20C compositions was required to ascertain the fibre diameter.

SEM was used to assess the fibre diameters of the compositions (JEOL-6V and LEO-1525 microscopes). Samples were sputter coated with chromium to a maximum coating of 20 nm using the pre-set conditions on a Q150T S sputter coater (Quorum Technologies, UK*)*, and were observed under a 5 kV accelerating voltage and at a working distance of 8 mm. The SEM images of the fibres were collected and the scale bar in each of the SEM images was measured in ImageJ and used as a reference length. The fibre diameters were measured using ImageJ software and were compared with the reference length scale bar in each of the images. Between six and ten in focus fibre diameters were measured in each image (n=4 per fibre). The fibre diameters were averaged and a standard deviation was taken.

Nitrogen sorption (Autosorb1; Quantachrome, Fleet, UK) was used to investigate the surface area of the electrospun bioactive glass samples. 50 mg of each composition was weighed accurately before being degassed for 12 h at 760 Torr and at room temperature. After degassing, the samples were moved across to the nitrogen sorption analysis chamber an isotherm collected with 40 points for adsorption and 40 for desorption were selected. Eleven point BET method was carried out on the adsorption branch [207]. Three repeats were made for each sample and the surface area values were averaged and a standard deviation was calculated.

Nuclear magnetic resonance

Solid-state ^{29}Si magic angle spinning-nuclear magnetic resonance (^{29}Si MAS-NMR) was used to measure the atomic structure of the bioactive glass compositions, particularly identification of the Q^n species in the 70S30C and 80S20C bioactive glass samples, which was useful in defining the connectivity of the bioactive glass network. The Q^n species refers to the structural species $Si(OSi)_nO(R)_{4-n}$ (with R representing either Ca or H in the case of these glass formulations) of the material.

To prepare the samples for ^{29}Si MAS NMR, the fibres were ground into a powder and were recorded on a 7.0 T Varian/Chemagnetics InfinityPlus spectrometer operating at 59.62 MHz. A Bruker 7 mm probe was used with an MAS frequency of 5 kHz. Single pulse acquisition used a minimum of 230 transients (depending on sample amount) and were collected using a $\pi/2(^{29}Si)$ pulse of 4.3 μs with a 240 s recycle delay. In addition, ^{1}H (71 kHz) radiofrequency (RF) decoupling was utilised during the acquisition. Deconvolution using OriginPro 2015 isotropic chemical shift assignment was obtained from cross polarization measurements where a $\pi/2(^{1}H)$ of 3.5 μs and a contact time of 4 ms were optimised on the chemical shift reference (kaolinite, -92 ppm) in addition to the aforementioned decoupling. For all experiments, the 70S30C and 80S20C fibres were prepared at relative humidity values between 30-45% relative humidity.

This process was carried out through a collaboration with the University of Warwick in the Department of Physics

Fibre surface analysis

X-ray photoelectron spectroscopy (XPS) was used to analyse the composition of the fibre surface and to provide further information of the oxidation states of the species. XPS was performed using a K-Alpha+ system (Thermo Scientific UK) operating at a pressure of 2×10^{-9} mbar. Samples were mounted onto black carbon tape and attached to the sampler holder using clips before being placed on to the loadlock. The monochromated and microfused Al Kα X-ray source ($h\upsilon$ = 1486.6 eV) was used with a 180° double focusing hemispherical analyser containing a two-dimensional detector. The pressure in the analysis chamber reached ~2 E^{-9} bar before the sample was transferred from the loadlock. The X-ray source had an emission current of 6 mA and the anode bias was 12 kV.

A survey scan of each composition was initially carried out to show the typical expected XPS spectra for the elements contained within the bioactive glass samples. This was followed by high resolution core-level XPS scans which was performed for Si 2p, O 1s and Ca 2p and were evaluated using Advantage XPS

software. To minimise the effects of charging on the samples, a flood gun was used. Any additional shifts in the spectra were corrected using the Carbon core line (C 1s) which is found at a binding energy of 285.0 eV. Information regarding the pass energy and dwell time can be found in *Table 11*. An X-ray spot size of 400 μm was used for all of the samples.

Table 11. The parameters used for the high resolution XPS scans.

	Pass Energy [eV]	Scan No.	Dwell Time [s]	Binding Energy [eV]		Energy Steps
				Start	End	
Si 2p	20.00	20	50	95	110	0.1
C 1s	20.00	20	50	279	298	0.1
Ca 2p	20.00	20	50	335	360	0.1
N 1s	20.00	20	200	390	415	0.1
O 1s	20.00	20	50	520	540	0.1

5.2.2. Dissolution in DMEM

The dissolution of the 70S30C and 80S20C compositions in DMEM were assessed to determine the ion concentration of silicate and calcium ions into the media and assess their suitability as materials for wound healing applications. Evidence for the formation of an HCA layer was investigated alongside changes in morphology and pH of the 70S30C and 80S20C samples as a result of exposure to the DMEM at time points of 4 h, 24 h, 96 h and 168 h. Here each sample was viewed using SEM and changes in the fibres were evaluated.

To verify the dissolution of the fibres in DMEM and its impact on the morphology of the fibres, this study aimed to investigate the following:

1. A dissolution study to determine the ion concentration and pH of silica and calcium at different time points.
2. FTIR, XRD and SEM characterisation of the 70S30C and 80S20C bioactive glass samples after dissolution in DMEM to determine the impact of the dissolution and precipitation on the chemistry and morphology of the fibres themselves.

The ion concentration of the 70S30C and 80S20C fibres

Low glucose DMEM (Gibco®) was used to conduct dissolution studies and cellular studies. The DMEM containing L-glutmine, sodium pyruvate with a Phenol red indicator was refrigerated before being opened for dissolution and cellular studies. An unopened bottle was used at the start of each study and any unused DMEM was discarded at the end of each study. DMEM is a commonly used basal medium which is used for supporting the growth of a variety of mammalian cells. It is mainly comprised of Amino Acids, vitamins and inorganic salts, a full description of its composition is described by Dulbecco *et al.,* [208].

A dissolution study was conducted in DMEM to determine the ion concentration of the 70S30C and 80S20C fibres at 4 h, 24 h, 72 h and 168 h. Using a ratio of 1.5 mg mL^{-1}, 37.5 mg of each of the bioactive glass fibrous samples was immersed in 25 mL of DMEM (n=3). Based on the recommendations of Maçon *et al.,* [186], the samples were each placed in cellulose dialysis tubing before being immersed in DMEM. The protocol used is as described in the TRIS study in Chapter 4. The samples were incubated at 37 °C at 120rpm.

The 0.5 mL removed at each time point was filtered with a 0.2 μm surfactant-free cellulose acetate filter (Corning, USA) and filtered with DI water (as the nitric acid used in the TRIS study would interfere with the DMEM media). The samples were then analysed using ICP-AES analysis at wavelengths of 317.9 nm (Ca), 251.6 nm (Si).

The pH of 70S30C and 80S20C samples were measured at each time point by a pH meter with a thermal probe (Oakton pH 11 meter with Oakton general purpose glass pH probe, Ag/AgCl electrode, and Oakton ATC probe) attached to it.

Effect of dissolution on fibres

The impact of the degradation of the 70S30C and 80S20C fibres was assessed. Fibres were immersed in DMEM using the ratio of 1.5 mg mL^{-1} for 4 h, 24 h, 72 h and 168 h in the cellulose dialysis tubing. The samples were then placed in an incubator shaker at 37 °C and 120 rpm [186]. The samples were then removed from the DMEM at each time point, were removed from the cellulose dialysis tubing and were rinsed in acetone and then in DI water and left to dry at 40°C for 24 h. Characterisation techniques were used to then asses chemical and physical changes in the fibre composition and morphology.

X-Ray diffraction (XRD)

XRD was used to identify any areas of crystallinity as a result of immersion in DMEM. XRD measurements were carried out as described in Chapter 4.

Fourier transform infrared spectroscopy

FTIR was used to identify any changes in the bonding of the fibres as a result of immersion of the 70S30C and 80S20C compositions in DMEM at different time points. Measurements were carried out as described in Chapter 4.

Scanning electron microscopy (SEM)

SEM was used to assess the change in morphology of the fibres as a result of immersion in DMEM. Both the 70S30C and 80S20C compositions were analysed at each time point. Sample preparation was carried out as described in Section 4.2.3 and the SEM was carried out according to the parameters outlined in Section 4.2.3.

5.2.3. Cell Studies

Cell studies were carried out on HDFs to understand the impact of the dissolution of the bioactive glass compositions on key cells involved in the wound healing process. The study was designed to determine if the ion concentrations of silica and calcium from the fibres was sufficient to produce a therapeutic effect on the HDFs and to ascertain whether the release was damaging to the cells at all in terms of reducing the metabolic activity or proliferation of the cells. The study was completed three times and within each study between 5 and 7 repeats were made in order to test different batches of the 70S30C and 80S20C fibres. In all cases the samples were electrospun to produce a 3D material at a relative humidity values between 30 – 45%.

A HDF cell line (ATCC, UK) with passage numbers from 20-30 was expanded in DMEM supplemented with 10% (v/v) foetal bovine serum (FBS), 1% penicillin and streptomycin. The 70S30C and 80S20C cotton-wool-like structures were pre-conditioned in DMEM for 4 h in an incubator at 37°C, 5% CO_2 and 21% O_2 at 200 rpm. The bioactive glass samples were not placed in the Snakeskin cellulose membrane for this study as at the 4 h time point, the media was filtered using 0.2 µm sterile filters to remove the bioactive glass fibres from the dissolution product. 0.5 mL samples (n=3) were also removed from the DMEM to be

analysed using ICP-AES to determine a more exact quantity of silicon and calcium ions in the dissolution product being used for each of the cell studies. A silicon control (Si control) was prepared using sodium metasilicate based on the Si mM value found by ICP-AES at the 4 h time point for both samples. The remaining dissolution product was supplemented with 10 % (v/v) FBS and 1% (v/v) penicillin/streptomycin.

HDFs were harvested and suspended in DMEM at a concentration of 20,000 cells per mL. 500 µL of cell suspension was added to each well in a 48 well-plate. After 18 h, the cell media was replaced with the supplemented 70S30C and 80S20C dissolution product and DMEM was used as control. At day 1, 3 and 7, the supernatant was collected for further analysis. The metabolic activity, the total DNA (tDNA) and the VEGF production of the dissolution product of both of the samples was investigated.

Metabolic activity

The metabolic activity of the HDFs was investigated at day 1, 3 and 7. An AlamarBlue® cell viability reagent was used to determine the metabolic activity of the compositions assessed. At each time point the dissolution product in each of the wells was removed and replaced with AlamarBlue made up to a 10% concentration and mixed with the 70S30C and 80S20C conditioned media. This was then placed on each of the cells. This was protected from the light and incubated for a period of 4 h. After this, 200 µL of the solution was transferred into a black well plate and fluorescence was measured at an excitation wavelength of 540 nm and an emission wavelength of 620 nm using a fluorescent microplate reader (Fluoroskan Ascent FL, Thermo Labsystems, UK). For each dissolution condition measured, n=5.

Total DNA

Total DNA (tDNA) was quantified using the Hoeschst H332598 fluorescent dye according to manufacturer instructions (tDNA, Sigma-Aldrich, UK). After the AlamarBlue cell viability reagent was removed, the cells were washed with PBS and 200 µL of DI H_2O was added to each cell well. The cells were then lysed with 5 freeze-thaw cycles. A standard curve was prepared with calf thymus DNA and producing a DNA standard serial dilution from 0-10 µg DNA/mL. The assay was prepared at a dilution of 1:1000 with 10% assay buffer and water. 100 µL of the lysates and standard dilution was transferred to a black 96 well plate and 100 µL of the Hoechst dye assay was added. Fluorescence was measured using an excitation wavelength of 360 nm and an emission wavelength of 460 nm in a microplate reader (Fluoroskan Ascent FL, Thermo Labsystems, UK).

Human vascular endothelial growth factor (VEGF)

VEGF plays a central role is angiogenesis, it is a signal protein produced by cells that stimulates the formation of blood vessels contributing to wound healing. Studies carried out by *Day et al.,* [209] have shown the ability of bioactive glasses to stimulate fibroblasts to secrete VEGF. Detsch *et al.,* [210] identified the glass particle size in the S53P4 (53% SiO_2, 23% Na_2O, 20% CaO, 4% P_2O_5) composition as an important factor in VEGF secretion in human CD-18CO fibroblasts, finding evidence that small particles (1-2 mm) enhanced VEGF release compared with larger particles (2-3.15 mm) which lead to an inhibition of VEGF production. It was concluded that these observations may be related to surface-area to solution volume relation which influences the dissolution of the glass. The use of small fibres in this study could provide interesting results in VEGF secretion compared with studies conducted on monolith or particles.

A Quantikine® ELISA kit was used to determine the amount of human vascular endothelial growth factor (VEGF) found in the cell supernatant. The cell supernatant removed prior to the AlamarBlue study was transferred to a new 48-well plate and frozen until required for the VEGF study. The supernatant was thawed and the Quantikine® ELISA kit assay was performed according to the manufacturer's instructions (R&D Systems, UK). 200 µL of supernatant collected at each time point was required and a standard dilution series of VEGF was produced ranging from 0 pg/mL to 1000 pg mL^{-1}. The optical density was measured with a microplate reader (BioTek, Instruments) set to 450 nm and correction wavelength 562 nm. The experiment was repeated twice, and within each experiment, each condition was repeated 6 times (n=6).

Statistical significance

The statistical significance of the results was compared using a Kruskal-Wallis test followed by Dunn's Multiple Comparison was used to detect significance of each composition with respect to DMEM at each time point (n=3, * $P < 0.05$, ** $P < 0.01$, *** $P < 0.001$, **** $P < 0.0001$).

5.3. Results and discussion

5.3.1. Characterisation of fibres

The 70S30C and 80S20C compositions were electrospun according to the parameters in *Table 9*. All samples were electrospun within a relative humidity range 30 – 55% and produced long and uniform fibres.

Fibre morphology

The surface area and diameter of the 70S30C and 80S20C fibre compositions were investigated for their suitability for use in wound healing applications.

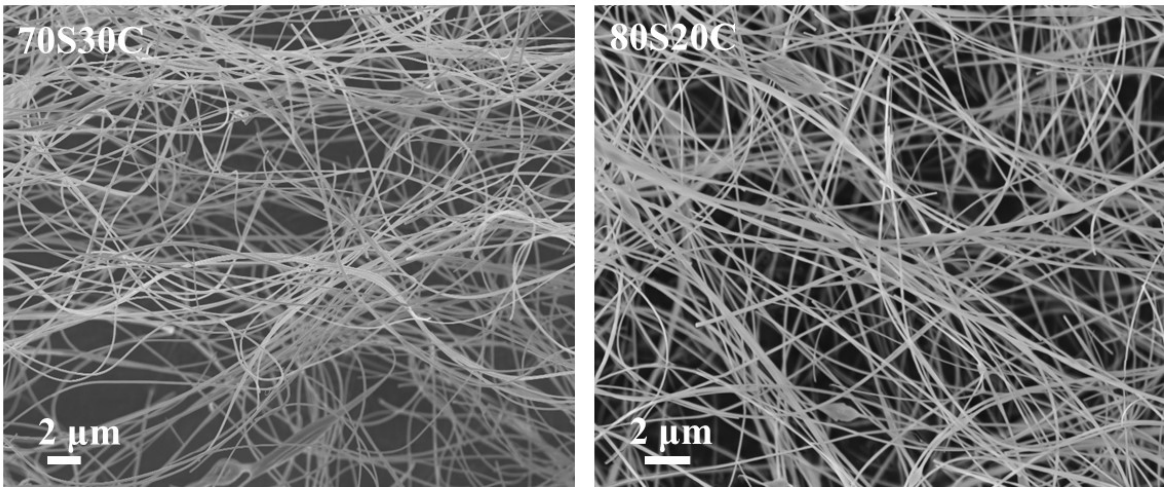


Figure 22. SEM-SE images of the electrospun bioactive glass 70S30C and 80S20C compositions.

Table 12. Electrospun sol-gel bioactive glass fibre diameter and specific surface area determined by N_2 sorption.

Sample	Surface Area [m^2 g^{-1}]	Fibre Diameter [µm]
70S30C	43.1	0.34 ± 0.11
80S20C	40.0	0.21 ± 0.02

The morphology of the two 3D bioactive glass compositions was investigated to determine their potential for interaction with HDFs (*Figure 22*). *Table 12* describes the mean fibre diameter of the 70S30C and 80S20C compositions determined from SEM images. The 70S30C composition was found to have a larger fibre diameter (0.34 μm ± 0.11) compared with 80S20C (0.21 μm ± 0.02), however the standard deviation in this sample was also greater indicating that there was no significant difference in the two compositions. Poologasundarampillai *et al.,* [7] produced 70S30C fibres with a diameter of 1.5 ± 0.4 μm which is over four times greater than the fibres electrospun under the conditions post heat treated with the binder removed. Cotton wool-like poly(L-lactic acid) and siloxane-doped vaterite (SiV) composite fibrous scaffolds developed by Obata *et al.,* [175] were electrospun with even larger diameters between 10-20 μm. Mouse osteoblast-like cells (MC3T3-E1 cells) were cultured onto the cotton-wool like material, into which cells penetrated and successfully proliferated on the fibres. Sun *et al.,* [211] concluded that a minimum fibre diameter of 10 μm was required for the cell adhesion and migration of HDF onto 3D electrospun polystyrene and poly-L-lactic acid samples.

The production of a 3D cotton-wool-like structure provides a potential surface, similar to the ECM, for the HDFs to attach to. The ability of cells and nutrients to move through the structure would depend on the packing of the 3D cotton-wool-like structure. As the fibres degrade, releasing therapeutic ions, inter-fibre spacing would increase, potentially enabling penetration and movement of HDFs through the scaffold. The reduced size of the fibres compared with those produced by Poologasundarampillai *et al.,* [7] is unexpected but may be due to the difference in electrospinning parameters. Poologasundarampillai *et al.,* [7] produced fibres at a higher voltage of 15 kV and without the use of a polymer binder. Literature [184] reports that an increase in the applied voltage produces a fibre of smaller diameter as a higher voltages causes stretching in the polymer solution which correlates with the charge repulsion with the polymer jet. Therefore, it is expected that the decrease in voltage to 10 kV would have resulted in larger fibre diameters. The flow rate used by Poologasundarampillai *et al.,* [7] was quoted to be 0.68 μl s^{-1} and that used in the study presented here was set at 0.12 μl s^{-1} (0.007 ml/min) as it was found that diameters electrospun at faster flow rates caused the sol-gel to splutter, forming beads . Literature shows [212] that the effect of flow rate on fibre diameter is complex as increasing flow rate can lead to an increase in the fibre diameter but additionally increases the formation of beads [169]. Work in Chapter 4 showed that fibres electrospun under the conditions outlined in *Table 9* and within the humidity and viscosity range identified in Chapter 4 produced fibres without or with very little beads.

Nitrogen sorption was carried out to determine the specific service area (BET method) of the 70S30C and 80S20C bioactive glass fibres were 43.1 m^2 g^{-1} and 40.0 m^2 g^{-1} respectively as shown in *Table 12*. The

surface areas of these compositions are higher than those determined by Poologasundarampillai *et al.,* [7] due to the smaller fibre diameters, enabling a greater area of attachment and release of silica and calcium ions into the wound area.

Nuclear magnetic resonance

The 70S30C and 80S20C compositions exhibited chemical shifts which were assigned to Q^1, Q^2, Q^3 and Q^4 units, respectively (*Table 13*).

Table 13. Relative Qn unit distribution in the glass structure (from solid-state 29Si MAS-NMR) and degree of condensation of the 70S30C and 80S20C bioactive glass samples. Dc is defined as the degree of condensation

Sample	Q^1		Q^2		Q^3		Q^4		D_c [%]	Connectivity
	δ [ppm]	I [%]	δ [ppm]	I [%]	δ [ppm]	I [%]	δ [ppm]	I [%]		
70S30C	-84.42	10.00	-93.10	12.10	-100.56	17.90	-109.66	60.00	81.98	3.28
80S20C	-82.18	4.60	-91.44	16.70	-100.02	23.60	-110.15	55.00	82.20	3.29

Figure 23 shows the broad ^{29}Si resonances which characterise the Q^n species. These resonances indicate the structure distributions and disorder which influence the silica positions within the bioactive glass network. Lin *et al*., [97] demonstrated results consistent with these observations, where a 70S30C bioactive glass structure heated to 700°C was also influenced by significant structure distributions and disorder in the structure of the SiO_2-CaO glass network.

The 70S30C and 80S20C compositions both have a larger proportion of Q^4 (70S30C at 60% and 80S20C at 55%)) and correspondingly have much smaller proportions of Q^1 (70S30C at 10% and 80S20C at 4.6%) compared with 70S30C sol-gel glass compositions prepared as a monolith (Q^1 of 17%, Q^4 of 36%) [97].

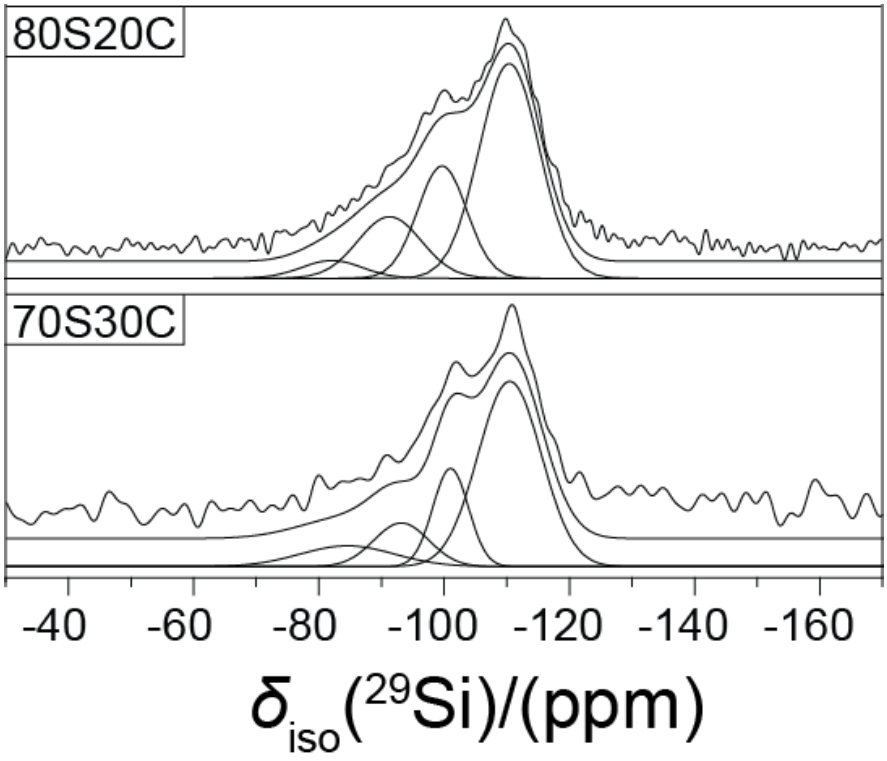


Figure 23. Solid-state 29Si MAS-NMR data of electrospun sol-gel glass 70S30C and 80S20C samples.

The D_c of the two compositions were similar. Lin *et al.* [97] found that the pre-stabilisation network connectivity for a 70S30C bioactive glass monolith was 3.65 and D_c was 91.3%. After stabilisation at 600 °C, network connectivity was found to have reduced to 2.62 and D_c was 65% which is considerably lower than pre stabilization network connectivity and D_c values and lower than obtained in the study presented here, indicating that perhaps not all the calcium had entered the network of the 70S30C and 80S20C fibrous samples. The study by Lin *et al.* [97] showed that calcium was not incorporated into the network as modifier until a stabilisation temperature of ~450 °C was reached. The pre-stabilisation D_c of 70S30C of ~90% was confirmed by Poologasundarampillai *et al.* [7] suggesting that calcium was not fully incorporated into the silica network [140]. Poologasundarampillai *et al.* however did not stabilise the 70S30C glass fibres. The electrospun 70S30C and 80S20C fibres presented in this study had a reduced network connectivity and D_c [7] as they were heated to 600°C. The differences is the post-stabilisation values of network connectivity and D_c could also be impacted by the difference in surface area of the samples. In the study conducted here, the fibrous scaffolds have a much higher surface area than that of the monolith 70S30C samples developed by Lin *et al.* [97].

X-ray photoelectron spectroscopy

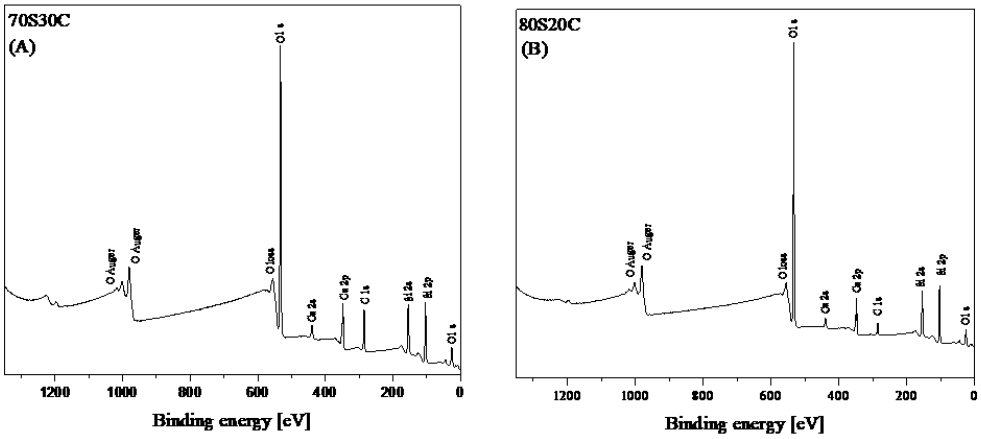


Figure 24. XPS Survey spectra of the bioactive glass compositions: (A) 70S30C and (B) 80S20C.

XPS was used to provide further information on the oxidation states of the species. The survey scan (*Figure 24*) of the compositions shows the typical and expected XPS and Auger lines from the elements present in the bioactive glasses. A high resolution XPS spectra of C 1s was used to find the adventitious carbon peak, which is related to the absorption of hydrocarbon impurities on the glass surface [192]. This is useful for the calibration of the binding energy and was set to 285 eV to correct any charging in each of the samples.

The high resolution XPS spectra were performed for Si, O and Ca spectra producing graphs showing the binding energy of each of the constituent elements in the bioactive glass compositions. The Si 2p high resolution spectra for 70S30C and 80S20C (*Figure 25*) show a maximum peak at 103.5 eV for 70S30C and 103.7 eV for 80S20C.

The binding energies obtained from the Si 2p verifies the findings from the NMR results. They suggest a high degree of condensation in the structure due to the Si 2p binding energies corresponding to the presence of tetrahedral Si, which is coordinated with four oxygen atoms (SiO_4^{4-}) [213].

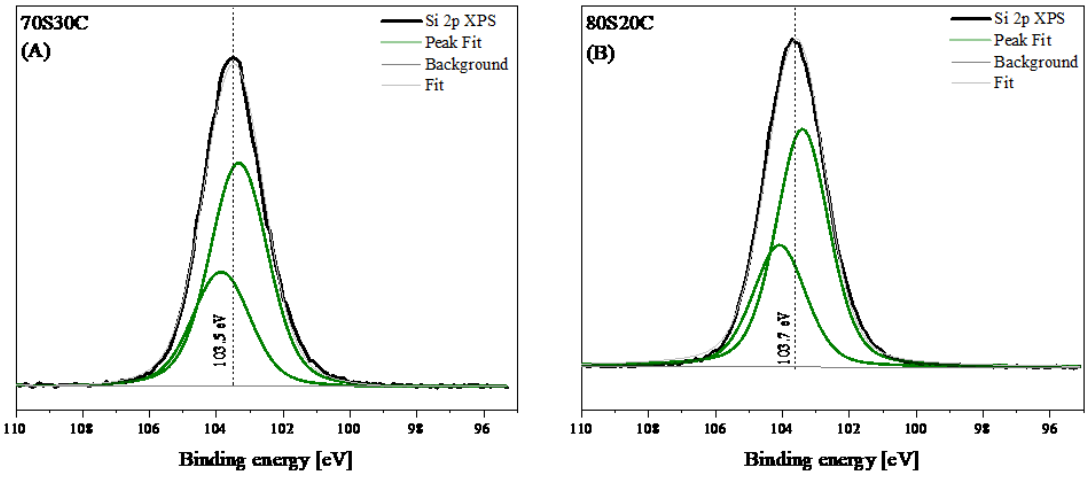


Figure 25. High-resolution XPS spectra of Si 2p for the bioactive glass compositions (A) 70S30C and (B) 80S20C.

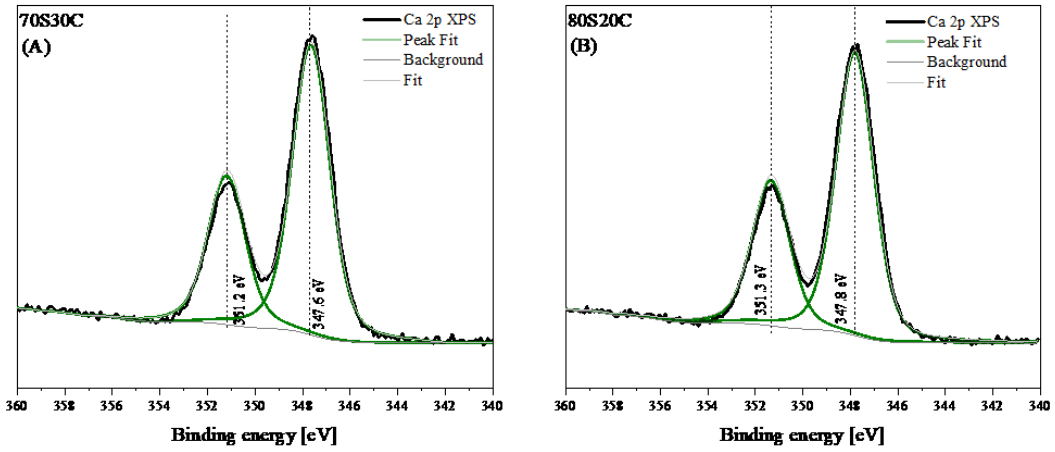


Figure 26. High-resolution XPS spectra of Ca 2p for the bioactive glass compositions (A) 70S30C and (B) 80S20C.

The Ca 2p XPS spectra (*Figure 26*) exhibit a peak at 347.6 eV with a satellite peak at 351.2 eV for the 70S30C sample whereas the 80S20C Ca 2p is shifted slightly with a peak at 347.8 and a satellite at 351.3 eV. For both these compositions, literature shows that the Ca 2p peaks are attributable to the ionisation of the Ca 2p3/2 and Ca 2p1/2 electrons of the Ca^{2+} oxidation state [214] [215]. Cui *et al.,* [216] showed peaks between ~346 eV and ~347 eV with satellites at ~350 to ~350.5 eV and attributed them to CaO.

The O 1s spectra (*Figure 27*) was used to confirm these observations. The 70S30C composition identified peaks at 530.8 eV and at 532.9 eV and the 80S20C at 530.8 eV and 533.1 eV.

The peak at ~533 eV is typically attributed to oxygen bonded with silica and the second O 1s peak at ~530 eV is often associated with additional metal oxides. Serra *et al*., [192] used XPS alongside FTIR to study glasses in the Na_2O–CaO–P_2O_5–K_2O–MgO–B_2O_3–SiO_2 system and identified well resolved peaks at 532 eV were associated with bridging oxygen groups (the Si-O-Si vibration). Serra *et al*., [192] attributed their second peak at ~530 eV with non-bridging oxygen groups (such as Si-ONa or Si-OCa). Similar observations were made by Miura *et al.,* [217]. Pérez-Pariente *et al.* [218] related the second, O 1s peak with a lower binding energy, to oxygen in the phosphate structure in bioactive glasses in the SiO_2-CaO-P_2O_5 and SiO_2-CaO-P_2O_5-MgO systems. The binding energy for this second O 1s peak observed by Pérez-Pariente *et al*, [218] is within the same region as those for phosphates associated with hydroxyapatite [218].

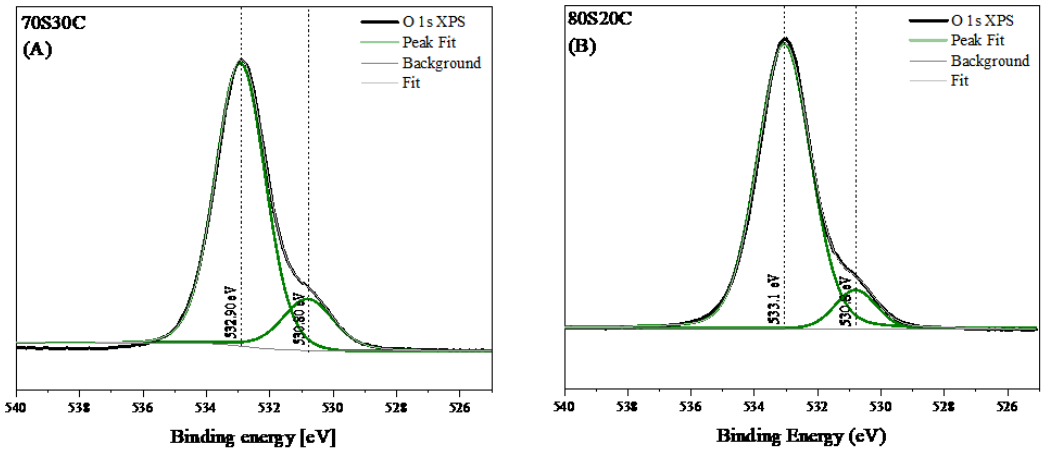


Figure 27. High-resolution XPS spectra of O 1s for the 70S30C and 80S20C bioactive glass compositions (A) 70S30C and (B) 80S20C.

5.3.2. Degradation in DMEM

This study presents the dissolution of the 70S30C and 80S20C bioactive glass compositions in DMEM to determine the ion concentrations of silica and calcium, and if they are suitable for use on a HDFs.

Dissolution with DMEM

The dissolution study in DMEM (*Figure 28*) shows the silica and calcium ion concentrations by time point of the 70S30C and 80S20C samples. The two compositions released fewer silica and calcium ions compared with the release in TRIS conducted in Chapter 4.2.5.

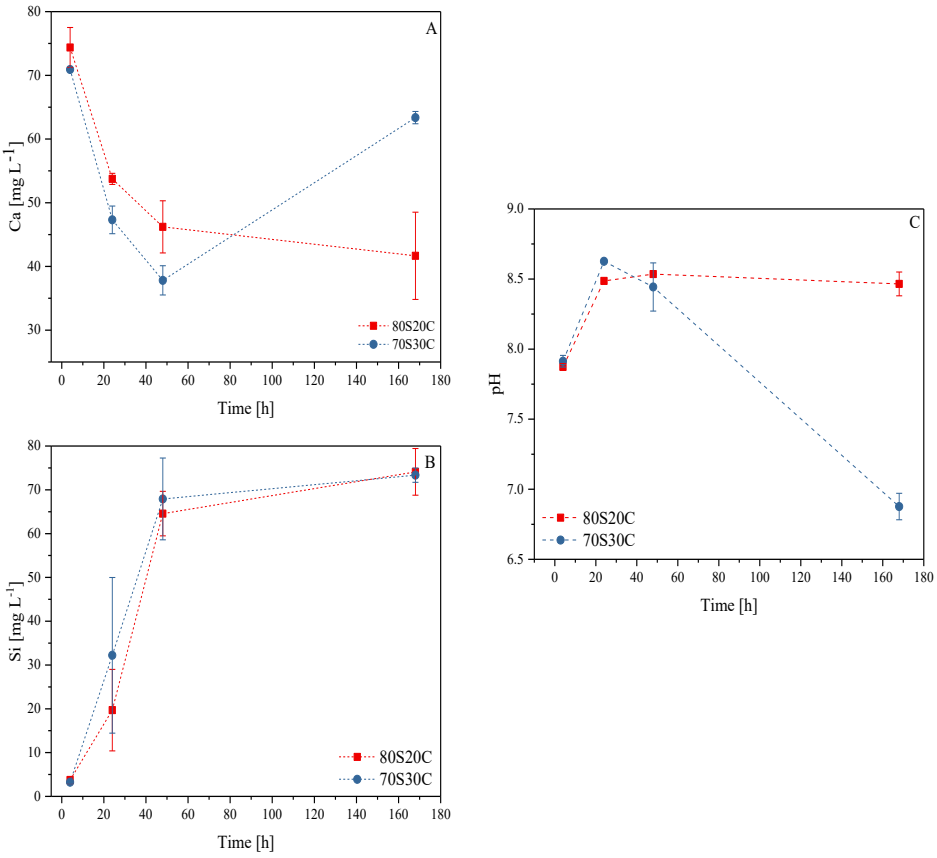


Figure 28. (A) Dissolution profiles from ICP of electrospun sol-gel glasses in DMEM at time points of 4 h, 1 day, 3 day and 7 day, (B) pH profile of DMEM during glass dissolution.

The calcium profile (*Figure 28A & B*) shows a similar calcium ion concentration at 4 h for both bioactive glass compositions (70.9 mg L^{-1} for 70S30C and 74.4 mg L^{-1} for 80S20C), which then decreased at day 1

and dropped further at day 3, before increasing again by day 7. The 70S30C composition shows a Ca concentration at day 7 of 63.4 mg L^{-1} and 41.7 mg L^{-1} for the 80S20C sample. This differs from the TRIS profile (Chapter 4.2.5), which showed a burst release of calcium ions in the first 24 h, increasing the cation concentration, before plateauing to a concentration of 251.7 mg L^{-1} for 70S30C and 193.0 mg L^{-1} for 80S20C at day 7. The DMEM contains calcium as well, so the concentration of calcium at each time point is made up of concentrations which have been released from the bioactive glass and that which is already contained in the DMEM dissolution media. Therefore it can be difficult to quantify changes in the Ca ion concentrations in the media due to the dissolution of the fibres. The fluctuations in concentrations of calcium in the DMEM is characteristic of a solution where the species are involved in both dissolution and precipitation (e.g. formation of HCA [219]), it would have been useful to have measured the change in concentration of some of the other ions present in the DMEM media such as Phosphorus, to have investigated if fluctuations in concentration followed a similar pattern to that observed for the Calcium .

Kulesz-Martin *et al.* [220] showed that dermal fibroblasts grew best at concentrations of 1.4 mM Ca^{2+} (56.1 mg L^{-1}). The dissolution in DMEM (*Figure 28A & B*) showed that the 70S30C and 80S20C composition were nearest this value at the 4 h time point and therefore the dissolution products at this time point was determined to be the most appropriate for use in the further cell studies. The pH for samples in DMEM (*Figure 28C*) showed higher values when compared with those in TRIS in Chapter 4.2.5. The 70S30C sample showed a decrease in pH at day 7 in DMEM.

The silica release for both samples in DMEM was similar and over the 7 day study the silica concentration plateaued at similar values to that of the study conducted in TRIS. This indicates that the use of DMEM did not have an impact on the release of silica as it did on the release of calcium from the dissolution of the bioactive glass samples.

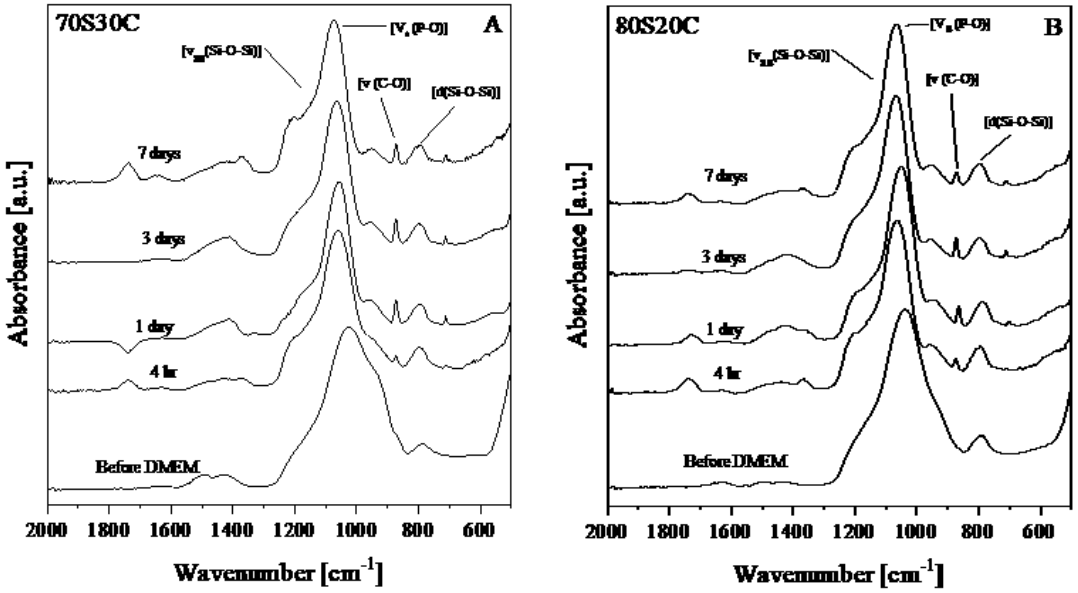


Figure 29. FTIR spectra electrospun sol-gel glasses before and after being soaked in DMEM for 7 days: (A) 70S30C and (B) 80S20C.

FTIR spectra (*Figure 29*) of the compositions post dissolution in DMEM identified an additional band at ~872 cm^{-1}which was attributed to the C-O stretching peak of the CO_2^{3-} group, which is typically associated with the formation of HCA on glasses [221]. Other bands associated with C-O at ~1400 cm^{-1} were however not identified [222]. An increase in intensity at ~800 cm^{-1} was also observed at 4 h onwards, this expected band is associated with the bending motion of oxygen in Si-O-Si groups [223]. A band at ~711 cm^{-1} developed after 1 day of immersion in both samples but could not be identified.

XRD analysis after 4 h in DMEM (*Figure 30*) showed a significant change in the 70S30C fibres, with the presence of peaks at 23°, 29°, 36°, 39°, 43°, 47°, 48°, 57°, 61°, 62°, 64°, 65° and 69°. While some of these peaks could be attributed to hydroxyapatite, which displays similar peaks at ~28°, ~32°, ~39°, ~43° and ~49°, hydroxyapatite also has additional peaks which were not found in the XRD pattern presented in *Figure 30*. Crucially, the primary peak associated with hydroxyapatite (2θ = ~32°) [224] was not present in the spectra produced from this study. Peak fitting software and comparisons in literature showed that the pattern of peaks fitted most loosely with Calcite [224]. The use of peak fitting software (PANalytical X'Pert HighScore Plus) additionally identified Calcite as a likely candidate, with the ICDD reference of 00-005-0586 in a rhombohedral crystal system. These peaks were identified at 4 h, 1 day, 3 days and 7 days immersion of 70S30C fibres in DMEM indicating the formation of calcite happens very quickly after

immersion. Figure 38 shows a similar array of peaks at each of the 4 h, 1 day 3 day and 7 day time points, indicating that the formation of calcite in the 80S20C sample is similar. The XRD spectrum of the day 7 peak of the 80S20C sample additionally shows peaks at 33°, 46° and 56° which can be attributed to Sodium Chloride. The peak fitting software identified Halite with an ICDD reference of 00-001-0994 with a Cubic crystal system.

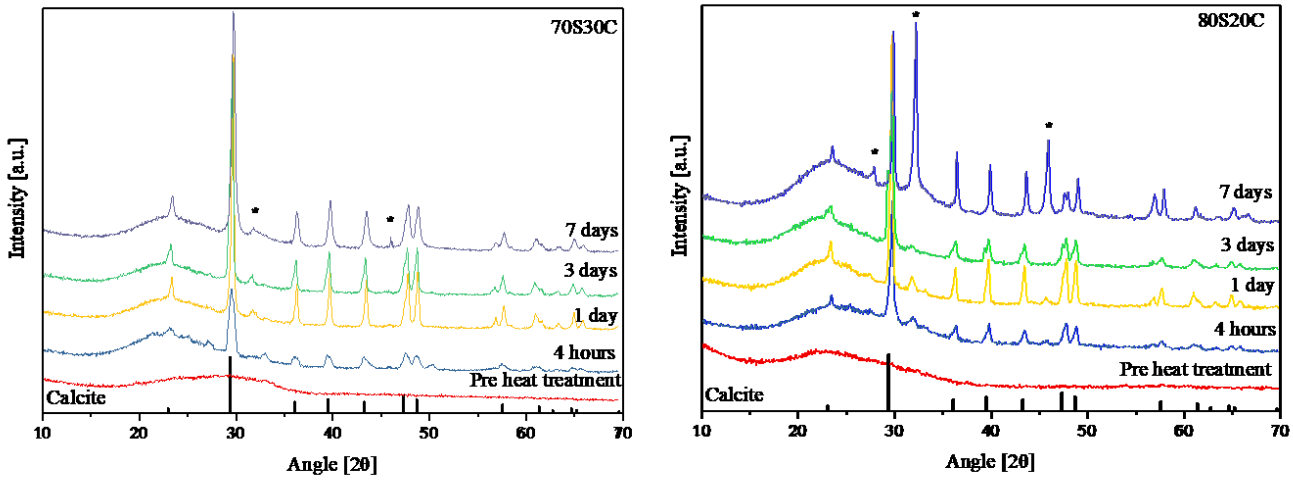


Figure 30. XRD patterns of electrospun sol-gel glasses before and after being immersed in DMEM for 7 days (a) 70S30C and (b) 80S20C. Peaks associated with calcite are also included. Calcium carbonate oxide peak reference file number 00-005-0586. (*) inducates the presence of peaks not identified as Calcium Carbonate. ICDD identified this to be Halite with a reference of 00-001-0994. Samples were scanned at room temperature.

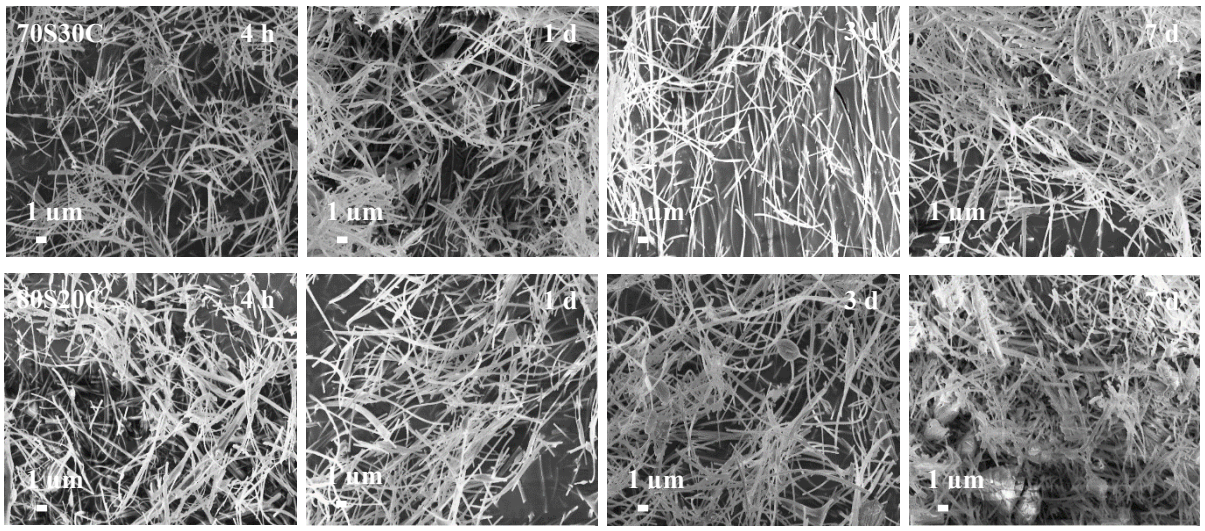


Figure 31. SEM image of 70S30C and 80S20C electrospun sol-gel glasses after being immersed in DMEM at 4 h, 1 day, 3 days and 7 days.

SEM was used to view the fibres and assess any physical changes in the morphology after being exposed to DMEM over the 7 day period. *Figure 31* shows no visible deposition of material on the fibres and no 'globular cauliflower-like morphology [7] which is typically observed in bioactive glasses [225] where HCA formation has taken place. Poologasundarampillai *et al.* [7] found evidence of the formation of a HCA layer on fibres within the first 12 h of soaking in simulated body fluid. Kim *et al.,* [226] produced similar results when developing a nanocomposite made up of bioactive glass nanofibres which was combined with a degradable synthetic polymer. Kim *et al.,* [226] found that the fibre surface showed a pronounced formation of apatite nanocrystallines after three days when incubated in simulated physiological medium (Kokubo's medium). The results presented in Fig 31 show that for both the 70S30C and 80S20C samples HCA formation did not happen over the 7 day study when fibres were incubated in DMEM. A study produced by Clupper *et al.,* [225] tested the formation of HCA on S520 bioactive glass fibres (52.0 mol % SiO_2, 20.9 Na_2O, 7.1 K_2O, 18.0 CaO, and 2.0 P_2O_5) in two different dissolution media, SBF and DMEM. It showed HCA formation on fibres after 5 h when immersed in SBF and a continuous HCA layer was formed after a 20 day immersion. Samples immersed in DMEM showed the presence of a continuous HCA layer after 20 days, the study did not indicate whether the formation of HCA in the samples incubated in DMEM occurred before this point. DMEM was investigated in these studies as a dissolution media as it was used as a media for the cellular studies. The fibres were immersed in DMEM for a total period of 7 days, which may have not been long enough to show the formation of HCA. The study from

Clupper *et al.,* [225] provided evidence for the formation of bioactive glasses in HCA only after 20 days of immersion. In addition, the studies outlined above focused on the desire for bone regeneration, and therefore samples were left immersed in media for long periods to mimic the desired, slower ion release rates. For wound healing applications, quicker ion release rates are required as the first days of wound healing are key in preventing infection and to engage all the stages of wound healing. Alongside side this desire for quicker healing, frequent changes in wound dressing means that dressings containing bioactive glass fibres could be changed every few days if they have not degraded and therefore would not be in contact with the wound long enough to produce HCA.

5.3.3. Cell study with HDFs

Cell studies were carried out using HDFs as outlined in Section 5.2.3. In Section 5.3.2, ICP analysis showed the concentrations of silica and calcium at each time point. The 4 h time point was selected as the most promising ion concentration to be used for cell studies as the concentration of calcium ions was sufficient to produce a proliferative effect on the HDFs. *Table 14* shows the actual average release of each element over the three experiments conducted. This result is much higher than anticipated and suggests that the individual time points in the 7 day dissolution study may not a reliable prediction of actual silica and calcium ion concentrations.

Table 14. Measured silica and calcium concentration (ICP) after 4 h immersion in DMEM after filtering

	Ca [mg L^{-1}]	Si [mg L^{-1}]
70S30C	170.75 ± 18.67	82.01 ± 13.26
80S20C	184.80 ± 19.21	83.46 ± 15.18

The significant increase in calcium and silica ions released still ensures that both samples were above the 1.4 mM (56.1 mg L^{-1}) calcium concentration threshold that is deemed to be beneficial for the growth of fibroblasts [220]. However, a maximum value for the impact of calcium on fibroblasts has not been reported in literature. The Silica control was produced by averaging the two results (the 70S30C and 80S20C) to produce a value of 82.85 mg L^{-1} (2.95 mM).

Metabolic activity

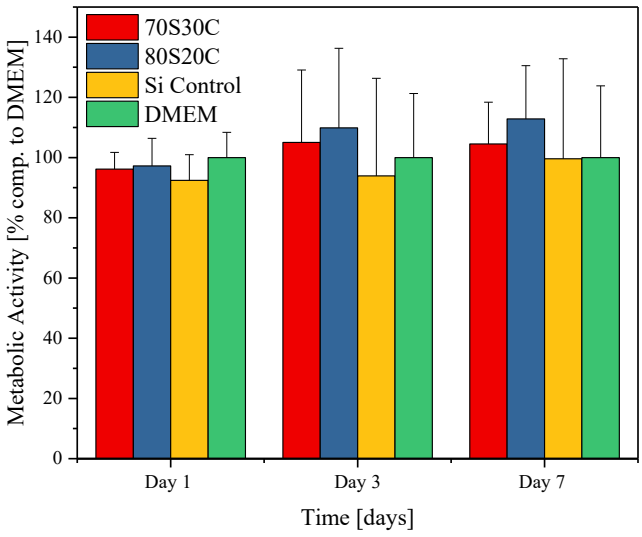


*Figure 32. The metabolic activity of the HDFs after immersion in the dissolution product of the 70S30C and 80S20C samples, the Si control and the DMEM control at day 1, day 3 and day 7. The metabolic activity is displayed as a percentage of the DMEM control. None of the samples cause a significant change in metabolic activity of the HDFs. A Krustal-Wallis test followed by Dunn's Multiple Comparison were used to determine statistical significance in the metabolic activity relative to the DMEM result of samples at each time point. (n=6, * P < 0.05, ** P < 0.01, *** P < 0.001, **** P < 0.0001).*

The data shown in *Figure 32* displays the metabolic activity as a percentage comparison with the DMEM value at each time point, with the DMEM value is set to 100% at each time point and the corresponding samples are calculated as a percentage of the DMEM. There were no statistical differences in metabolic activity of the HDFs whether they were exposed to the 70S30C and 80S20C bioactive glasses or the Si control (*Figure 32*) at any of the time points. This lack of statistical differences in *Figures 32* indicates that the presence of the bioactive glass dissolution product on the HDFs have no adverse impact on the metabolic activity at day 1, 3 and 7 of the study. This result is encouraging as it demonstrates that the concentration of calcium and silicon ions at the 4 h dissolution time point do not have a negative impact on the metabolic activity of the HDFs. This result indicates a likely positive reaction of the HDFs when exposed to the fibrous bioactive glass structure. A reduction in metabolic activity of the 70S30C and 80S20C bioactive glass compositions at any of the time points tested for in *Figure 32* would have implied that the ion concentrations of silicon and calcium after 4 hours of exposure were cytotoxic to the HDFs.

Total DNA

The tDNA of the HDFs was investigated to determine the proliferation of cells when exposed to the dissolution product of the 70S30C and 80S20C bioactive glass compositions. *Figure 33* shows a statistical increase in the proliferation of HDFs exposed to the 80S20C solution at day 3 and day 7 relative to the total DNA value observed of pre-study, day 0 proliferation result. The HDFs exposed to the Si control solution and to the DMEM solution also exhibited a significant increase in proliferation at day 7, however this was not the case at Day 3 where no significant increase in proliferation was observed. The increase in proliferation of HDFs exposed to the Si control and 80S2C solutions suggests that it could be the presence of Si in the bioactive glass dissolution product which provides an environment for the HDFs to proliferate. Studies show that the presence of silicon ions can improve wound healing rates. The mechanism for this is through increasing the production of the TGF-b growth factor which can support healing in the inflammation, proliferation and tissue remodelling stages of wound healing. The results back this hypothesis further by showing that the Si control has the most significant increase at day 7. The proliferation of the HDFs exposed to the 70S30C composition indicates that the cells grow at a slower rate, it is important to note however that the proliferation of HDFs is not impaired by the presence of the 70S30C dissolution product.

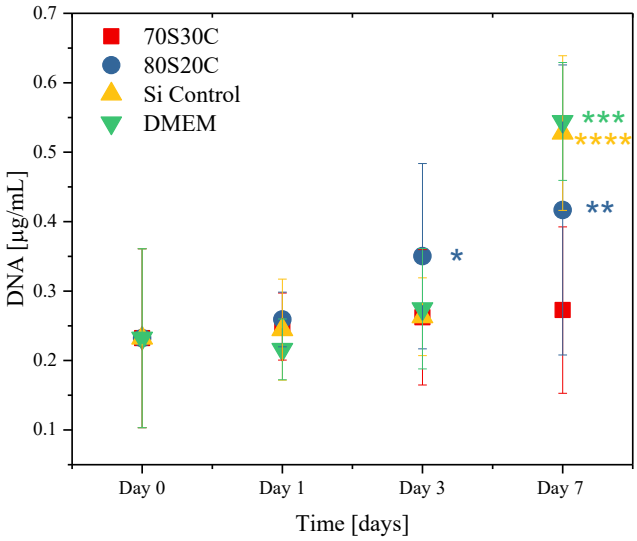


*Figure 33. The proliferation [µg/mL] of HDF cultures exposed to DMEM containing the dissolution products of the 70S30C and 80S20C samples, the Si control and DMEM after 1 day, 3 day and 7 day. HDFs exposed to the 80S20C sample expressed a significant increase in proliferation at day 3 and day 7. Kruskal-Wallis test followed by Dunn's Multiple Comparison to detect significant changes in the proliferation of each composition with respect to the cell proliferation of HDFs at day 0, pre-exposure of HDFs to the different conditions. (n=6, * P < 0.05, ** P < 0.01, *** P < 0.001, **** P < 0.0001).*

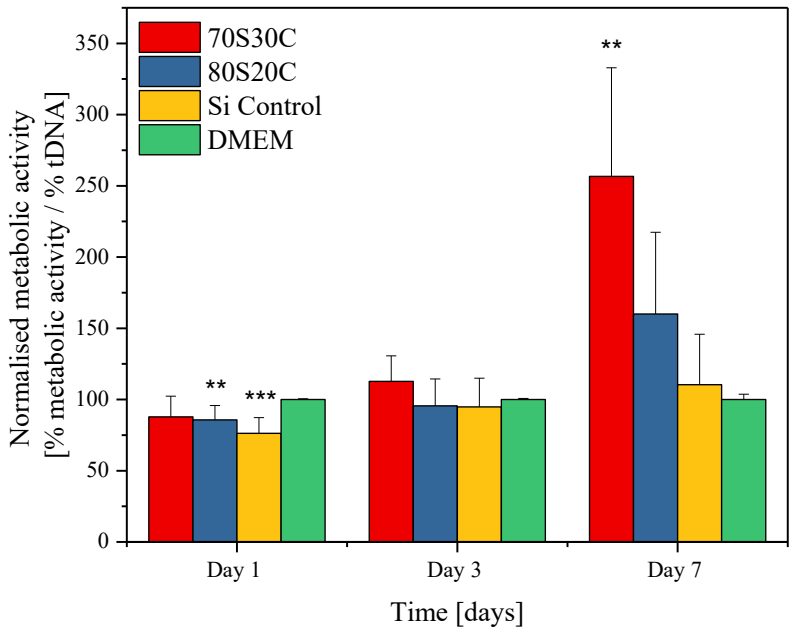


*Figure 34. The metabolic activity of the HDFs normalised to cell number (calculated as percentages with respect to DMEM). The normalised metabolic activity per cell of HDFs immersed in the 70S30C bioactive glass was significantly increased at day 7. A Krustal- Wallis test followed by Dunn's Multiple Comparison were used to detect any statistical significance between each control and the DMEM at each time point. (n=6, * P < 0.05, ** P < 0.01, *** P < 0.001, **** P < 0.0001).*

The metabolic activity per cell is a useful way to analyse the activity or the health of HDFs per cell. Figure 34 shows that the metabolic activity per cell significantly increased in the 70S30C sample at day 7 compared with that of the DMEM at day 7. This result is possibly due to a significant reduction in proliferation at this time point paired with a metabolic activity which is not significantly different with the control. This suggests that the 70S30C sample may reduce the rate of proliferation of the HDFs but not that it is cytotoxic to the HDFs.

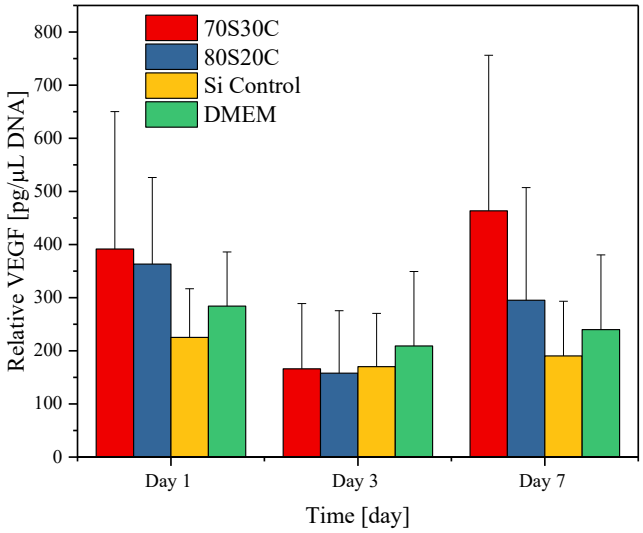


*Figure 35. Normalised VEGF production of HDF cultures exposed to DMEM containing the dissolution products of bioactive glasses 70S30C and 80S20C, the Si control samples and DMEM after 1 day, 3 day and 7 day normalised to tDNA. A Kruskal-Wallis test followed by Dunn's Multiple Comparison was used to detect statistical significance of each composition with respect to DMEM at each time point (n=3, * P < 0.05, ** P < 0.01, *** P < 0.001, **** P < 0.0001).*

VEGF analysis

The quantity of the growth factor VEGF was measured to determine if the concentration of silicon and calcium ions impacted the production of the growth factor over the course of a 7 day study. The VEGF results were normalised to the total DNA, resulting in the VEGF production per cell. The exposure of HDFs to the 70S30C and 80S20C conditioned media showed an increase in the normalised VEGF at days 1 and 7 with respect to that of the DMEM at the aforementioned time points (*Figure 35*). However this increase in VEGF in the HDFs exposed to the 70S30C and 80S20C dissolution products were not considered to be statistically significant. The results presented in *Figure 35* have substantial error bars in all samples including the DMEM control so conclusions cannot be explicitly drawn. The results suggest however that the dissolution product of the 70S30C and 80S20C compositions do not inhibit the production of VEGF which is encouraging as provides potential opportunity for the incorporation of therapeutic ions which may be beneficial in increasing the VEGF production of HDF cells.

5.4. Concluding remarks

The 70S30C and 80S20C compositions were produced and electrospun according to the parameters outlined in Chapter 4. The primary objectives of this study were to further characterise the fibrous scaffolds of the two bioactive glass compositions and to understand whether the compositions have the potential to be beneficial for wound healing applications. This was done through analysing the impact of dissolution in DMEM of the fibres and through cell studies conducted on HDFs.

For the characterisation of the two compositions, physical factors such as the morphology of the fibres were investigated alongside chemical characterisation which was achieved through NMR and XPS. The fibre diameters were measured from SEM images and were quantified using ImageJ software and found to be in the range of 0.21 – 0.34 μm which is much smaller than samples quoted by Poologasundarampillai *et al* [7]. (1.5 ± 0.4 μm) and Obata *et al,* [175] (10-20 μm). The fibres electrospun in the present study were also found to be much smaller than HDFs (10-15 μm) [227] which may provide issues with cell attachment as studies have shown that fibre diameters larger than that of the HDFs are appropriate for cell attachment [175].

BET analysis found that the surface area of the fibrous samples was greater than those produced by Poologasundarampillai *et al.* [7]. The difference in surface areas is surprising as Poologasundarampillai *et al.* [7] produced fibres using a similar sol-gel protocol which suggests that the difference in surface area and fibre diameter results from either the use of the polymer binder prior to electrospinning or the electrospinning parameters themselves. The eletrospinning parameters used by Poologasundarampillai *et al.* differed in the applied voltage and in the distance between the needle tip and the collector plate. The larger surface area presented in this study is beneficial as it creates the potential opportunity for increased cell contact with the fibres and enables a higher release of calcium and silicate ions.

XPS and NMR analysis provide a valuable insight into the chemistry of the two bioactive glass compositions. XPS produced evidence for the chemical states of the elements, the Si 2p and O 1s spectra corresponded to the Si coordinated with four oxygen atoms producing SiO_4^{4-}. ^{Si}MAS-NMR showed that both compositions had a larger proportion of Q^4 units. The network connectivity and degree of condensation of the 70S30C and 80S20C samples were similar to reported literature values of 70S30C compositions. Neither XPS nor ^{Si}MAS-NMR provided discernible differences between the 70S30C and 80S20C compositions.

The dissolution study showed that the concentrations of silica were similar for both compositions and that the 70S30C sample produced a marginally higher concentration of calcium. The purpose of this study was

to firstly quantify the ion concentrations obtained from the 70S30C and 80S20C compositions in DMEM media and compare it with the results obtained in TRIS in Chapter 4.2.5. The results identified that for DMEM the calcium ion concentration was considerably lower compared with in TRIS across the 7 day time period, whereas the silica ion concentration remained similar. XRD and FITR were conducted on the samples after exposure to the DMEM at each time point. FTIR produced an additional band at ~872 cm^{-1} which is typically attributed to the C-O stretching band. XRD peaks formed after exposure to DMEM produced evidence of calcite formation as the key peak associated with hydroxyapatite (2θ = ~32°) was not present in this study. The formation of Calcite was checked using peak fitting software and an ICDD reference was identified as a match. The investigation into the fibre morphology of the samples immersed in DMEM for 4 h, 1 Day, 3 Days and 7 Days produced SEM results which did not show any globules on the surface of fibres providing evidence of the formation of HCA on the fibres.

The cell studies with HDFs were a first step in determining the suitability of the 70S30C and 80S20C bioactive glass compositions for providing a beneficial response to wound healing. The metabolic activity of the cells were not significantly impacted by the presence of the bioactive glass compositions. This was a useful indicator of the HDF response to the concentrations of silicon and calcium ions expected from the exposure of HDFs to the bioactive glass fibrous scaffolds. The tDNA of the HDFs was also investigated with the objective of providing an insight into the proliferation of HDFs when exposed to the dissolution product of the 70S30C and 80S20C bioactive glass samples. The tDNA results displayed an increase in proliferation in the 80S20C sample and Si control at day 7 when compared with the samples at day 0. Normalised metabolic activity results showed a significant increase in the metabolic activity per cell of the HDFs exposed to the 70S30C sample at day 7.

The VEGF study was conducted to determine the quantity of VEGF secreted by the HDFs after exposure to the 70S30C, 80S20C, Si control and DMEM compositions. No significant increase in VEGF production was observed, however the 70S30C composition produced the highest levels of VEGF at day 1 and day 7.

The results presented in this Chapter provide a starting point for investigating the suitability of different ions for use in wound healing. The bioactive glass fibres were found to not inhibit HDF metabolic activity and proliferation and were found to have some benefit in terms of VEGF production. The 70S30C sample provides an interesting starting point for investigation into the therapeutic effect of different ions.

CHAPTER SIX

DETERMINING A SUITABLE COPPER CONCENTRATION FOR USE IN BIOACTIVE GLASS

6. 1. Introduction

The cellular studies conducted in Chapter 5 have shown that the 3D electrospun bioactive glasses do not inhibit the metabolic activity or the proliferation of a HDF cell line. The cell culture results also showed that the 70S30C bioactive glass composition produced a significant increase in VEGF production at day 7. These results indicate that the 70S30C composition is a useful starting point for investigation into the potential therapeutic effects of different ions and their impact on VEGF production in HDFs.

The preliminary study presented here aims to understand if it is possible to incorporate copper ions into electrospun bioactive glass fibres, produced via the same sol-gel electrospinning route as the 70S30C and 80S20C compositions. This study aims to incorporate 1 mol% CuO and 5 mol% CuO (labelled as 1% CuBG and 5% CuBG) into the 70S30C composition substituting for calcium in the bioactive glass composition. The copper containing bioactive glass (CuBGs) compositions chosen as a starting point were 1% CuBG and 5% CuBG as Jinyan *et al.* [228] found pulsed laser deposition bioactive glass nanostructure compositions containing 1 mol% and 5 mol% copper stimulated angiogenesis in HUVECs. Wu *et al.* [124] also showed that sol-gel derived mesoporous bioactive glasses with concentrations of 0, 1, 2 and 5 mol% copper stimulated VEGF production in hBMSCs.

The second aim was to investigate how the presence of copper in the composition impacts the metabolic activity and the proliferation of HDF cell lines. Few studies have been carried out on the effect of copper on fibroblasts, perhaps due to the unexpected and often contradictory viability and proliferation results as observed by Bejarano *et al.* [125] and Mortazavi *et al.* [229].

The Chapter then aims to develop a series of copper controls to assess the response of HDFs to different copper concentrations. Here copper chloride was used to produce the controls and the metabolic activity and cell proliferation were assessed.

Based on the results of the copper concentration study, the third part of this Chapter aims to develop a series of CuBGs with revised compositions which promote the production of VEGF in HDFs.

6. 2. Methods and materials

Physical, chemical and biological characterisation was carried out on the developed bioactive glass copper compositions. Chemical characterisations included the assessment of the compositions using FTIR, XRD and lithium metaborate fusion/ICP as described in Chapter 4.2.4 to assess the chemical effects of including copper into the bioactive glass network. Characterisation using SEM was used to assess the morphology of the fibres to determine if the inclusion of copper affected features such as the fibre diameter, fibre uniformity and the presence of beads.

Dissolution studies were also carried out as described in Chapter 4.2.5 to determine the ion concentration and pattern of the samples and to understand the impact of different concentrations of copper in the bioactive glass structure and how they affected glass dissolution. Cell studies on the dissolution products of the copper containing bioactive glass samples and copper controls were carried out to determine the metabolic activity and the cell proliferation of HDFs.

6.2.1. Preliminary Study of copper containing glass fibres

Three copper containing samples based on the 70S30C bioactive glass composition were obtained through the sol-gel route as described in Chapter 5.2.1. Copper nitrate was used as the copper precursor and was incorporated into the bioactive glass structure by replacing some of the calcium content of the sol. The copper nitrate was added into the sol after the addition of calcium nitrate. Initially two copper containing sol-gels were developed, shown in *Table 15* alongside the 70S30C composition produced and investigated in previous chapters. Copper nitrite trihydrate was sourced from Sigma Aldrich puriss p.a. 99-104% (CAS 10031-43-3) was used as a precursor for copper.

Table 15. Nominal sol-gel compositions and the quantities of TEOS, nitric acid, ethanol, calcium nitrate and copper nitrate used. The samples were named 0% CuBG (70S30C), 1% CuBG (70S29C1Cu) and 5% CuBG (70S25C5Cu).

Compositions	TEOS [mL]	Nitric Acid [mL]	Ethanol [mL]	$Ca(NO_3)_2 \cdot 4H_2O$ [g]	Cu(NO3)2•6H2O [g]
70S30C (0 Cu)	7.2	1.7	3.7	3.2	0.00
70S29C1Cu (1 Cu)	7.2	1.7	3.7	3.09	0.11
70S25C5Cu (5 Cu)	7.2	1.7	3.7	2.67	0.55

The samples were electrospun using the electrospinning parameters outlined in in *Table 16*. The relative humidity range was retained at between 30% - 55% as this produced the desired 3D structure in the compositions studied in Chapters 4 and 5.

Table 16. The electrospinning parameters used to produce copper containing bioactive glass fibres.

Relative humidity [%]	Voltage [kV]	Distance [mm]	Flow rate [$\mu L\ s^{-1}$]
30-55%	10.0	10 – 12	0.12

Physical and chemical characterisation on the fibres produced were carried out:

1. XRD and FTIR were conducted to identify any changes in the chemistry of the material. Changes in the material structure or shifts in the 2θ or wavenumber bands as a result of introducing copper into the bioactive glass composition were also investigated;
2. SEM was used to assess the morphology of the copper containing bioactive glass fibres and to determine the fibre diameter;
3. Lithium metaborate fusion and ICP analysis was undertaken to determine the actual composition of the bioactive glasses and two dissolution studies was carried out in TRIS and DMEM to determine the release rate of the bioactive glass scaffolds;
4. The metabolic activity and cell proliferation of the HDFs on exposure to the dissolution products of the bioactive glasses was investigated.

Materials characterisation of fibres

XRD and FTIR were used to identify any areas of crystallinity as a result of the addition of copper ions into the glass network. Measurements for XRD and FTIR were conducted as described in Chapter 4.2.3. The morphology of the different fibrous copper containing compositions was imaged using SEM to determine if the concentration of copper impacted the appearance and diameters of the fibres produced. SEM images were obtained through the use of a LEO-1525 as described in Chapter 4.2.3.

The fibre diameters were measured using ImageJ software and were compared with the scale bar in each of the images which was used as a reference length. Between six and ten in focus fibre diameters were measured in each image (n=4 per fibre). The fibre diameters were averaged and a standard deviation was taken.

A lithium metaborate fusion study was used to ascertain the actual composition of the different CuBG samples produced using the nominal composition outlined in *Table 15*. The lithium metaborate study was conducted as described in Chapter 4.2.4.

Dissolution Study in TRIS buffer and DMEM

Chapters 4 and 5 outline the methodology for dissolution studies conducted in TRIS and DMEM. Here, both dissolution studies were conducted to ascertain the release rate of silica, calcium and copper from bioactive glass fibres over a period of seven days.

The dissolution protocol was revised slightly in this study as both studies used a reduced mass of fibres compared with the studies previously outlined in Chapter 4.2.5 and Chapter 5.2.2. Here a ratio of 1.5 mg mL^{-1} was used, where 25 mg of fibres were immersed in 16.7 mL of TRIS or DMEM (n=3), these revised quantities are based on the ratio recommendations of Maçon *et al.,* [186]. The fibre masses and media volumes were reduced in this investigation as this was a preliminary study into the suitability of these CuBGs. The 25 mg samples were placed in the individual cellulose dialysis tubing and 2 mL of DMEM or TRIS was added to the tube. The samples were immersed in the remaining 14.7 mL of TRIS and DMEM In this study, 0.5 mL of sample was removed from each sample at each time point (1 h, 2 h, 3 h, 4 h, 8 h, 24 h, 24 h, 48 h, 72 h, 96 h and 168 h). The rest of the study was conducted as described in Chapter 3.2.5. The samples were then analysed using ICP-AES analysis at wavelengths of 317.9 nm (Ca), 251.6 nm (Si) and 324.7 nm (Cu).

The pH of CuBG samples was measured at each time point by a pH meter with a thermal probe (Oakton pH 11 meter with Oakton general purpose glass pH probe, Ag/AgCl electrode, and Oakton ATC probe) attached to it.

Cell Studies

Cell studies were carried out on HDFs to understand the impact of the dissolution of the bioactive glass compositions on key cells involved in the wound healing process. The study was designed to determine if the release of the silica, calcium and copper ions from the fibres was at a rate to produce a therapeutic effect on the HDFs and to ascertain whether the release was damaging to the cells at all in terms of reducing the metabolic activity or proliferation of the cells. The preliminary study was completed with between 5 and 7 repeats. In all cases the samples were electrsopun to produce a 3D material at a relative humidity values between 30 – 45%.

The HDF cell line (ATCC, UK) with passage numbers from 20-30 was expanded and supplemented as described in Chapter 5.2.2. The CuBGs were pre-conditioned in DMEM for 4 hours in an incubator at 37°C, 5% CO_2 and 21% O_2 at 200 rpm using the protocol described in Chapter 5.2.2. Controls for silica and copper were prepared using sodium metasilicate and copper chloride based on the Si mM and Cu mM values found

by ICP-AES at the 4 h time point of the dissolution study for the copper containing samples. The remaining dissolution product was supplemented with 10 % (v/v) FBS and 1% (v/v) penicillin/streptomycin.

HDFs were harvested and suspended in DMEM at a concentration of 20,000 cells per mL. 500 µL of cell suspension was added to each well in a 48 well-plate. After 18 h, the cell media was replaced with the supplemented dissolution product from CuBGs and DMEM was used as control. At day 1, 3 and 7, the supernatant was collected for further analysis.

The metabolic activity of the cells in response to contact with the dissolution product from copper containing compositions was investigated at day 1, 3 and 7 using an AlamarBlue cell viability reagent following the protocol as described in Chapter 5.2.3.

Total DNA (tDNA) was quantified using the Hoeschst H332598 fluorescent dye according to manufacturer instructions (Total DNA, Sigma-Aldrich, UK) as described in Chapter 5.2.3.

Statistical significance

The statistical significance of the results was compared using a Kruskal-Wallis test followed by Dunn's Multiple Comparison was used to detect significance of each composition with respect to DMEM at each time point (n=3, * $p < 0.05$, ** $p < 0.01$, *** $p < 0.001$, **** $p < 0.0001$).

6.2.2. Cellular response to copper control solutions

This study is based on the outcome of the study outlined in Section 5.2.1, and aims to identify a concentration or a range of concentrations of copper which will produce a therapeutic effect on HDFs. Six copper concentrations were exposed to HDFs for a period of 7 days. AlamarBlue and tDNA studies were conducted on the cells at time points of 1 day, 3 days and 7 days.

1. ICP was used to check the copper concentrations of the copper controls produced.
2. The metabolic activity of the copper controls was ascertained to understand if any of the copper controls were toxic to the HDF and develop an idea of appropriate levels of copper for the bioactive glasses.
3. The tDNA of the copper controls was also assessed to understand how the copper levels affected the proliferation of the HDF.

The copper control concentrations were produced by dissolving weighed quantities of copper chloride in DI water and producing a solution with a 20 mM concentration. Quantities of this solution, were then added to DMEM producing copper control solutions of 6 mg L^{-1}, 3 mg L^{-1}, 2 mg L^{-1}, 1.2 mg L^{-1} and 0.6 mg L^{-1}.

ICP-AES Analysis

ICP-AES was used to determine the actual concentration of copper in the control solutions produced to compare with the nominal values used to produce the controls. This was useful in ensuring the correct concentration of copper ions were achieved. The protocol was followed exactly as described in Chapter 4.2.5. Standard solutions were produced diluted in 2 mol. nitric acid as the samples. A standard curve was produced at wavelengths of 317.9 nm (Ca), 251.6 nm (Si) and 324.7 nm (Cu) for 1 mg L^{-1}, 2 mg L^{-1}, 5 mg L^{-1}, 10 mg L^{-1}, 20 mg L^{-1} and 40 mg L^{-1}. The copper controls were then placed directly into an inductively coupled plasma-atomic emission spectrometer (ICP-AES).

Cell Studies

The cell studies were carried out as described in Chapter 5.2.3.

Metabolic activity

The metabolic activity of the cells in response to contact with the dissolution product from copper control solutions was investigated at day 1, 3 and 7. An AlamarBlue cell viability reagent was used to determine the metabolic activity exactly as described in Chapter 5.2.3.

Total DNA

The tDNA of the copper control solutions was quantified using the same protocol as described in Chapter 5.2.3.

Statistical significance

The statistical significance of the results was compared using a Kruskal-Wallis test followed by Dunn's Multiple Comparison was used to detect significance of each composition with respect to DMEM at each time point (n=3, * $p < 0.05$, ** $p < 0.01$, *** $p < 0.001$, **** $p < 0.0001$).

6.2.3. Assessing the therapeutic effect of copper containing bioactive glasses

The aim of the previous study outlined in Section 6.2.2 was to understand the impact of a range of copper concentrations on the metabolic activity and cell proliferation of HDFs. In the study presented in Section 6.2.3, the aim is to incorporate the selected concentrations of Copper into 3D electrospun 70S30C bioactive glass fibres via the sol-gel route described in Chapter 5.2.1. The copper precursor used was copper nitrate which was inserted into the sol-gel network as outlined in Chapter 6 Section 6.2.1. The relative humidity range was retained at between 30% - 55% as this produced the desired 3D structure in the compositions studied in Chapters 4 and 5. The electrospinning parameters are shown in *Table 14*.

The aim of this study is to conduct cellular studies on the dissolution product of the revised copper containing bioactive glasses. The metabolic activity and cell proliferation of the HDFs will be assessed as will the VEGF production at time points of day 1, day 3 and day 7.

1. ICP-AES will be used to determine the exact ion concentrations of silica, calcium and copper in the dissolution product of each of the copper containing bioactive glass samples listed in *Table 13*.
2. HDFs will be added to the dissolution product of each of the copper containing bioactive glass compositions and the metabolic activity and proliferation of the HDFs will be assessed using AlamarBlue and Total DNA analysis
3. A VEGF ELISA will be used to determine how each composition impacts the production of VEGF and provides an insight in the ability of each sample to stimulate angiogenesis.
4. A LIVE/DEAD™ test will be conducted to visually assess the HDFs cells at each time point.

Ion concertation study

ICP-AES was used to determine the actual concentration of copper, silica and calcium in the CuBGs and compare with the expected nominal composition. A lithium metaborate fusion was used for this following exactly the procedure outlined in Chapter 4.2.4. ICP-AES analysis was additionally used to determine the concentration of the silica, calcium and copper ions present in the dissolution product applied to the HDFs for the cellular studies. Here, 1 ml of each sample was placed in a 15 mL Falcon tube and then diluted with 4 ml of 2 mol. DI water (n=3). A standard curve was produced at wavelengths of 317.9 nm (Ca), 251.6 nm (Si) and 324.7 nm (Cu) for 1 mg L^{-1}, 2 mg L^{-1}, 5 mg L^{-1}, 10 mg L^{-1}, 20 mg L^{-1} and 40 mg L^{-1}.

Cell Studies

The cell studies were carried out as described in Chapter 5.2.3.

Metabolic activity and cell proliferation

The metabolic activity of the HDFs exposed to the dissolution product of copper containing bioactive glass fibres was assessed using an AlamarBlue cell viability reagent following the protocol outlined in Chapter 4 Section 4.2.3. The proliferation of the HDFs was assessed following a Hoeschst H332598 fluorescent dye kit at days 1, 3 and 7. The protocol is described in Chapter 5.2.3.

LIVE/DEAD Assay

A LIVE/DEAD cell viability assay was conducted to collect qualitative evidence of the appearance of the HDFs at each time point. It is used to determine cytotoxicity and viability of the cells through labelling the HDFs as live or dead with fluorescent dyes.

The dye for the LIVE/DEAD assay was prepared using 2.4 mL of PBS combined with 2.4 μL calcein (for the live cells) and 7.2 μL of Ethidium homodimer-1 (EthD-1) (for the dead cells).

For this assay, HDFs were harvested and suspended at a concentration of 20,000 cells per mL in parallel with the HDFs prepared for the metabolic activity and cell proliferation studies outlined above.

For each CuBGs condition and control condition, three cell wells were prepared with 500 μL of cell suspension (n=3). As with the metabolic activity study, three plates were prepared for each time point, one at 1 day, 3 days and 7 days. At the relevant time point, the cell supernatant was removed and replaced with 100 μL of the prepared dye. The plate was protected from the light with aluminium foil and was left at room temperature for 30 minutes. After 30 minutes the aluminium foil was removed and the cell wells were viewed on a microscope with a conventional fluorescein longpass filter. The same procedure was repeated for the other time points.

VEGF analysis

A Quantikine® ELISA kit was used to determine the amount of human vascular endothelial growth factor (VEGF) found in the HDF supernatant. The protocol was followed as described and outlined in Chapter 5.2.3.

Statistical significance

The statistical significance of the results was compared using a Kruskal-Wallis test followed by Dunn's Multiple Comparison was used to detect significance of each composition with respect to DMEM at each time point (n=3, * $p < 0.05$, ** $p < 0.01$, *** $p < 0.001$, **** $p < 0.0001$).

6. 3. Results and discussion

6.3.1. Preliminary study of copper containing fibres

Bioactive glass 70S30C samples were combined copper nitrate to produce Cu containing samples (CuBG) and were investigated for their potential as a material to be used in wound healing applications.

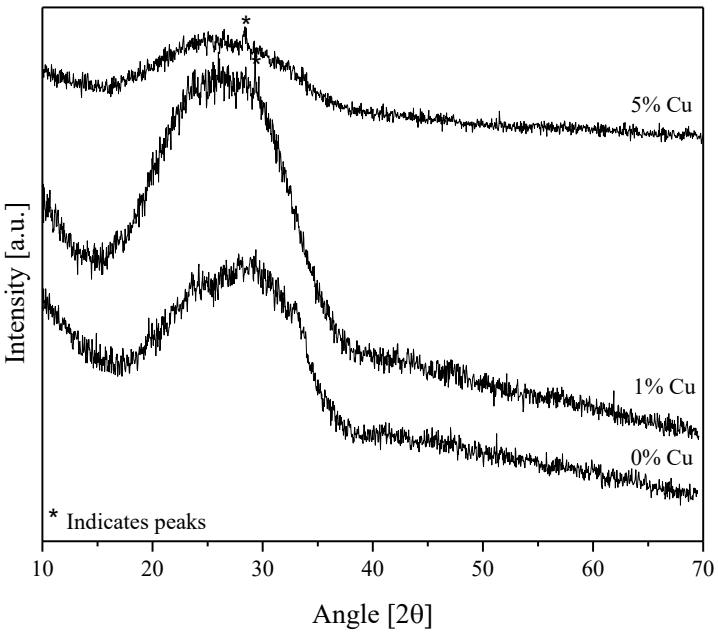


Figure 36. XRD patterns of 5% CuBG, 1% CuBG and 0% CuBG electrospun bioactive glass samples. (*) indicates possible peaks of copper nitrate but analysis carried out using PANalytical X'Pert HighScore plus software did not concretely provide any matches.

XRD patterns (*Figure 36*) of the 5% CuBG, 1% CuBG and 0%CuBG compositions all show amorphous silica halos. XRD patterns from sol-gel derived bioactive glass scaffolds containing 1, 2, and 3% copper by Wu *et al.,* [124] showed no peaks in XRD patterns. A possible peak on the 5% CuBG sample was identified at 29° however in repeats, this peak was not identified in subsequent 5% Cu samples. A possible peak at 31° was also identified in the 1% Cu sample, however this sample also contained a more noise and so peaks were more difficult to determine. Copper nitrate peaks can be identified at 2θ angles of 15°, 16°, 19°, 22°, 29°, 34° and 50° [230] suggesting that this peak at 29° could result from the copper nitrate precursor. A

very small peak can also be seen at 34° and 50° which also suggests the presence of copper nitrate in the 5% Cu sample, however due to the small size of the peak, it is difficult to determine if this is due to noise or if it is a peak. Analysis carried out using PANalytical X'Pert HighScore plus software did not concretely provide any solutions.

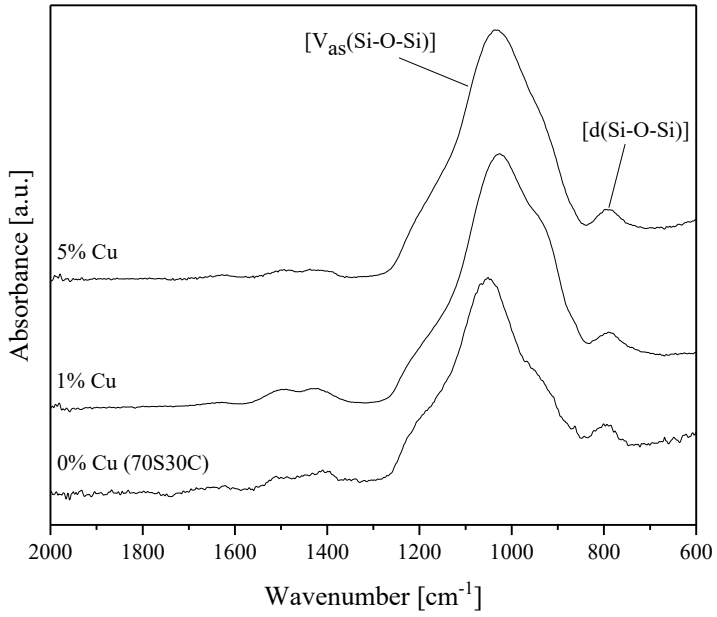


Figure 37. FTIR spectra of electrospun 5% CuBG, 1% CuBG and 0% CuBG bioactive glass compositions.

FTIR was used to analyse the bonding present in the fibres with different copper contents. *Figure 37* presents the FTIR spectra of the 5% CuBG, 1% CuBG and 0% CuBG compositions. All samples show bands at approximately ~1040 cm^{-1} and ~790 cm^{-1}, attributed to Si-O-Si. The Si-O stretch were found to be at wavenumbers of 1051 cm^{-1}, 1026 cm^{-1} and 1035 cm^{-1} for 0% CuBG, 1% CuBG and 5% CuBG samples respectively. The shift in the wavenumber of the main Si-O stretch is indicative of a change in the structure of the material, as copper is introduced, the Si-O-Si bonds become stretched to accommodate the presence of copper into the network. It was expected that the addition of 5% CuBG into the network would have resulted in a greater shift in the Si-O-Si band compared with 1% CuBG. However, the FTIR spectra shows that the 1% CuBG sample caused the greater shift in the Si-O-Si band. This unexpected result perhaps suggests a limit to the amount of Cu that can enter the glass network. The possible presence of copper

nitrate on some of the XRD samples showin in Figure 34 suggests that an amount of copper nitrate did not enter the glass network suggesting that a molecular weight of 5% Cu may be in excess of what can be incorporated into the 70S30C bioactive glass network The lithiutm metaborate study will be useful in determining the actual composition of the fibres indicating if Cu incorporation has taken place. It is difficult to draw conclusions from just two compositions, however by using additional analysis techniques such as XPS and additional copper containing samples with different quantities of copper incorporated, the relationship between the shift in wavelength of the Si-O-Si bands and the copper content of the bioactive glasses can be properly investigated. Analysis using XPS is discussed further in Chapter 7.

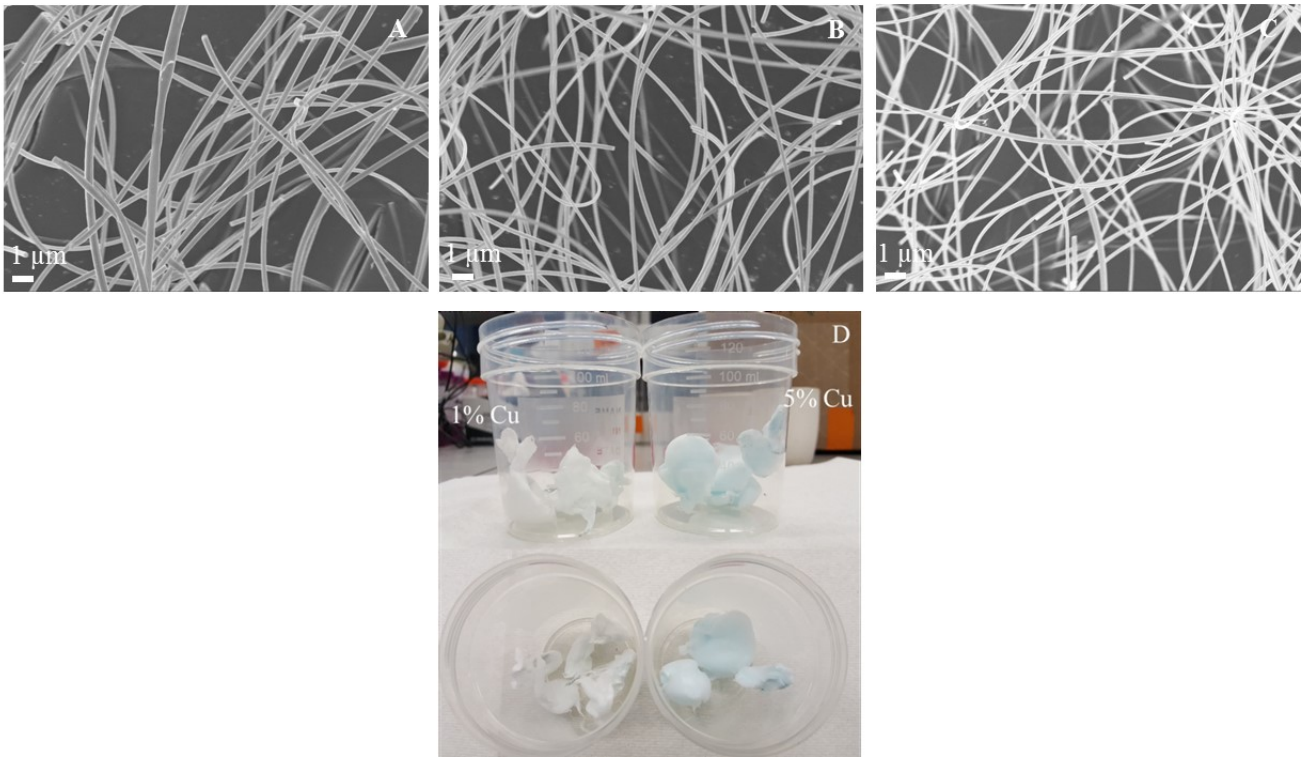


Figure 38. SEM images of electrospun bioactive glass fibres: (A) 5% CuBG, (B) 1% CuBG, (C) 0% CuBG; and (D) photographic images of the 5% CuBG and 1% CuBG 3D bioactive glass samples.

SEM images (*Figure 38A-C*) show long and uniform fibres in all three of the compositions. The photographic images of the 1% CuBG and 5% CuBG compositions show the 3D cotton-wool-like structure and presence of 5% Cu copper has coloured the 3D fibremat a characteristic blue hue, which can be observed throughout the sample (*Figure 33D*). The fibre diameter of the three compositions are outlined in *Table 17*. The average diameter of the fibres appears to increase slightly as copper is added into the glass

network which could be the result of Cu incorporation or even the presence of unremoved copper nitrate on the surface of the fibres. The standard deviation between the fibre diameters is very high, suggesting that there is no significant difference between the fibre diameters across the three samples.

Table 17. Electrospun sol-gel bioactive glass fibre diameter of 0% CuBG, 1% CuBG and 5% CuBG compositions

Sample	Fibre Diameter [μm]
0% CuBG (70S30C)	0.20 ± 0.05
1% CuBG (70S29C1Cu)	0.22 ± 0.04
5% CuBG (70S25C5Cu)	0.29 ± 0.05

Lithium metaborate was used to determine the actual compositions made, these can be seen in *Table 18*. All the CuBGs and controls produced the expected compositions which suggests that Cu was incorporated into the glass network fully.

Table 18. The actual compositions produced in molecular weight for the 0% CuBG, 1% CuBG and 5% CuBG compositions as determined by lithium metaborate analysis.

Sample	Composition [mol%]		
	SiO	CaO	CuO
0% CuBG	68.1 ± 0.2	31.9 ± 0.2	0.0 ± 0.0
1% CuBG	69.0 ± 0.1	29.4 ± 0.1	1.0 ± 0.0
5% CuBG	68.2 ± 0.1	24.8 ± 0.1	4.9 ± 0.0

Dissolution studies

The following dissolution studies compared the ion concentrations obtained for the different CuBGs compositions and aimed to determine if the quantity of copper in the bioactive glass samples impacted the

dissolution of silica and calcium species. The dissolution study in TRIS (*Figure 39*) shows similar calcium ion concentrations for the three CuBG samples over the 7 days, with the 0% CuBG producing a calcium ion concentration of 264.1 mg L^{-1}, the 1% CuBG sample 268.4 mg L^{-1} and the 5% CuBG sample 270.0 mg L^{-1}. The ion concentrations of silica was also similar for all three compositions at over the 7 days, the 0% CuBG sample released 64.6 mg L^{-1} , the 1% CuBG sample 64.2 mg L^{-1} and the 5% CuBG sample 81.3 mg L^{-1}. There is no evidence that the concentration of copper affected the ion concentration of silica or calcium ions present in the TRIS. The concentration of copper in TRIS corresponded, as expected, to the quantity of copper in the CuBG itself, with a higher quantity of copper in the CuBG creating higher concentration of copper: : ~0 mg L^{-1} for the 70S30C (0% CuBG) sample, 10.2 mg L^{-1} mM for the 1% CuBG sample and 78.9 mg L^{-1} for the 5% CuBG sample. This indicates that the presence of copper in the structure did little to effect the dissolution of the other ions. This is positive as the concentrations of silica and calcium ions in the 70S30C has previously been shown in Chapter 5.3.3 to have no significant effect on the metabolic activity and cell proliferation on HDFs when exposed to dissolution product.

The pH profile in TRIS shows (*Figure 40*) shows a higher pH in the 0% CuBG sample with a pH of 8.07 at the 7 day time point. The pH values for the 1% CuBG sample at 7 days is 8.0 and for the 5% CuBG sample 7.9 respectively. The pH values are very close, and as outlined in Chapter 4.2.5, the increase in pH [97] [198] are a result of the ion exchange between modifier cations, such as Ca^{2+}, and protons from the dissolution media [199]. During dissolution studies, changes in the pH provide an indication of the amount of ion exchange occurring [200] in the solution. The pH results could suggest that the presence of copper ions inhibit ion exchange but as the values are so close, it is unlikely to be due to this. Zheng *et al.,* [231] found that where copper ions were used as bioactive fillers for a gelatin coating on a bioactive glass scaffold, the addition of copper significantly improved the apatite forming ability of the scaffolds. *Figure 40* shows a reduction in pH across all samples at Day 3 before increasing again at Day 4 and plateauing to Day 7. The reduction in pH at Day 3 could be due to a change in the dissolution of samples at Day 3 either caused by the chemistry of the fibres themselves or due to an experimental error in the incubation of the fibres during the experimental process.

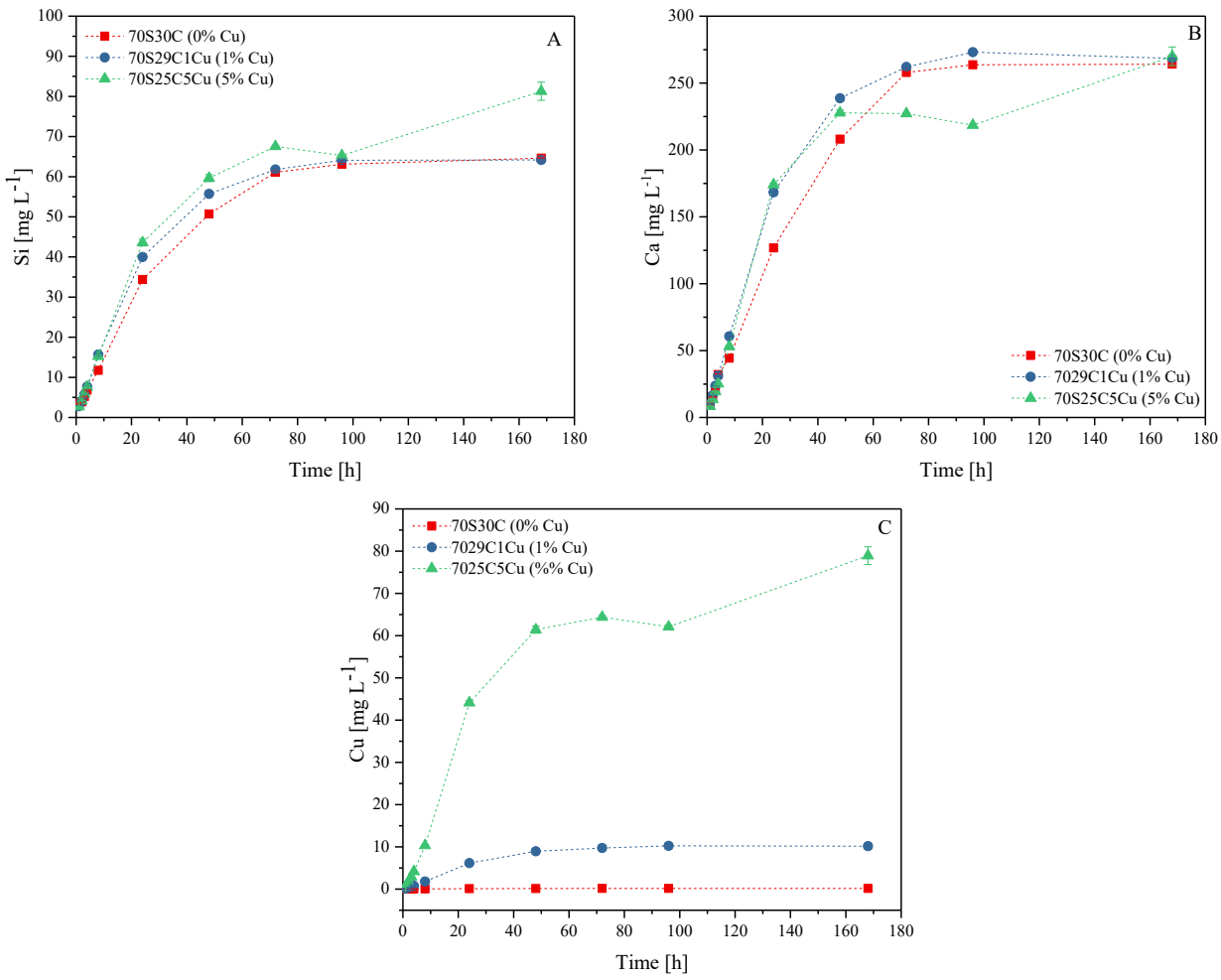


Figure 39. Dissolution profiles from ICP of electrospun sol-gel glasses in TRIS at time points of 1 h, 2h, 3h, 4h, 8h, 1 day, 2 days, 3 days, 4 days and 7 days of (a) Si [mg L^{-1}], (b) Ca [mg L^{-1}] and (c) Cu [mg L^{-1}]. TRIS was omitted as it was found to be at zero in each graph.

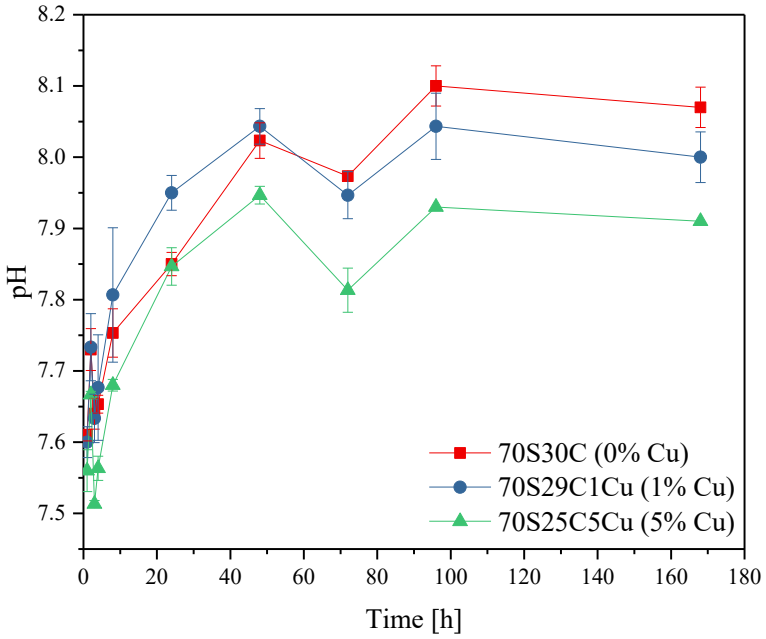


Figure 40. pH profiles of TRIS during the bioactive glass dissolution of the 0% CuBG, 1% CuBG and 5% CuBG samples.

The dissolution study in DMEM (*Figure 41*) shows the ion concentrations obtained from the 0% CuBG, 1% CuBG and 5% CuBG samples. The profile of ion concentration of silicon in DMEM was consistent with that in TRIS with a release of 63.2 mg L^{-1} for the 0% CuBG sample, 61.5 mg L^{-1} for the 1% CuBG sample and 63.9 mg L^{-1} for the 5% CuBG sample. The calcium profile in (*Figure 36B*) shows an ion concentration of 41.3 mg L^{-1} for the 0% CuBG sample, 70.4 mg L^{-1} for the 1% CuBG sample and 61.4 mg L^{-1} for the 5% CuBG sample at Day 7. The ion concentration in calcium was lower than that of the TRIS at this time point.. As with the 70S30C and 80S20C samples outlined in Chapter 4 (TRIS) and Chapter 5 (DMEM), here there was a difference in the concentration of calcium ions in TRIS compared with DMEM, but also a difference in the profile of the changes in ion concentration over time. With the samples in TRIS, the calcium ions show an initial ion concentration which plateaued after approximately 48 h. The same samples in DMEM showed a higher calcium concentration initially of approximately 68 mg L^{-1} across the three samples after 1 h, before dropping to a low of approximately 40 mg L^{-1} at 48 h and then increasing again at day 7. It is also important to consider that the DMEM itself contains calcium as well, so the concentration of calcium at each time point is made up of concentrations which have been released from the bioactive glass and that which is already contained in the DMEM dissolution media. Therefore it can

be difficult to quantify changes in the Ca ion concentrations in the media due to the dissolution of the fibres. Therefore it is key to measure the changes of other ion concentrations in the DMEM media. The ion concentrations of phosphorous were measured for this reason. Phosphorous has no presence in the bioactive glass compositions being investigated but it does have a presence in the DMEM. *Figure 41* shows a decrease in the ion concentration of Phosphorous similar to that observed with the Calcium ion concentrations. The phosphorous shows a sharp decrease over the 7 day study whereas the calcium ion concentration decreases in initially before increasing slightly and then plateauing, most probably due to the dissolution of the bioactive glass samples increasing the ion concentration of calcium. However, on balance, the fluctuation in the calcium ion concentration pattern (*Figure 41B*) is similar to that of the phosphorous levels (*Figure 41 D*), providing evidence of dissolution and precipitation of species in the media over the course of the 7 day study. Kulesz-Martin *et al.,* [220] has shown that the HDFs grew best at concentrations of 1.4 mM Ca^{2+} (~56 mg L^{-1}) In this case, all three of the samples are above this at the 4 h time point with the 0% Cu sample producing a Ca ion concentration of 69.7 mg L^{-1} at 4 h, the 1% Cu producing an ion concentration of 70.9 mg L^{-1} and 5% Cu at 74.5 mg L^{-1} at 4 hours.

The ion concentration of copper (*Figure 41C*) at the 7 day time point was 9.76 mg L^{-1} 1% CuBG and 0. 43.56 mg L^{-1} for 5% CuBG, with no concentration of copper present from the 0% CuBG sample. These results are similar to that in the TRIS study conducted showing that changes in the concentration of copper followed a similar, non-fluctuating rate in both media, indicating that the copper ions are not involved in the precipitation of species.

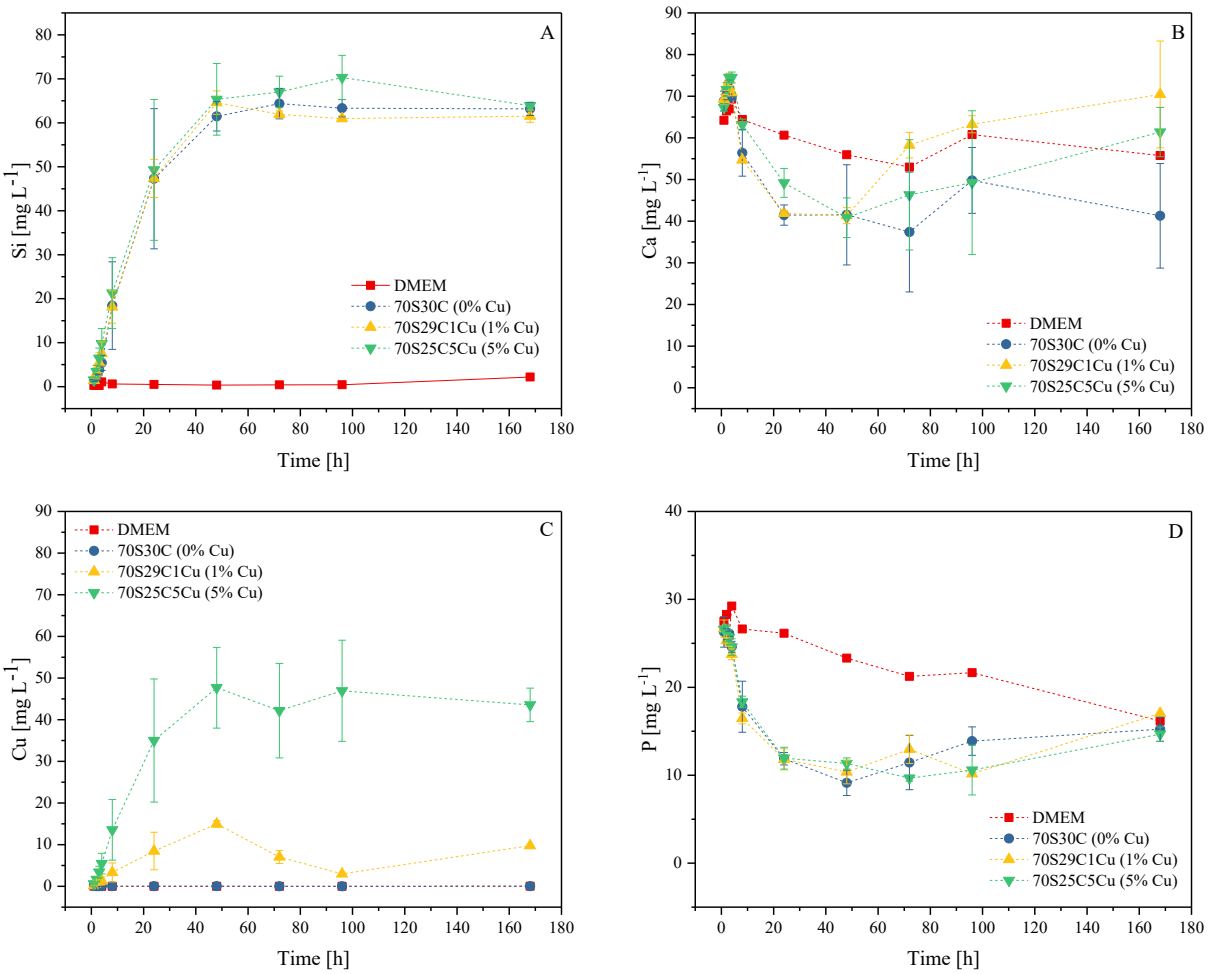


Figure 41. Dissolution profiles from ICP of electrospun sol-gel glasses in DMEM at time points of 1 h, 2 h, 3 h, 4 h, 8 h, 1 day, 2 days, 3 days, 4 days and 7 days of (A) Si [mg L^{-1}], (B) Ca [mg L^{-1}], (C) Cu [mg L^{-1}] and (D) P [mg L^{-1}].

Table 19. The ion release rate in mM at the 4 h time point from the dissolution study in DMEM.

	Ca [mg L^{-1}]	**Si [mg L^{-1}]**	**Cu [mg L^{-1}]**	**P [mg L^{-1}]**
0% Cu (70S30C)	69.68 ± 0.27	5.39 ± 1.71	0.02 ± 0.00	24.61 ± 0.62
1% Cu (70S29C1Cu)	70.90 ± 0.80	7.55 ± 2.64	1.36 ± 0.94	23.75 ± 0.61
5% Cu (70S25C5Cu)	74.49 ± 1.32	9.74 ± 3.47	5.46 ± 2.47	24.58 ± 0.94

Table 19 shows the ion concentrations at the 4 h time point, taken from *Figure 41*. *Table 19* shows concentrations of 1.36 mg L^{-1} copper for the 1% CuBG sample and 5.46 mg L^{-1} for the 5% CuBG sample. These results were used as a baseline to produce the copper and silica control samples used in the cell study. A copper control was made using copper chloride diluted in DI water at a concentration of 2.25 mg L^{-1} (0.04 mM) a value placed in between the 5% CuBG sample and the 1% CuBG sample. The silica control was made as described in Chapter 5.3.3, with the same concentration of 82.85 mg L^{-1}. This silica control value is much higher than the silica values quoted in *Table 19,* which show the silica and calcium values obtained for the 0% CuBG composition (70S30C) at the 4 h time point to be lower than those described in Chapter 5. The reduction in these values could be due to an unreliability in the ICP-read ion concentrations at 4 h despite a low standard deviation between repeats for silica and calcium ions, suggesting that the ion concentrations between samples may vary more than initially assumed.

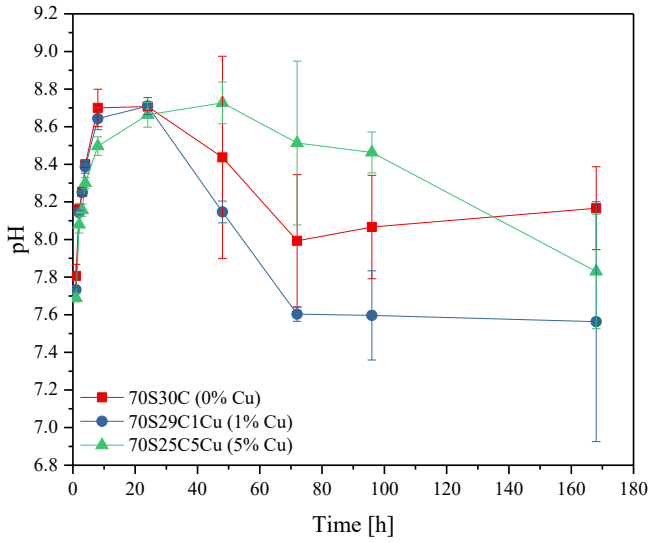


Figure 42. pH profile of DMEM during the bioactive glass dissolution of the 0% CuBG, 1% CuBG and 5% CuBG samples.

The pH profile in DMEM (*Figure 42*) shows a rapid increase in pH value for all samples in the first 24 h before decreasing again 7 days. The samples do not show a pattern of release as displayed in *Figure 40* of the pH profile of TRIS. This is perhaps because while dissolution is taking place (as evidenced from the dissolution study *Figure 41*), the exchange of ions taking is different here as the use of DMEM provides a different ion exchange between modifier cations such as Ca^{2+} and protons in the media.

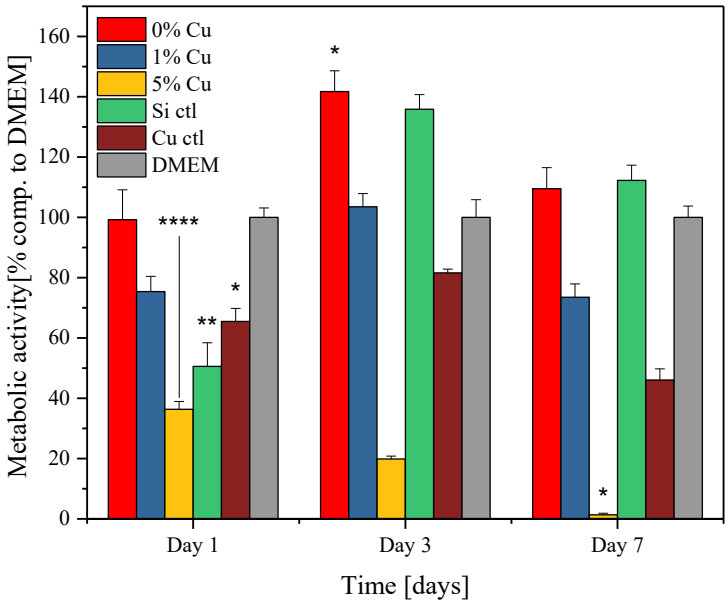


*Figure 43. The metabolic activity of the HDFs after immersion in the dissolution product of the 5% CuBG, 1% CuBG and 0% CuBG samples and Si, Cu amnd DMEM controls at day 1, day 3 and day 7. The metabolic activity is displayed as a percentage of the DMEM control. The 5% CuBG fibre composition inhibited the metabolic activity of HDF at day 1 and 7. A Krustal-Wallis test followed by Dunn's Multiple Comparison were used to determine statistical significance in the metabolic activity relative to the DMEM result of samples at each time point. (n=6, * P < 0.05, ** P < 0.01, *** P < 0.001, **** P < 0.0001).*

Figure 43 presents the metabolic activity of the HDFs exposed to the dissolution extracts as a percentage of the metabolic activity of the HDF cells exposed to DMEM control. Scaling the metabolic activities of the sample in relation to DMEM is useful for comparing differences between the samples across the 7 day study. The HDFs exposed to the 5% CuBG composition and the Si and Cu controls show a significant reduction in metabolic activity at day 1. According to the statistical analysis, the Day 3 result for 5% CuBG was not considered to be significant after the Dunn's multiple comparison but the Krustal-Wallis test indicated that one of the sample stochastically dominates another sample within the samples compared however, the Krustal-Wallis test does not identify where this stochastic dominance occurs. The result obtained is despite the HDFs showing a further reduced metabolic activity compared with day 1. The lack of significance is perhaps the result of an increase in the spread of the data at day 3, with the HDFs exposed

to the 0% CuBG, 1% CuBG samples and Si control showing an increase in metabolic activity (significantly so in the case of the 0% CuBG sample). The metabolic activities of all samples reduced at day 7 with the HDFs exposed to the 5% CuBG sample showing virtually no metabolic activity. These results indicate that the 5% CuBG sample was cytotoxic to the HDFs, and that both the Si and Cu controls caused some cytotoxic affects at day 1. While the 1% CuBG sample was not considered to significantly reduce the metabolic activity at day 7, it reduced the activity of the HDFs to approximately 50% of those exposed to the DMEM control.

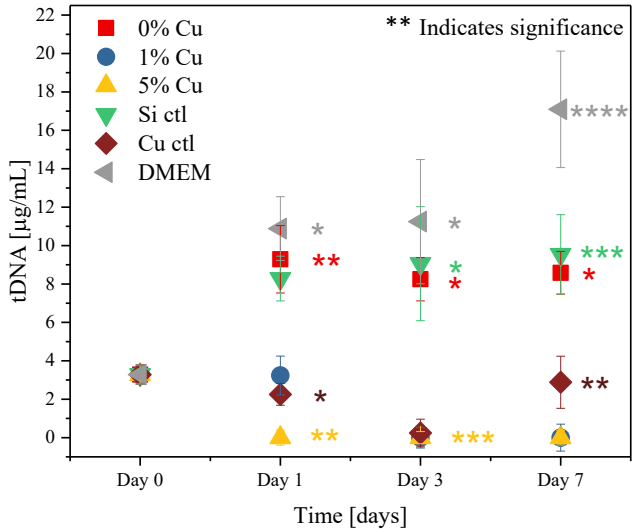


*Figure 44. The proliferation [µg/mL] of HDF cultures exposed to DMEM containing the dissolution products of the 5% CuBG, 1% CuBG and 0% CuBG samples, the Si and Cu controls and DMEM after 1 day, 3 day and 7 day. The 5% CuBG composition significantly inhibited the the proliferation of HDFs at day 1 and 3 indicating its cytotoxicity to HDFs. Statistical analysis was carried out via a Kruskal-Wallis test followed by Dunn's Multiple Comparison to detect significant changes in the proliferation of each composition with respect to the cell proliferation of HDFs at day 0, pre-exposed to the different conditions. (n=6, * P < 0.05, ** P < 0.01, *** P < 0.001, **** P < 0.0001).*

The tDNA data (*Figure 44*) shows changes in the proliferation of the HDFs in response to the different CuBGs and controls. The significance is calculated with respect to the proliferation of the HDFs at day 0 (before they were exposed to any of the bioactive glass or control conditions).

The 0% CuBG composition and the Si control had a similar effect to the DMEM control on the HDF proliferation at day 1 and day 3. They were both found to significantly increase the proliferation of HDFs compared with the pre-study result at day 0, and were found to increase proliferation with a similar significance to the DMEM. At day 7, the DMEM continued to increase the proliferation of HDFs, whereas the proliferation of the HDFs exposed to the 0% CuBG sample stayed at the day 3 level and the HDFs exposed to the Si control increased very slightly.

The 1% CuBG showed no significant change in HDF cell proliferation at day 1 compared with the pre-study value at day 0, and at day 3 reduced cell proliferation to zero. The 5% CuBG composition was also found to reduce the HDF proliferation to zero, this indicates that both these copper concentrations are cytotoxic to HDFs.

The Cu control has a copper concentration of 2.73 mg L^{-1}. This concentration was selected as an approximate mid-point between the copper concentration of the 1% CuBG sample and the 5% CuBG sample obtained at the 4 h time point of the dissolution study (*Figure 41*). *Figure 44* shows that both the 1% CuBG and 5% CuBG samples reduce the proliferation of HDFs, indicating that a concentration of 2 mg L^{-1} (0.03 mM) is cytotoxic. This is not the case with the Cu control which was designed to have a higher copper concentration of 2.25 mg L^{-1} (0.04 mM). The HDFs exposed to the Cu control appear to have a reduced metabolic activity at day 3 and then recover by day 7 where the cell proliferation increases slightly.

One possible explanation is that the presence of silica and calcium ions in the cytotoxic bioactive glass 5% CuBG and 1% CuBG samples contribute to the cytotoxicity of the HDFs. However, the results for the 0% CuBG composition (comprised of just calcium and silica ions) show positive cell proliferation and metabolic activity results at day 1, 3 and 7 and do not provide any evidence of cytotoxicity. This suggests that the presence of the silica and calcium ions do not have a negative effect on the tDNA, and therefore are unlikely to be causing the reduction in tDNA in the 1% CuBG and 5% CBGu samples.

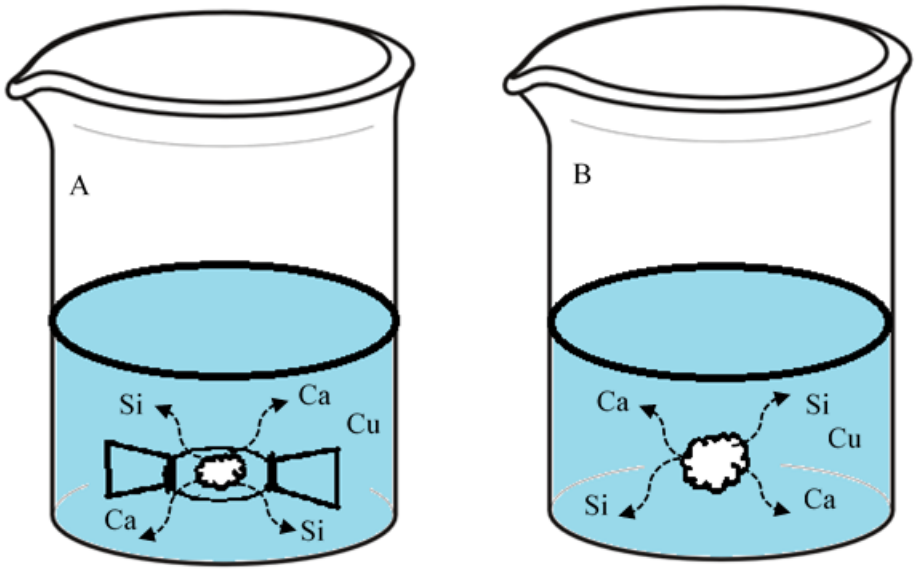


Figure 45. Diagram showing the difference in the dissolution setup between (A) the dissolution studies conducted over 7 days with samples taken over multiple time points (including at 4 h). The cellulose membrane is used to prevent accidental removal of fibres which have become loose (but have not fully dissolved) into the media. The cellulose membrane should allow full movement of ions into the dissolution product, and (B) the dissolution of fibres for cell studies. The fibres are removed after 4 h and the dissolution product is used directly onto the HDF cell lines. As only one time point is required, and the fibres are removed fully through filtering, no cellulose membrane is required.

A second explanation could be due to the actual concentration of copper obtained from the dissolution product of the 1% CuBG and 5% CuBG samples. When the ion concentrations from the dissolution product actually applied to cells was tested via ICP, the ion concentrations were found to be much higher than those obtained at the 4 h time point of the 7 day dissolution study. This may be explained by the difference in protocol and set up used to

The dissolution study and cell studies in DMEM in Chapter 5.3.2 showed a discrepancy between the actual ion concentrations at 4 h of samples used for cell studies and the ion concentration at the 4 h time point during the 7 day dissolution study. There is a difference in set up between the two studies which may explain the discrepancy in the ion concentrations obtained. The 7 day dissolution study, pictured in *Figure*

45A used a cellulose membrane to hold the fibres in position in the dissolution media and to prevent accidently removal of fibres at each time point when a sample of the dissolution media is removed, the cellulose membrane is commonly used in dissolution studies and is designed to allow the movement of ions through the membrane so that the release of ions from the samples is not effected. *Figure 45B* shows the setup of the dissolution product actually applied to the HDFs. Here, no cellulose membrane was used and at the set time point, the fibres are removed from the media through filtration.

Table 20. Comparison of the copper ion concentrations at 4 h of the dissolution study value using a cellulose membrane with that of the actual copper concentrations in the dissolution product used for HDF cell studies.

	Cu [mg L^{-1}] 4 h dissolution Study (with cellulose membrane)	Cu [mg L^{-1}] 4 h dissolution product (no cellulose membrane)
5 CuBG	5.46 ± 2.47	49.96 ± 0.59
1 CuBG	1.36 ± 0.94	12.08 ± 0.19

In the present study, the same observations can be made. *Table 20* shows a discrepancy in the ion concentrations of the 7 day dissolution study (setup pictured in *Figure 45A*) and that carried out for the cell studies (the setup depicted in *Figure 45B*). It can be assumed from both the study carried out in Chapter 5 and the one presented here that the use of the cellulose membrane reduces the number of ions present in the media. The copper concentration in the 5% CuBG sample (determined from ICP-AES using the setup in *Figure 45A*) was underestimated. The study conducted for the cellular studies showed that the copper concentration was in fact, much higher. This leads to a need to develop a revised range of copper concentrations to determine an accurate and favourable copper concentration which does not inhibit cell proliferation and metabolic activity.

6.3.2. Cellular response to copper control solutions

The previous study showed that the 5% CuBG bioactive glass composition significantly reduced the metabolic activity and proliferation of the HDF cell line. Six copper concentrations were chosen based on

the actual mg L^{-1} copper values outlined in *Table 20*. The 1% CuBG value was chosen as the most concentrated control as the metabolic activity and the tDNA study in *Section 6.3.1* showed this copper concentration to be cytotoxic to HDFs. *Table 21* outlines the compositions investigated and the equivalent actual ICP-AES results. The ICP-AES result for each composition show results similar to that of the designed compositions.

For the highest copper control concentration, a nominal concentration of 6 mg L^{-1} was selected, this is approximately 50% of the concentration used in the 1% CuBG sample in the previous study. This was selected at as the 1% CuBG displayed cytotoxicity in the TDNA at day 3 and 7. The other values were chosen to provide a range of concentrations to be tested.

Table 21. The compositions investigated and the actual copper compositions.

Nominal Cu-concentration	Actual Cu-concentration used of HDF study
6 mg L^{-1} (0.10 mM)	5.81 ± 0.04 mg L^{-1} (0.10 ± 0.00 mM)
3 mg L^{-1} (0.05 mM)	2.25 ± 0.04 mg L^{-1} (0.04 ± 0.00 mM)
2 mg L^{-1} (0.03 mM)	1.84 ± 0.02 mg L^{-1} (0.03 ± 0.00 mM)
1.2 mg L^{-1} (0.02 mM)	1.11 ± 0.01 mg L^{-1} (0.02 ± 0.00 mM)
0.6 mg L^{-1} (0.01 mM)	0.63 ± 0.01 mg L^{-1} (0.01 ± 0.00 mM)

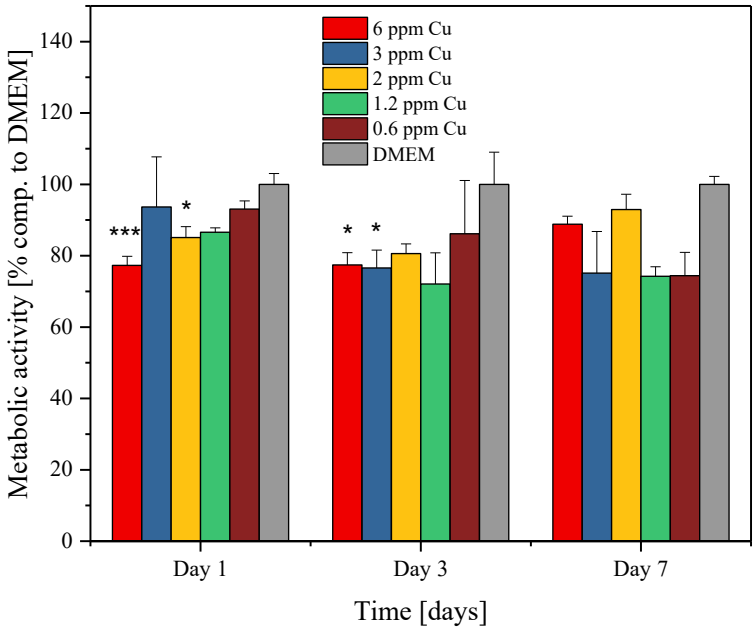


*Figure 46. The metabolic activity of the HDFs after exposure to copper concentrations for 1, 3 and 7 days. The metabolic activity is displayed as a percentage of the DMEM control. A Krustal-Wallis test followed by Dunn's Multiple Comparison were used to determine determine statistical significance in the metabolic activity relative to the DMEM result of samples at each time point. (n=6, * P < 0.05, ** P < 0.01, *** P < 0.001, **** P < 0.0001).*

The metabolic activity (*Figure 46*) shows a significantly reduced metabolic activity for the 6 mg L^{-1} copper control at day 1 and day 3. The 3 mg L^{-1} copper control and 2 mg L^{-1} copper control also showed significant decreases in metabolic activity at day 1 and day 3 respectively. At the 7 day time point, all the copper concentrations had a metabolic activity of over 70% of the metabolic activity of DMEM. This indicates that none of the samples had a significantly reduced metabolic activity over the course of the 7 days.

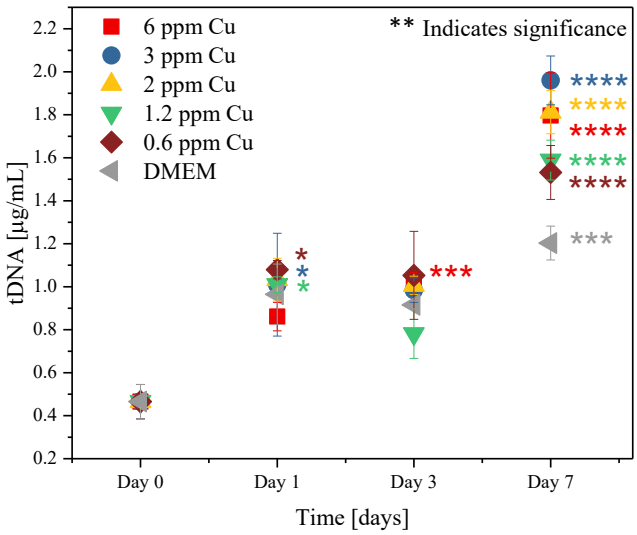


*Figure 47. The proliferation [µg/mL] of HDF cultures exposed to DMEM containing the copper controls and DMEM after 1 day, 3 day and 7 day. None of the copper inhibit the proliferation of HDFs at day 1, 3 or 7. Statistical analysis was carried out via a Kruskal-Wallis test followed by Dunn's Multiple Comparison to detect significant changes in the proliferation of each composition with respect to the cell proliferation of HDFs at day 0, pre-exposed to the different conditions. (n=6, * P < 0.05, ** P < 0.01, *** P < 0.001, **** P < 0.0001).*

All the copper concentrations and DMEM exposed to HDFs increased the proliferation of the cells compared with the pre-exposed proliferation at day 0. At day 1, the 0.6 mg L^{-1}, 1.2 mg L^{-1} and the 3 mg L^{-1} concentrations showed a significant increase in proliferation (*Figure 47)*. The 6 mg L^{-1} concentration showed a significant increase at day 3 and by day 7 all samples exhibited a significant increase compared with day 0. This suggests that all samples are within a copper concentration range which does not inhibit the proliferation of HDFs.

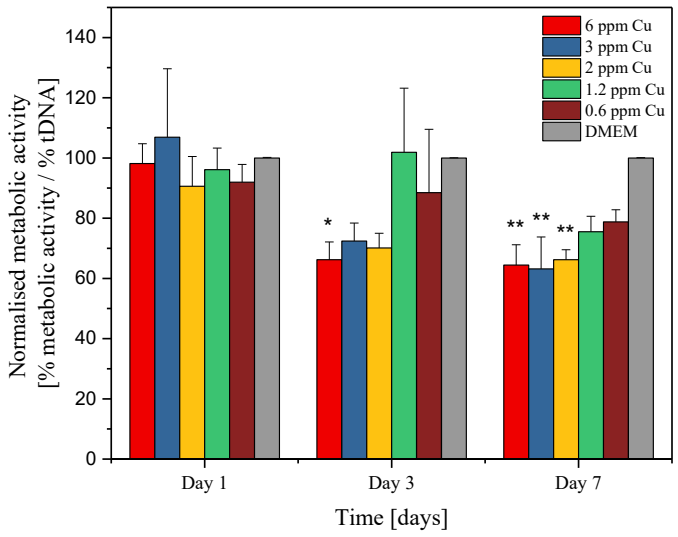


Figure 48. Metabolic activity of the HDFs normalised to cell number (tDNA). The metabolic activity as a percentage of DMEM was normalised to the tDNA as a percentage of DMEM at each time point. There is a significant reduction in the metabolic activity of the HDFs per cell at day 7 when exposed to copper controls containing 6 mg L^{-1} *at day 3 and 3* mg L^{-1} *and 2* mg L^{-1}. *A Krustal-Wallis test followed by Dunn's Multiple Comparison were used to firstly detect any statistical significance between each control and the DMEM at each time point.*

Metabolic activity per cell significantly reduced in the 6 mg L^{-1}, 3 mg L^{-1} and 2 mg L^{-1} Cu controls at day 7 (*Figure 48*), and at day 3 for the 6 mg L^{-1} sample. This indicates that HDFs struggle with copper concentrations of 2 mg L^{-1} over a 7 day period. Based on this, a number of copper concentrations were identified to be inserted into bioactive glasses to investigate the VEGF production of copper in 3D electrospun bioactive glass fibres. This indicates that the 1.2 mg L^{-1} and 0.6 mg L^{-1} concentrations are promising concentrations for copper in 3D fibrous bioactive glasses. These concentrations were investigated alongside higher ones (such as 6 mg L^{-1} and higher) in bioactive glass fibres to determine if higher concentrations encourage the production of VEGF in HDFs despite reducing metabolic activity per cell. For this reason, it will be interesting to investigate which concentrations yield the most promising results.

6.3.3. Assessing the therapeutic effect of copper containing bioactive glasses

The previous study assessed a range of copper concentrations between 0.6 mg L^{-1} and 6 mg L^{-1} and found concentrations in the range of 0.6 – 1.2 mg L^{-1} had no significant impact on the cytotoxicity or the proliferation of HDFs. Here, CuBG compositions were produced (*Table 20*) via the sol-gel and electrospinning routes outlined in Chapter 4 and 5.

Table 22. The bioactive glass compositions made via the sol-gel route.

Compositions	TEOS [mL]	Nitric Acid [mL]	Ethanol [mL]	$Ca(NO_3)_2•4H_2O$ [g]	$Cu(NO_3)2•6H_2O$ [g]
0% CuBG (70S30C)	7.2	1.7	3.7	3.2	0.00
0.1% CuBG (70S29.9C0.1Cu)	7.2	1.7	3.7	3.18	0.01
0.5% CuBG (70S25.5C0.5Cu)	7.2	1.7	3.7	3.15	0.03
1% CuBG (70S29C1Cu)	7.2	1.7	3.7	3.09	0.11

Three copper concentrations for the CuBGs were chosen based on the concentrations investigated in Section 6.3.2. The bioactive glass compositions were designed to have a specific concentration of copper ions at a 4 h time point (*Table 22*) to match the concentrations obtained in Section 6.3.3. The 1% CuBG value was chosen as the most concentrated control as the metabolic activity and the tDNA study in *Section 6.3.1* showed this copper concentration to be cytotoxic to HDFs, this was used to compare with the 0.5% CuBG and 0.1% CuBG compositions. Two copper concentrations were also produced using copper chloride through the method described in Section 6.2.1. They were chosen to have copper concentrations of 4 mg L^{-1} and 1.2 mg L^{-1} matching approximately the copper concentrations of the 0.5% CuBG sample and the 0.1% CuBG sample at 4 h dissolution in DMEM.

Table 23 shows the results of lithium metaborate fusion used to identify the actual composition of the revised CuBGs compositions produced. *Table 23* shows a breakdown of copper, calcium and silica percentage compositions similar to that in the nominal values outlined in *Table 22*

Table 23. The actual CuBG compositions as determined by lithium metaborate analysis.

	CaO [%]	CuO [%]	SiO_2 [%]
0 Cu %	31.9 ± 0.2	0.0 ± 0.0	68.1 ± 0.2
0.1 Cu %	33.0 ± 1.1	0.1 ± 0.0	66.9 ± 1.0
0.5 Cu %	42.5 ± 0.0	0.7 ± 0.0	57.3 ± 0.1
1 Cu %	29.4 ± 0.1	1.0 ± 0.0	69.0 ± 0.1
5 Cu %	24.8 ± 0.1	4.9 ± 0.0	68.2 ± 0.1

Table 24. Shows the release rate at 4 h of the bioactive glass compositions in mg L^{-1} and mM.

	Ca [mg L^{-1}]	Cu [mg L^{-1}]	P [mg L^{-1}]	Si [mg L^{-1}]
DMEM	59.08 ± 0.27	0.03 ± 0.02	28.14 ± 0.37	0.07 ± 0.06
0 Cu %	135.00 ± 0.44	0.15 ± 0.00	5.19 ± 0.03	70.07 ± 0.24
0.1 Cu %	52.27 ± 0.19	1.18 ± 0.02	6.57 ± 0.05	71.62 ± 0.30
0.5 Cu %	118.85 ± 0.65	4.63 ± 0.07	8.18 ± 0.13	74.38 ± 1.34
1 Cu %	129.50 ± 1.00	13.20 ± 0.12	4.25 ± 0.07	84.67 ± 0.82
5 Cu %	112.1 ± 0.00	49.18 ± 0.59	4.42 ± 0.32	67.85 ± 0.60
	Ca [mM]	Cu [mM]	P [mM]	Si [mM]
DMEM	1.47 ± 0.01	0.00 ± 0.00	0.91 ± 0.01	0.00 ± 0.00
0 Cu %	3.37 ± 0.01	0.00 ± 0.00	0.17 ± 0.00	2.49 ± 0.01
0.1 Cu %	1.30 ± 0.00	0.02 ± 0.00	0.21 ± 0.00	2.55 ± 0.01
0.5 Cu %	2.97 ± 0.02	0.07 ± 0.00	0.26 ± 0.00	2.65 ± 0.05
1 Cu %	3.23 ± 0.02	0.21 ± 0.00	0.14 ± 0.00	3.01 ± 0.03
5 Cu %	2.80 ± 0.00	0.77 ± 0.00	0.13 ± 0.00	2.42 ± 0.00

The bioactive glass sample release rates at 4 h (*Table 24*) show that the 0.1% CuBG composition released 1.18 mg L^{-1} copper, which was similar to the 1.2 mg L^{-1} copper control sample in Section 6.3.2 that was shown not to inhibit the metabolic activity or the cell proliferation of the samples. The 0.5% CuBG sample was chosen at it released 4.73 mg L^{-1}, which was between the 6 mg L^{-1} and 5 mg L^{-1} copper concentrations, studied in Section 5.3.2, that displayed some evidence of cytotoxicity to the HDFs. This particular composition was chosen to determine whether VEGF production of the HDF cells would increase, despite some cytotoxicity to the cells.

The metabolic activity results (*Figure 49*) show a significantly reduced a metabolic activity for the HDFs exposed to the 1% CuBG and 0.5% CuBG samples at day 1 and day 7. A reduced metabolic activity was also observed in the 4 ppm (0.5% Cu-ctl) control sample. These values are expected given the findings in Section 6.3.1 and Section 6.3.2, which showed these concentrations to inhibit metabolic activity of HDFs.

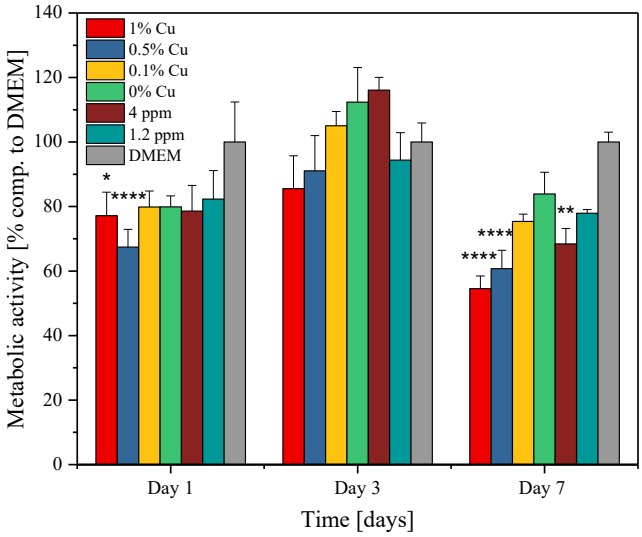


*Figure 49. The metabolic activity of the HDFs after immersion in the dissolution product of the 1% CuBG, 0.5% CuBG, 0.1% CuBG and 0% CuBG samples,Cu and DMEM controls at day 1, day 3 and day 7. The metabolic activity is displayed as a percentage of the DMEM control. The 1% CuBG and 0.5% CuBG fibre compositions inhibited the metabolic activity of HDF at day 1 and 7. A Krustal-Wallis test followed by Dunn's Multiple Comparison were used to determine statistical significance in the metabolic activity relative to the DMEM result of samples at each time point. (n=6, * P < 0.05, ** P < 0.01, *** P < 0.001, **** P < 0.0001).*

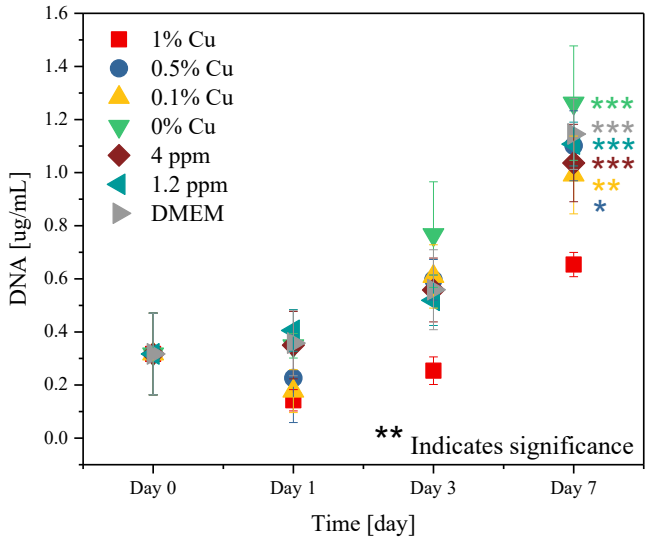


*Figure 50. The proliferation [µg/mL] of HDF cultures exposed to DMEM containing the dissolution products of the 1% CuBG, 0.5% CuBG, 0.1% CuBG and 0% CuBG samples, the 1.2 mg L^{-1} and 4 mg L^{-1} Cu controls and DMEM after 1 day, 3 day and 7 day. The 1% CuBG sample was the only sample not to exhibit a significant increase in proliferation of the HDFs at day 7. Statistical analysis was carried out via a Kruskal-Wallis test followed by Dunn's Multiple Comparison to detect significant changes in the proliferation of each composition with respect to the cell proliferation of HDFs at day 0, pre-exposed to the different conditions. (n=6, * P < 0.05, ** P < 0.01, *** P < 0.001, **** P < 0.0001).*

The 1% CuBG sample did not show a significant increase in cell proliferation at day 7 compared with day 0 (*Figure 50*). The proliferation of the HDFs increased as the quantity of copper in the bioactive glasses was reduced (the 0.5% CuBG sample had a significance at day 7 of $p < 0.05$ compared with the 0% CuBG sample which had a significance at day of $p < 0.001$). *Figure 50* shows that the 0% CuBG sample caused the highest proliferation of HDFs at day 3 and day 7.

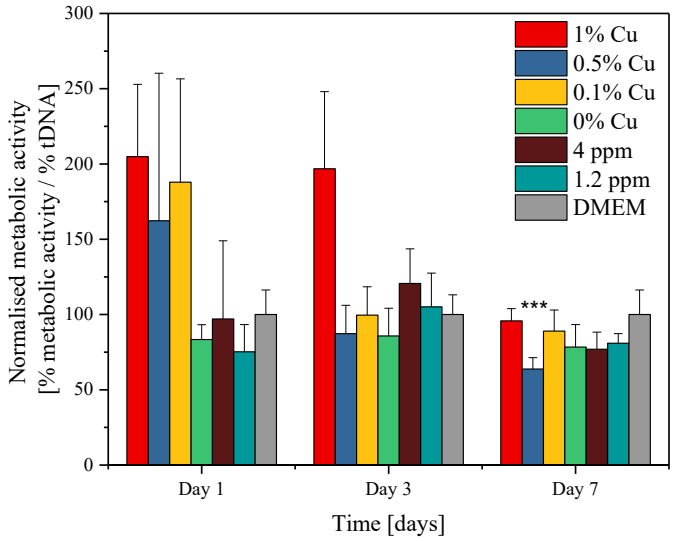
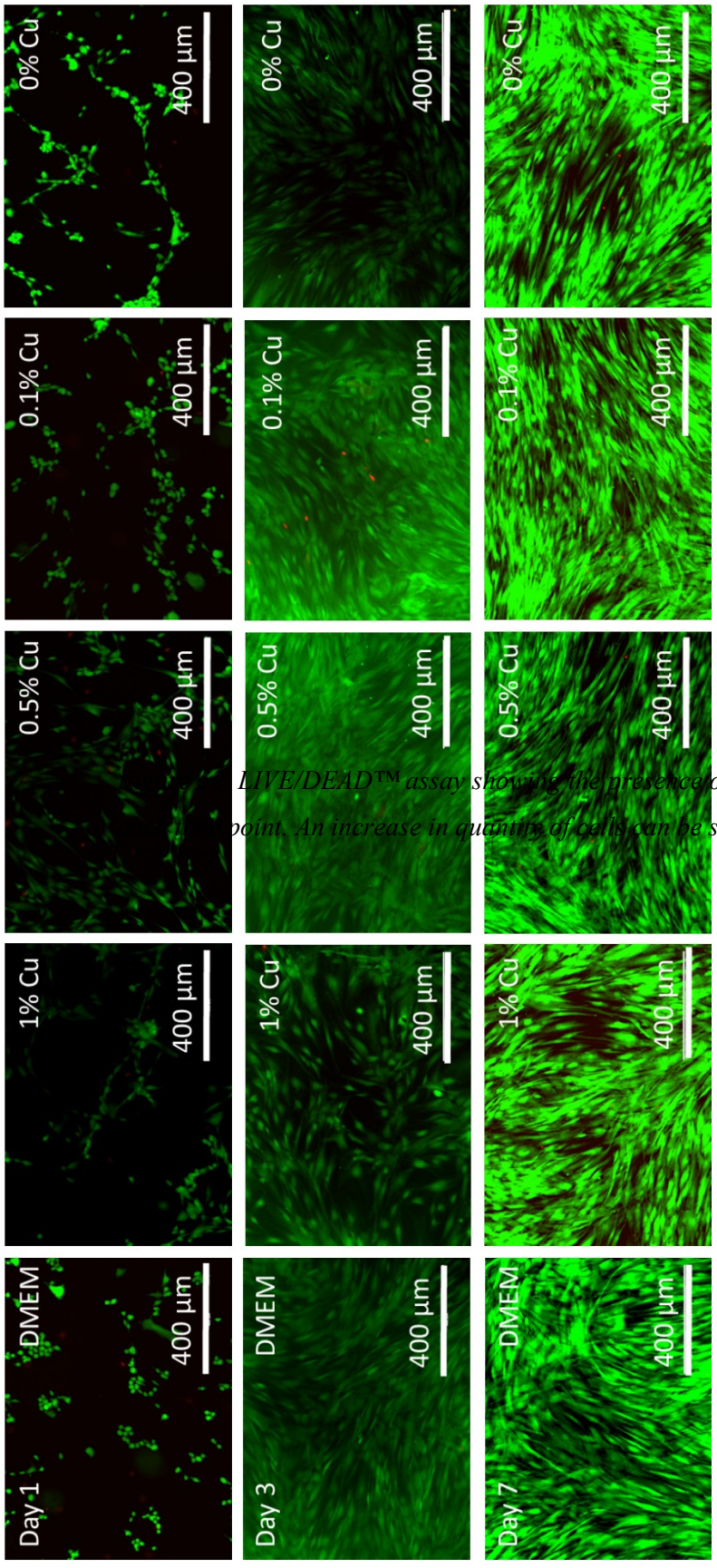


*Figure 51. Metabolic activity of the HDFs normalised to cell number (calculated as percentages with respect to DMEM). The normalised metabolic activity of HDFs immersed in the 0.5% CuBG bioactive glass dissolution product was considered to be significantly reduced compared to DMEM at day 7. A Krustal-Wallis test followed by Dunn's Multiple Comparison were used to detect any statistical significance between each control and the DMEM at each time point. (n=6, * P < 0.05, ** P < 0.01, *** P < 0.001, **** P < 0.0001).*

The metabolic activity per cell (*Figure 51*) was increased in HDFs exposed to the 1% CuBG sample at day 1 and day 7 although this was not statistically significant. The metabolic activity (*Figure 49*) showed no significant difference in HDFs at Day 3 and showed a significant decrease in metabolic activity at day 1 and day 7 compared with the DMEM controls at the respective time points. The tDNA results showed a reduced cell proliferation at each day compared with the other samples and controls, however this was not considered to statistically significant. This results in (*Figure 51*) an increase in metabolic activity per cell at Day 1 and Day 3 relative to the DMEM at Day 1 and Day 3

The LIVE/DEAD assay showed qualitatively the increase in HDFs at each time point for cells exposed to each of the bioactive glass samples. *Figure 52* shows that all compositions expressed an increase in HDFs present at each time point. The 1% CuBG show marginally fewer HDFs at Day 3 compared to that of the DMEM control, the 0% CuBG, 0.5% CuBG and the 0.1% CuBG compositions



LIVE/DEAD™ assay showing the presence of Live (green) and dead (red) cells for each bioactive g

point. An increase in quantity of cells can be seen at each time point for each composition.

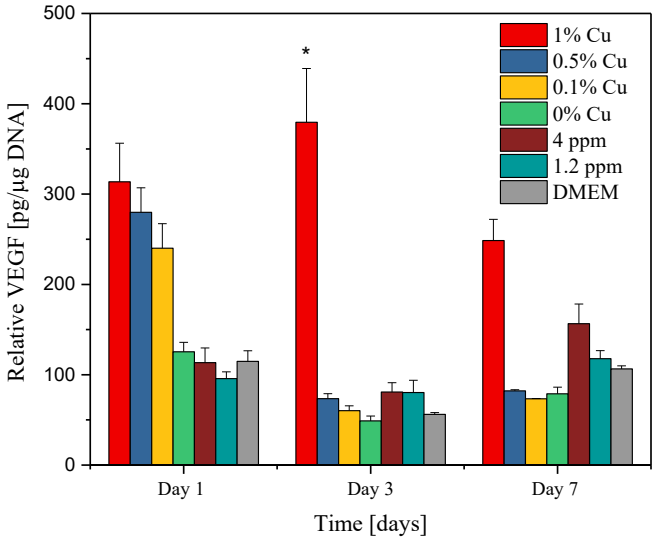


Figure 53. Normalised VEGF production [pg/µL] of HDF cultures exposed to DMEM containing the dissolution products of bioactive glass glasses 1% CuBG, 0.5% CuBG, 0.1% CuBG and 0% CuBG and controls in DMEM, 1.2 mg L^{-1} *and 4* mg L^{-1} *Cu at 1 day, 3 day and 7 day normalised to tDNA [µg/mL]. A Kruskal-Wallis test followed by Dunn's Multiple Comparison was used to detect statistical significance of each composition with respect to DMEM at each time point (+n=3, * p < 0.05, ** p < 0.01, *** p < 0.001, **** p < 0.0001).*

The exposure of HDF cells to the DMEM media conditioned in the 1% CuBG (ion concentration of 13.2 mg L^{-1} or 0.21 mM) bioactive glass fibre composition showed an increase in the VEGF production normalised to cell number at day 1, 3 and 7 compared to that of DMEM (*Figure 53*), although this was only found to be statistically significant at day 3. The 0.5% CuBG and 0.1% CuBG samples were additionally found to be higher than DMEM at day 1 however, they did not produce a statistical difference in the production of VEGF. The copper controls did not produce a quantity of VEGF that could be considered statistically significant; however the VEGF production of the 4 mg L^{-1} control sample was higher when compared with the DMEM control at day 7. The 0% CuBG sample caused no significant change in the normalised VEGF, this was similar to the result for 70S30C obtained in Chapter 5.3.3. The results also both show a decrease in VEGF at day 3 before increasing to day 7. These results confirm that while the 70S30C fibres do not have a negative impact on the VEGF, they are not causing the significant increase in normalised VEGF, this must be the result of copper.

5.4. Concluding remarks

The 1% CuBG and 5% CuBG compositions were produced and electrospun according to the parameters outlined in Chapter 4. The initial objectives of this Chapter were to ascertain the physical and chemical impact of additions of copper into the 3D bioactive glass fibres. The morphology of the fibres were investigated with SEM and simple chemical characterisation was undertaken using FTIR and XRD. SEM was additionally used to measure the fibre diameters, which were found to be in the range of 0.20-0.29 μm which is similar to the 70S30C/80S20C samples (0.21 – 0.34 μm) and smaller than Poologasundarampillai *et al* [7]*., (*1.5 ± 0.4 μm) and Obata *et al.,* [175] who produced fibres of 10-20 μm in diameter. XRD analysis showed amorphous peaks similar to that of the 70S30C structure and FTIR spectra showed shifts in the wavenumbers of the main Si-O-Si band with the insertion of copper ions into the bioactive glass structure.

Dissolution studies were carried out in TRIS and in DMEM at 1 h, 2 h, 3 h, 4 h, 8 h, 1 day, 2 days, 3 days, 4 days and 7 days. The study showed that the ion concentration in TRIS was similar for silica and calcium ions but a 1.2 mM ion concentration of copper ions was observed for the 5% CuBG sample compared with a 0.1 mM ion concentration at the 7 day time point for the 1% CuBG sample. The dissolution study carried out in DMEM showed a similar initial ion concentration for the silica ions but a higher initial ion concentration of calcium ions for both the CuBGs, as with the TRIS study, the release rate of copper ions was greatest in the 5% CuBG sample.

The study highlighted discrepancies between ion concentration in the 7 day dissolution studies and the actual ion concentration results obtained for each of the compositions when the dissolution product for the cell studies were produced. The results from the 7 day dissolution study at 4 h are lower compared with that of the ion concentration of each copper composition used for the cell studies. This discrepancy is believed to be due to the use of cellulose membrane during the 7 day dissolution study, which is used to contain and prevent accidental removal of fibres during the study, but it is believed to have also prevented the natural dispersion of ions through into the DMEM media. This highlights possible inaccuracies in the numerical value of ion release of all samples in both the TRIS and DMEM studies, however these dissolution studies are still useful in displaying the general trends of the and changes in the ion concentrations over time.

The cell studies with HDFs cell lines were a first step in determining if the 5% CuBG and 1% CuBG compositions affected the metabolic activity and the proliferation of the HDFs cells. The results showed that the metabolic activity of the 5% CuBG sample was significantly impeded at each of the time points.

The proliferation of the HDFs was also impeded by the 5% CuBG sample to the extent where 0 µg/mL was obtained at day 1, 3 and 7 of the study. The 1% CuBG composition also showed cytotoxicity towards the HDFs at day 3 where the cell proliferation was observed to be at 0 µg/mL. This evidence suggests that both the 5% CuBG and 1% CuBG were cytotoxic to the HDFs and therefore a new range of copper concentrations for use in bioactive glass fibres needed to be investigated.

The second study presented in this Chapter focuses on determining a new range of copper concentrations which do not inhibit the metabolic activity and the cell proliferation of the HDFs. The desired copper concentrations (between 0.6 mg L^{-1} and 6 mg L^{-1}) were made up using copper chloride and their actual copper concentrations were determined by a lithium metaborate study. The actual copper concentrations were found to be close to the nominal concentrations in each of the samples. The metabolic activity and cell proliferation analyses indicated that the 3 mg L^{-1} copper control sample maybe the optimum concentration of copper. The study found concentrations in the range of 0.6 – 1.2 mg L^{-1} had no significant impact on the cytotoxicity or the proliferation of HDFs.

The final study presented here focuses on the incorporation of revised copper concentrations into bioactive glasses. Three copper containing compositions were chosen: 0.1% CuBG and 0.5% CuBG (from the range of samples identified in the second study which did not inhibit the metabolic activity and cell proliferation) and 1% CuBG which, as determined in the first study presented in this Chapter, presents evidence of cytotoxicity to HDFs. The metabolic activity and cell proliferation tests were repeated and similar results to what had been determined in the first and second study for each of the CuBGs were presented. A VEGF ELISA was conducted on the revised CuBGs and the 1% CuBG was found to have the highest VEGF production of all samples and controls and produce a significant increase in VEGF at day 3 compared with DMEM. The reduced proliferation (although not significantly reduced) and reduced metabolic activity of the 1% CuBG sample coupled with the increase in VEGF production is unexpected. LIVE/DEAD was used as a technique to image the cells and look for cell death. Evidence of extensive cell death could suggest that the increase in VEGF detected is the result of HDFs leaching VEGF into the dissolution product. However, the LIVE/DEAD images show no evidence of extensive cell death, therefore the 1% CuBG sample is producing higher quantities of VEGF per cell.

This study provides evidence that copper-doped 70S30C compositions increase the production of VEGF per cell in HDFs. The 1% CuBG compostion shows that a concentration of 13.20 ± 0.12 mg L^{-1} or 0.21 ± 0.00 mM is sufficient to induce VEGF production in HDFs. This result is below the concentrations determined for hBMSCs of 152.7 mg L^{-1} (2.40 mM) [126] which display a similar trait in a reduction in cell proliferation but an increase in VEGF production. It is however a higher concentration to that obtained

in the study conducted by Bejarano *et al.* [125] which found 0.08 mM concentrations were toxic to SaOS-2 cells. These comparisons suggest that the cytotoxicity is very dependent on cell type.

CHAPTER SEVEN

THE CHEMICAL CHARACTERISTAION OF COPPER IN BIOACTIVE GLASSES

7.1. Introduction

A basic understanding of how the addition of copper ions impacts the structure of the bioactive glasses was outlined in Chapter 6.2.1. XRD and FTIR analysis of the 5% CuBG and 1% CuBG compositions showed that copper was successfully incorporated into the bioactive glass. Metabolic activity and cell proliferation studies identified a concentration of copper ions which significantly increased the VEGF production of HDFs, highlighting the wound healing potential of bioactive glass fibres.

In this chapter, XPS, FTIR and NMR studies are presented which aim to provide an insight into how copper incorporation affects the atomic structure of the bioactive glasses. The open structure of the silica glass enables copper to enter and disrupt or modify the glass network, leading to the formation of non-bridging oxygens [191]. These non-bridging oxygens are important as they control the ability and the rate at which the glass dissolves which impacts the bioactivity of the material [192]. While the dissolution and the bioactivity of copper containing bioactive glasses have been shown and proven in Chapter 6.2.1, this chapter presents an investigation into the bonding configuration, identification of the non-bridging oxygen groups and the state in which copper presents itself in the 3D bioactive glass fibres containing copper.

7.2. Methods and materials

The bioactive glass fibres were produced as described in Chapter 4 with the additions of copper, the compositions analysed are shown in *Table 25*.

Table 25. The sol-gel compositions and the quantities of TEOS, nitric acid, ethanol, calcium nitrate and copper nitrate used.

Compositions	TEOS [mL]	Nitric Acid [mL]	Ethanol [mL]	$Ca(NO_3)_2 \cdot 4H_2O$ [g]	$Cu(NO_3)_2 \cdot 6H_2O$ [g]
0 Cu	7.2	1.7	3.7	3.2	0.00
0.1 Cu	7.2	1.7	3.7	3.18	0.01
0.5 Cu	7.2	1.7	3.7	3.15	0.03
1 Cu	7.2	1.7	3.7	3.09	0.11
5 Cu	7.2	1.7	3.7	2.67	0.55

The bioactive glass sol-gels were electrospun as described in Chapter 4.

The following techniques were used to investigate the structure of the bioactive glass fibres produced:

1. FTIR was conducted to identify any changes in the structure of the material such as changes in Si-O-Si vibrational modes as a result of introducing copper into the bioactive glass composition. FTIR analysis was carried out on the 0.1% CuBG and 0.5% CuBG and these results were combined with those obtained in Chapter 5 for 1% CuBG, 5% CuBG and 0% CuBG.
2. XPS analysis was conducted on all samples. High resolution spectra was obtained for Cu 2p, Si 2p, Ca 2p, O 1s, N 1s and C1s. XPS analysis was used to define the state of the copper within the bioactive glass structure and to determine if copper incorporation affects the shape, intensity or the binding energies of the peaks obtained for the other elements within the glass network.

3. NMR was used to measure the atomic and chemical structure of the bioactive glass compositions doped with copper. The effect of the doping on the network connectivity of the glass was also investigated.

7.2.1. Fourier-transform infrared spectroscopy (FTIR)

FTIR was carried out as described in Section 4.2.3 on the revised copper containing samples 0.1 %, 0.5 %, 1 % and 0 % Cu. Results from the Section 6.3.1. Preliminary study will be viewed alongside to determine a shift in the Si-O-Si band as a result of the increase in copper content.

7.2.2. X-ray photoelectron spectroscopy (XPS)

XPS was performed as described in Chapter 4.2.3. A survey scan of each composition was initially carried out to show the typical expected XPS spectra for the elements contained within the bioactive glass samples. This was followed by high resolution core-level XPS scans which was performed for Si 2p, O 1s, Ca 2p and Cu 2p and were evaluated using Advantage XPS software. Any additional shifts in the spectra were corrected using the Carbon core line (C 1s) which is found at a binding energy of 285.0 eV. Information regarding the pass energy and dwell time can be found in *Table 24*.

Table 26. The parameters use for the high resolution XPS scans.

	Pass Energy [eV]	Scan No.	Dwell Time [s]	Binding Energy [eV]		Energy Steps
				Start	End	
Si 2p	20.00	20	50	95	110	0.1
C 1s	20.00	20	50	279	298	0.1
Ca 2p	20.00	20	50	335	360	0.1
N 1s	20.00	20	200	390	415	0.1
Cu 2p	20.00	20	200	925	970	0.1
O 1s	20.00	20	50	520	540	0.1

7.2.3. Solid-state ^{29}Si magic angle spinning-nuclear magnetic resonance (29Si MAS-NMR)

^{29}Si MAS NMR was used to identify the Q^n species in the copper containing bioactive glass samples which was useful in defining the bioactive glass network. NMR was carried out as described in Chapter 5.2.1.

7.3. Results and discussion

7.3.1. Fourier-transform infrared spectroscopy (FTIR)

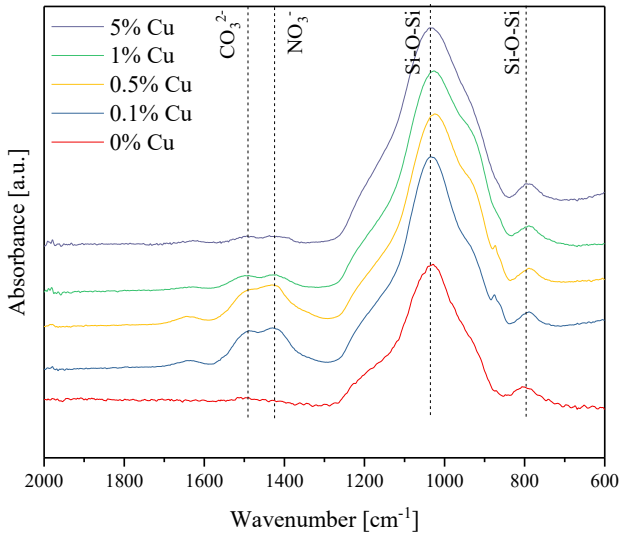


Figure 54. FTIR absorbance spectra of the copper containing bioactive glasses samples 0% Cu, 0.1% Cu, 0.5% Cu, 1% Cu and 5% Cu.

*Figure 54*shows the FTIR spectra for the four copper containing bioactive glass compositions and 70S30C (0% CuBG) glass fibres. The bands from 1020 cm^{-1} and 1040 cm^{-1} can be assigned to Si-O-Si along with the band at ~800 cm^{-1}. The peaks at ~1500 cm^{-1} and 1420 cm^{-1} in some samples refer to CO_3^{2-} and NO_3^-. The peaks present at ~900 cm^{-1} in the 0.5% CuBG and 0.1% CuBG samples could not be identified. There are no major differences in the CuBG samples compared to that of the copper-free 0% CuBG sample. However, the non-bridging oxygen band identified at ~930 cm^{-1} in all samples [191] changes in intensity with changes in the copper concentration. Hoppe *et al.,* [232] identified this in copper doped 45S5 samples but found that the Si-O_{NBO} peak decreased in intensity with an increase in copper content. In this present study this is not clear.

7.3.2. X-Ray photoelectron spectroscopy (XPS)

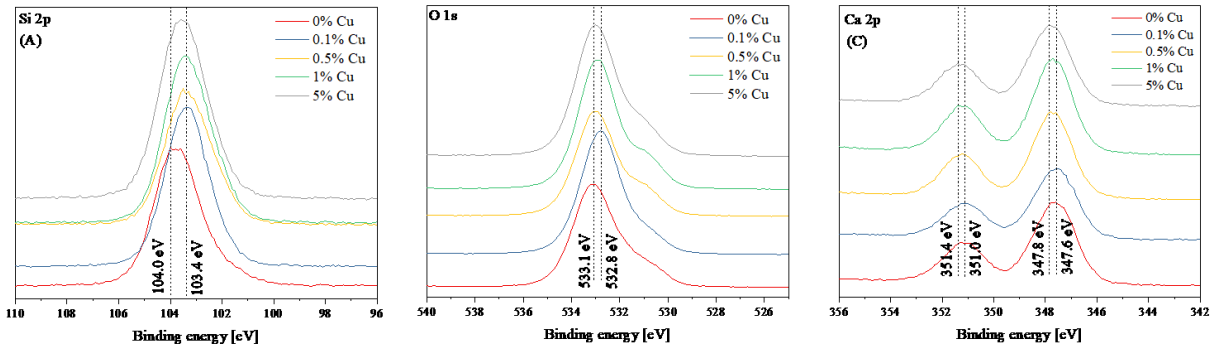


Figure 55. (A) The Si2p, (B) O1s and (C) Ca2p photoelectron spectra for the four copper containing bioactive glass compositions and 70S30C glass fibres. All spectra show a shift in binding energy with the incorporation of copper into the bioactive glass compositions.

The high resolution XPS spectra was performed for Si, O, Ca and Cu for each of the CuBG compositions and the 0% CuBG reference composition. *Figure 55(A)* depicts a shift in the peak binding energy of the Si 2p high resolution spectra as copper is inserted into the bioactive glass. They show maximum peaks varying between 103.4 eV and 104.0 eV which correspond to a tetrahedral silica which is coordinated with four oxygen atoms (SiO_4^{4-}) [213].

The O 1s high resolution spectra also shows a shift towards lower binding energies (*Figure 55B*), however the largest shift between the two maximum binding energies was only 0.3 eV. The asymmetrical spectra shows a shoulder at lower binding energies which is typically associated with metal oxides such as calcium and copper oxide [233] [119]. *Figure 55B* shows that this shoulder changes as more copper is incorporated into the structure, becoming more prominent in the 0.1% CuBG and 0.5% CuBG samples and then less prominent in the 5% CuBG sample. It is important to remember that the shoulder is made up of both the calcium and copper metal oxides [233], so while copper does have an effect on the shoulder, calcium has the most significant affect as the percentage of calcium in the network is much greater than the percentage of copper.

The high resolution spectra of the Ca 2p (*Figure 55C*) shows a very small shift in binding energy between the CuBGs and noticeable change in the shape of the peaks between samples.

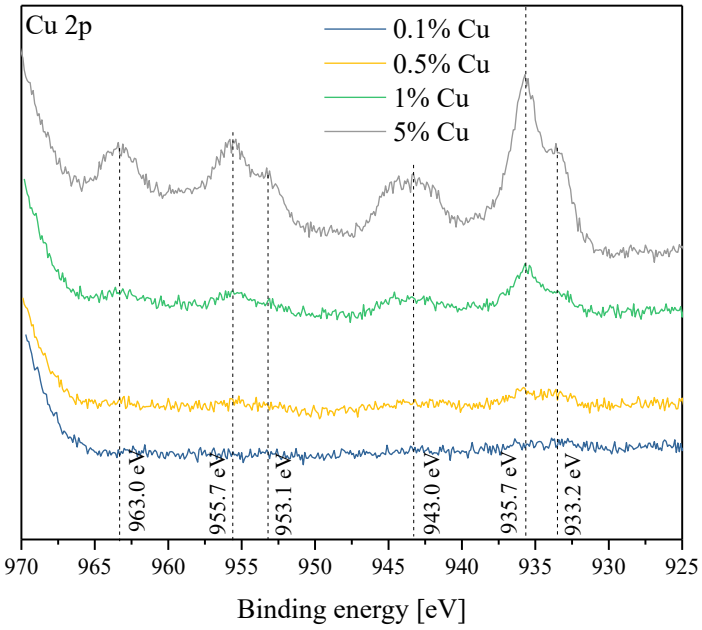


Figure 56. The Cu 2p photoelectron spectra for the four copper containing bioactive glass compositions and 70S30C glass fibres.

A high resolution XPS spectra obtained for Cu 2p for each of the CuBG compositions (*Figure 56)* peaks can only clearly be seen in the 5% CuBG composition and some evidence of peaks in the 1% CuBG composition. The high resolution spectra for the 5% CuBG composition contained significant noise but was peak fitted (*Figure 57*) and binding energies were found at Cu 2p 3/2 of 933.2 eV and 935.7 eV and at 2p 1/2 of 953.1 eV and 955.7 eV. Satellite features were also observed at ~943 eV, ~945 eV and ~963 eV. The binding energies for copper metal, copper (II) oxide and copper (I) oxide are all within a similar range, but the pattern of the peaks and satellite features is characteristic of a copper (II) oxide spectra or of copper nitrate [234]. XPS high resolution spectra of N 1s was carried out (*Figure 58*) and showed no presence of N 1s in the post heat treated 5% CuBG, 1% CuBG samples or the original 70S30C fibres. A peak was obtained however in the pre-sintered 70S30C fibres which indicates that the heat treatment successfully removed all the nitrates and that characteristic spectra for the 5% CuBG obtained is more likely to be copper (II) oxide. The copper (II) oxide spectra can be confirmed by a number of features [234].

Shaikh *et al.* [235] investigated ruthenium doped CuO thin films and found that un-doped copper (II) oxide produced a similar pattern to what is observed in *Figure 57*. The presence of satellites is unique to copper

(II) oxide and Poulston *et al.* [236] identified the satellite peaks at 942.4 eV and 944.6 eV for Cu 2p 3/2 and at 963.3 eV for Cu 2p 1/2 which are values reasonably similar to what was obtained in *Figure 52*. The study also showed that the separation in binding energy between the Cu 2p 3/2 and Cu 2p 1/2 was higher than 20 eV. The separation in the present study (*Figure 57*) was at approximately 20 eV. Wanger *et al.* [215] and Lim *et al.* [237] state that separation in binding energies ≥ ~19.9 eV is typically associated to be copper (II) oxide, binding energy separations of ≤ ~19.9 eV are typically associated with pure metallic Cu or copper (I) oxide.

The results presented in *Figure 57* also show the presence of another two peaks, each close to the Cu 2p 3/2 peak (935.7 eV) and the Cu 2p 1/2 peak (955.7 eV) respectively. These do not typically feature on XPS spectra for copper (II) oxide and may be the result of inaccuracies in peak fitting due to the amount of noise present in the high resolution spectra. However Lim *et al.* [237] did show a similar, additional peak or shoulder. Lim *et al.* compared the spectra of two copper thin films with different microstructures and crystallographic textures which have been exposed to air long term. They showed the formation of extra peaks/shoulders in one sample which has been exposed to air for 800 h, similar to those extra peaks presented in *Figure 57*, these are explained by the differences in texture and microstructure of the materials.

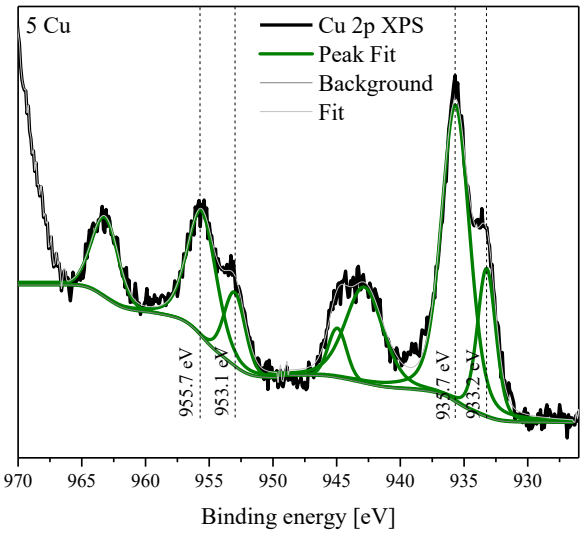


Figure 57. The Cu 2p high resolution XPS spectra for the 5% CuBG composition. Peaks at 933.2 eV and 953.1 eV alongside the characteristic satellites indicate the presence of CuO. The secondary shoulders at 935.7 eV and 955.7 eV can be attributed to long exposure

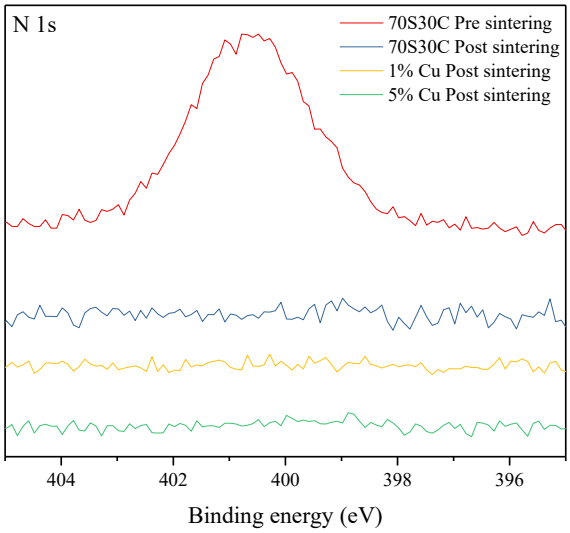


Figure 58. The N 1s high resolution XPS spectra for the 5% CuBG, 1% CuBG and original 70S30C (0% CuBG) post heat treatment and the 70S30C (0% CuBG) compositions post heat treatment.

Meghana *et al.* [238] investigated the antibacterial activity of copper (I) oxide and copper (II) oxide and found that both copper (I) oxide and copper (II) oxide demonstrated toxicity towards E.coli, with copper (I) oxide providing the most antibacterial effect. It additionally commented on the significant reactive oxygen species (ROS) produced by copper (II) oxide, whereas copper (I) oxide did not produce a significant quantity by comparison. ROS plays an important role in wound healing, they are able to aid the regulation of angiogenesis at the wound site and additionally communicate to immunocytes and non-lymphoid cells to aid the repair process [239]. The presence of copper as copper (II) oxide in the bioactive glass structure is encouraging as it provides evidence to why the copper containing bioactive glass fibres presented in this study are suitable for the stimulation of angiogenesis for wound healing applications.

7.3.3. Solid-state ^{29}Si magic angle spinning-nuclear magnetic resonance (29Si MAS-NMR)

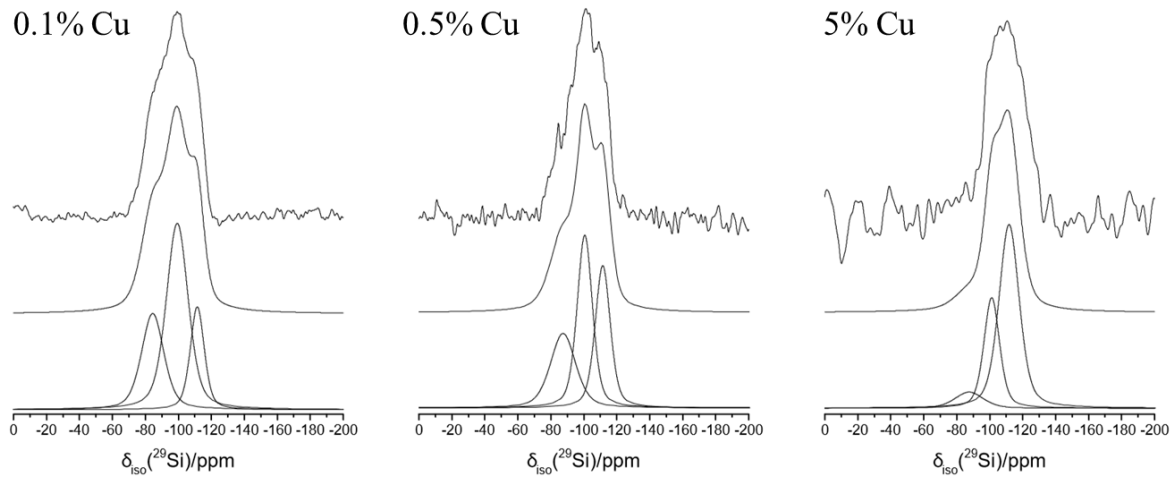


Figure 59. Solid-state 29Si MAS-NMR data of electrospun sol-gel glass 5% Cu, 0.1% Cu and 0.5% Cu samples. PPM can be equated to mg L^{-1}

The 5% CuBG, 0.5% CuBG and 0.1% CuBG compositions were chosen for the NMR study. The ^{29}Si spectra of the compositions is shown in *Figure 59*. For all three samples, signals centred around ~100 ppm for Q^3 and ~111 ppm for Q^4. The Q^2 and Q^3 peaks appeared to decrease as the copper content increased, and the Q^4 peak increased as the copper increased. The chemical shift in ppm highlights this as well in *Table 27.* There is a shift of -3.1 ppm between the 0.1% CuBG and 5% CuBG compositions in Q^2, -1.9 pm in Q^3 and -0.02 ppm in Q^4. *Table 27* shows an increased network connectivity in the 5% CuBG sample compared with the 0.1% CuBG sample. Copper therefore has a different role in the network to calcium, as *Table 13* in Chapter 5.3.1 shows a negligible change in network connectivity between the 70S30C and 80S20C despite a difference in calcium content of 10 mol.%.

Similar trends have been noted by Wang *et al.* [240] and Hoppe *et al.* [232], who suggested that the increase in network connectivity is likely to do with Cu-O having a more covalent character compared with that of the Ca-O bond. According to Hoppe *et al.,* this likely enables the re-polymerisation of Si-NBOs and thus increase in the network connectivity. Hoppe *et al.* suggest that evidence for this could also be found in FTIR, where a reduction in the intensity of NBO peak would correspond to lower quantities of free NBOs in the glass network. The results presented in *Figure 54* show a smaller (flatter) NBO peak in the 5% CuBG

composition with the highest network connectivity, compared with the 0.1% CuBG and 0.5% CuBG compositions.

Table 27. Percentage of Qn Si species determined from the 29Si MAS NMR (vr = 5 kHz) data for 5% Cu, 0.1% Cu and 0.5% Cu

Samples	Q^2		Q^3		Q^4		Dc [%]	Connectivity
	δ_{iso} [ppm]	I [%]	δ_{iso} [ppm]	I [%]	δ_{iso} [ppm]	I [%]		
0.1% Cu	-84.4	33.3	-99.3	27.3	-111.5	39.4	76.5	3.1
0.5% Cu	-87.4	29.1	-100.6	24.6	-111.5	46.3	79.3	3.2
5% Cu	-87.5	13.4	-101.2	15.0	-111.7	71.6	89.5	3.6

7.4 Conclusion

The three analysis techniques were used to reveal information about the chemical structure of the copper containing bioactive glasses. FTIR results showed no major differences in the spectra of the different compositions but showed some shifting of the Si-O-Si bands and some changes in intensity in the non-bridging oxygen band which changes in concentration. However, visually, this change was not clear enough to determine a direct relationship with intensity and changes in copper concentration. This is perhaps due to the relatively small amounts of copper incorporated into the glass network in terms of the percentage over all of network modifiers.

XPS results provided evidence to suggest that copper was present in the form of CuO, which has been linked to enhanced ROS production, providing evidence for the use of copper containing bioactive glasses for use in wound healing applications.

NMR results support the findings from FTIR and show an increase in shift to Q^4 and network connectivity as the quantity of copper is increased in the bioactive glass network. Literature suggests that this could be due Cu-O having a more covalent character than CaO which enables repolymersiation of Si-NBOs.

This study presents some answers to the state of copper in the bioactive glass network and information as to how its incorporation affects the bond formation. Copper is incorporated into the glass fibres successfully as a network modifier which highlights its reliability for use in wound healing applications.

CHAPTER EIGHT

CONCLUDING REMARKS

8.1. Review of objectives

The aim of this thesis was to develop a material based on a bioactive glass composition, which had no adverse effects on the body, could successfully promote angiogenesis and therefore contribute to the healing of chronic wounds. An electrospun, 3D, cotton-wool-like bioactive glass structure was produced which was chemically and physically characterised and successfully released therapeutic ions *in vitro* studies

A key result from this project was the role of copper in successfully increasing the production of VEGF in HDFs after being incorporated into electrospun bioactive glass fibres. This is an exciting result as copper has been frequently incorporated into bioactive glasses but is typically investigated for its antibacterial properties. Few studies have looked at copper for wound healing applications as the majority of work on the insertion of cations into bioactive glass compositions focuses on their use in bone and cartilage regeneration. A range of copper concentrations were investigated, producing mixed results, with some displaying a cytotoxic effect on HDFs while other concentrations were found to increase the production of the growth factor VEGF. A copper concentration was identified which significantly increased the VEGF production compared to the copper controls, DMEM and other bioactive glass compositions not containing copper. This is particularly exciting as it appears to be the combination of the bioactive glass with the copper that provides this increased VEGF production which is not matched by the 70S30C bioactive glass composition without the copper inserted or by the matching copper control concentration. The copper concentration identified was not found to be cytotoxic to cells, providing an indication of the copper concentrations appropriate for contact with HDFs in wound healing dressings.

A new protocol for electrospinning a 3D cotton-wool-like bioactive glass structure was developed and the key factors affecting the formation of the 3D structure were identified and controlled, enabling the reliable production of long and uniform fibres. This result provided evidence of the impact humidity and composition can have on the structure of electrospun materials. This work identified patterns of how materials can respond to atmospheric changes, identifying some of the impacts of the less frequently tested electrospinning parameters on materials. A humidity 'window' was identified for the production of 3D cotton-wool like fibre structures. The composition of the sol-gel was also investigated following previous work [7] and the relationship between composition, humidity and scaffold structure was identified and understood. The 3D fibres produced in the SiO_2-CaO system were characterised and VEGF studies confirmed that the 70S30C and 80S20C fibrous compositions do not inhibit the metabolic activity or proliferation of HDFs and do not inhibit production of VEGF. .

Characterisation techniques were also used to determine the state and the chemical role of copper in the bioactive glass network. . It was established that additions of copper increased the network connectivity of

the bioactive glass which differed from the effect of calcium. This result was particularly interesting as both copper and calcium have the same role and behave as network modifiers in a bioactive glass network. The network connectivity of the 70S30C and 80S20C samples was found to be the same when tested dispite the increase in the amount of calcium entering the network in the 70S30C sample. This result for copper suggests that copper may have a dual role in the network.

8.1.1. The factors determining the formation of a 3D electrospun scaffold.

The work carried out to develop knowledge of the electrospinning factors which affect the production of a 3D cotton-wool-like scaffolds was useful in determining some of the needs required for possible future commercialisation of 3D cotton-wool-like fibres. Many review articles outline the impact of physical and chemical parameters which affect the ability for a solution to electrospin [146] [152] but few focus on the effects of relative humidity. Humidity is known to affect electrospinning [241] but rarely studies define specific relative humidity parameters or other environmental factors for materials which, as evidenced in this work, can greatly affect the morphology of the fibres produced.

The electrospinning studies also provided more evidence for the role of composition and how the distribution of different charges affect the morphology of fibres produced. This work was developed initially by Poologasundarampillai *et al.,* [7] and was found to be difficult to repeat, and so a new protocol for electrospinning was developed which made use of a binder to obtain the correct viscosity and surface tension for electrospinning to take place. The electrospinning parameters required to obtain a reliable 3D morphology made the physical process of electrospinning very slow. The flow rate was much lower (0.12 $\mu l\ s^{-1}$ or 0.007 $mL\ min^{-1}$) compared with the process used by Poologasundarampillai *et al.,* [7] which limited the amount of fibres that could be electrospun significantly. Other factors such as a lack of humidity control in the laboratory meant that electrospinning could only take place within the correct relative humidity range. For commercialisation purposes, this is significant, as climate control would be necessary for any sort of scale up.

8.1.2. 3D bioactive glass scaffold development and its effect on HDFs

The scaffold developed in this chapter provided an interesting development in the use of sol-gel bioactive glasses for wound healing. Two bioactive glass compositions were produced and successfully electrospun. Characterisation techniques were carried out to measure the fibre diameter and determine the surface area of the fibres. The results showed that the fibres had a much smaller diameter (0.21 – 0.34 μm) than others

previously produced [175] which indicated that cell attachment to HDFs may be difficult. Immersion in DMEM showed that the fibres did not form HCA, which despite being desirable for bonding with bone, is not needed in wound healing applications. The cytotoxicity and VEGF ELISA study results asserted the benefits of bioactive glasses in the SiO_2-CaO system, as they provide a non-cytotoxic base composition for the insertion of different ions to encourage different therapeutic effects.

8.1.3. Incorporation of Copper ions, stimulation of VEGF in HDFs and characterisation

The novel insertion of the copper ions into 3D electrospun bioactive glass fibres helped to identify copper concentrations which stimulated VEGF production in HDFs. The comparison with literature-quoted copper concentrations, which either produce therapeutic effects or are cytotoxic to various cells types, highlighted the different responses of cells to copper ions. This is of relevance clinically when designing bioactive glasses containing copper for different target tissues, as different cells respond very differently.

Chemical characterisation was carried out on the copper containing bioactive glass samples which identified the chemical state of copper within the bioactive glass. This was an important development as it has previously been identified that copper states provide different effects on cells [238]. It found that copper (II) oxide provided a significant increase reactive oxygen species which play a crucial role in wound healing.

8.2. Further Work

The work presented in this thesis is an interesting starting point for the development of 3D copper-containing bioactive glasses for use in wound healing, however the results have provided new questions and directions of future work.

8.2.1. Cell attachment studies

To determine the impact of the fibres on HDFs, studies should be conducted with the material itself. Potential problems with the diameter of the fibres have been identified but a study to ascertain if cell attachment to the fibrous scaffold is critical for the future development of the project. It would be interesting to repeat the cell metabolic activity, proliferation and VEGF ELISA studies to compare results. These *in vitro* studies would be carried out on the same sample compositions for direct comparison. They would help to provide a further understanding of the cytotoxicity limits for the HDFs.

8.2.2. Optimising copper concentration

In conjunction with the cell attachment studies, it would be key to determine the ideal concentration of copper ions to achieve an optimum VEGF production per cell without being cytotoxic to the cells. Concentrations around the 1% CuBG sample would be a logical starting point. It would also be important to investigate the incorporation of copper into other sol-gel derived bioactive glass compositions such as 58S and see if this enhances or reduces VEGF production. Comparison studies of different bioactive glass compositions with the same concentration of metal ions inserted have previously shown discrepancies in cytotoxicity [125] so this investigation would be important. In addition to this, investigating the impact of copper-containing bioactive glasses on different cell lines, such as endothelial cells, would also provide valuable information.

8.2.3. Optimising the electrospinning process

As mentioned previously, the electrospinning parameters identified have meant that the electrospinning process is very inefficient. Further studies on the electrospinning parameters would be of interest to potentially offset some of the effects of humidity and also to increase the diameter of the fibres. Studies show that larger diameter fibres are appropriate for cell attachment and so a study to increase this would be of use [175]. Improving the electrospinning set up is critical for the commercialisation of 3D cotton-wool-like bioactive glass fibres.

9.0 REFERENCES

[1] **M. B. Dreifke, A. A. Jayasuriya, and A. C. Jayasuriya, "Current wound healing procedures and potential care," *Mater. Sci. Eng. C*, vol. 48, pp. 651–662, 2015.**

[2] **S. Guo and L. A. DiPietro, "Critical review in oral biology & medicine: Factors affecting wound healing," *J. Dent. Res.*, vol. 89, no. 3, pp. 219–229, Mar. 2010.**

[3] **S. Enoch and D. J. Leaper, "Basic science of wound healing," *Surg.*, vol. 23, no. 2, pp. 37–42, Feb. 2005.**

[4] **L. L. Hench, "The story of Bioglass," *J. Mater. Sci. Mater. Med.*, vol. 17, no. 11, pp. 967–978, 2006.**

[5] **P. G. Rodriguez, F. N. Felix, D. T. Woodley, and E. K. Shim, "The role of oxygen in wound healing: a review of the literature," *Dermatologic Surg.*, vol. 34, no. 9, pp. 1159–69, 2008.**

[6] **W. Feng, F. Ye, W. Xue, Z. Zhou, and Y. J. Kang, "Copper regulation of hypoxia-inducible factor-1 activity.," *Mol. Pharmacol.*, vol. 75, no. 1, pp. 174–182, 2009.**

[7] **G. Poologasundarampillai *et al.*, "Cotton-wool-like bioactive glasses for bone regeneration.," *Acta Biomater.*, vol. 10, no. 8, pp. 3733–46, Aug. 2014.**

[8] **E. Proksch, J. M. Brandner, and J. M. Jensen, "The skin: An indispensable barrier," *Exp. Dermatol.*, vol. 17, no. 12, pp. 1063–1072, 2008.**

[9] **R. a F. Clark, K. Ghosh, and M. G. Tonnesen, "Tissue engineering for cutaneous wounds.," *J. Invest. Dermatol.*, vol. 127, no. 5, pp. 1018–1029, 2007.**

[10] **A. D. Metcalfe and M. W. J. Ferguson, "Tissue engineering of replacement skin: The crossroads of biomaterials, wound healing, embryonic development, stem cells and regeneration," *J. R. Soc. Interface*, vol. 4, no. 14, pp. 413–417, 2007.**

[11] **F. Baino, G. Novajra, V. Miguez-Pacheco, A. R. Boccaccini, and C. Vitale-Brovarone, "Bioactive glasses: Special applications outside the skeletal system," *J. Non. Cryst. Solids*, Mar. 2015.**

[12] **J. F. Guest *et al.*, "Health economic burden that wounds impose on the National Health Service in the UK," *BMJ Open*, vol. 5, no. 12, pp. 1–8, 2015.**

[13] **D. Harper, A. Young, and C.-E. McNaught, "The physiology of wound healing," *Surg.*, vol. 32, no. 9, pp. 445–450, Sep. 2014.**

[14] **P. Beldon, "Basic science of wound healing," *Surgery*, vol. 28, no. 9, pp. 409–412, 2010.**

[15] **D. G. Greenhalgh, "The role of apoptosis in wound healing.," *Int. J. Biochem. Cell Biol.*, vol. 30, no. 9, pp. 1019–1030, 1998.**

[16] **M. A. Fonder, G. S. Lazarus, D. A. Cowan, B. Aronson-Cook, A. R. Kohli, and A. J. Mamelak, "Treating the chronic wound: A practical approach to the care of nonhealing wounds and wound care dressings," *J. Am. Acad. Dermatol.*, vol. 58, no. 2, pp. 185–206, 2008.**

[17] **R. G. Frykberg and J. Banks, "Challenges in the Treatment of Chronic Wounds," *Adv. Wound Care*, vol. 4, no. 9, pp. 560–582, 2015.**

[18] **A. Persoon, M. M. Heubeb Van Der Vleuten, C.J.M., De Rooi, J.M.J., P. C. M. Van de Kerkhof, and T. Van Achterberg, "Leg Ulcers: A review of their impact on daily life," *J Clin Nurs*, vol. 13, pp. 341–354, 2004.**

[19] **C. K. Sen *et al.*, "Human skin wounds: A major and snowballing threat to public health and the economy: Persepective article," *Wound Repair Regen.*, vol. 17, no. 6, pp. 763–771, 2009.**

[20] **D. Upton, C. Hender, and K. Solowiej, "Mood disorders in patients with acute and chronic wounds: a health professional perspective," *J. Wound Care*, vol. 21, no. 1, pp. 42–48, 2012.**

[21] **Wild, "Estimates for the year 2000 and projections for 2030," *World Health*, vol. 27, no. 5, pp. 1047–1053, 2004.**

[22] **G. E. et al. Reiber, "Causal Pathways for Incidence Lower-extremity ulcers in patients with diabetes from two settings," *Diabetes Care*, vol. 22, no. 1, pp. 157–162, 1999.**

[23] **"Wound care centres. How diabetes affects wound healing," *http://www.woundcarecenters.org/article/living-with-wounds/how-diabetes-affects-wound-healing*. .**

[24] **H. Brem and M. Tomic-Canic, "Cellular and molecular basis of wound healing in diabetes.," *J. Clin. Invest.*, vol. 117, no. 5, pp. 1219–1222, 2007.**

[25] **A. Bishop, "Role of oxygen in wound healing.," *J. Wound Care*, vol. 17, no. 9, pp. 399–402, 2008.**

[26] **A. A. Tandara and T. A. Mustoe, "Oxygen in Wound Healing - More than a Nutrient," *World J. Surg.*, vol. 28, no. 3, pp. 294–300, 2004.**

[27] **M. A. C. Déry, M. D. Michaud, and D. E. Richard, "Hypoxia-inducible factor 1: Regulation by hypoxic and non-hypoxic activators," *Int. J. Biochem. Cell Biol.*, vol. 37, no. 3, pp. 535–540, 2005.**

[28] **G. Han and R. Ceilley, "Chronic Wound Healing: A Review of Current Management and Treatments," *Adv. Ther.*, vol. 34, no. 3, pp. 599–610, 2017.**

[29] **G. Mulder, R. Jones, S. Cederholm-Williams, G. Cherry, and R. Terence, "Fibrin cuff lysis in chronic venous ulcers treated with hydrocolloid dressing," *Int. J. Dermatol.*, vol. 32, no. 4, 1993.**

[30] **P. E. Prete, "Growth effects of Phaenicia sericata larval extracts on fibroblasts: Mechanism for wound healing by maggot therapy," *Life Sci.*, vol. 60, no. 8, pp. 505–510, 1997.**

[31] **K. Vyas and H. Vasconez, "Wound Healing: Biologics, Skin Substitutes, Biomembranes and Scaffolds," *Healthcare*, vol. 2, no. 3, pp. 356–400, 2014.**

[32] **W. Marston, J. Hanft, P. Norwood, and R. Pollak, "The Efficacy and Safety of Dermagraft in improving the healing of chronic diabetic foot ulcers," *Diabetes Care*, vol. 26, no. 6, pp. 1701–1705, 2003.**

[33] **E. Pinney, K. Liu, B. Sheeman, and J. Mansbridge, "Human three-dimensional fibroblast cultures express angiogenic activity," *J. Cell. Physiol.*, vol. 183, no. 1, pp. 74–82, 2000.**

[34] **C. Niels, A. H. Krejci-Papa, and J. F. Hansbrough, "Fibroblast Sheets Enable Epithelialization of Wounds That Do Not Support Keratinocyte Migration," *Tissue Eng.*, vol. 5, no. 6, 2007.**

[35] **Y. M. Bello and a F. Falabella, "The role of graftskin (Apligraf) in difficult-to-heal venous leg ulcers.," *J. Wound Care*, vol. 11, no. 5, pp. 182–3, 2002.**

[36] **A. Veves, V. Falanga, D. G. Armstrong, and M. L. Sabolinski, "Graftskin, a human skin equivalent, is effective in the management of noninfected neuropathic diabetic foot ulcers: A prospective randomized multicenter clinical trial," *Diabetes Care*, vol. 24, no. 2, pp. 290–295, 2001.**

[37] **B. Fagrell and G. Jorneskog, "Disturbed microvascular reactivity and shunting - A major cause for diabetic complications," *Vasc. Med.*, vol. 4, no. 3, pp. 125–127, 1999.**

[38] **A. Langer and W. Rogowski, "Systematic review of economic evaluations of human cell-derived wound care products for the treatment of venous leg and diabetic foot ulcers," *BMC Health Serv. Res.*, vol. 9, 2009.**

[39] **S. M. Jones, P. E. Banwell, and P. G. Shakespeare, "Advances in wound healing: Topical negative pressure therapy," *Postgrad. Med. J.*, vol. 81, no. 956, pp. 353–357, 2005.**

[40] **M. L. Venturi, C. E. Attinger, A. N. Mesbahi, C. L. Hess, and K. S. Graw, "Mechanisms and Clinical Applications of the Vacuum-Assisted Closure (VAC) Device," *Am J Clin Dertmatol*, vol. 6, no. 3, pp. 185–194, 2005.**

[41] **D. G. Greenhalgh, K. H. Sprugel, M. J. Murray, and R. Ross, "PDGF and FGF stimulate wound healing in the genetically diabetic mouse.," *Am. J. Pathol.*, vol. 136, no. 6, pp. 1235–46, 1990.**

[42] **R. D. Galiano *et al.*, "Topical vascular endothelial growth factor accelerates diabetic wound healing through increased angiogenesis and by mobilizing and recruiting bone marrow-derived cells," *Am. J. Pathol.*, vol. 164, no. 6, pp. 1935–1947, 2004.**

[43] **C. Wu and J. Chang, "Mesoporous bioactive glasses: structure characteristics, drug/growth factor delivery and bone regeneration application," *Interface Focus*, vol. 2, no. 3, pp. 292–306, 2012.**

[44] **W. J. E. M. Habraken, J. G. C. Wolke, and J. A. Jansen, "Ceramic composites as matrices and scaffolds for drug delivery in tissue engineering," *Adv. Drug Deliv. Rev.*, vol. 59, no. 4–5, pp. 234–248, 2007.**

[45] **A. Hoppe, N. S. Güldal, and A. R. Boccaccini, "A review of the biological response to ionic dissolution products from bioactive glasses and glass-ceramics," *Biomaterials*, vol. 32, no. 11, pp. 2757–2774, 2011.**

[46] **K. E. Johnson and T. A. Wilgus, "Vascular Endothelial Growth Factor and Angiogenesis in the Regulation of Cutaneous Wound Repair," *Adv. Wound Care*, vol. 3, no. 10, pp. 647–661, 2014.**

[47] **T. A. Wilgus *et al.*, "Novel function for vascular endothelial growth factor receptor-1 on epidermal keratinocytes," *Am. J. Pathol.*, vol. 167, no. 5, pp. 1257–1266, 2005.**

[48] **N. N. Nissen, P. J. Polverini, R. L. Gamelli, and L. A. DiPietro, "Basic fibroblast growth factor mediates angiogenic activity in early surgical wounds," *Surgery*, vol. 119, no. 4, pp. 457–465, 1996.**

[49] **L. F. Brown, "Expression of vascular permeability factor (vascular endothelial growth factor) by epidermal keratinocytes during wound healing," *J. Exp. Med.*, vol. 176, no. 5, pp. 1375–1379, 1992.**

[50] **M. Detmar *et al.*, "Increased microvascular density and enhanced leukocyte rolling and adhesion in the skin of VEGF transgenic mice," *J. Invest. Dermatol.*, vol. 111, no. 1, pp. 1–6, 1998.**

[51] **J. J. Vranckx *et al.*, "In vivo gene delivery of Ad-VEGF121to full-thickness wounds in aged pigs results in high levels of VEGF expression but not in accelerated healing," *Wound Repair Regen.*, vol. 13, no. 1, pp. 51–60, 2005.**

[52] **C. J. Corral, A. Siddiqui, L. Wu, C. L. Farrell, D. Lyons, and T. A. Mustoe, "Vascular endothelial growth factor is more important than basic fibroblastic growth factor during ischemic wound healing," *Arch. Surg.*, vol. 134, no. 2, pp. 200–205, 1999.**

[53] **J. Jacobi *et al.*, "Discordant effects of a soluble VEGF receptor on wound healing and angiogenesis," *Gene Ther.*, vol. 11, no. 3, pp. 302–309, 2004.**

[54] **T. A. Wilgus, A. M. Ferreira, T. M. Oberyszyn, V. K. Bergdall, and A. Dipietro, "Regulation of scar formation by VEGF," *Lab Invest.*, vol. 88, no. 6, pp. 579–590, 2008.**

[55] **K. Raju, G. Alessandri, M. Ziche, and P. Gullino, "Ceruloplasmin, copper ions and angiogenesis," *J Natl Cancer Inst*, vol. 69, no. 5, pp. 1183–8, 1982.**

[56] **C. K. Sen *et al.*, "Copper-induced vascular endothelial growth factor expression and wound healing," *Am. J. Physiol. - Hear. Circ. Physiol.*, vol. 282, no. 5, pp. H1821–H1827, 2002.**

[57] **G. F. Hu, "Copper stimulates proliferation of human endothelial cells under culture.," *J. Cell. Biochem.*, vol. 69, no. 3, pp. 326–335, 1998.**

[58] **H. Xie and Y. J. Kang, "Role of copper in angiogenesis and its medicinal implications.," *Curr. Med. Chem.*, vol. 16, no. 10, pp. 1304–1314, 2009.**

[59] **J. M. Gleadle, B. L. Ebert, J. D. Firth, and P. . Ratcliffe, "Regulation of angiogenic growth factor expression by hypoxia, transition metals, and chelating agents," *Am. J. Physiol.*, vol. 268, no. 6, pp. 1362–1368, 1995.**

[60] **J. Milosevic *et al.*, "Non-hypoxic Stabilization of Hypoxia-Inducible Factor Alpha (HIF-α): Relevance in Neural Progenitor/Stem Cells," *Neurotox. Res.*, vol. 15, no. 4, pp. 367–380, 2009.**

[61] **J. R. Jones, "Review of bioactive glass : From Hench to hybrids," *Acta Biomater.*, vol. 9, no. 1, pp. 4457–4486, 2013.**

[62] **R. G. Hill and D. S. Brauer, "Predicting the bioactivity of glasses using the network connectivity or split network models," *J. Non. Cryst. Solids*, vol. 357, no. 24, pp. 3884–3887, 2011.**

[63] **M. N. Rahaman *et al.*, "Bioactive glass in tissue engineering," *Acta Biomater.*, vol. 7, no. 6, pp. 2355–2373, 2011.**

[64] **V. Miguez-Pacheco, L. L. Hench, and A. R. Boccaccini, "Bioactive glasses beyond bone and teeth: Emerging applications in contact with soft tissues.," *Acta Biomater.*, vol. 13, pp. 1–15, Nov. 2014.**

[65] **L. L. Hench, R. J. Splinter, W. C. Allen, and T. K. Greenlee, "Bonding mechanisms at the interface of ceramic prosthetic materials," *J. Biomater. Res.*, vol. 5, no. 6, pp. 117–141, 1971.**

[66] **L. L. Hench, "Bioceramics: From Concept to Clinic," *J. Am. Ceram. Soc.*, vol. 74, no. 7, pp. 1487–1510, 1991.**

[67] **A. E. Greenspan, D. C., Zhong, J. P., and LaTorre, G. P. Andersson, O.H. and Yli-Urpo, "Effect of surface area to volume ratio on in vitro surface reactions of Bioactive glass particulates.," in *Bioceramics 7*, 1994, pp. 28–33.**

[68] **D. C. Greenspan *et al.*, "The evaluation of degradability of melt and sol-gel derived bioglass® in-vitro," in *Bioceramics 10*, vol. 10, 1997, pp. 391–394.**

[69] **D. L. Greenspan, D. C., Zhong, J. P., and Wheeler, "Bioactivity and biodegradability: Melt vs sol-gel derived Bioglass® in vitro and in vivo," in *Bioceramics 11*, 1998, pp. 345–348.**

[70] **Q. Fu, E. Saiz, M. N. Rahaman, and A. P. Tomsia, "Bioactive glass scaffolds for bone tissue engineering: State of the art and future perspectives," *Mater. Sci. Eng. C*, vol. 31, no. 7, pp. 1245–1256, 2011.**

[71] **J. E. Shelby, *Introduction to glass science and technology*, 2nd Editio. Royal Society of Chemistry, 2005.**

[72] **N. J. Coleman and J. W. Nicholson, *Glass Bones*. 2006.**

[73] **J. Zarzycki, *Glasses and the Vitreous State*. Cambridge University Press, 1991.**

[74] **W. Kingery, H. Bowen, and D. Uhlmann, "Introduction to Ceramics 2nd Edition," Wiley-Interscience, 1976.**

[75] **R. Hill, "An alternative view of the degradation of Bioglass," *J. Mater. Sci. Lett.*, vol. 15, no. 13, pp. 1122–1125, 1996.**

[76] **M. M. Pereira and L. L. Hench, "Mechanisms of hydroxyapatite formation on porous gel-silica substrates," *J. Sol-Gel Sci. Technol.*, vol. 7, no. 1–2, pp. 59–68, 1996.**

[77] **L. L. Clark, A. E., Patano, C. G., and Hench, "Corrosion of glass," *Magazines for Industry*, pp. 1–7, 1979.**

[78] **T. Kokubo, S. Kushitani, S. Sakka, T. Kitsugi, and T. Yamamuro, "Solutions able to reproduce in vivo surface-structure changes in bioactive glass-ceramic A-W3," *J. Biomed. Mater. Res.*, vol. 24, no. 6, pp. 721–734, 1990.**

[79] **E. Gentleman *et al.*, "The effects of strontium-substituted bioactive glasses on osteoblasts and osteoclasts in vitro," *Biomaterials*, vol. 31, no. 14, pp. 3949–3956, 2010.**

[80] **V. G. Varanasi, J. B. Owyoung, E. Saiz, S. J. Marshall, G. W. Marshall, and P. M. Loomer, "The ionic products of bioactive glass particle dissolution enhance periodontal ligament fibroblast osteocalcin expression and enhance early mineralized tissue development," *J. Biomed. Mater. Res. - Part A*, vol. 98 A, no. 2, pp. 177–184, 2011.**

[81] **L. L. Hench and J. K. West, "The sol-gel process," *Chem. Rev.*, vol. 90, no. 1, pp. 33–72, 1990.**

[82] **B. Yu, "New sol-gel derived bioactive glasses and organic/inorganic hybrids for bone regeneration," 2010.**

[83] **B. Lei, X. Chen, Y. Wang, N. Zhao, C. Du, and L. Fang, "Surface nanoscale patterning of bioactive glass to support cellular growth and differentiation," *J. Biomed. Mater. Res. - Part A*, vol. 94, no. 4, pp. 1091–1099, 2010.**

[84] **J. R. Jones, "Bioactive Glass 3D Scaffolds for Tissue Engineering," 2002.**

[85] **G. W. Brinker, C. J., Scherer, *Sol-gel science*. Academic Press Inc., 1990.**

[86] **M. D. Sacks and R.-S. Sheu, "Rheological properties of silica sol-gel materials," *J. Non. Cryst. Solids*, vol. 92, no. 2–3, pp. 383–396, Jul. 1987.**

[87] **S. Sakka and K. Kamiya, "The sol-gel transition in the hydrolysis of metal alkoxides in relation to the formation of glass fibers and films," *J. Non. Cryst. Solids*, vol. 48, no. 1, pp. 31–46, Mar. 1982.**

[88] **W. Vogelsberger, W. Vogelsberger, A. Seidel, A. Seidel, R. Fuchs, and R. Fuchs, "Contribution to the Determination of Kinetic Parameters of the Sol–Gel Transformation by Rheological Measurements," *J. Colloid Interface Sci.*, vol. 271, pp. 268–271, 2000.**

[89] **G. J. Klein, L. C., Garvey, "Drying and firing monolithic silica shapes from sol-gel.," in *Ultrastructure Processing of Ceramics, Glasses and Composites.*, New York: John Wiley & Sons Inc, 1984, pp. 88–99.**

[90] **M. Ishizaki, K., Komameni, S., Nanko, "Sol-Gel Processing: Designing Porosity, Pore Size and Polarity and Shaping Processes," in *Porous Materials: Process Technology and Applications*, London: Kluwer Academic Publishers, 1998, pp. 67–180.**

[91] **F. Balas, D. Arcos, J. Perez-Pariente, and M. Vallet-Regi, "Textural properties of SiO2-CaO-P2O5 glasses prepared by the sol-gel method," *J. Mater. Res.*, vol. 16, no. 5, pp. 1345–1348, 2001.**

[92] **M. Arcos, D., Greenspan, D.C., Vallet-Regi, "Influence of the stabilisation temperature on textural, structural and ion release in SiOi-CaO- P2O5 sol-gel glasses," *Chem. Mater.*, vol. 14, no. 4, pp. 1515–1522, 2002.**

[93] **A. J. Salinas, A. I. Martin, and M. Vallet-Regí, "Bioactivity of three CaO-P2O5-SiO2 sol-gel glasses," *J. Biomed. Mater. Res.*, vol. 61, no. 4, pp. 524–532, 2002.**

[94] **L. L. Hench and R. O. Þ, "Sol – Gel Technology," no. 1, pp. 1–13, 1864.**

[95] **S. H. Hench, L. L., Wang, "The sol-gel transformation of silica," *Phase Transitions*, vol. 24–26, pp. 785–834, 1990.**

[96] **L. L. Pereira, M. M., Clark, A. E., and Hench, "Calcium phosphate formation on sol-gel-derived bioactive glasses in vitro," *J. Biomed. Mater. Res.*, vol. 28, no. 693–698, 1994.**

[97] **S. Lin, C. Ionescu, K. J. Pike, M. E. Smith, and J. R. Jones, "Nanostructure evolution and calcium distribution in sol–gel derived bioactive glass," *J. Mater. Chem.*, vol. 19, pp. 1276–1282, 2009.**

[98] **J. R. Jones, D. S. Brauer, L. Hupa, and D. C. Greenspan, "Bioglass and Bioactive Glasses and Their Impact on Healthcare," *Int. J. Appl. Glas. Sci.*, vol. 7, no. 4, pp. 423–434, 2016.**

[99] **J. Wilson, G. Pigott, F. Schoen, and L. Hench, "Toxicology and biocompatibility of bioglasses," *J Biomed Mater Res*, vol. 15, no. 6, pp. 805–17, 1981.**

[100] **R. M. Day, "Bioactive Glass Stimulates the Secretion of Angiogenic Growth Factors and Angiogenesis *in Vitro*," *Tissue Eng.*, vol. 11, no. 5–6, pp. 768–777, 2005.**

[101] **R. M. Day and A. R. Boccaccini, "Effect of particulate bioactive glasses on human macrophages and monocytes in vitro," *J. Biomed. Mater. Res. - Part A*, vol. 73, no. 1, pp. 73–79, 2005.**

[102] **J. Wilson, G. H. Pigott, F. J. Schoen, and L. L. Hench, "Toxicology and biocompatibility of bioglasses," *J. Biomed. Mater. resarch*, vol. 15, no. 6, pp. 805–817, 1981.**

[103] **N. Lindfors, "Antibacterial Bioactive Glass, S53P4, for Chronic Bone Infections – A Multinational Study," in *A Modern Approach to Biofilm-Related Orthopaedic Implant Infections. Advances in Experimental Medicine and Biology*, Springer, Cham, 2016.**

[104] **D. M. Reffitt *et al.*, "Orthosilicic acid stimulates collagen type 1 synthesis and osteoblastic differentiation in human osteoblast-like cells in vitro," *Bone*, vol. 32, no. 2, pp. 127–135, 2003.**

[105] **K. W. Finnson, S. McLean, G. M. Di Guglielmo, and A. Philip, "Dynamics of Transforming Growth Factor Beta Signaling in Wound Healing and Scarring," *Adv. Wound Care*, vol. 2, no. 5, pp. 195–214, 2013.**

[106] **S. Naseri, W. C. Lepry, and S. N. Nazhat, "Bioactive glasses in wound healing: Hope or hype?," *J. Mater. Chem. B*, vol. 5, no. 31, pp. 6167–6174, 2017.**

[107] **W. Xie, X. Chen, G. Miao, J. Tang, and X. Fu, "Regulation of cellular behaviors of fibroblasts related to wound healing by sol–gel derived bioactive glass particles," *J. Biomed. Mater. Res. - Part A*, vol. 104, no. 10, pp. 2420–2429, 2016.**

[108] **H. Yu, J. Peng, Y. Xu, J. Chang, and H. Li, "Bioglass Activated Skin Tissue Engineering Constructs for Wound Healing," *ACS Appl. Mater. Interfaces*, vol. 8, no. 1, pp. 703–715, 2016.**

[109] **A. B. G. Lansdown, "Calcium: A potential central regulator in wound healing in the skin," *Wound Repair Regen.*, vol. 10, no. 5, pp. 271–285, 2002.**

[110] **K. Kawai *et al.*, "Calcium-based nanoparticles accelerate skin wound healing," *PLoS One*, vol. 6, no. 11, 2011.**

[111] **J. T. Seil and T. J. Webster, "Antimicrobial applications of nanotechnology: Methods and literature," *Int. J. Nanomedicine*, vol. 7, pp. 2767–2781, 2012.**

[112] **J. R. Morones *et al.*, "The bactericidal effect of silver nanoparticles.," *Nanotechnology*, vol. 16, no. 10, pp. 2346–2353, 2005.**

[113] **Y. Matsumura, K. Yoshikata, S. Kunisaki, and T. Tsuchido, "Mode of bactericidal action of silver zeolite and its comparison with that of silver nitrate mode of bactericidal action of silver zeolite and its comparison with that of silver nitrate," *Appl. Environ. Microbiol.*, vol. 69, no. 7, pp. 4278–4281, 2003.**

[114] **Q. Feng, J. Wu, and G. Chen, "A mechanistic study of the antibacterial effect of silver ions on Escherichia coli and Staphylococcus aureus," *J Biomed Mater Rev*, vol. 52, no. 4, pp. 662–8, 2000.**

[115] **M. Bellantone, "Bacteriostatic action of a novel four-component bioactive glass," *J. Biomed. Mater. resarch*, vol. 51, no. 3, pp. 484–490, 2000.**

[116] **A. A. Ahmed, A. A. Ali, D. A. R. Mahmoud, and A. M. El-Fiqi, "Preparation and characterization of antibacterial P_2O5-CaO-Na_2O-Ag_2O glasses.," *J. Biomed. Mater. Res. A*, vol. 98, no. 1, pp. 132–142, 2011.**

[117] **C. Wu *et al.*, "Hypoxia-mimicking mesoporous bioactive glass scaffolds with controllable cobalt ion release for bone tissue engineering," *Biomaterials*, vol. 33, no. 7, pp. 2076–2085, 2012.**

[118] **M. Azevedo, G. Jell, M. O'Donnell, R. Law, R. Hill, and M. Stevens, "Synthesis and characterization of hypoxia-mimicking bioactive glasses for skeletal regeneration," pp. 8854–8864, 2010.**

[119] **B. R. Barrioni, E. Norris, J. R. Jones, and M. de M. Pereira, "The influence of cobalt incorporation and cobalt precursor selection on the structure and bioactivity of sol–gel-derived bioactive glass," *J. Sol-Gel Sci. Technol.*, vol. 88, no. 2, pp. 309–321, 2018.**

[120] **E. A. Abou Neel, I. Ahmed, J. Pratten, S. N. Nazhat, and J. C. Knowles, "Characterisation of antibacterial copper releasing degradable phosphate glass fibres," *Biomaterials*, vol. 26, no. 15, pp. 2247–2254, 2005.**

[121] **A. M. Mulligan, M. Wilson, and J. C. Knowles, "Effect of increasing silver content in phosphate-based glasses on biofilms of Streptococcus sanguis," *J. Biomed. Mater. Res. - Part A*, vol. 67, no. 2, pp. 401–412, 2003.**

[122] **C. Gérard, L. J. Bordeleau, J. Barralet, and C. J. Doillon, "The stimulation of angiogenesis and collagen deposition by copper," *Biomaterials*, vol. 31, no. 5, pp. 824–831, 2010.**

[123] **S. Zhao *et al.*, "Wound dressings composed of copper-doped borate bioactive glass microfibers stimulate angiogenesis and heal full-thickness skin defects in a rodent model," *Biomaterials*, vol. 53, pp. 379–391, 2015.**

[124] **C. Wu *et al.*, "Copper-containing mesoporous bioactive glass scaffolds with multifunctional properties of angiogenesis capacity, osteostimulation and antibacterial activity," *Biomaterials*, vol. 34, no. 2, pp. 422–433, 2013.**

[125] **J. Bejarano, P. Caviedes, and H. Palza, "Sol–gel synthesis and in vitro bioactivity of copper and zinc-doped silicate bioactive glasses and glass-ceramics," *Biomed. Mater.*, vol. 10, no. 2, p. 025001, 2015.**

[126] **Y. Zhu *et al.*, "Preparation, characterization and in vitro bioactivity of mesoporous bioactive glasses (MBGs) scaffolds for bone tissue engineering," *Microporous Mesoporous Mater.*, vol. 112, no. 1–3, pp. 494–503, 2008.**

[127] **H. Fu *et al.*, "In vitro evaluation of borate-based bioactive glass scaffolds prepared by a polymer foam replication method," *Mater. Sci. Eng. C*, vol. 29, no. 7, pp. 2275–2281, 2009.**

[128] **W. Huang, D. E. Day, K. Kittiratanapiboon, and M. N. Rahaman, "Kinetics and mechanisms of the conversion of silicate (45S5), borate, and borosilicate glasses to hydroxyapatite in dilute phosphate solutions," *J. Mater. Sci. Mater. Med.*, vol. 17, no. 7, pp. 583–596, 2006.**

[129] **A. Yao, D. Wang, W. Huang, Q. Fu, M. N. Rahaman, and D. E. Day, "In vitro bioactive characteristics of borate-based glasses with controllable degradation behavior," *J. Am. Ceram. Soc.*, vol. 90, no. 1, pp. 303–306, 2007.**

[130] **Q. Fu, M. N. Rahaman, H. Fu, and X. Liu, "Silicate, borosilicate, and borate bioactive glass scaffolds with controllable degradation rate for bone tissue engineering applications. I. Preparation and in vitro degradation," *J. Biomed. Mater. Res. - Part A*, vol. 95, no. 1, pp. 164–71, 2010.**

[131] **L. A. Haro Durand *et al.*, "In vitro endothelial cell response to ionic dissolution products from boron-doped bioactive glass in the SiO2-CaO-P2O5-Na2O system," *J. Mater. Chem. B*, vol. 2, no. 43, pp. 7620–7630, 2014.**

[132] **Q. Fu, M. N. Rahaman, B. S. Bal, L. Bonewald, K. Kuroki, and R. F. Brown, "Silicate, borosilicate, and borate bioactive glass scaffolds with controllable degradation rate for bone tissue engineering applications. II. In vitro and in vivo biological evaluation," *J biomed mater Res. A*, vol. 95, no. 1, pp. 172–9, 2010.**

[133] **C. Lin, C. Mao, J. Zhang, Y. Li, and X. Chen, "Healing effect of bioactive glass ointment on full-thickness skin wounds," *Biomed. Mater.*, vol. 7, no. 4, p. 045017, 2012.**

[134] **T. A. Ostomel, Q. Shi, and G. D. Stucky, "Oxide hemostatic activity," *J. Am. Chem. Soc.*, vol. 128, no. 26, pp. 8384–8385, 2006.**

[135] **T. A. Ostomel, Q. Shi, C. K. Tsung, H. Liang, and G. D. Stucky, "Spherical bioactive glass with enhanced rates of hydroxyapatite deposition and hemostatic activity," *Small*, vol. 2, no. 11, pp. 1261–1265, 2006.**

[136] **S. Tokoro, T. Satoh, Y. Okubo, K. Igawa, and H. Yokozeki, "Latent dystrophic subcutaneous calcification in patients with chronic venous insufficiency," *Acta Derm. Venereol.*, vol. 89, no. 5, pp. 505–508, 2009.**

[137] **S. Enoch, S. Kupitz, D. Miller, and K. Harding, "Dystrophic calcification as a cause for non healing leg ulcers," *Int Wound J.*, vol. 2, no. 2, pp. 142–7, 2005.**

[138] **S. Agarwal, J. H. Wendorff, and A. Greiner, "Use of electrospinning technique for biomedical applications," *Polymer (Guildf).*, vol. 49, no. 26, pp. 5603–5621, Dec. 2008.**

[139] **S. W. Lee, Y. U. Kim, S. S. Choi, T. Y. Park, Y. L. Joo, and S. G. Lee, "Preparation of SiO2/TiO2 composite fibers by sol-gel reaction and electrospinning," *Mater. Lett.*, vol. 61, pp. 889–893, 2007.**

[140] **W. Li, C. T. Laurencin, E. J. Caterson, R. S. Tuan, and F. K. Ko, "Electrospun nanofibrous structure : A novel scaffold for tissue engineering," *J Biomed Mater Res*, vol. 60, no. 4, pp. 613–21, 2002.**

[141] **Y. Ji, K. Ghosh, B. Li, J. C. Sokolov, R. A. F. Clark, and M. H. Rafailovich, "Dual-syringe reactive electrospinning of cross-linked hyaluronic acid hydrogel nanofibers for tissue engineering applications," *Macromol. Biosci.*, vol. 6, no. 10, pp. 811–817, 2006.**

[142] **W. J. Li, R. L. Mauck, J. A. Cooper, X. Yuan, and R. S. Tuan, "Engineering controllable anisotropy in electrospun biodegradable nanofibrous scaffolds for musculoskeletal tissue engineering," *J. Biomech.*, vol. 40, no. 8, pp. 1686–1693, 2007.**

[143] **V. Thomas, M. V Jose, S. Chowdhury, J. F. Sullivan, D. R. Dean, and Y. K. Vohra, "Mechano-morphological studies of aligned nanofibrous scaffolds of polycaprolactone fabricated by electrospinning.," *J. Biomater. Sci. Polym. Ed.*, vol. 17, no. 9, pp. 969–984, 2006.**

[144] **R. Murugan and S. Ramakrishna, "Design strategies of tissue engineering scaffolds with controlled fiber orientation.," *Tissue Eng.*, vol. 13, no. 8, pp. 1845–1866, 2007.**

[145] **C. E. Ayres, G. L. Bowlin, R. Pizinger, L. T. Taylor, C. A. Keen, and D. G. Simpson, "Incremental changes in anisotropy induce incremental changes in the material properties of electrospun scaffolds," *Acta Biomater.*, vol. 3, no. 5, pp. 651–661, 2007.**

[146] **N. Bhardwaj and S. C. Kundu, "Electrospinning: a fascinating fiber fabrication technique.," *Biotechnol. Adv.*, vol. 28, no. 3, pp. 325–47, 2010.**

[147] **J. Xie, X. Li, and Y. Xia, "Putting Electrospun Nanofibers to Work for Biomedical Research.," *Macromol. Rapid Commun.*, vol. 29, no. 22, pp. 1775–1792, Nov. 2008.**

[148] **Y. F. Goh, I. Shakir, and R. Hussain, "Electrospun fibers for tissue engineering, drug delivery, and wound dressing," *J. Mater. Sci.*, vol. 48, no. 8, pp. 3027–3054, 2013.**

[149] **J. A. Matthews, G. E. Wnek, D. G. Simpson, and G. L. Bowlin, "Electrospinning of collagen nanofibers," *Biomacromolecules*, vol. 3, no. Iii, pp. 232–238, 2002.**

[150] **G. Taylor, "Electrically Driven Jets," *Proceedings of the Royal Society of London*, vol. 313, no. 1515. pp. 453–475, 1969.**

[151] **D. Li and Y. Xia, "Electrospinning of Nanofibers: Reinventing the Wheel?," *Adv. Mater.*, vol. 16, no. 14, pp. 1151–1170, Jul. 2004.**

[152] **D. H. Reneker and A. L. Yarin, "Electrospinning jets and polymer nanofibers," *Polymer (Guildf).*, vol. 49, no. 10, pp. 2387–2425, May 2008.**

[153] **J. C. Ro and I. J. Chung, "The rheology of silica sols during the gelation process," *J. Non. Cryst. Solids*, vol. 126, pp. 259–266, 1990.**

[154] **S. H. Tan, R. Inai, M. Kotaki, and S. Ramakrishna, "Systematic parameter study for ultra-fine fiber fabrication via electrospinning process," *Polymer (Guildf).*, vol. 46, pp. 6128–6134, 2005.**

[155] **M. M. Hohman, M. Shin, G. Rutledge, and M. P. Brenner, "Electrospinning and electrically forced jets. II. Applications," in *Physics of Fluids*, vol. 13, no. 8, 2001, pp. 2221–2236.**

[156] **Q. P. Pham, U. Sharma, and A. G. Mikos, "Electrospun poly (E-caprolactone) microfiber and multilayer nanofiber/microfiber scaffolds: Characterization of scaffolds and measurement of cellular infiltration," *Biomacromolecules*, vol. 7, no. 10, pp. 2796–2805, 2006.**

[157] **C. Zhang, X. Yuan, L. Wu, Y. Han, and J. Sheng, "Study on morphology of electrospun poly(vinyl alcohol) mats," *Eur. Polym. J.*, vol. 41, no. 3, pp. 423–432, 2005.**

[158] **C. S. Ki, D. H. Baek, K. D. Gang, H. L. Ki, I. C. Um, and Y. H. Park, "Characterization of gelatin nanofiber prepared from gelatin-formic acid solution," *Polymer (Guildf).*, vol. 46, pp. 5094–5102, 2005.**

[159] **X. Geng, O. H. Kwon, and J. Jang, "Electrospinning of chitosan dissolved in concentrated acetic acid solution," *Biomaterials*, vol. 26, no. 27, pp. 5427–5432, 2005.**

[160] **J. S. Lee *et al.*, "Role of molecular weight of atactic poly(vinyl alcohol) (PVA) in the structure and properties of PVA nanofabric prepared by electrospinning," *J. Appl. Polym. Sci.*, vol. 93, no. 4, pp. 1638–1646, 2004.**

[161] **D. H. Reneker and I. Chun, "Nanometre diameter fibres of polymer, produced by electrospinning," *Nanotechnology*, vol. 7, pp. 216–223, 1999.**

[162] **M.M Demir, I Yilgor, E Yilgor, and B Erman, "Electrospinning of polyurethane fibers," *Polymer (Guildf).*, vol. 43, no. 11, pp. 3303–3309, 2002.**

[163] **L. Larrondo and R. St. John Manley, "Electrostatic fiber spinning from polymer melts. I. Experimental observations on fibre formation and properties," *J. Polym. Sci. Polym. Phys. Ed.*, vol. 19, no. 6, pp. 909–920, 1981.**

[164] **L. Larrondo and R. St. John Manley, "Electrostatic fiber spinning from polymer melts. II. Examination of the flow field in an electrically driven jet," *J. Polym. Sci. Polym. Phys. Ed.*, vol. 19, no. 6, pp. 921–932, 1981.**

[165] **L. Larrondo and R. St. John Manley, "Electrostatic fiber spinning from polymer melts. III. Electrostatic deformation of a pendant drop of polymer melt," *J. Polym. Sci. Polym. Phys. Ed.*, vol. 19, no. 6, pp. 933–940, 1981.**

[166] **D. S. Katti, K. W. Robinson, F. K. Ko, and C. T. Laurencin, "Bioresorbable Nanofiber-Based Systems for Wound Healing and Drug Delivery: Optimization of Fabrication Parameters," *Am. J. Dermatopathol.*, vol. 70B, no. 2, pp. 286–296, 2004.**

[167] **L. Wannatong, A. Sirivat, and P. Supaphol, "Effects of solvents on electrospun polymeric fibers: Preliminary study on polystyrene," *Polym. Int.*, vol. 53, no. 11, pp. 1851–1859, 2004.**

[168] **X. Y. Yuan, Y. Y. Zhang, C. Dong, and J. Sheng, "Morphology of ultrafine polysulfone fibers prepared by electrospinning," *Polym. Int.*, vol. 53, no. 11, pp. 1704–1710, 2004.**

[169] **S. Megelski, J. S. Stephens, D. Bruce Chase, and J. F. Rabolt, "Micro- and nanostructured surface morphology on electrospun polymer fibers," *Macromolecules*, vol. 35, no. 22, pp. 8456–8466, 2002.**

[170] **H. W. Kim, H. E. Kim, and J. C. Knowles, "Production and potential of bioactive glass nanofibers as a next-generation biomaterial," *Adv. Funct. Mater.*, vol. 16, pp. 1529–1535, 2006.**

[171] **F. Quintero *et al.*, "Laser Spinning of Bioactive Glass Nanofibers," *Adv. Funct. Mater.*, vol. 19, no. 19, pp. 3084–3090, Oct. 2009.**

[172] **D. Jung, Steven B. Delbert E, "Scaffolds with trace element for tissue regeneration in mammals," US8287896 B2, 2010.**

[173] **C. S. Ki *et al.*, "Development of 3-D nanofibrous fibroin scaffold with high porosity by electrospinning: Implications for bone regeneration," *Biotechnol. Lett.*, vol. 30, pp. 405–410, 2008.**

[174] **Y. Ji *et al.*, "Electrospun three-dimensional hyaluronic acid nanofibrous scaffolds," *Biomaterials*, vol. 27, pp. 3782–3792, 2006.**

[175] **A. Obata, H. Ozasa, T. Kasuga, and J. R. Jones, "Cotton wool-like poly(lactic acid)/vaterite composite scaffolds releasing soluble silica for bone tissue engineering," *J. Mater. Sci. Mater. Med.*, vol. 24, pp. 1649–1658, 2013.**

[176] **T. Kasuga, A. Obata, H. Maeda, Y. Ota, X. Yao, and K. Oribe, "Siloxane-poly(lactic acid)-vaterite composites with 3D cotton-like structure," *J. Mater. Sci. Mater. Med.*, vol. 23, no. 10, pp. 2349–2357, 2012.**

[177] **X. Zong, K. Kim, D. Fang, S. Ran, B. S. Hsiao, and B. Chu, "Structure and process relationship of electrospun bioabsorbable nanofiber membranes," *Polymer (Guildf).*, vol. 43, no. 16, pp. 4403–4412, Jul. 2002.**

[178] **A. L. Yarin, W. Kataphinan, and D. H. Reneker, "Branching in electrospinning of nanofibers," *J. Appl. Phys.*, vol. 98, 2005.**

[179] **G. Srinivasan, "Structure and morphology of electrospun polymer fibres," University of Akron, PhD Thesis, 1994.**

[180] **P. Sepulveda, J. R. Jones, and L. L. Hench, "Bioactive sol-gel foams for tissue repair," *J Biomed Mater Res*, vol. 59, no. 2, pp. 340–348, 2002.**

[181] **K. Fujikura, A. Obata, and T. Kasuga, "Cellular Migration to Electrospun Poly(Lactic Acid) Fibermats," *J. Biomater. Sci.*, vol. 23, no. January 2015, pp. 37–41, 2012.**

[182] **H. Lu, T. Zhang, X. P. Wang, and Q. F. Fang, "Electrospun submicron bioactive glass fibers for bone tissue scaffold," *J. Mater. Sci. Mater. Med.*, vol. 20, pp. 793–798, 2009.**

[183] **H. Fong, I. Chun, and D. H. Reneker, "Beaded nanofibers formed during electrospinning," vol. 40, pp. 4585–4592, 1999.**

[184] **T. J. Sill and H. A. von Recum, "Electrospinning: applications in drug delivery and tissue engineering.," *Biomaterials*, vol. 29, no. 13, pp. 1989–2006, May 2008.**

[185] **C. L. Casper, J. S. Stephens, N. G. Tassi, D. B. Chase, and J. F. Rabolt, "Controlling surface morphology of electrospun polystyrene fibers: Effect of humidity and molecular weight in the electrospinning process," *Macromolecules*, vol. 37, no. 2, pp. 573–578, 2004.**

[186] **A. L. B. Macon *et al.*, "A unified in vitro evaluation for apatite-forming ability of bioactive glasses and their variants," *J. Mater. Sci. Mater. Med.*, vol. 26, no. 2, p. 115, 2015.**

[187] **A. Martinez, I. Izquierdo-Barba, and M. Vallet-Regi, "Bioactivity of a CaO - SiO2 binary glasses system," *Chem. Mater.*, vol. 12, no. 10, pp. 3080–3088, 2000.**

[188] **J. Zhong and D. C. Greenspan, "Processing and properties of sol-gel bioactive glasses.," *J. Biomed. Mater. Res.*, vol. 53, no. January, pp. 694–701, 2000.**

[189] **H. Peterlik, S. Kubuki, and K. Sinko, "Structural Characterization of Gel-Derived Calcium Silicate Systems," *J. Phys, Chem. A*, vol. 114, pp. 10403–10411, 2010.**

[190] **D. H. Reneker, A. L. Yarin, H. Fong, and S. Koombhongse, "Bending instability of electrically charged liquid jets of polymer solutions in electrospinning," *J. Appl. Phys.*, vol. 87, no. 9, pp. 4531–4547, 2000.**

[191] **J. Serra *et al.*, "Influence of the non-bridging oxygen groups on the bioactivity of silicate glasses," *J. Mater. Sci. Mater. Med.*, vol. 13, no. 12, pp. 1221–1225, 2002.**

[192] **J. Serra *et al.*, "FTIR and XPS studies of bioactive silica based glasses," *J. Non. Cryst. Solids*, vol. 332, no. 1–3, pp. 20–27, 2003.**

[193] **T. Hayashi and H. Saito, "Preparation of CaO-SiO glasses by the gel method," *J. Mater. Sci.*, vol. 15, pp. 1971–1977, 1980.**

[194] **S. L. Percival, S. McCarty, J. A. Hunt, and E. J. Woods, "The effects of pH on wound healing, biofilms, and antimicrobial efficacy," *Wound Repair Regen.*, vol. 22, no. 2, pp. 174–186, 2014.**

[195] **R. Hoffman, J. Noble, and M. Eagle, "The use of proteases as prognostic markers for the healing of venous leg ulcers," *J. Wound Care*, vol. 8, no. 6, pp. 273–276, 2014.**

[196] **G. Gethin, "The significance of surface pH in chronic wounds Palliative Wound Care View project Management of Patients With Venous Leg Ulcers View project," *Wounds UK*, vol. 3, no. 3, pp. 52–55, 2007.**

[197] **H. H. Leveen *et al.*, "Chemical acidification of wounds. An adjuvant to healing and the unfavorable action of alkalinity and ammonia," *Ann. Surg.*, vol. 178, no. 6, pp. 745–753, 1973.**

[198] **L. S. Connell *et al.*, "Chemical characterisation and fabrication of chitosan-silica hybrid scaffolds with 3-glycidoxypropyl trimethoxysilane," *J. Mater. Chem. B*, vol. 2, no. 6, pp. 668–680, 2014.**

[199] **G. Kirste, J. Brandt-Slowik, C. Bocker, M. Steinert, R. Geiss, and D. S. Brauer, "Effect of chloride ions in Tris buffer solution on bioactive glass apatite mineralization," *Int. J. Appl. Glas. Sci.*, vol. 8, no. 4, pp. 438–449, 2017.**

[200] **N. K. et al L. Bingel, D. Groh, "Influence of dissolution medium pH on ion release and apatite formation of Bioglass 45S5," *Mater Lett.*, vol. 143, pp. 279–282, 2015.**

[201] **S. Vicente, C. Moia, H. Zhu, and X. Vigé, "In vitro evaluation of the internalization and toxicological profile of silica nanoparticles and submicroparticles for the design of dermal drug delivery strategies," *J. Appl. Toxicol.*, vol. 37, no. 12, pp. 1396–1407, 2017.**

[202] **Y. Zhang, L. Hu, D. Yu, and C. Gao, "Influence of silica particle internalization on adhesion and migration of human dermal fibroblasts," *Biomaterials*, vol. 31, no. 32. pp. 8465–8474, 2010.**

[203] **S. E. McNeil, S. A. Hobson, V. Nipper, and K. D. Rodland, "Functional calcium-sensing receptors in rat fibroblasts are required for activation of SRC kinase and mitogen-activated protein kinase in response to extracellular calcium," *J. Biol. Chem.*, vol. 273, no. 2, pp. 1114–1120, 1998.**

[204] **B. A. Allo, A. S. Rizkalla, and K. Mequanint, "Synthesis and electrospinning of ε-polycaprolactone-bioactive glass hybrid biomaterials via a sol-gel process," *Langmuir*, vol. 26, no. 23, pp. 18340–18348, 2010.**

[205] **S. Midha, T. B. Kim, W. Van Den Bergh, P. D. Lee, J. R. Jones, and C. A. Mitchell, "Preconditioned 70S30C bioactive glass foams promote osteogenesis in vivo," *Acta Biomater.*, vol. 9, no. 11, pp. 9169–9182, 2013.**

[206] **J. R. Jones, O. Tsigkou, E. E. Coates, M. M. Stevens, J. M. Polak, and L. L. Hench, "Extracellular matrix formation and mineralization on a phosphate-free porous bioactive glass scaffold using primary human osteoblast (HOB) cells," *Biomaterials*, vol. 28, pp. 1653–1663, 2007.**

[207] **S. Brunauer, L. S. Deming, W. E. Deming, and E. Teller, "On a Theory of the van der Waals Adsorption of Gases," *J. Am. Chem. Soc.*, vol. 62, no. 7, pp. 1723–1732, 1940.**

[208] **R. Dulbecco and G. Freeman, "Plaque production by the polyoma virus," *Virology*, vol. 8, no. 3, p. 396, 1959.**

[209] **R. M. Day, "Bioactive glass stimulates the secretion of angiogenic growth factors and angiogenesis in vitro.," *Tissue Eng.*, vol. 11, no. 5–6, pp. 768–777, 2005.**

[210] **R. Detsch, P. Stoor, A. Grünewald, J. A. Roether, N. C. Lindfors, and A. R. Boccaccini, "Increase in VEGF secretion from human fibroblast cells by bioactive glass S53P4 to stimulate angiogenesis in bone," *J. Biomed. Mater. Res. - Part A*, vol. 102, no. 11, pp. 4055–4061, 2014.**

[211] **T. Sun, D. Norton, R. J. McKean, J. W. Haycock, A. J. Ryan, and S. MacNeil, "Development of a 3D cell culture system for investigating cell interactions with electrospun fibers," *Biotechnol. Bioeng.*, vol. 97, no. 5, pp. 1318–1328, 2007.**

[212] **A. Haider, S. Haider, and I. K. Kang, "A comprehensive review summarizing the effect of electrospinning parameters and potential applications of nanofibers in biomedical and biotechnology," *Arab. J. Chem.*, vol. 11, no. 8, pp. 1165–1188, 2018.**

[213] **A. M. Toufiq, F. Wang, Q. U. A. Javed, and Y. Li, "Influence of SiO2 on the structure-controlled synthesis and magnetic properties of prismatic MnO2 nanorods," *Nanotechnology*, vol. 24, no. 41, 2013.**

[214] **R. Koirala, K. R. Gunugunuri, S. E. Pratsinis, and P. G. Smirniotis, "Effect of zirconia doping on the structure and stability of CaO-based sorbents for CO2 capture during extended operating cycles," *J. Phys. Chem. C*, vol. 115, no. 50, pp. 24804–24812, 2011.**

[215] **C. D. Wager, W. M. Riggs, L. E. Davis, J. F. Moulder, and M. P.-E. Corp., *Handbook of X-ray Photoelectron Spectroscopy*. 1981.**

[216] **Y. Cui *et al.*, "Evolution of the electronic structure of CaO thin films following Mo interdiffusion at high temperature," *Phys. Rev. B - Condens. Matter Mater. Phys.*, vol. 91, no. 3, pp. 1–6, 2015.**

[217] **Y. Miura, H. Kusano, T. Nanba, and S. Matsumoto, "X-ray photoelectron spectroscopy of sodium borosilicate glasses," *J. Non. Cryst. Solids*, vol. 290, no. 1, pp. 1–14, 2001.**

[218] **J. Perez-Pariente, F. Balas, and M. Vallet-Regi, "Surface and chemical study of SiO2·P2O5·CaO·(MgO) bioactive glasses," *Chem. Mater.*, vol. 12, no. 3, pp. 750–755, 2000.**

[219] **G. Lusvardi, G. Malavasi, L. Menabue, V. Aina, and C. Morterra, "Fluoride-containing bioactive glasses: Surface reactivity in simulated body fluids solutions," *Acta Biomater.*, vol. 5, no. 9, pp. 3548–3562, 2009.**

[220] **M. F. Kulesz-Martin, D. Fabian, and J. S. Bertram, "Differential Calcium Requirements for growth of mouse skin Epithelial and Fibroblasts Cells," *Cell Prolif.*, vol. 17, no. 5, pp. 525–533, 1984.**

[221] **H. K. Ting *et al.*, "Phosphate content affects structure and bioactivity of sol-gel silicate bioactive glasses," *Int. J. Appl. Glas. Sci.*, vol. 8, no. 4, pp. 372–382, 2017.**

[222] **N. S. Chickerur, M. S. Tung, and W. E. Brown, "A mechanism for incorporation of carbonate into apatite," *Calcif. Tissue Int.*, 1980.**

[223] **A. Chrissanthopoulos, N. Bouropoulos, and S. N. Yannopoulos, "Vibrational spectroscopic and computational studies of sol-gel derived CaO-MgO-SiO2binary and ternary bioactive glasses," *Vib. Spectrosc.*, vol. 48, no. 1, pp. 118–125, 2008.**

[224] **J. D. H. Ana Walt, H. W. Rinn, and L. K. Frevel, "Chemical Analysis by X-Ray Diffraction: Classification and Use of X-Ray Diffraction Patterns," *Ind. Eng. Chem. - Anal. Ed.*, vol. 10, no. 9, pp. 457–512, 1938.**

[225] **D. C. Clupper, J. E. Gough, M. M. Hall, a G. Clare, W. C. LaCourse, and L. L. Hench, "In vitro bioactivity of S520 glass fibers and initial assessment of osteoblast attachment.," *J. Biomed. Mater. Res. A*, vol. 67, pp. 285–294, 2003.**

[226] **H. W. Kim, H. H. Lee, and G. S. Chun, "Bioactivity and osteoblast responses of novel biomedical nanocomposites of bioactive glass nanofiber filled poly(lactic acid)," *J. Biomed. Mater. Res. - Part A*, vol. 85, no. 3, pp. 651–663, 2008.**

[227] **A. J. Vander, J. A. Sherman, and D. Luciano, *Human Physiology: The Mechanisms of Body Function*. New York: McGraw-Hill Publishing Company, 1990.**

[228] **J. Li *et al.*, "Preparation of copper-containing bioactive glass/eggshell membrane nanocomposites for improving angiogenesis, antibacterial activity and wound healing," *Acta Biomater.*, vol. 36, pp. 254–266, 2016.**

[229] **V. Mortazavi, M. Mehdikhani Nahrkhalaji, M. H. Fathi, S. B. Mousavi, and B. Nasr Esfahani, "Antibacterial effects of sol-gel-derived bioactive glass nanoparticle on aerobic bacteria," *J. Biomed. Mater. Res. - Part A*, vol. 94, no. 1, pp. 160–168, 2010.**

[230] **J. M. Aguirre, A. Gutierrez, and O. Giraldo, "Simple Route for the Synthesis of Copper Hydroxy Salts," *Int. J. Intell. Enterp.*, vol. 22, no. 3, pp. 546–551, 2011.**

[231] **K. Zheng, J. Wu, W. Li, D. Dippold, Y. Wan, and A. R. Boccaccini, "Incorporation of Cu-Containing Bioactive Glass Nanoparticles in Gelatin-Coated Scaffolds Enhances Bioactivity and Osteogenic Activity," *ACS Biomater. Sci. Eng.*, vol. 4, no. 5, pp. 1546–1557, 2018.**

[232] **A. Hoppe *et al.*, "In vitro reactivity of Cu doped 45S5 Bioglass® derived scaffolds for bone tissue engineering," *J. Mater. Chem. B*, vol. 1, no. 41, pp. 5659–5674, 2013.**

[233] **J. C. Dupin, D. Gonbeau, P. Vinatier, and A. Levasseur, "Systematic XPS studies of metal oxides, hydroxides and peroxides," *Phys. Chem. Chem. Phys.*, vol. 2, no. 6, pp. 1319–1324, 2000.**

[234] **M. C. Biesinger, "Advanced analysis of copper X-ray photoelectron spectra," *Surf. Interface Anal.*, vol. 49, no. 13, pp. 1325–1334, 2017.**

[235] **J. S. Shaikh *et al.*, "Synthesis and characterization of Ru doped CuO thin films for supercapacitor based on Bronsted acidic ionic liquid," *Electrochim. Acta*, vol. 56, no. 5, pp. 2127–2134, 2011.**

[236] **S. Poulston, P. M. Parlett, P. Stone, and M. Bowker, "Surface oxidation and reduction of CuO and Cu2O studied using XPS and XAES," *Surf. Interface Anal.*, vol. 24, no. 12, pp. 811–820, 1996.**

[237] **J. W. Lim *et al.*, "Nanoscale investigation of long-term native oxidation of Cu films," *Thin Solid Films*, vol. 516, no. 12. pp. 4040–4046, 2008.**

[238] **S. Meghana, P. Kabra, S. Chakraborty, and N. Padmavathy, "Understanding the pathway of antibacterial activity of copper oxide nanoparticles," *RSC Adv.*, vol. 5, no. 16, pp. 12293–12299, 2015.**

[239] **C. Dunnill *et al.*, "Reactive oxygen species (ROS) and wound healing: the functional role of ROS and emerging ROS-modulating technologies for augmentation of the healing process," *Int. Wound J.*, vol. 14, no. 1, pp. 89–96, 2017.**

[240] **H. Wang *et al.*, "Influence of Cu doping in borosilicate bioactive glass and the properties of its derived scaffolds," *Mater. Sci. Eng. C*, vol. 58, pp. 194–203, 2016.**

[241] **S. De Vrieze, T. Van Camp, a. Nelvig, B. Hagström, P. Westbroek, and K. De Clerck, "The effect of temperature and humidity on electrospinning," *J. Mater. Sci.*, vol. 44, pp. 1357–1362, 2009.**